Modelling of Airwake Hazards for Helicopter Flight Simulation

Thesis submitted in accordance with the requirements of the University of Liverpool for the degree of

Doctor in Philosophy

by

Sergio Henriquez Huecas

January 2023

Blank Page

Modelling of Airwake Hazards for Helicopter Flight Simulation

Abstract

This thesis summarises the work performed in the use of flight simulation to assess the impact of wake encounters and turbulence on the safety of helicopter operations. An initial literature search is presented, revealing a lack of previous research regarding the impact of wind turbine wakes on helicopter operations and a lack of accurate and easy to implement modelling tools for the assessment of the impact of turbulence on rotorcraft handling. The work is divided in two main parts:

In the first part, following a literature review, results of flight simulation tests representing the accidental crossing of a wind turbine wake by a helicopter are presented. Encounters are of a 'mild' severity, flight safety was not compromised and resulted mainly in excursions in the yaw axis and deviations in roll. The pilot workload required in the recovery of from the initial encounter was strongly related to the aircraft's handling qualities, especially yaw to pitch and yaw to roll cross couplings.

The second part of the thesis details the development and implementation of a new turbulence modelling method for flight simulation. The model is based on an adaptation of a synthetic eddy method (SEM). It generates a random turbulence field surrounding the aircraft by filling a control volume with turbulence generating eddies which are displaced by ambient flow; this is the first time this type of modelling has been implemented in real-time piloted flight simulation. The induced turbulence automatically cross correlates disturbances across all aircraft elements and can be adjusted by changing strength, shape and size of eddies and combining series of eddies with different properties. Average frequency of the induced turbulence is proportional to the cube root of the number of eddies; increasing the frequency results in increased computational costs. Nevertheless, the SEM turbulence generator can produce real time disturbances within the 0.1 – 1Hz frequency range which has the most impact on pilot workload. Offline and piloted simulation was used to evaluate the model and compare against a precomputed wake using a Mann turbulence model. Results show that SEM induced turbulence can impact handling in similar manners as the precomputed wake, while offering random turbulence in real time.

Acknowledgments

The work reported in this thesis was a part of project NITROS (Network for Innovative Training on ROtorcraft Safety). Project NITROS has received funding from the European Union's Horizon H2020 research and innovation program under the Marie Skłodowska-Curie grant agreement No. 2016-721920.

I wanted to express my gratitude to all the people who have helped me during these years and without whom this thesis would not have been possible.

My supervisors. Professor Mark White from the University of Liverpool and Professor George Barakos from the University of Glasgow. For their mentorship and their guidance, advice, effort, support and help and their infinite patience during my thesis.

To my second supervisor Professor Michael Jump for his support and help, especially during the last year of my thesis.

To the NITROS program for the funding of this project, and all the unique opportunities it provided.

To Wajih Memon, Christopher Dadswell, Neil Cameron, Thomas Fell, Mushfiqul Alam. For all their invaluable help with flight simulation modelling and testing.

To the test pilots Andy Berrymann, Christopher Dennis Brown and Mark Prior. For their expert flying and their advice in planning and preparation of all the trials for this project.

To my friends and colleagues from the Flight Science Laboratory in Liverpool, the Simulation Laboratory in Glasgow and within the NITROS program for their help and for all the good conversations and great moments.

To Mom, Dad and my brothers, for all their, support, patience, help, encouragement and love.

To all of them:

Thank you

Publications:

Journal Paper:

- Henriquez Huecas, S.; White, M. D.; Barakos, G.: *A turbulence model for flight simulation and handling qualities analysis based on a synthetic Eddy method*, Journal of the American Helicopter Society (2020), Volume 67, Number 3, July 2022, pp. 85-97(13). https://doi.org/10.4050/JAHS.67.032007

Conference Proceedings:

- Henriquez Huecas, S.; White, M. D.; Barakos, G.: *Helicopter handling qualities analysis using a synthetic eddy turbulence model*, April 2021, NITROS International Workshop on Engineering for Rotorcraft Safety, April 2021
- Henriquez Huecas, S.; White, M. D.; Barakos, G.: *Flight simulation testing of a turbulence model based on a Synthetic Eddy Method*, Published in 46th European Rotorcraft Forum, Moscow, Russia, September 2020. Cancelled due to Covid – 19 pandemic.
- Henriquez Huecas, S.; White, M. D.; Barakos, G.: *A turbulence model for flight simulation and handling qualities analysis based on a synthetic Eddy method*, 76th Vertical Flight Society Forum, October 2020.
- Quaranta G, Masarati P, White MD, Barakos G, Pavel MD, Fasiello S, Henriques Huecas S, Morelli M, Ghiasvand S, Noor NH, Taymourtash N, Akel E, Ying Y, Friesen D, Scaramuzzino PF.: *Assesment of the feasibility of an extended range helicopter operational standard for offshore flights,* 44th European Rotorcraft Forum, Delft, Netherlands, September 2018

Reports:

- White, M. D.; Barakos, G.; Henriquez Huecas, S.: (2018), GARTEUR HC-AG23: *Wind turbine wakes and helicopter operations. Final report. Work package 4. Flight simulation activities at the University of Liverpool*. Distribution Limited.

Nomenclature:

A_{ij}	Cholesky decomposition of Reynolds stress tensor (*m/s*)
b	Aircraft wingspan (*m*)
b_k	Filter coefficient for term or axis k
C	Gaussian shape function normalization coefficient
c	Wing or blade chord (*m*)
Cl / Cl_α	Lift coefficient / lift coefficient slope
C_{M_x}, C_{M_y}, C_{M_z}	Roll, pitch, yaw moment coefficient
E(ω), E(k)	Energy spectra across frequency, across wavelength coefficient
F_f	Flatness or Kurtosis of function f
$\mathcal{F}(f)$	Fourier transform of function f
g	Acceleration of gravity (m/s^2)
G(s)	Transfer function
GS	Glideslope
h	Aircraft flight height (*m* or *ft*)
$K_{\frac{n}{m}}$	Bessel function of order n/m
K	gain
$\boldsymbol{k}$, $\lvert k\rvert = \sqrt{k_1^2 + k_2^2 + k_3^2}$	Wave number vector, wave number modulus
l	length
L / l(r)	Lift (*N*)/ lift distribution along r (*N/m*)
L	Characteristic turbulence wavelength
M_x, M_y, M_z	Roll, pitch, yaw moment (*Nm*)
M_β	Flapping moment at rotor hub (*Nm*)
M	Mass (*kg*)
M_{Vortex}	Vortex induced induced roll moment
N	Number of eddies
N_b	Number of rotor/ turbine blades
n	Loads factor
p	Flow pressure (*Pa*)
p_m	Eddy strength scaling coefficient
p, q, r	Aircraft roll, pitch and yaw rates (*rad/s* or *deg/s*)
q_m	Eddy size scaling coefficient
r_c	Radius of vortex core (*m*)
R, r	Radius, Radial distance (*m*)
$R_{ij}(\xi)$	Turbulence cross correlation function for distance metric ξ
Re	Reynolds number
Re_{ij}	Reynolds Stress Tensor (m^2/s^2)
S	Aircraft wing area (m^2)
S_{uj}	Skewness for turbulent velocity component u_i
S_{Rotor}	Vorticity source due to rotor
St	Strouhal number
t	time (*s*)
u, v, w / u_i	Velocity components / velocity component along i-th axis (*m/s*)
U	Norm of velocity vector
V_B	Eddy control volume for the synthetic eddy method (m^3)
V_c	Vortex core flow velocity

V_T, V_P	Velocity tangential to rotor, Velocity perpendicular to rotor (*m/s*)
Vgn	Aircraft ground speed
V_{Vortex}	Vortex flow velocity
W	Weight (*N*)
x, y, z	Cartesian coordinates
$\boldsymbol{Z}(\boldsymbol{k})$	Fourier–Stieltjes vector

α	Angle of attack (*rad* or *deg*)
β	Angle of sideslip (*deg*)
$\beta = \beta_0 + \beta_{1s} * \sin(\psi) + \beta_{1c} * \cos(\psi)$	Helicopter rotor blade flapping components (*rad* or *deg*)
γ	Helicopter lock number
Γ	Vortex strength (m^2/s)
Γ	Boundary layer shear
δ_{lat} ; δ_{long} ; δ_{col} ; δ_{pedal}	Control inputs in lateral, longitudinal, collective, pedal
ϵ	Turbulent energy transfer
ε_i	Intensity of turbulent eddy along i-th axis
ζ	Eddy series size scaler
η	Kolmogorov scale
$\theta = \theta_0 + \theta_{1s} * \sin(\psi) + \theta_{1c} * \cos(\psi)$	Helicopter rotor blade pitch components (*rad* or *deg*)
λ	Rotor inflow
$\mu_x, \mu_z, \mu = \sqrt[2]{\mu_X^2 + \mu_Z^2}$	Helicopter/rotor advance ratio, longitudinal, vertical, norm
ν	Kinematic viscosity
ν_β	Rotor flapping frequency ratio
ξ	Distance metric for cross correlation (m or non dimensional)
ξ	Damping ratio
ξ	Filter scale
ρ	Air density (kg/m^3)
τ	Characteristic time length (*s*)
τ_p	Temporal phase delay (*s*)
σ_i	Standard deviation
$\boldsymbol{\sigma} = [\sigma_x, \sigma_y, \sigma_z]$	Characteristic length of turbulent eddies (*m*)
Φ ; ΔΦ	Phase; Angular phase delay (*rad* or *deg*)
$\phi_{ij}(\omega)$	Power spectral density for frequency ω
Φ, θ, ψ	Aircraft roll, pitch and yaw angles (*rad* or *deg*)
ψ	Rotor blade azimuth (*rad* or *deg*)
ω	Temporal frequency (*Hz* or *rad/s*)
ω	Flow vorticity (m^2/s)
$\omega_{BW_{gain}}$; $\omega_{BW_{phase}}$	Gain bandwidth ; phase bandwidth
ω_n	Natural frequency (*rad/s* or *Hz*)
Ω	Spatial frequency (*1/m*)
Ω	Rotor angular velocity (*rpm* or *rad/s*)

Abbreviations:

ABL	Atmospheric boundary layer
AC	Aircraft
ACP	Aerodynamic Computation Point
ADS – 33	Aeronautical Design Standard Performance Specification: Handling Qualities Requirements for Military Rotorcraft
AR	Aircraft aspect ratio
ASRA	Canadian Research Council - Advanced Systems Research Aircraft
AW	Airwake
BWR	Bedford Workload Rating
CAA	Civil Aviation Authority
CAP	CAA paper
CETI	Control Equivalent Turbulence Inputs
CFD	Computational Fluid Dynamics
CRIT	Critical value
CS	Certification Specifications
DES	Detached Eddy Simulations
DIPES	Deck Interface Pilot Effort Scale
DLR	Deutsches Luft – und Raumfahrtzentrum ; German Aerospace Centre
DNS	Direct Numerical Simulation
DVE	Degraded Visual Environment
EASA	European Aviation Safety Agency
EMS	Emergency Medical Services
erf	Error function
FAA	Federal Aviation Administration
FHQ	Flight Handling Qualities
FFT	Fast Fourier Transform
GARTEUR	Group for Aeronautical Research and Technology in Europe
GVE	Good Visual Environment
HSAR	Helicopter Search and Rescue
HSDI	Helicopter – Ship dynamic Interface
HOMP	Helicopter Operations Monitoring Programme
HQ / HQR	Handling Qualities / Handling Qualities rating
IAS	Indicated Air Speed
ICAO	International Civil Aviation Organization
ILS	Instrument Landing System
LES	Large Eddy Simulation
LIDAR	Light detection and ranging
LOS	Line of sight
MBB	Messerschmitt-Bölkow-Blohm
MCA	United Kingdom - Maritime Coastguard Agency
MIL – STD	United States Military Standards
MOR	Mandatory Occurrence Reports
MTE	Mission task element
NASA	National Aeronautics and Space Administration
NITROS	Network for Innovative Training on ROtorcraft Safety
NREL	National Renewable Energy Laboratory

NRC	National Research Council - Canada
NRL	Netherlands Aerospace Research Centrum
NS	Navier Stokes
OFE	Operational flight envelope
PH	Precision Hover
PhD	Doctor of Philosophy
PIO	Pilot Induced Oscillations
pk	Peak values
PSD	Power Spectral Density
RANS	Reynolds Averaged Navier – Stokes
RCAH	Rate Command Attitude Hold
RCR	Roll control ratio
RD	Rotor diameter
RECAT – EU	European Wake Turbulence Categorisation and Separation Minima on Approach and Departure
RFR	Rotor flapping ratio
RMC	Roll moment coefficient
RMS	Root Mean Square
SAR	Search and rescue
SAS	Stability augmentation system
SCAS	Stability and control augmentation system
SHOL	Ship – helicopter operating limits
SEM	Synthetic Eddy Method
S&L	Steady and level flight
SORBET	Simulation Of Rotor Blade Element Turbulence
TAS	True Air Speed
UK	United Kingdom
US	United States
VK	Von Karman turbulence spectra
WT	Wind turbine
WVE	Wake vortex encounter

Contents

List of tables

List of figures

1 Introduction

1.1 Overview of NITROS Program

Due to their flexibility, helicopters are used in a wide variety of roles which exposes them to a large range of environmental hazards. When combined with their technical complexity and difficulty of flying compared to fixed-wing aircraft, this results in significantly higher accident rates [1], [2]. Increased demand for the services provided by rotorcraft, as well as the possibilities of new applications (for example: on – demand point to point transportation), requires important improvements in safety if an increase in the total number of accidents is to be avoided.

The main aim of the Network for Innovative Training on ROtorcraft Safety (NITROS) [3], a Marie Sklowdoska Curie Action Joint European Doctorate programme, was to train future engineering researchers to understand the complex phenomena characterizing rotorcraft and take measures to improve rotorcraft safety and design standards. To this end, twelve double doctorate projects were undertaken at four leading European universities in the field of aerospace engineering (Politecnico Di Milano, Technical University of Delft, University of Glasgow and University of Liverpool). These projects are interrelated and performed multidisciplinary research and development to address rotorcraft safety issues in three main areas:

- Rotorcraft modelling and vehicle design
- Rotorcraft pilot training and human-machine interface
- Environment – rotorcraft interactions

1.2 Mitigation of Airwake Hazards

This PhD study was NITROS project number 7, focusing on the hazards posed by encounters with airwakes or turbulence. The novelty here is the development of new turbulence models for use in piloted flight simulation and examining its impact on aircraft handling qualities and pilot workload.

Maintaining safe flight conditions in these environments is of great relevance in all aerial operations and an important limiter in airport capacity [4]. There has been significant research and regulatory effort in the fixed-wing aircraft community to enhance safety and improve operations [4], [5], [6].

In contrast, there has been only a limited number of similar efforts regarding rotorcraft operations, which are dispersed across a larger variety of scenarios, especially offshore and shipborne missions [7], [8] and combined fixed wing aircraft – rotorcraft operations [9]. An increasingly important area of concern is the impact on safety resulting from encounters with wind turbine airwakes. Between 2005 and 2017 installed wind power generating capacity in Europe has more than tripled from 40GW to over 160GW [10] (see Figure 1-1), wind turbine installations have grown in size and number, and occasionally are being installed near airfields and heliports [11]. Helicopters are employed in the maintenance and installation of offshore or remote wind turbines [12] and are essential for Search and Rescue (SAR) or Emergency Medical Service (EMS) missions near wind turbine fields. The risk of a rotorcraft/wind turbine wake encounter is therefore becoming more likely, and the severity of those encounters requires examination. Despite this, the CAA does not provide any clear regulations on flight near wind farms in their policy and guidelines on wind turbines document [13], while the Netherlands Aerospace Research Centrum (NLR) proposes helicopters keep a separation to wind turbines of 6 diameters [14]. Wind turbines, especially offshore installations are becoming increasingly bigger (see Figure 1-2) and such a separation criterion might require the deactivation of large proportions of wind farms during maintenance operations. Also, the impact of such large wakes might not be possible to extrapolate from what is known from smaller installations. Communications with NITROS partners', as well as other industry stakeholders in the wind energy and helicopter services sectors, have confirmed there is a lack of data and the need of further research to address this.

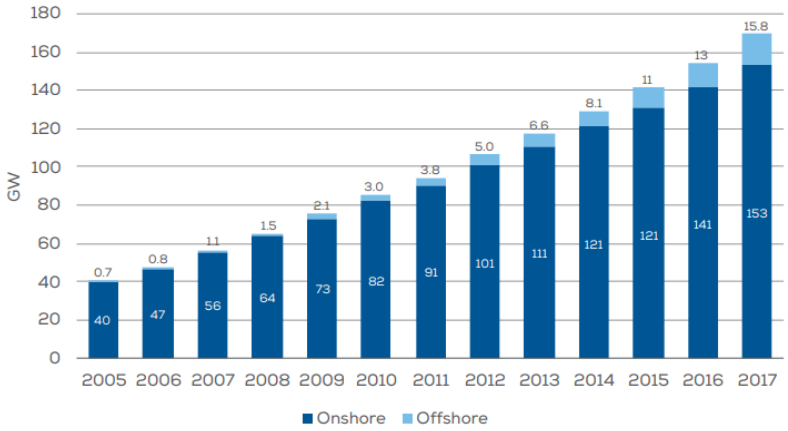

Figure 1-1: Installed wind energy generation capacity in Europe 2005 - 2017. [10]

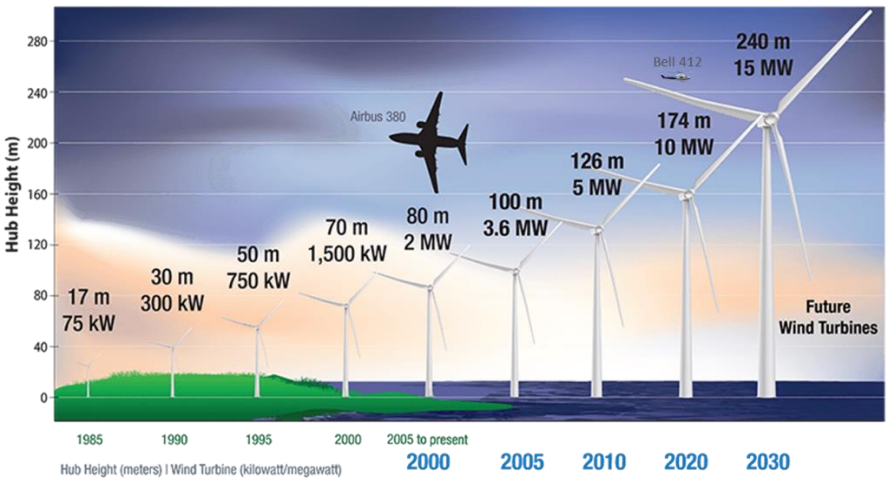

Figure 1-2: Characteristic sizes of current and proposed wind turbine designs compared with size of A380. Bell 412 added for scale. Source: National Renewable Energy Laboratory (NREL) newsletter: https://www.nrel.gov/wind/newsletter-202004.html

This thesis seeks to better understand rotorcraft and pilot behaviour during such operations to reduce the impact of a turbulent encounter event on safety. Airwake and turbulence models, flight dynamic analysis and piloted flight simulation tests were employed to research pilot – rotorcraft dynamics and pilots' concerns during airwake encounters and flight within turbulence with the aim to identify and quantify resulting hazards. The resulting findings will inform future developments towards mitigation of these hazards such as improvements in simulation fidelity, training procedures and regulations, new operational guidance, or the development of new warning systems.

This thesis is structured as follows. Chapter 2 contains a literature review detailing the current status of research in the field of aircraft encounters with airwakes, current techniques employed in the modelling of turbulence for rotorcraft flight simulations and wind turbine airwake modelling techniques. Chapter 3 describes the objectives of the project. Chapter 4 describes simulator trials of wind turbine wake encounters and discusses the results. Following this, Chapter 5 describes initial steps in the development of a turbulence model based on a Synthetic Eddy Method (SEM) for the future assessment of turbulence effects on rotorcraft flight. Chapter 6 describes initial flight simulation testing to assess the feasibility of the SEM for handling qualities analysis. Chapter 7 describes calibration of the SEM and the subsequent flight simulation trials which used this model are described in Chapter 8 comparing the impact on handling of SEM induced turbulence with the disturbances from a Mann turbulence model. Finally, the thesis conclusions and suggestions for future work are presented in Chapter 9.

Throughout this thesis the term turbulence modelling is used, in the context of flight simulation, as the reproduction of atmospheric flow velocity variations representative of those produced by atmospheric turbulence, those resulting from aircraft downwash disturbances or those generated from flow structures shed by wind turbines.

2 Literature Review

2.1 Introduction

This chapter provides an overview of the literature relevant to this research. While the initial focus of this work was on the theme of rotorcraft encounters with wind turbine wakes, due to the limited previous research on the topic, the review has also considered other types of atmospheric turbulence and wake encounters to identify possible areas of read-across.

The second part of the thesis focused to the development of a simple modelling tool to represent wake and atmospheric turbulence for use in flight simulation trials of such encounters. A review of the available literature of wake and turbulence modelling was also performed, focussing on applications for flight simulation.

The literature review is structured in several parts. Section 2.2 introduces the current regulatory and certification framework covering rotorcraft and fixed wing operations when encountering airwakes and under turbulence. Section 2.3 focuses on wind turbine airwake aerodynamics and modelling and Section 2.4 discusses airwake and turbulence modelling techniques applied for flight simulation and flight dynamics research. Finally a series of cases studies are discussed, covering research into rotorcraft encounters with wakes from fixed wing aircraft (Section 2.5), use of flight simulation to support ship – helicopter operations (Section 2.6) and rotorcraft and fixed wing encounters with wind turbine wakes (Section 2.7). The findings of the literature review are summarised and discussed in Section 2.8.

2.2 Current regulatory framework

2.2.1 Airplane encounters with airplane wakes:

The economic and societal importance of civilian air transportation means that most research related to aircraft airwake encounters focuses on the problem of a large fixed-wing aircraft encountering the vortex wake shed by another large fixed-wing aircraft. A regulatory framework currently exists to minimize the risk of civilian airplanes encountering the vortex wake of other airplanes. Based on aircraft size and weight classification, separation distances are defined to allow for dissipation of the shed

vortices between lead and following aircraft during take–off and landing phases of flight.

A flight test campaign conducted by Airbus to assess the airwake risks posed by the A380 to following aircraft on approach and landings, led to an Europe wide effort to optimize these rules to increase traffic capacity without reducing safety. This resulted in the European Wake Turbulence Categorization and Separation Minima on Approach and Departure document (RECAT – EU) [4]. The new categorization (see Figure 2-1) retains the existing light and superheavy categories, as F and A respectively, and divides the current medium heavy categories into 4: E, D, C and B. By keeping current separation distance for the lighter follower aircraft in these categories, the heavier follower can safely reduce their distance to the leading aircraft.

Vortex encounters by a follower aircraft mainly result in upsets in the aircraft roll axis. The Roll Moment Coefficient (RMC) [15] has been the main parameter employed to define the new RECAT-EU separation criteria and has been positively correlated with pilot ratings of encounter severity during simulation experiments [16].

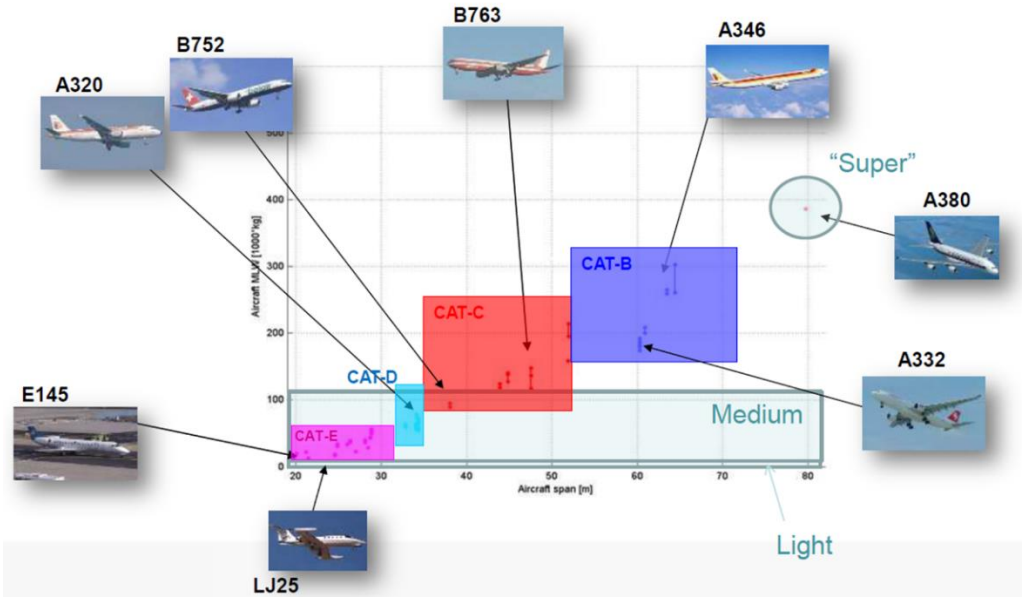

Figure 2-1: New RECAT-EU airplane categories. ICAO's heavy category is divided into categories B and C and the medium category is divided into categories D and E [17].

The RMC is derived from the roll control ratio defined as the ratio between the wake induced roll moment (M_{Vortex}) on the aircraft and a simplified assumption of the maximum moment the follower aircraft can counteract:

$$RMC = \frac{M_{Vortex}}{\frac{1}{2}\rho U_f^2 S_f b_f} \quad 2\text{-}1$$

where ρ is the air density, U_f is the following aircraft's indicated airspeed, S_f, is its wing area and b_f is its wingspan.

M_{Vortex} can be obtained from measurements or simulations or it can be estimated from the leading aircraft's geometry and a simplified vortex strength model as given in Eq 2-2.

$$\Gamma_0 = \frac{W_l}{\rho U_l S_l b_l} \quad 2\text{-}2$$

where Γ_0 is the initial vortex strength shed by the leading aircraft, W_l its total weight, U_l its flight speed and S_l and b_l its wing area and wingspan respectively. The resulting RMC estimation employed in the elaboration of the RECAT-EU separation criteria is:

$$M_{Vortex} = \frac{\Gamma(r)}{U_f b_f}\frac{AR_f}{AR_f + 2} * F\left(\frac{b_l}{b_f}\right)$$

$$F\left(\frac{b_l}{b_f}\right) = 1 - 2\left(2a\frac{b_l}{b_f}\right)\left(\sqrt{1 + \left(2a\frac{b_l}{b_f}\right)^2} - \left(2a\frac{b_l}{b_f}\right)\right) \quad 2\text{-}3$$

with $\Gamma(r)$ being the vortex strength at distance $r = \sqrt{(y - y_v)^2 + z_v^2}$ from the following aircraft's wing centre, AR_f being the follower aircrafts aspect ratio, and b_l and b_f the wingspan of the leading and follower aircraft respectively. a = 0.035 is a coefficient dependent on the vortex core radius and the wingspan of the generating aircraft.

Other parameters have been suggested which take into account flight conditions during an aircraft wake encounter. Using data and pilot feedback from a flight simulation campaign conducted by Airbus, Luckner et al. [18] proposed a series of metrics derived from encounter induced glideslope deviations and roll control ratio:

$$\Delta GS_{CRIT} = \left(\Delta GS + 4 * \Delta\dot{GS}\right) * K_{\Delta GS}$$
$$RCR_{CRIT} = \frac{RCR}{0.006 * h + 0.5} \quad 2\text{-}4$$

with ΔGS and $4 * \Delta \dot{GS}$ being the current induced glideslope deviations and its expected value in 4 seconds and $K_{\Delta GS}$ is a function that decreases as the aircraft approaches the ground and deviations from the glideslope increase as the pilot manoeuvres for final approach. RCR_{CRIT} are roll control ratio values scaled by the inverse of aircraft flight height, *h*, reflecting the increase severity of encounters near the ground. Using data obtained from the simulation tests, these metrics produce a better prediction of Go Around events than either one by themselves.

2.2.2 Rotorcraft certification and performance requirements: EASA CS – 27, CS – 29 and ADS – 33E-PRF

The regulatory framework and performance requirements for helicopters operating in turbulent environments is less well defined than for fixed wing aircraft. Currently, there is no unified approach to the assessment of turbulence or gust effects on rotorcraft operations or for severity mitigation through design, regulations or training. EASA Certification Specifications for small (CS – 27, [19]) and large (CS – 29, [20]) rotorcraft only establish the need to ensure controllability and structural resistance under expected gust conditions: "*Rotorcraft must be controllable at critical, weight, centre of gravity distribution, rotor regimes and power off conditions under wind of up to 31 km/h under all azimuths and must withstand loads from vertical and horizontal gusts of up to 9.1 m/s."*

The US Army Aeronautical Design Standard Performance Specification: Handling Qualities Requirements for Military Rotorcraft, ADS – 33E-PRF (ADS-33) [21] provides a more comprehensive set of handling qualities metrics and standardised mission task elements with defined performance targets for their assessment. Yaw rate limits are defined in response to step lateral gust for all aircraft. Aircraft with attitude hold control systems have to comply with limits on peak deviations when subjected to single disturbances in roll and pitch, which shall be modelled as direct inputs in actuator surfaces. Level 1 requires return to less than 10% of peak deviations in roll and pitch within 10s (20s for pitch under good visual conditions) after a pulse disturbance. When evaluating control systems against periodic, high frequency, low amplitude disturbances, aircraft response bandwidth is evaluated using the same boundaries for temporal phase delay, τ_p, and control bandwidth, ω_{BW}, as defined for response to pilot control inputs, which are shown in Figure 2-2.

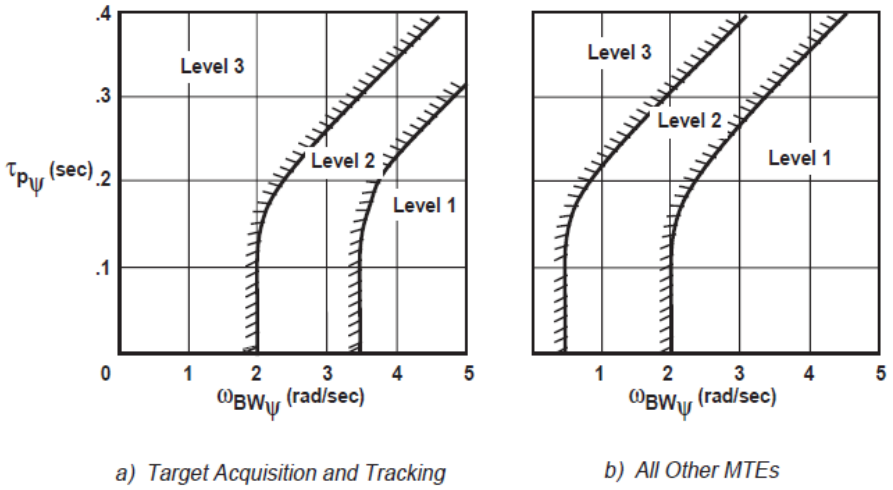

Figure 2-2: ADS-33 defined boundaries for delay and bandwidth boundaries for aircraft response to control inputs or disturbances [21]

Bandwidth values are the lower of either gain bandwidth, $\omega_{BW_{gain}}$, or phase bandwidth, $\omega_{BW_{phase}}$, and are obtained as defined in Figure 2-3 and phase delay is obtained from the formula:

$$\boldsymbol{\tau_p = \frac{\Delta\Phi_{2\omega_{180}}}{57.3(2\omega_{180})}} \qquad 2\text{-}5$$

were $\Delta\Phi_{2\omega_{180}}$ is the angular phase delay at the double of ω_{180} which is the frequency at which phase delay is 180 deg.

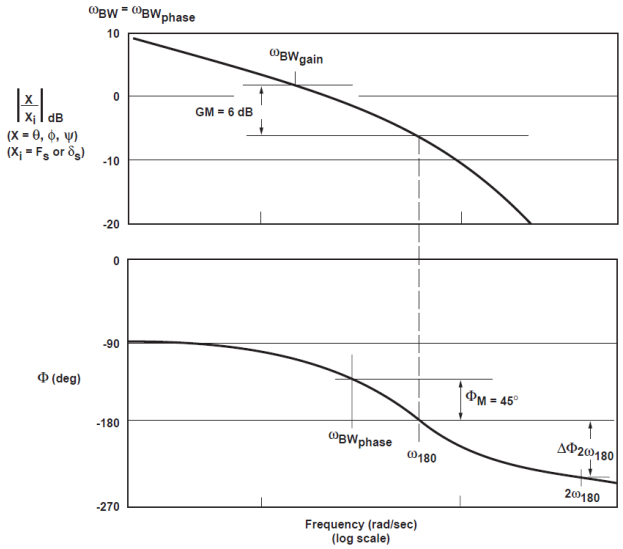

Figure 2-3: Definition of phase delay and gain bandwidth for evaluation of ADS-33 aircraft response criteria.

While the required boundaries for bandwidth response to pilot control inputs are obtained from analysis of data from flight test and piloted flight simulations [22], there seems to be little supporting data for applying the same criteria to aircraft response to disturbances. An analysis of pilot workload during flight tests performed by Lusardi et al. [23] for the extraction of data (see Section 2.3.3) suggests that these requirements might not be adequate. This criteria is intended to be replaced by a disturbance response bandwidth criteria in the future [24].

2.2.3 Rotorcraft Operations

In contrast to the separation rules to prevent fixed-wing aircraft from encountering airwakes during take-off or landing approaches, no similar rules exist for rotorcraft operations. However, there are ongoing research efforts to examine the hazards posed by turbulent flows in aircraft operations in/around civil airfields, naval launch and recovery activities, to offshore platform and in wind turbine farms.

A variety of test and simulation studies have been performed covering specific encounter conditions, and are presented in Section 2.5 of this literature review.

2.2.3.1 RECAT – EU and helicopters:

Garcia and Barakos [25], proposed a methodology to include helicopters within the new European wake categorization and separation criteria (RECAT-EU). For helicopters in forward flight, the rotor far wake, defined as further away than 3 rotor diameters, can be approximated to a vortex pair similar to that produced by a fixed wing aircraft which is dependent on the helicopter's weight and rotor size. By applying a decay model obtained from experimental measurements [26], a minimum safe distance for follower aircraft can be defined.

Helicopters present a different dynamic during airwake encounters compared with fixed wing aircraft, with pilots expressing much greater concern for upsets in the pitch axis rather than in roll (see Section 2.5). To determine a safe separation criterion for following helicopters, Garcia proposed an estimation of pitch upsets:

$$\boldsymbol{\theta(t)} = \frac{\frac{\boldsymbol{V_{Vortex}}}{\boldsymbol{R}}\boldsymbol{\mu\gamma}}{\mathbf{8}\left(\mathbf{1}-\frac{\mathbf{1}}{\mathbf{2}}\boldsymbol{\mu^2}\right)} * \boldsymbol{t} \qquad \textit{2-6}$$

with V_{Vortex} being the vortex induced flow velocity, γ the helicopter's Lock number and $\mu = \sqrt[2]{\mu_X^2 + \mu_Z^2}$ the helicopter advance ratio.

By limiting the maximum upset to 10 degrees and applying existing limits of rolling moment coefficient for following airplanes, helicopters can be classified within the existing RECAT-EU airplane categories based on weight and rotor diameter.

2.2.3.2 Ship Helicopter Operating Limits

Considerable research effort has been dedicated to studying the safe handling of helicopters during shipborne operations. Turbulence produced by the flow of air over and around the superstructure of naval vessels is a significant contributing factor of pilot workload [27]. Each new combination of naval vessel class and helicopter type requires the definition of the Ship Helicopter Operating Limit (SHOL), the conditions of wind over deck velocity and azimuth under which launch and recovery operations can be safely conducted (see Figure 2-4). These limits are usually determined through flight test campaigns.

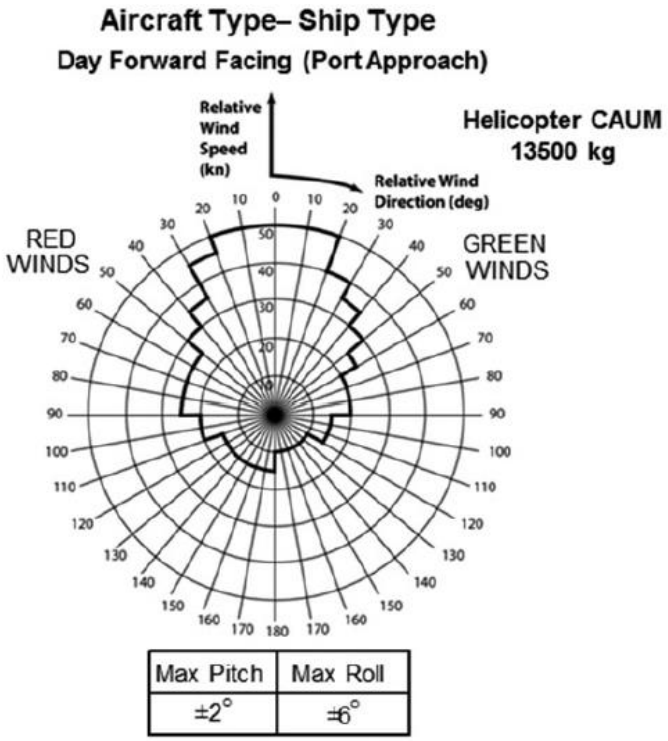

Figure 2-4: Example SHOL showing wind-over-deck envelope for a UK port-side landing manoeuvre. [8]

Such tests are expensive and inherently dangerous and are subject to variations in weather conditions which make it impossible to adequately cover all possible

environmental conditions. Similar limitations also affect the capability to conduct pilot training.

Whilst there has been considerable research conducted in the use of modelling and simulation to examine pilot workload issues related to, in part, the turbulence on and around the ship's deck [8] further work is required to characterise the ship's airwake and its impact on aircraft handling. There are some promising new developments in predicting safety limits [28], but these may still rely on computationally expensive turbulent airwake calculation methods (see Section 2.4.1) and there is scope for examining simplified, but representative, airwake models.

2.2.3.3 Turbulence Criteria for Helicopter Offshore Operations

For civilian offshore or shipboard operations, the UK Civil Aviation Authority (CAA) has established a maximum of 1.75m/s on the standard deviation of vertical wind velocity over landing areas [29]. These limits were defined after a series of piloted and offline flight simulation studies using time accurate data recordings from wind tunnel measurements [7]. Pilots were tasked to perform a landing approach and to maintain their position over the helideck under different wind and turbulence conditions.

The standard deviation of the control inputs used by the pilot model were used as a metric to quantify the approach difficulty and, together with results from piloted simulations, were used to find a relation between predicted ratings and standard deviations in vertical flow velocity due to turbulence.

The obtained ratings predictor and turbulence criteria were tested against the data from the Helicopter Operations Monitoring Programme (HOMP) [30]. A proposed limit on maximum standard deviation in vertical flow velocities of $\sigma(w) = 1.75\frac{m}{s}$ over offshore landing areas, corresponding to a predicted rating of *5.5*, was adopted by the CAA.

Other proposed metrics for workload prediction exist based on control stick activity metrics. A higher frequency of pilot control inputs usually correlates with a higher workload [31]. In a similar way, wavelet analysis of control inputs has been used to discriminate guidance and stabilization inputs, the latter being usually of lower amplitude and higher frequency and usually correlated to greater workload requirements, in order to predict handling quality ratings [32].

2.2.4 Impact of wind farms on aviation and helicopters

Assessing the impact of wind turbine installations on aircraft safety and defining operational guidance is still a work in progress. The CAA document CAP 764 “Policy and Guidelines on Wind Turbines” [13], describes possible risks for air traffic. For example, wind turbines can present obstacles and provide confusing returns to radar and navigation systems. The document provides guidance for the planning process of wind energy developments near existing airfields or heliports, focussing mainly on ensuring enough clearance to ensure obstacle free airspace, assure that wind turbines do not interfere with navigation aids, communications equipment or weather radar and that adequate lightning and signalling is provided to avoid collisions. But decisions are being undertaken on a case by case basis based on local conditions and requirements.

CAP 764 refers to research conducted at the University of Liverpool [11] (see Section 2.7.1.2) in regards of general aviation encounters with wind turbine wakes and confirms the need for further research in the hazards presented by wind turbine wakes: “*Although research on wind turbine wakes has been carried out, the effects of these wakes on aircraft are not yet known*” and while there have been no “*Mandatory Occurrence Reports (MOR) or aircraft accident reports related to wind turbines in the UK*” there have been “*anecdotal reports of aircraft encounters with wind turbine wakes representing a wide variety of views as to the significance of the turbulence*”.

The UK Maritime Coastguard Agency (MCA), also defines requirements to reduce the risk of helicopter search and rescue (HSAR) operations near or within wind farms [33]. These include, arranging wind turbines in straight, parallel lines to provide, and allow for safe access to, flight lanes within wind farms and the installation of adequate visual cues to prevent collisions with wind turbines. If navigation through the wind farm is solely reliant on instruments, any aircraft shall not access areas where there is less than 500m separation between different turbines.

Winching operations, whether commercial or for SAR purposes, should be performed with the aircraft oriented towards the incoming wind, and the turbine should be oriented accordingly. Turbine rotation should be locked and the blades set to a position where they can be used by the pilot as a visual reference. The MCA also considers that a malfunction in the wind turbine might prevent it from shutting down to allow safe aircraft operations. As a result, SAR might require operating within the turbine wake in unfavourable wind conditions and with limited visual cueing. No

substantiated safety guidance has been provided regarding operations in the proximity of wind turbines or how to assess their impact during SAR operations.

2.3 Wind turbine airwake aerodynamics

The previous section focussed on the regulatory issues involved with helicopter operations in turbulent environments. Modelling and simulation can be used to inform new safety regulations but there are significant challenges that need to be examined to determine the fidelity requirements of such approaches.

2.3.1 Wind turbine airwake structure

Wind turbine wakes are characterized by a decrease in flow pressure, axial velocity and an addition of rotational velocity downstream of the rotor approximately along the main wind direction. As they do so, the diameter of the airwake increases and flow velocity gradually increases until reaching ambient flow velocity again.

Airwake length is usually defined by the distance at which this axial velocity deficit can still be measured. The maximum value of the velocity deficit can be over 70% of freestream wind velocity and declines exponentially after the first 2 diameters (Figure 2-5). It can still be significant 5 diameters downstream and velocity deficits of around 5% of freestream velocity have been measured up to 15 diameters behind the wind turbine rotor [34].

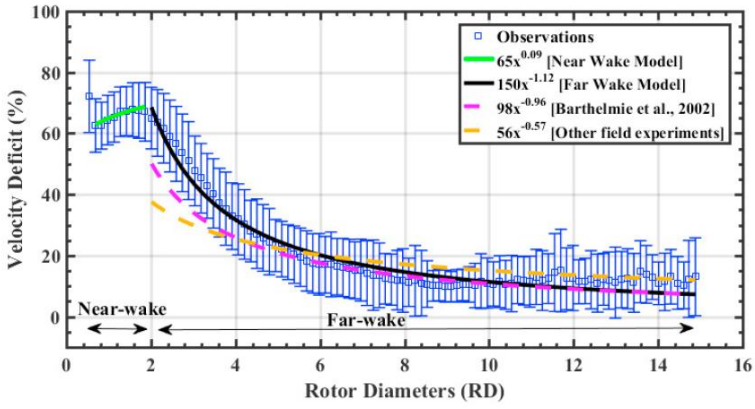

Figure 2-5: Average wind turbine wake velocity deficit over 252 measurement samples, as a function of normalized downwind distance (in Rotor Diameter [RD]) from the wind turbine. The error bars indicate one standard deviation of all the samples. Measurements performed by Krishnamurthy [34]

Due to the changes in their structure as they extend downstream from the rotor, it is usual to identify two or three separate regions in the wake (Figure 2-6). The near wake extends immediately behind the blade rotor and can extend up to 2 or 4 diameters

downstream. In this region the influence of turbine geometry on the flow can be clearly identified [35]. The most notable effects are the vortex structures shed by the blade, forming a structure consisting of a core vortex extending along the centre of the wake and a spiral structure of tip vortexes which surround the wake and resulting in a strong velocity gradient in its vicinity.

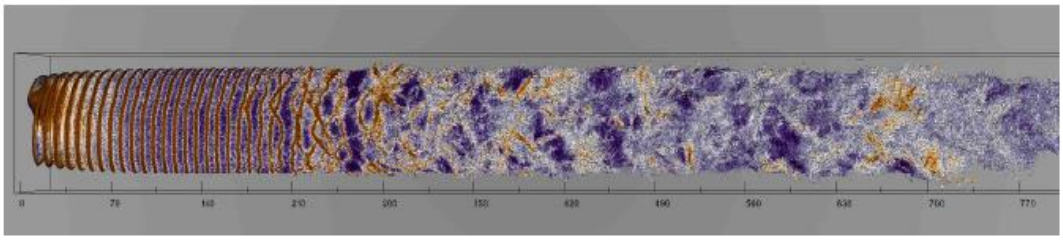

Figure 2-6: Instantaneous surfaces of the velocity magnitude of 8.5 m/s coloured by density demonstrating the evolution and breakdown of the wind turbine wake. CFD simulations of the NREL WindPACT-1.5MW wind turbine, performed by Kirby [36]

The region between 2 diameters and 6 diameters downstream is sometimes known as the mid – wake [36]. Vortex structures, begin to show instabilities and interact between themselves, resulting in the deformation of the vortex core and the merging of vortices leading to the formation of larger flow structures [37].

The far wake is considered to be the region extending beyond 6 diameters downstream of the wind turbine [38]. In this region vortex structures become unstable and progressively break down into smaller scale structures, dissipating energy progressively until the flow is dominated by small scale turbulence. In free shear flows, the rate of energy transfer from large to smaller eddies, ϵ, was quantified by Kolmogorov [39] and is only dependent on flow velocity, u, and a characteristic length, L:

$$\boldsymbol{\epsilon = \frac{u^3}{L}} \qquad 2\text{-}7$$

Flow mixing continues until the smallest possible scale, which depends on the kinematic viscosity, $\boldsymbol{\nu}$, and the value of the energy transfer and is known as the Kolmogorov scale, η, which dissipates fully before breaking down:

$$\boldsymbol{\eta = \left(\frac{\nu^3}{\epsilon}\right)^{\frac{1}{4}} = \frac{L}{Re^{\frac{3}{4}}}} \qquad 2\text{-}8$$

This results in a Gaussian and axisymmetric distribution of axial velocity along the wake and its ultimate dissipation until it is no longer possible to recognize the wake from the ambient freestream flow.

The exact nature and location of vortex breakdown and transition from the near wake to the far wake and the resulting total wake length is still not clearly understood and appears to be dependent on a multitude of factors. Higher wind speeds result in larger separation between successive tip vortices, delaying their interaction and merging [37]. Atmospheric turbulence seems to be the dominant factor and Sorensen et al. propose a logarithmic relationship between turbulence intensity and start of wake breakdown [38]. Irregular terrain also influences surrounding turbulence, and offshore wind turbines tend to present more stable and longer wakes for this reason [34].

2.3.2 Airwake Modelling

Flow behaviours, including the wake behind wind turbines, are described by the Navier – Stokes (NS) equations (2-9). For the simulation of wind turbine wakes and wind farms, the assumption of incompressible flow is reasonable.

$$\boldsymbol{\nabla} * \boldsymbol{u} = \mathbf{0}$$
$$\frac{\boldsymbol{\partial u}}{\boldsymbol{\partial t}} + (\boldsymbol{u} * \boldsymbol{\nabla}) * \boldsymbol{u} = -\frac{\mathbf{1}}{\boldsymbol{\rho}}\boldsymbol{\nabla p} + \boldsymbol{\nu \nabla^2 u} \qquad \textit{2-9}$$

Direct solution of Navier Stokes equations, known as Direct Numerical Simulations (DNS) are the most precise for low Reynolds number flows at small scales. The wide range of characteristic size, velocity and time scales influencing the aerodynamics of wind turbine wakes, makes such complete detailed modelling impossible with today's computational means [38]. A variety of methodologies are therefore applied according to the region and the phenomena of the airwake of interest. Rotor models are employed to estimate power extracted and structural loads on the wind turbine and introduce the loads and rotational velocities it induces on the flow. These are used as inputs for modelling the wake. Potential flow models can model the large-scale vortex structures of the near and mid wake. Navier – Stokes solvers can provide greater accuracy and are necessary for modelling of the far wake turbulence. Adequate modelling of vortex breakdown and the transition from the near wake to the far wake still remains an issue [40].

2.3.2.1 Rotor Models:

Actuator models directly apply the required force or vorticity components to the flow based on tabulated airfoil data. Depending on the required accuracy, three possible implementations are possible.

Actuator disk models provide the simplest formulation. The force components are averaged across the rotor surface disk or across each annular section for non-uniformly loaded disks. For vorticity formulations, a distribution of circular vortex sheets is shed at regular intervals. They cannot be applied for accurate near wake modelling. They however provide reasonable results for far wake simulations [41].

Actuator line models distribute force or vorticity components along rotating lines located at the aerodynamic centre of the blade. Actuator line models provide greater accuracy than actuator disk models for simulating near and middle wake characteristics, such as tip and root vortex, for a higher computational cost [38].

Finally, in actuator surface models, blades are represented by planar surfaces. Compared with actuator line models they present additional improvements in modelling of flow near the airfoils and in the near wake. They require, however, tabulated data of the skin friction and pressure distribution of the employed airfoil [41].

2.3.2.2 Potential formulations

In potential and vorticity based formulations the airwake is described as spiral sheets or lines of vortices shed by the applied rotor model and induced flow velocities are computed applying Biot-Savart law [42]. These methods are used extensively by the rotorcraft community for flight dynamics modelling and flight simulation [43] and have also seen limited application for fast calculation of far wind turbine wakes. They tend to fall in two main categories: prescribed and free wake models.

In prescribed wake models, the geometry of the wake has been predefined from experimental data, they require few computational resources and provide good agreement with experimental results as shown by Wang et al. [44]. While prescribed wake models are limited in solving unsteady and time varying conditions, results can be used as seed values of more complex methods.

Free wake models allow the wake vortex structure to deform itself under its own influence. This reduces reliance on experimental results and allows simulating time changing conditions or external influences on the wake, like ground effect. However, they require more computational resources, with simulation time being proportional to the square of the number of total vortex elements [40], [43]. Among others, some strategies employed to reduce the costs are reducing the number of vortex elements used to represent the wake and grouping or neglecting the effect of far field vortex segments [43].

Potential formulations do not simulate turbulence and their effects on the structure of the airwake. They have to be modelled separately, usually based on empirical data. Vortex strength decay is usually assumed to be exponential with distance or vortex age. Vortex instability and merging can be imposed by adding small initial imperfections in the vortex structure [45].

2.3.2.3 Turbulence modelling

Large Reynolds number flows means a reduction in the Kolmogorov scale of the smallest turbulent structures (Eq. 2-8). Grid sizes and computation time steps need to be larger for computations to be feasible, which require making an assumption about the behaviour of turbulence at scales below grid sizes. The two main methodologies employed for simulation of turbulence while maintaining a reasonable grid size are Reynolds Averaged Navier Stokes (RANS) and Large Eddy Simulations (LES) [41], [42].

RANS methods employ a statistical description of the flow, splitting the velocities into the sum of a constant velocity distribution and a distribution of velocity fluctuation with time:

$$\begin{aligned} \boldsymbol{u}(\vec{\boldsymbol{x}}, \boldsymbol{t}) &= \bar{\boldsymbol{u}}(\boldsymbol{x}) + \boldsymbol{u}'(\boldsymbol{x}, \boldsymbol{t}) \\ \bar{\bar{\boldsymbol{u}}}(\boldsymbol{x}) &= \bar{\boldsymbol{u}}(\boldsymbol{x}) \\ \bar{\boldsymbol{u}}'(\boldsymbol{x}, \boldsymbol{t}) &= \mathbf{0} \end{aligned} \qquad \text{2-10}$$

When substituting into the Navier Stokes equations, the term $(\overline{\boldsymbol{u}'\boldsymbol{u}'})$ is unclosed. It is known as the Reynolds stress tensor and can be interpreted as the effect of diffusive turbulent forces. It is considered using algebraic models, such as Kolmogorov's energy decay model, Jones and Launder's $k-\epsilon$ model [46], or based on experimental data.

RANS methods offer a fast engineering method capable of solving the flow in wind turbine airwakes in a few hours of simulation. Its applicability is however limited to those situations where the applied turbulence model is valid. Carrion et al. [37] have shown the capability of RANS methods for full airwake simulations, including predicting the occurrence of vortex breakdown. However, accurate modelling requires fine mesh structures with cell size smaller than the vortex core, otherwise artificial breakdown of the wake might occur due to numerical dissipation, all of which increases the computational cost.

LES models solve some of this issue by solving large scale turbulence components and filtering out turbulence components smaller than the size of the grid by means of a convolution integral.

$$\widetilde{\boldsymbol{u}}(\boldsymbol{x},\boldsymbol{t}) = \int \boldsymbol{u}(\boldsymbol{\xi},\boldsymbol{t}) * \boldsymbol{G}(\boldsymbol{x}-\boldsymbol{\xi},\boldsymbol{\Delta})\boldsymbol{d\xi} \qquad 2\text{-}11$$

With the convolution kernel $\boldsymbol{G}(\boldsymbol{x}-\boldsymbol{\xi},\Delta)$ dependent on the filter width Δ. Application of the filtering to the Navier Stokes equations leads to the appearance of the term $(\widetilde{\boldsymbol{u}\boldsymbol{u}} - \widetilde{\boldsymbol{u}}\widetilde{\boldsymbol{u}})$ representing the effect of sub grid scale stresses and are solved using viscosity models, which relate stresses with the resolved strain and an estimated viscosity or experimental data.

LES methods tend to provide more accurate results for a wider range of situations than RANS, however computational costs scale with the square of the Reynolds number, making them unsuitable for many engineering applications but are useful to provide benchmark results which can be used to calibrate other models.

2.3.2.4 Boundary conditions and inflow turbulence models

Boundary conditions have an important effect on the resulting flow field simulations. RANS simulations use models to represent the impact of turbulence on average flow velocities. In the case of LES and DNS simulations, for a realistic simulation of flow behaviour at the point of interest, the simulation domain upstream needs to be large enough to allow for the boundary layer and turbulence to fully develop. This adds important computational costs to the simulation.

Adding disturbances at the inflow can reduce the required upstream distance for turbulence conditions to fully develop [47]–[49] if the required turbulence properties are to be reproduced with ‘sufficient’ fidelity. Ideally such methods should be easy to

implement and have low computational and storage requirements and should not induce spurious or artificial periodicity in the resulting turbulence. Such models should be able to reproduce low order turbulence statistics such as mean velocity profile, turbulent kinetic energy, Reynolds Stress tensor and two point spatial and time correlations and produce turbulent eddies of the correct shape and size.

2.3.2.4.1 Precursor simulations

Precursor simulations are performed independently of the main simulation. Using a control volume which includes ground boundary conditions and ground obstacles or initial disturbances and can be added to start the generation of turbulence. The outflow plane is usually connected to the inflow. When adequate conditions of turbulence and velocity profile are reached at a given location in the domain, these conditions are used to generate the inflow at the main simulation.

Precursor simulations can be performed concurrently with the main simulation, this avoids the need to precompute the inflow and saves storage but requires performing additional computations during the simulation.

On the other hand, velocity distributions can be stored and reproduced periodically at the inflow of the main simulation, this can be time evolving turbulence at a given location or a snapshot of the entire domain reproduced one slice at a time using Taylors frozen field hypothesis. This requires preparation and storage of the precursor simulation but the stored turbulence can be applied to multiple simulations with similar geometry and scaled to the required amplitude conditions [50].

Precursor simulations can be performed using LES or DNS simulations, and result in the most accurate method of generating turbulence, the main drawback being the additional expense in time or computational resources to perform the additional simulation [41]. In the case of simpler geometries, such as atmospheric flow over flat terrain, faster turbulence models, such as the Mann atmospheric turbulence model [51] (see Section 7.2) can be used to generate inflow planes [52].

2.3.2.4.2 Synthetic turbulence models.

Synthetic turbulence models apply random fluctuations in real time at low computational costs directly at the inflow without the need of a stored library of precomputed or measured turbulence. The eddies generated by these models tend to be

of incorrect shape and size, requiring some downstream development distance, but this still allows for faster generation of turbulence in a precursor simulation or directly at the main simulation. Most methods allow adjustment of the model inputs to reproduce the desired values of one or more of possible turbulent statistics, mean velocity profile, turbulent kinetic energy, Reynolds Stress tensor and two point spatial and time correlations. However, prior knowledge of the flow to be simulated is required to correctly adjust for these values.

Synthetic turbulence methods can be broadly classified as algebraic methods that generate random fluctuations in physical space and spectral methods which generate random disturbances in the frequency space.

2.3.2.4.3 Algebraic methods

Algebraic methods work in the physical space, disturbances are generated using random number generation. A series of random numbers, r_j, with normal distribution and variance $\sigma = 1$, will result in disturbances with zero cross-correlation as well as two-point and two-time correlation and with equal distribution of energy across all turbulence scales.

In order to produce disturbances with the intended cross – correlation from a series of random numbers, r_j, with normal distribution and variance $\sigma = 1$, scaling using the Cholesky decomposition of the target Reynolds stress tensor, ($Re_{ij} = \langle u'_i u'_j \rangle$) is applied [50]:

$$\boldsymbol{u'_i = r_j * A_{ij}} \qquad \textit{2-12}$$

where A_{ij} is the Cholesky decomposition of the target Reynolds stress tensor, ($Re_{ij} = \langle u'_i u'_j \rangle$):

$$\boldsymbol{A} = \begin{bmatrix} \sqrt{\boldsymbol{Re_{11}}} & \boldsymbol{0} & \boldsymbol{0} \\ \dfrac{\boldsymbol{Re_{21}}}{\boldsymbol{A_{11}}} & \sqrt{\boldsymbol{Re_{22} - A_{21}^2}} & \boldsymbol{0} \\ \dfrac{\boldsymbol{Re_{31}}}{\boldsymbol{A_{11}}} & \dfrac{\boldsymbol{Re_{32} - A_{21}A_{31}}}{\boldsymbol{A_{22}}} & \sqrt{\boldsymbol{Re_{33} - A_{31}^2 - A_{32}^2}} \end{bmatrix} \qquad \textit{2-13}$$

To obtain a more realistic spread of turbulent energy across frequency scales and improve two point and two time correlation, filter coefficients, b_k, can be used to scale the resulting turbulence [53]:

$$\boldsymbol{u'(j)} = \sum_{\boldsymbol{k=-N}}^{\boldsymbol{N}} \boldsymbol{b_k r(j+k)} \qquad 2\text{-}14$$

with the resulting two-point correlation based on the shape of the applied filter:

$$< \boldsymbol{u'(j)u'(j+m)} > = \sum_{\boldsymbol{k=-N+m}}^{\boldsymbol{N}} \boldsymbol{b_k b_{k+m}} \qquad 2\text{-}15$$

A recent Algebraic turbulence generator is the Synthetic Eddy Model (SEM) which was developed by Jarrin [54] and has been widely applied in the generation of inflow conditions for LES simulations. The method defines a control volume surrounding the inflow and fills it with randomly placed synthetic eddies which are convected with the main flow direction through this volume and regenerated upstream once they leave it. Each eddy generates random turbulence oscillations within its 'reach' based on its shape function $f(\boldsymbol{x})$ and a randomly assigned sign ε:

$$\boldsymbol{{u'}_i^{\,k}} = \frac{\boldsymbol{1}}{\sqrt{\boldsymbol{N}}} \boldsymbol{A_{ij} \varepsilon_j^k f_\sigma (x - x^k)} \qquad 2\text{-}16$$

Due to its potential to produce turbulence associated to a specific location in space and time, this method has been further explored in this work as a potential turbulence generator for flight simulation. A more extensive explanation of the method can be found in Section 5.2.

2.3.2.4.4 Spectral based methods

Spectral turbulence models generate disturbance in the frequency or wavelength domain and then apply inverse fast Fourier transformations (FFT) to transform them to the physical domain. The signal is synthetized from a prescribed energy spectrum, $E(|k|)$, and a phase dependent on time, ϕ. For a flow evolving in the *x*-direction:

$$\boldsymbol{u'(x)} = \sum_{\boldsymbol{k_y}} \sum_{\boldsymbol{k_z}} \sqrt{\boldsymbol{E(k_y, k_z, \omega)}}\, \boldsymbol{e^{i\phi(k_y, k_z, \omega, t)}} \qquad 2\text{-}17$$

To reduce signal periodicity, phases, ϕ are shifted once every characteristic time interval at a random moment by a random amount. However, the greater phase dependence on time will produce turbulence that differs from the intended energy spectrum and shape of turbulent structures. Turbulent velocities can be rescaled to match intended values of, Re_{ij}. Alternatively, amplitudes can be varied randomly, preserving energy spectra and turbulent structure information at the expense of losing the match with the target Reynolds Stress tensor.

Spectral methods are usually applied to reduce the flow length and computation time of precursor simulations. Additionally, they can be used in combination with algebraic methods, using Fourier generators, to produce isotropic turbulence fluctuations which are then filtered to produce the target energy spectra.

2.4 Turbulence and airwake modelling for flight simulation:

Direct application of turbulence models used for fixed wing aircraft design and certification is inappropriate for the broad range of possible flight and environmental conditions in which helicopters can operate, especially for low speed and low level flight [55]. There is a lack of validation data for proposed helicopter turbulence models [56]. Instead, a variety of methods can be applied to generate helicopter 'relevant' turbulence depending on the objectives of the simulation and the available resources. They can be very broadly classified in three main methods: use of stored time accurate airwake solutions, random gust generation and generation of equivalent control inputs.

2.4.1 Time accurate airwakes:

Time-accurate airwake solutions can be precomputed using Computational Fluid Dynamics tools (CFD). The resulting flow field is interpolated into a structured grid and stored as a look up table. During flight simulation the flow field at the relevant locations of the aircraft's model, known as aerodynamic computation points or ACPs, is extracted by interpolating from the surrounding points in the grid at each time step. This is one of the most realistic means of simulating a particular environmental turbulence and corresponding aircraft responses. The method was first proposed by Bunnel [57] and has been widely employed in the simulation of the Helicopter-Ship Dynamic Interface (HSDI) [58] [8]. However, the computational costs and storage

requirements limits the duration of an airwake (to about ~30s) which are typically time-looped to produce longer periods for the disturbance.

To reduce the number of airwakes that need to be generated, flow velocities can be directly scaled with ambient wind speed [59] while the frequency at which the airwake is reproduced has to be adjusted to preserve the same value of the Strouhal number [58]:

$$St = \frac{\omega * L}{|U|} \qquad 2\text{-}18$$

where **ω** is the frequency at which the airwake is replayed, *l* is the size of the obstacle generating the turbulence and |*U*| is the magnitude of ambient wind. This also allows to scale the airwake with the size of the wake generating object [60].

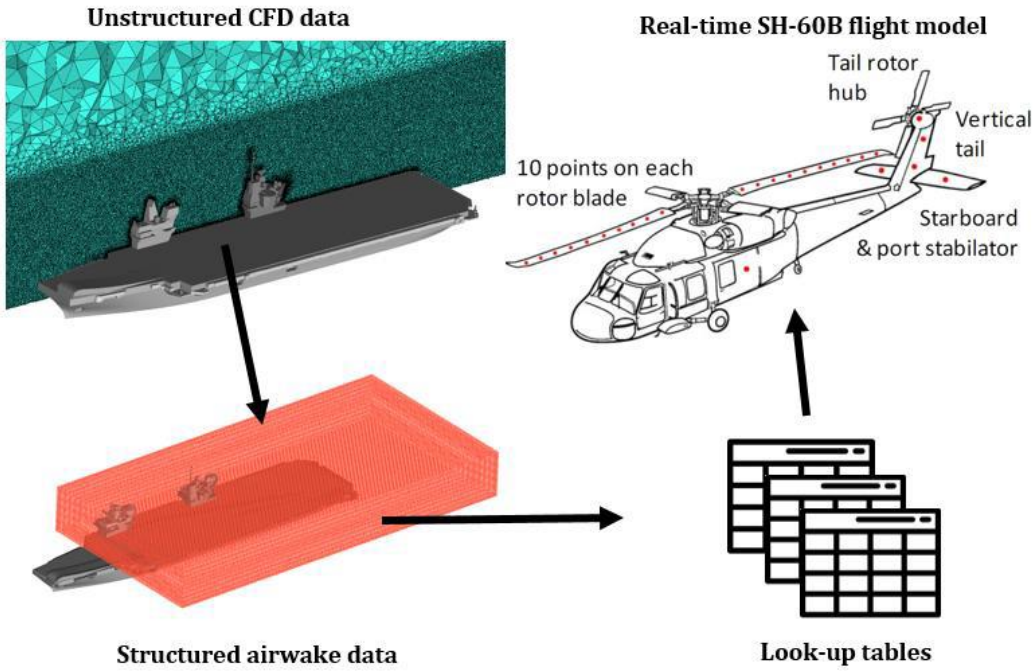

Figure 2-7: Generation of time-accurate airwakes and integration with flight dynamics model [61]

Only one way coupling of airwake effects on the aircraft can be modelled this way. The simultaneous solution of the fluid field and resulting aircraft dynamics, might be required for accurate modelling of hover and low speed flight as discussed by Whitehouse at al. [62]. Crozon et al. [63] demonstrated the technical feasibility of non-real-time fully coupled CFD – flight mechanics simulations. The process is, however, too computationally expensive for real-time simulation with current computational capabilities. Watson et al. [63], demonstrated how a large CFD dataset can be integrated into a real-time piloted simulation environment (Figure 2-7). The

CFD data are interpolated onto a structured grid and velocity perturbations from the freestream values are applied to the aircraft model's ACPs.

2.4.2 Stochastic gust modelling

Stochastic gust models are based on the random generation of turbulent flow velocities on the relevant locations of the simulated aircraft model. Most models are usually built around implementation of von Karman's formula [64] or Dryden's model [65]. Both assume a homogeneous, isotropic and frozen turbulence field, meaning that the spatial distribution of flow velocities does not change with time. For fixed wing aircraft, this approximation is considered valid as long as the ratio of wind to flight speed stays above 1/3 [66]. For helicopters in hover or low speed flight, the assumption is made that the turbulence field drifts towards the aircraft with ambient wind velocity [67].

The spectral density for homogeneous, isotropic turbulence is given by [55]:

$$\boldsymbol{\phi_{ij}(\bar{\Omega}) = \frac{E(\Omega_s)}{4\pi\Omega_s^4}\left(\Omega_s^2\delta_{ij} - \Omega_i\Omega_j\right)} \qquad 2\text{-}19$$

with Ω_i being the spatial frequency component along axis i, $\Omega_s = \sqrt{\Omega_x^2 + \Omega_y^2 + \Omega_y^2}$ and $E(\Omega_s)$ the energy spectra, which is given by von Karman's high altitude turbulence formula as:

$$\boldsymbol{E(\Omega_s) = \frac{\frac{55}{9\pi}\sigma^2 L(aL\Omega_s)^4}{(1 + (aL\Omega_s)^2)^{\frac{17}{6}}}} \qquad 2\text{-}20$$

with σ being the turbulence velocity RMS value, L the characteristic length scale of turbulence, a is a constant whose value for high altitude turbulence is determined as $a = 1.339$.

The cross-correlation functions are given by the inverse Fourier transform of the spectra.

$$\boldsymbol{R_{ij}(\bar{\xi}) = \int_{-\infty}^{\infty}\int_{-\infty}^{\infty}\int_{-\infty}^{\infty}\phi_{ii}(\bar{\Omega})\, e^{i\bar{\Omega}\bar{\xi}} d\Omega_x d\Omega_y d\Omega_z} \qquad 2\text{-}21$$

where $\bar{\xi} = \xi_x\vec{\imath} + \xi_y\vec{\jmath} + \xi_z\vec{k}$ is the separation vector between two points.

von Karman's formula offers a good approximation for high altitude turbulence but fails to consider effects near the ground. Harris [68] suggested a correction in which the resulting turbulence spectra is represented as a power series of the form:

$$\widetilde{\boldsymbol{R_{uu}}}(\boldsymbol{\tau}) = \boldsymbol{\beta_{1u}}\boldsymbol{R_{uu}}(\boldsymbol{\tau}) + \boldsymbol{\beta_{2u}}\boldsymbol{R_{uu}^2}(\boldsymbol{\tau}) + \boldsymbol{\beta_{3u}}\boldsymbol{R_{uu}^3}(\boldsymbol{\tau}) + \cdots + \boldsymbol{\beta_{nu}}\boldsymbol{R_{uu}^n}(\boldsymbol{\tau}) \qquad 2\text{-}22$$

The parameters β_{1u}, β_{2u}, … must fulfil the condition:

$$\sum_{i=1}^{n} \boldsymbol{\beta_{iu}} = \mathbf{1} \qquad 2\text{-}23$$

and the functions for spectra and cross correlation must comply with the normalization conditions:

$$\frac{\mathbf{1}}{\boldsymbol{\sigma_i^2}}\int_0^\infty \widetilde{\boldsymbol{\phi_{ii}}}(\boldsymbol{\omega})\boldsymbol{d\omega} = \widetilde{\boldsymbol{R_{ii}}}(\mathbf{0}) = \mathbf{1}$$
$$\widetilde{\boldsymbol{\phi_{ii}}}(\mathbf{0}) = \mathbf{4}\boldsymbol{\sigma_i^2}\int_0^\infty \widetilde{\boldsymbol{R_{ii}}}(\boldsymbol{\tau})\boldsymbol{d\tau} = \mathbf{4}\boldsymbol{\sigma_i^2}\boldsymbol{T_i} \qquad 2\text{-}24$$

Equations [2-22] to [2-24] allow to obtain a solution for a and the parameters β_{iu} that fit the resulting spectra to results obtained from measurements or CFD simulations. This approach was also applied by Gaonkar et al. to account for obstacle induced effects [69] in shipboard operations.

For simplicity an approximate exponential model is often applied for the implementation of von Karman's turbulence:

$$\boldsymbol{R_{uu}}(\boldsymbol{\tau}) = \boldsymbol{\sigma_u^2}\boldsymbol{e}^{-\frac{\mathbf{2}\boldsymbol{\mu}\boldsymbol{R}}{\boldsymbol{L}}(\boldsymbol{\tau})} \qquad 2\text{-}25$$

While Dryden's turbulence model is considered to be less representative of real world atmospheric turbulence [66], it is applied for aircraft design and for handling qualities analysis. MIL – STD 1797A [70] provides the following model for turbulent power spectral densities for a given characteristic turbulence length, L_i, and spatial frequency, Ω_i:

$$\boldsymbol{\phi_u}(\boldsymbol{\Omega_u}) = \frac{\mathbf{2}\boldsymbol{\sigma_u^2}\boldsymbol{L_u}}{\boldsymbol{\pi}}\frac{\mathbf{1}}{\mathbf{1} + (\boldsymbol{L_u}\boldsymbol{\Omega_u})^2}$$
$$\boldsymbol{\phi_v}(\boldsymbol{\Omega_v}) = \frac{\mathbf{2}\boldsymbol{\sigma_v^2}\boldsymbol{L_v}}{\boldsymbol{\pi}}\frac{\mathbf{1} + \mathbf{12}(\boldsymbol{L_v}\boldsymbol{\Omega_v})^2}{(\mathbf{1} + \mathbf{4}(\boldsymbol{L_v}\boldsymbol{\Omega_v})^2)^2} \qquad 2\text{-}26$$

$$\boldsymbol{\phi_w(\Omega_w) = \frac{2\sigma_w^2 L_w}{\pi} \frac{1 + 12(L_w\Omega_w)^2}{(1 + 4(L_w\Omega_w)^2)^2}}$$

When generating turbulence directly on the rotorcraft's components, the rotation effect of the blades must be considered when computing the resulting spatial and temporal cross correlation functions. Gaonkar et al. [71] define a distance metric, $\xi_{ij} = \left|\boldsymbol{r_i}(t + \Delta t) - \boldsymbol{r_j}(t)\right|$, between all combinations of two blade elements *i* and *j* at time steps *t* and *t* + *Δt*. This metric is applied to compute a vertical turbulence cross correlation matrix, $R_{ww}(\xi_{ij})$, of size $QNxQN$, where *N* is the total number of rotor blades and *Q* is the number of elements on each blade:

$$\boldsymbol{\frac{R_{ww}(\xi_{ij})}{\sigma_w^2} = \frac{2^{\frac{2}{3}}}{\Gamma\left(\frac{1}{3}\right)}\left(\frac{\xi_{ij}}{1.339L_w}\right)^{\frac{1}{3}}\left[K_{\frac{1}{3}}\left(\frac{\xi_{ij}}{1.339L}\right) - \frac{1}{2}\left(\frac{\xi_{ij}}{1.339L}\right)K_{\frac{2}{3}}\left(\frac{\xi_{ij}}{1.339L}\right)\right]} \qquad 2\text{-}27$$

where $K_{1/3}$ and $K_{2/3}$ are the modified Bessel functions of order 1/3 and 2/3 respectively, and Γ is the Gamma function.

Their results show that considering the cross correlation between all rotor blades, and therefore all the non-diagonal elements on the cross-correlation matrix, is necessary for an accurate prediction of turbulence effects (Figure 2-8). However, the consideration of multiple blade segments has a limited effect compared to the application of turbulence at a point located at 75% of the blade radius (see Figure 2-9).

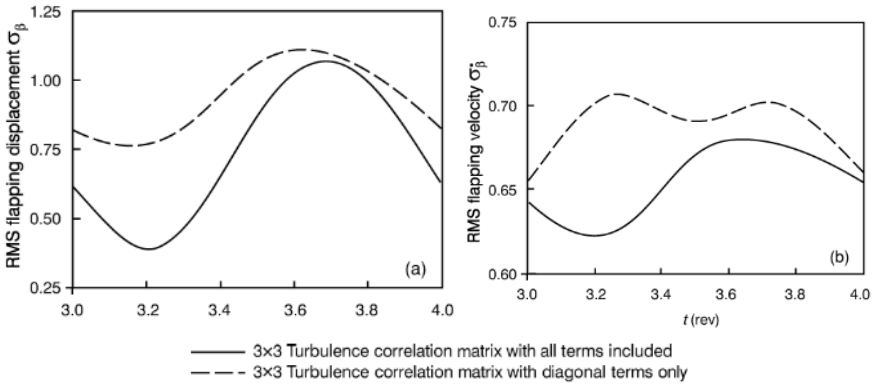

Figure 2-8: Blade flapping displacement and velocity RMS when for three blade rotors when considering blade to blade correlation (all terms included) and only single blade correlation (only diagonal terms).

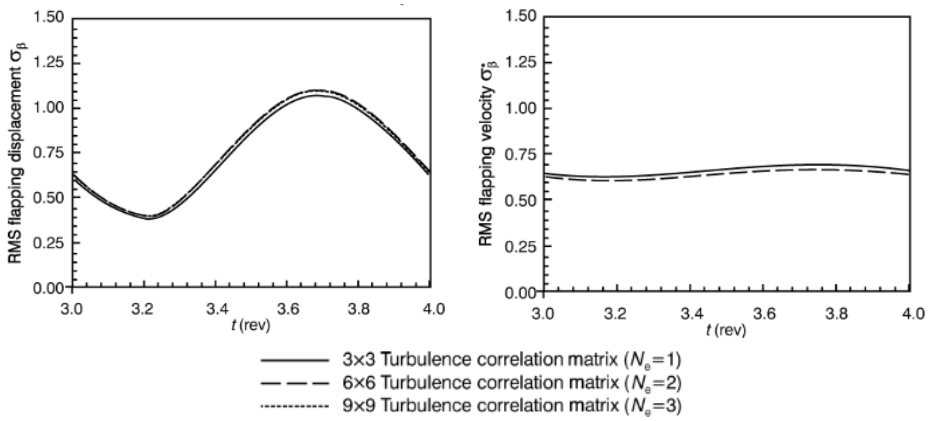

Figure 2-9: RMS of blade flapping displacement and velocity for a three bladed rotor for 1, 2 and 3 blade elements.

SORBET (Simulation Of Rotor Blade Element Turbulence) is a simpler approach developed by McFarland et al. [72]. The rotor disk surface is divided in stations along the direction of the incoming flow velocity projection, v_h, over the rotor plane and an initial velocity field is precomputed by assigning turbulent flow velocities to each station (Figure 2-10). At each time step, velocities on each station are moved to the next one and new correlated turbulent velocities at onset points at the first station are generated using Dryden's turbulence model. Induced velocities on each blade element are computed from the velocity distribution at their station by applying a Gaussian interpolation.

The implementation maintains the number of stored stations as a fixed value, and the rotor hub advances one station at each time step. Therefore, the size of stations increases with the aerodynamic velocity. Also, the minimum velocity for which this method is applicable is set by the ratio:

$$v_{h\,min} = \frac{2R}{N_{stations} * \Delta t} \qquad 2\text{-}28$$

where R is the rotor radius, $N_{stations}$ is the number of turbulence storage stations and Δt is the simulation time step. Under constant wind and flight conditions, this method ensures that disturbances across the rotor are coherent in space and time.

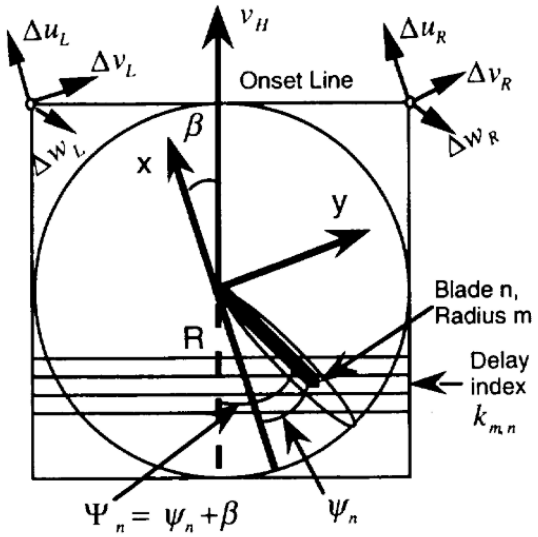

Figure 2-10: Definition of incoming aerodynamic velocity (v_h), onset points and turbulence stations across the rotor plane

Pilot comments after flight simulation testing indicated that the turbulence model generated realistic disturbances. However, pilots complained about the bland feeling of stochastic turbulence, the lack of upsets in the horizontal plane and in heading and the lack of correlation between turbulence and terrain. The first issue was addressed by adding random changes in mean wind speed and scaling the magnitude of turbulence, so that the model presented patches of turbulence and changes in wind within period of calm air. For the consideration of upsets within the horizontal plane, the implementation of turbulence effects on the aircrafts tail, tail rotor and fuselage would have to be considered.

A 3 dimensional extension of the method developed by Ji et al. is described in [73], (Figure 2-11). This allows to account for the impact of turbulence across all of the aircraft surfaces in addition to the rotor. A volume is defined surrounding the aircraft, oriented and divided into stations along the direction of aerodynamic velocity. The inflow station is populated by a grid of von Karman turbulence generators whose output is related by means of a correlation matrix. The generated turbulence is displaced towards the back of the volume at one station with each time step. The main limitation shared by both SORBET and Ji's approach, is that by distributing the turbulence by one fixed station each timestep, the model does not allow to account for rapid changes in flight or environmental conditions.

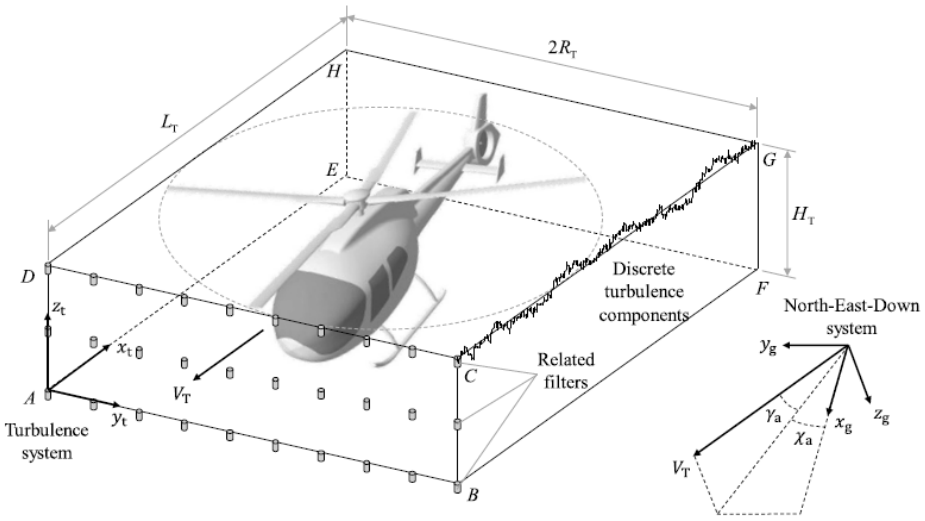

Figure 2-11: Distributed turbulence model by Ji. [73]

2.4.3 Equivalent control inputs

An alternative experimental method described by Lusardi et al. [56] is the use of system identification techniques to develop an empirical turbulence model from flight test measurements. The resulting disturbances are applied to the aircraft as control equivalent turbulence inputs (CETI) (Figure 2-12).

A series of flight tests were performed in which an instrumented UH-60A helicopter performed a hover task behind a hangar. The task was performed with “tight” (+/- 5ft deviations in x-y horizontal position) and “relaxed” (+/- 15ft deviations) position tolerance standards, with the aircraft orientation facing the hangar and perpendicular to it and under wind speeds of 17kts and 22kts.

The turbulence identification process involves comparing recorded pilot inputs with recorded aircraft attitude rates in the presence of a disturbance. By feeding recorded aircraft attitudes and rates into an inverse aircraft model, the resulting output provides an estimate of required control inputs to achieve, in the absence of disturbances the same aircraft response as recorded under turbulence. The difference between the required inputs and the real inputs made by the pilot are the turbulence equivalent inputs.

Extracted equivalent control inputs were bandpass filtered to preserve only the content within the 0.2 to 15 rad/s frequency range which has the largest effect on pilot workload. Recorded equivalent inputs for the “tight” tolerance task showed a higher coherence with real world recorded pilot inputs. So only equivalent inputs computed

from the relaxed task were employed in the generation of the turbulence model, as the aircraft motion used for their generation is mainly due to the turbulence generated upsets, rather than from pilot inputs.

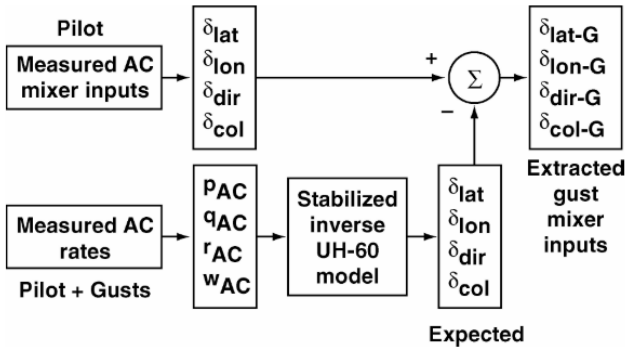

Figure 2-12: Extraction of turbulence equivalent control inputs from inverse aircraft model.

From these results, a gust to input transfer function was obtained that matches a turbulence model with the spectra of obtained equivalent control inputs. If $G_w(s)$ is the equivalent transfer function that produces the turbulent von Karman velocity spectra for vertical gust from a white noise input, $S_{nn}(\omega) = 1$:

$$\boldsymbol{\phi_{ww}(\omega) = = |G_w(\omega)|^2 \phi_{nn}(\omega)}$$

$$\boldsymbol{G_w(s) = 2\sigma_u \left(\frac{\sqrt{\frac{U_{wind}}{\pi L_u}}}{s + \alpha_u} \right)} \qquad 2\text{-}29$$

$$\boldsymbol{\alpha_u = \frac{2U_{wind}}{L_u}}$$

Then by multiplying by a scale factor, the gust to control transfer function can be obtained for lateral, longitudinal and collective inputs:

$$\boldsymbol{G_{\delta_g}(s) = K_g * G_w(s)} \qquad 2\text{-}30$$

To match the white noise input with the recorded collective equivalent input, a second order transfer function was required:

$$\boldsymbol{G_{\delta_g}(s) = K_g * \frac{\sigma_w \sqrt{\frac{U_{wind}}{\pi L_u}} \left(s + C_1 \frac{U_{wind}}{L_w} \right)}{\left(s + C_2 \frac{U_{wind}}{L_w} \right) \left(s + C_3 \frac{U_{wind}}{L_w} \right)}} \qquad 2\text{-}31$$

By matching the output of $\left|G_{\delta_g}(\omega)\right|^2$ to the obtained equivalent control spectra, the value of $K_g(\sigma_w)$ for each control axis can be obtained.

Piloted flight simulation tests [74] in which pilots performed the same task as during the flight tests were performed with the extracted turbulence model and the SORBET model (see Section 2.4.2). Results show that the pilot input cut off frequency, power spectral density and RMS, as well as resulting aircraft rates show similar behaviour between both models for tight and relaxed tasks under conditions of light and strong turbulence. The similar results of both methods were deemed as a good validation of SORBET.

Simulation results with both models also showed similar behaviour when compared to flight testing, although simulation testing resulted in the collective control being the main contributor to pilot workload in contrast with the longitudinal input for flight tests.

Seher-Weiss et al. [75] describe a similar experiment to develop a gust model for the EC-135 helicopter. Instead of using an inverse aircraft model, an observer centred approach is applied. The difference between the aircraft model response to recorded pilot control inputs and the actual recorded aircraft attitude rates is treated as an error to be minimized. This is achieved by adding the equivalent control inputs to the recorded pilot inputs, which requires estimating the corresponding gain function that links rate error to equivalent control inputs (Figure 2-13). The obtained equivalent control input spectra is used to obtain a gust to noise transfer function as given by equations [2-29] to [2-31].

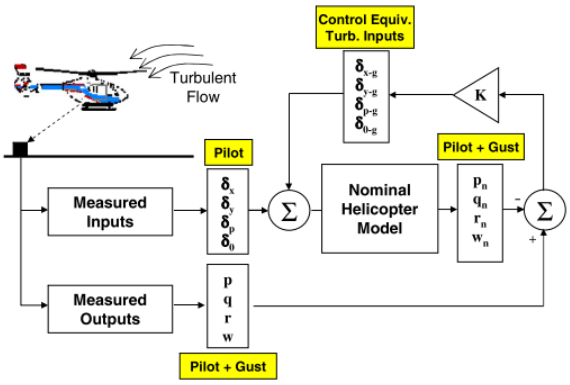

Figure 2-13: Observed centred extraction of turbulence equivalent rotor inputs.

This extraction of turbulence parameters from flight test data results in the generation of realistic turbulence models which also include all complex effects related to

rotorcraft systems and interaction with the environment that are not usually captured by flight simulation models. However, these models are valid only for very specific combinations of aircraft, environmental conditions and task and therefore not applicable for simulation in other conditions.

Hess [76] proposed a simple scaling methodology for equivalent control inputs between different helicopter sizes and flight speeds. The method relies on the assumption that turbulent length scales are large enough, when compared to the rotor diameter, that gust across the rotor disk can be approximated as a linear distribution. To ensure this, high frequencies are filtered out for the scaling process:

$$\boldsymbol{\phi'_{wg\,wg} = \phi_{wg\,wg} * \frac{\omega_0^2}{\omega^2 + \omega_0^2}} \qquad \boldsymbol{\omega_0 = \frac{2\pi * V_{inc}}{8 * 2R_{rotor}}} \qquad \textit{2-32}$$

Equivalent control inputs are obtained from gust upsets at the main rotor hub or tail rotor hub respectively:

$$\boldsymbol{\Delta\delta_{col} = \frac{w_g|_{hub}}{0.5R_{rotor} * \Omega_{rotor}}}$$

$$\boldsymbol{\Delta\delta_{\frac{lat}{long}} = \frac{\frac{dw_g}{dy}|_{hub} * 0.5R_{rotor}}{\frac{dx}{0.5R_{rotor} * \Omega_{rotor}}} = \frac{\pm\omega * w_g|_{hub}}{V_{inc} * \Omega_{rotor}}} \qquad \textit{2-33}$$

The approximation of control inputs from gust spectra would therefore be obtained as:

$$\boldsymbol{\phi_{\delta_c\,\delta_c}(\omega) = \phi_{wg\,wg}(\omega) * \frac{\omega_0^2}{\omega^2 + \omega_0^2} * \frac{1}{(0.5R_{rotor} * \Omega_{rotor})^2}}$$

$$\boldsymbol{\phi_{\delta_{\frac{lat}{long}}\,\delta_{\frac{lat}{long}}}(\omega) = \phi_{wg\,wg}(\omega) * \frac{\omega_0^2}{\omega^2 + \omega_0^2} * \frac{\omega^2}{(V_{inc} * \Omega_{rotor})^2}} \qquad \textit{2-34}$$

The scaling method has not been validated and is proposed for a first order approach for analysis or design.

A further improvement is made, and successfully demonstrated, by Memon et al. in [28] to adapt CETI disturbances based on precomputed airwake data to account for aircraft location. The process is shown in Figure 2-14. The RMS of turbulent flow velocities in all three axis, σ_u, σ_v, σ_w, at the aircraft's location are extracted from the

airwake and used as inputs for the transfer functions for each of the different control inputs: $G_{Lat}(\sigma_w)$, $G_{Long}(\sigma_w)$, $G_{Coll}(\sigma_w)$ and $G_{Ped}(\sigma_v)$.

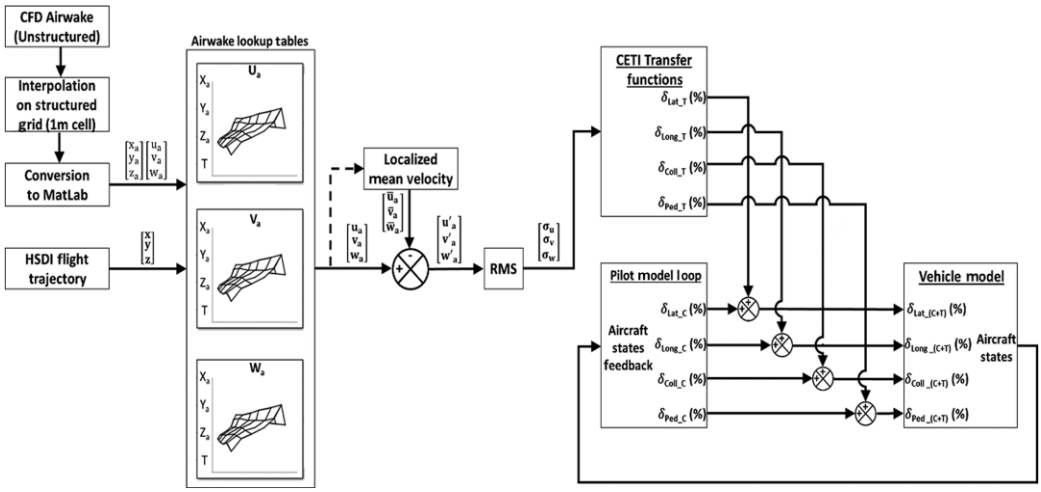

Figure 2-14: Enhanced spatial CETI model proposed by Memon. [28]

2.5 Case studies of rotorcraft and fixed-wing aircraft wake encounters

When compared with research related to wake encounters between fixed wing aircraft, there has been less research on the effect of fixed wing wakes on rotorcraft safety. Results from a flight test campaign conducted by NASA in 1977 [77] (see Section 2.5.1) represent the most significant study in this literature search. In addition some flight dynamics analyses were also conducted in the 1980s [78], [79] (see Section 2.5.2) but their relevance to the current research is limited. The possibility of increased frequency in simultaneous operations of helicopters and fixed-wing aircraft at civilian airports has led to a number of studies which have made use of flight simulation to investigate the effect of wake encounters between fixed wing aircraft and rotorcraft (Section 2.5.2) and a fluid dynamics study of aircraft and rotor wake interactions (Section 2.5.3). More recently, flight simulation was also employed at the University of Liverpool to assess the impact of helicopter wakes on the safety of light fixed wing aircraft (Section 2.5.4).

2.5.1 NASA Langley Research Center flight test campaign 1977

NASA Langley Research Center conducted a flight test campaign to study the response of a rotorcraft during an encounter with a fixed-wing aircraft wake [77]. This is the only flight test campaign results regarding these types of encounters that has been found during this literature review.

The campaign was conducted with an instrumented UH-1H helicopter and a C-54 aircraft to generate the wake. During each flight the aircraft flew at an indicated airspeed of 115kts and the helicopter at 60kts. The initial distance between aircraft and helicopter was reduced for each successive flight, covering a range of encounters with separations between 0.42 and 6.62 nautical miles. When the desired distance between rotorcraft and airplane was reached, the helicopter crossed the airwake obliquely from below left (Figure 2-15). After the first crossing, the helicopter would cross the wake several times as the distance between rotorcraft and airplane grew, leading to several encounters at different wake ages. Helicopter parameters, including attitude, engine output and main rotor angles, pilot control inputs and main and tail rotor blade bending were recorded. However, no pilot feedback on the severity of the encounters or workload ratings are reported.

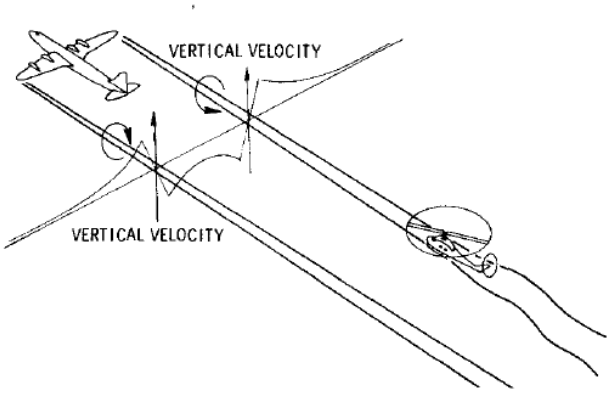

Figure 2-15: Schematic of vortex wake intercept by a helicopter. [77]

Identification of the resulting upsets was performed by comparison of helicopter attitude changes against pilot control inputs. The amplitude of changes in pitch and roll attitude rates was found to be linearly related to the size of the corresponding corrective control inputs, while no such correlation was found for yaw rates suggesting that yaw deviations were the main upsets from the encounters. Overall, the attitude response of the helicopter was lower than those observed for general aviation aircraft of the same weight encountering a similar wake. Finally, increases in loads on the main rotor were within the helicopter's operational envelope, and considered to not present any structural risk.

2.5.2 Flight simulation and analytical studies of rotorcraft wake encounters

A series of offline simulations were performed in 1986 and 1987 by Saito et al. [78], [79] studying the dynamic response of articulated and hingeless helicopters, as well as light fixed-wing aircraft, to the wake vortex induced by a Boeing B-747 sized aircraft.

A potential flow formulation was applied to relate vortex strength to the size of the generating aircraft and to define the induced flow velocity field. Simulations were performed comparing crossing the vortex at different encounter angles and distances to the generating aircraft. Both hingeless and articulated helicopters experienced similar attitude upsets which were usually less than those experienced by fixed-wing aircraft under the same conditions. Perpendicular crossings tended to result in pitch and yaw upsets and roll and yaw upsets were predominant for parallel encounters. Attitude upsets could reach up to 10deg. Losses in thrust coefficient and downward vertical acceleration were also obtained.

Piloted and offline flight simulation tests were conducted in the 2000s at the University of Liverpool by Padfield et al. [9], [80]–[82] with the aim of assessing the severity of rotorcraft encounters with fixed-wing wakes to explore criteria that could be utilised to quantify the effect on safety of these encounters.

Predictions of vortex strength and induced velocity provided by Burnham and Hallock's dispersion model (Eq. 2-35) were favourably compared against LIDAR measurements performed at London Heathrow airport [80]:

$$\boldsymbol{V_{Vortex}(r) = \frac{V_c\left(1 + ln\left(\frac{r}{r_c}\right)\right)}{\rho U_l S_l b_l} \quad if\ |r| > r_c}$$
$$\boldsymbol{V_{Vortex}(r) = V_c\left(\frac{r}{r_c}\right)\ \ if\ |r| < r_c} \qquad 2\text{-}35$$

with r_c being the radius of the vortex core, V_T being the vortex induced tangential flow velocity at a distance r from its axis and V_c the vortex induced flow velocity at $r = r_c$, ρ is the air density, U_l the indicated air speed of the vortex shedding aircraft and S_l and b_l its wing area and wingspan respectively.

Crosswinds can lead to displacement perpendicular to the runway of vortices near the ground [5] [83] and can result in more severe encounters when helicopter heading and vortex axis are parallel to each other [9], [78], [79].

Offline simulations [80] were conducted for a lateral encounter with a vortex representative of the wake of a Boeing B-747 ($\Gamma \approx 600$ m^2/s). The helicopter response following a wake encounter showed a significant initial upset in pitch, which is larger when the relative velocity between helicopter flight and vortex displacement decreases, resulting in longer crossing times. For an encounter at 3m/s, pitch upsets

could reach up to 40 deg and rates of up to 30 deg/s within the first three seconds following a wake encounter; inter-axis coupling led to subsequent upsets in roll. The wake encounter also resulted in alterations in heading and an initial vertical acceleration dependent on the position of the rotorcraft relative to the vortex and could reach up to 0.5g. Independently of the direction of the initial vertical accelerations, the helicopter tended to leave the encounter with a downwards vertical velocity, resulting in a net loss of altitude.

Increases in vertical distance between the helicopter's rotor and the vortex core resulted in less severe upsets, as did decreasing the strength of the wake vortex. Encounters in which the helicopter was moving at a higher indicated airspeed resulted in greater attitude rates and vertical accelerations, but lower total attitude upsets, possibly due to the shorter duration of the encounter. In contrast with the results obtained by Saito et al., helicopters with hingeless rotors or stiffer blade articulations suffered greater attitude upsets. Stability augmentation systems (SCAS) helped in mitigating total attitude upsets, whilst their effect in counteracting altitude losses seemed to be more limited.

Overall results are qualitatively similar as those from encounters with wind turbine wake vortices as will be described in Section 2.7.2.1, but are significantly larger due to the much higher strength of aircraft shed vortexes when compared to wind turbine vortices ($\Gamma \approx 600$ m^2/s against $\Gamma \approx 70$ m^2/s for a 3MW wind turbine).

Resulting upsets were compared against ADS-33 handling qualities requirements for control power, which is the maximum attitude rate achievable with full stick input, quickness (Figure 2-16), which gives a measure of how fast an aircraft can change its attitude, and maximum allowed attitude upset and loads transient after failure (Figure 2-17). This provides an idea of whether the rotorcraft satisfying the requirements for level – 1 or level – 2 handling qualities might allow for sufficient margin to mitigate the effects of an encounter.

While satisfying Level 1 control quickness and power margin requirements for tracking and aggressive manoeuvring provides the helicopter with sufficient margin to compensate the vortex induced upsets, this will not be the case when only general mission tasks criteria are considered [81] (Figure 2-18). Pitch attitude upsets and normal vertical loads within the first three seconds tend to reach or even surpass Level

3 transient limits after control failure. Resulting normal loads increase with encounter velocity while encounters without SCAS resulted in significantly worse upsets.

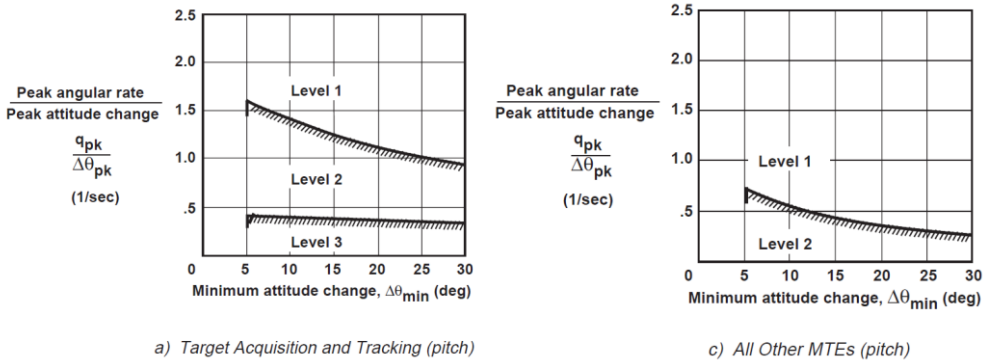

Figure 2-16: ADS - 33 moderate amplitude (quickness) limits for pitch control. [21]

LEVEL	FLIGHT CONDITION		
	HOVER AND LOW SPEED	FORWARD FLIGHT	
		NEAR-EARTH	UP-AND-AWAY
1	3° roll, pitch, yaw 0.05g n_x, n_y, n_z No recovery action for 3.0 sec	Both Hover and Low Speed and Forward Flight Up-and-Away requirements apply	Stay within OFE. No recovery action for 10 sec
2	10° attitude change or 0.2g acceleration. No recovery action for 3.0 sec	Both Hover and Low Speed and Forward Flight Up-and-Away requirements apply	Stay within OFE. No recovery action for 5.0 sec
3	24° attitude change or 0.4g acceleration. No recovery action for 3.0 sec	Both Hover and Low Speed and Forward Flight Up-and-Away requirements apply	Stay within OFE. No recovery action for 3.0 sec

Figure 2-17: ADS-33 Transient limits after flight control failure. [21]

Flight simulation tests of wake encounters were conducted where pilots were required to flight an Instrumented Landing (ILS) approach Mission Task Element (MTE) [9] which might lead to an airwake encounter. A pilot rating scale for Wake Vortex Encounter (WVE) severity, (Figure 2-19) was developed. Based on the pilots' subjective evaluation of excursions in flight path and aircraft attitudes and the effort and urgency necessary for recovery, pilots provided a rating ranging from A (minimal excursions and no corrective action needed) to H (catastrophic encounter with no recovery possible).

A trend was found of increasing severity ratings with greater attitude upsets, either averaged between all axes or the maximum individual axis value (Figure 2-20). By assigning a flight handling qualities value to the upset value based on ADS – 33 transient after failure upset limits (see Figure 2-17), pilot awarded ratings were assigned an ADS-33 handling qualities level.

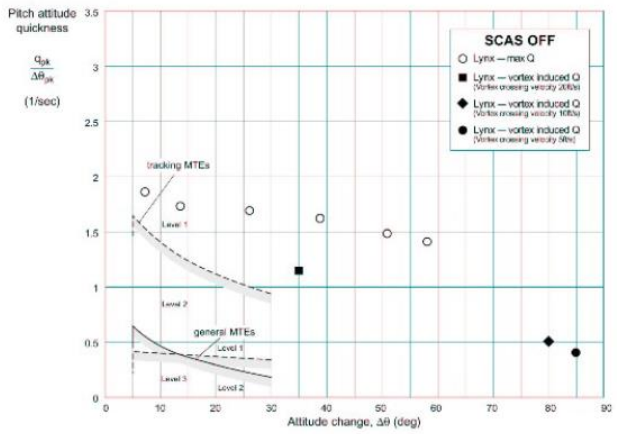

Figure 2-18: Pitch upset quickness against ADS-33 criteria.[81]

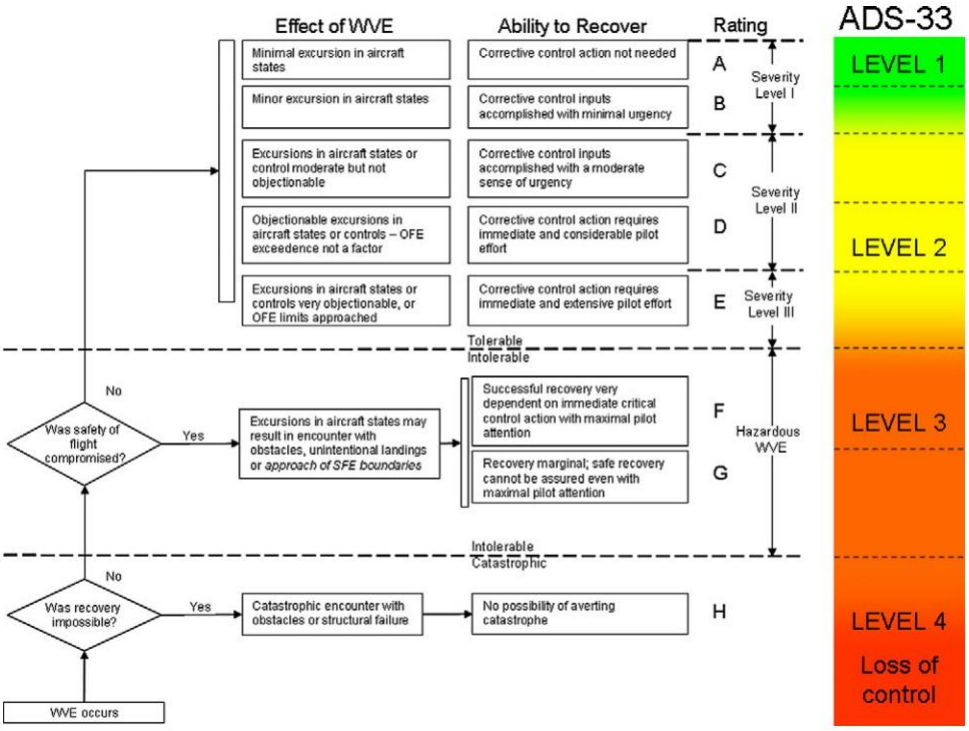

Figure 2-19: Wake Vortex Encounter severity scale. [7]

Pilot ratings and the tendency to perform a go-around were related to absolute deviation from intended flight path, especially in height [80], [82]; this has also been observed when studying fixed wing approaches [18]. Comparison of the average attitude upset in all axes against the ADS-33 transient after failure criteria suggested a link between upset and severity.

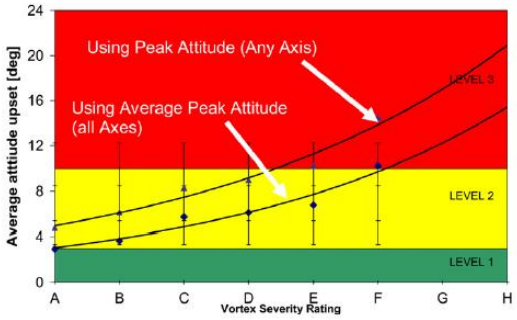

Figure 2-20: Pilot awarded wake vortex encounter severity ratings against averaged upset in all axes (lower line) or maximum upset in any axis (upper line) [9]*. Attitude upset values are classified for handling qualities levels according to ADS-33 transient after failure criteria.*

Visual conditions play an important effect on pilot's handling of a wake encounter. Under good visual conditions, encounters with vortices of greater strength and encounters at lower altitudes correlated strongly with higher pilot severity ratings and go-around frequency (Figure 2-21). Under degraded visual conditions, however, encounters at higher altitude, where the ground was not clearly visible, could disorient the pilots and also lead to a go-around. Also, upsets from lower strength vortices under conditions of poor visibility were also more difficult to perceive initially, and sudden changes in flow direction could catch pilots by surprise.

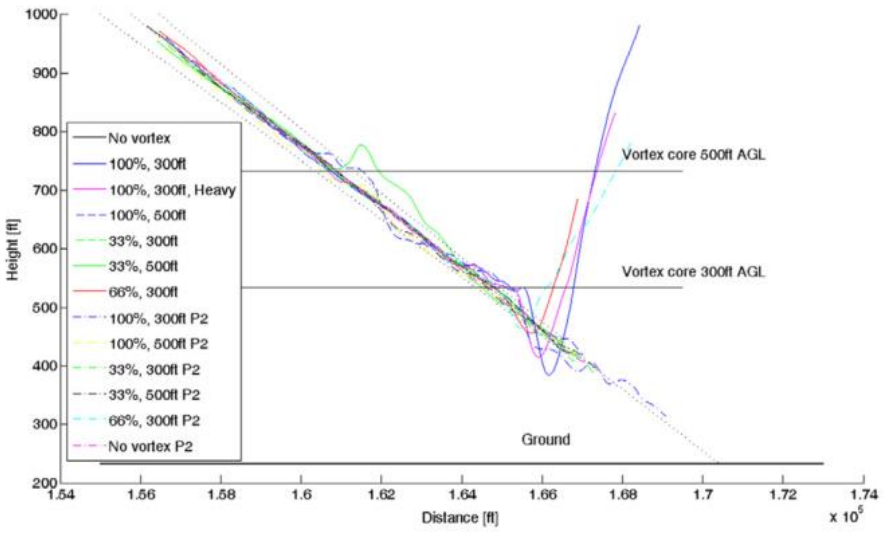

Figure 2-21: 3deg Approach profile for encounters at different vortex height and strength under good visual conditions. [9]

2.5.3 Interaction between helicopter rotor and airplane wakes

Whitehouse and Brown [62] modelled the mutual interaction between an airplane shed vortex and the airwake produced by a helicopter's rotor. Assuming that viscosity of air is negligible, velocity distributions, scaled by rotor tip speed Ω*R, can be defined as a

potential field, $\omega = \nabla \times v$, and the rotor as a vorticity source dependent on the local flow velocity distribution, $S_{rotor}(v_{Rotor})$.

Applying the vorticity transport equation, the resulting velocity fields induced by the rotor, the rotor wake and the airplane vortex can be described:

$$\frac{\partial}{\partial t}\boldsymbol{\omega_{Wake}} + \boldsymbol{v_{Wake}} \cdot \boldsymbol{\nabla \omega_{Wake}} - \boldsymbol{\omega_{Wake}} \cdot \boldsymbol{\nabla v_{Wake}} = \boldsymbol{S_{rotor}(v_{Rotor})} \quad \textit{2-36}$$

$$\frac{\partial}{\partial t}\boldsymbol{\omega_{Vortex}} + \boldsymbol{v_{Vortex}} \cdot \boldsymbol{\nabla \omega_{Vortex}} - \boldsymbol{\omega_{Vortex}} \cdot \boldsymbol{\nabla v_{Vortex}} = \boldsymbol{0} \quad \textit{2-37}$$

The interaction between all three elements results from the addition of the resulting velocity fields:

$$\begin{aligned} \boldsymbol{v_{Rotor}} &= -\boldsymbol{\mu} + \boldsymbol{v}(\boldsymbol{\omega_{Vortex}}) + \boldsymbol{v}(\boldsymbol{\omega_{Wake}}) \\ \boldsymbol{v_{Wake}} &= -\boldsymbol{\mu} + \boldsymbol{v}(\boldsymbol{\omega_{Vortex}}) + \boldsymbol{v}(\boldsymbol{\omega_{Wake}}) \\ \boldsymbol{v_{Vortex}} &= -\boldsymbol{\mu} + \boldsymbol{v}(\boldsymbol{\omega_{Vortex}}) + \boldsymbol{v}(\boldsymbol{\omega_{Wake}}) \end{aligned} \quad \textit{2-38}$$

Four levels of simulation fidelity were defined (named as 0, 1, 2 and 3) by progressively dismissing the deformation of the vortex due to the rotor wake, the deformation of the rotor wake due to the vortex and finally the influence of the rotor wake on the rotor's own flow field:

$$\begin{aligned} \boldsymbol{v_{Rotor}} &= -\boldsymbol{\mu} + \boldsymbol{v}(\boldsymbol{\omega_{Vortex}}) + \boldsymbol{v}(\boldsymbol{\omega_{Wake}}) \\ \boldsymbol{v_{Wake}} &= -\boldsymbol{\mu} + \boldsymbol{v}(\boldsymbol{\omega_{Vortex}}) + \boldsymbol{v}(\boldsymbol{\omega_{Wake}}) \\ \boldsymbol{v_{Vortex}} &= -\boldsymbol{\mu} \end{aligned} \quad \textit{2-39}$$

$$\begin{aligned} \boldsymbol{v_{Rotor}} &= -\boldsymbol{\mu} + \boldsymbol{v}(\boldsymbol{\omega_{Vortex}}) + \boldsymbol{v}(\boldsymbol{\omega_{Wake}}) \\ \boldsymbol{v_{Wake}} &= -\boldsymbol{\mu} + +\boldsymbol{v}(\boldsymbol{\omega_{Wake}}) \\ \boldsymbol{v_{Vortex}} &= -\boldsymbol{\mu} \end{aligned} \quad \textit{2-40}$$

$$\begin{aligned} \boldsymbol{v_{Rotor}} &= -\boldsymbol{\mu} + \boldsymbol{v}(\boldsymbol{\omega_{Vortex}}) \\ \boldsymbol{v_{Wake}} &= -\boldsymbol{\mu} + +\boldsymbol{v}(\boldsymbol{\omega_{Wake}}) \\ \boldsymbol{v_{Vortex}} &= -\boldsymbol{\mu} \end{aligned} \quad \textit{2-41}$$

The results were used to assess the validity of the frozen vortex assumption employed on most encounter simulations. Results of simulations with different degrees of fidelity tend to converge as the rotor advance ratio increases (Figure 2-22). During hover, interaction between rotor wake and vortex can lead to the airwake being re-ingested by the rotor. The resulting fluctuation in rotor response is not reflected by

lower fidelity models which tends to over predict vortex induced changes in rotor thrust and blade flapping.

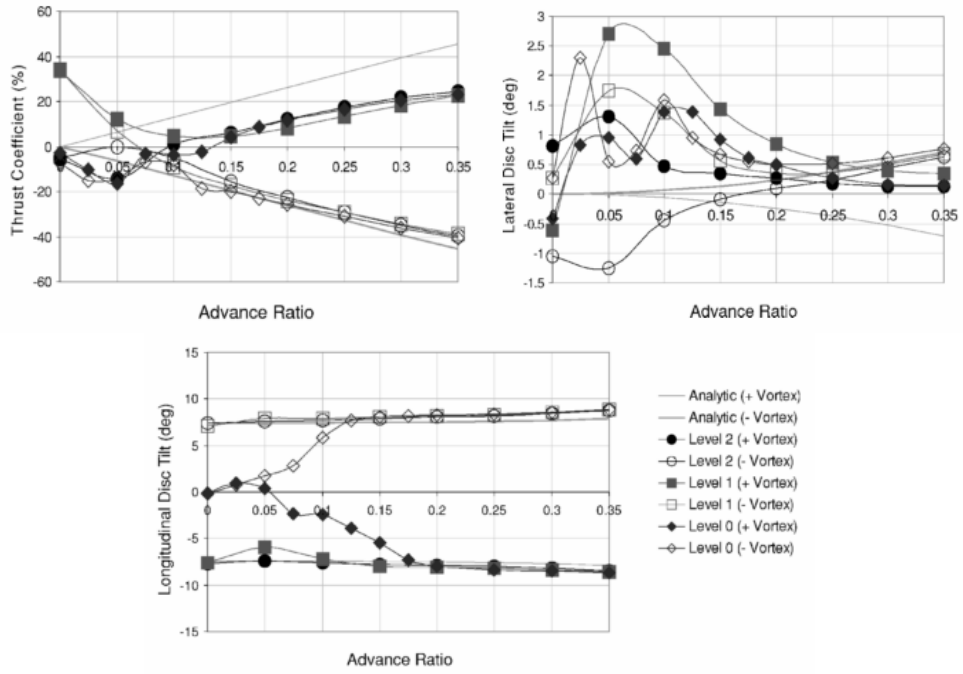

Figure 2-22: Perturbations to rotor trim states from vortex encounter.[62]

2.5.4 Helicopter wake encounter study

A more recent study conducted in 2015 by Wang et al., at the University of Liverpool for the CAA, employed flight simulation to assess the hazards that rotorcraft wakes could present to light aircraft during approach and level flight [84].

An evaluation of different wake modelling techniques for rotorcraft wakes for their fidelity and ease of computation was conducted. Beddoe's prescribed wake model combined with a decay model was applied to simulate encounters during level flight. For encounters during approach scenarios, a free wake model was employed to include ground effects on the flow field.

Several simulations were performed of a final landing approach. The airplane experienced upsets mainly in roll and vertical accelerations (Figure 2-23), pilot ratings on the WVE scale (see Section 2.5.2) ranged from mild (A-B) when happening above the helicopter rotor plane to hazardous (D-F) when the aircraft encountered the wake below a helicopter hovering or flying at low speed less than one diameter of distance to the wake centre. Pilot feedback revealed altitude to be most important factor

influencing their ratings, with encounters at low altitudes leaving little margin for recovery even for small attitude or flight path excursions.

Helicopter advance ratio also had an important effect, the wake of a hovering helicopter produced larger sudden upsets while the skewed wake produced by a helicopter in forward flight was easier to detect from a distance. Offsets between the rotorcraft and the runway tended to reduce severity, but for offsets lower than one rotor diameter, the asymmetry of induced flow across the airplane's wing could result in larger roll upsets.

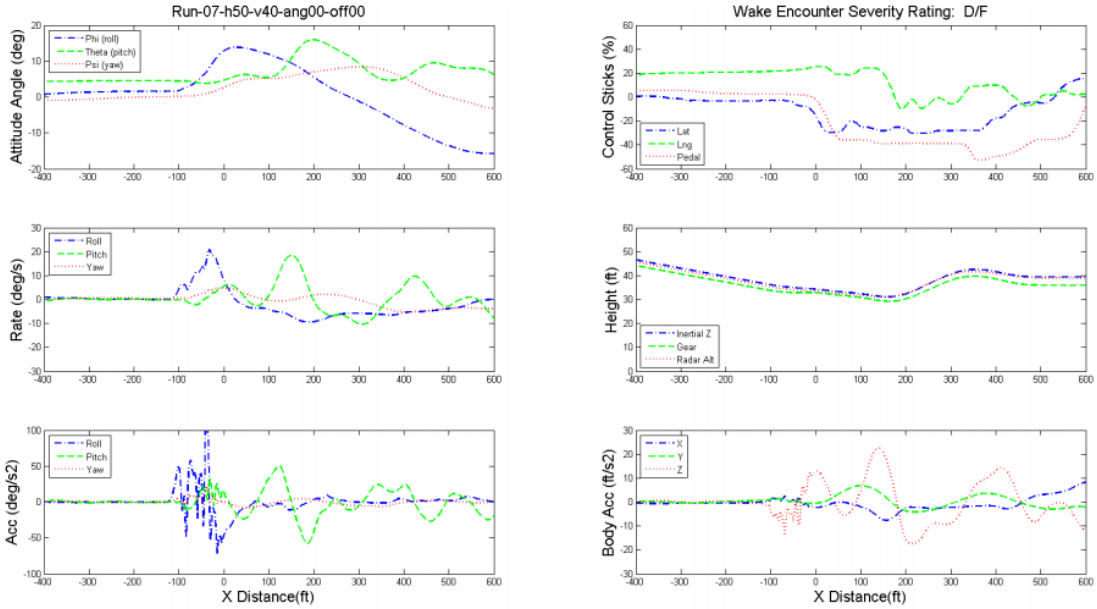

Figure 2-23: Airplane upsets during encounter with helicopter rotor wakes. Helicopter height 50ft, speed 40kts. Located over runway centre, heading parallel to runway. [84]

2.6 Case studies of flight simulation of ship helicopter operations

Currently the definition of ship helicopter operating limits requires the realization of flight test trials in order to declare a specific wind over deck speed and azimuth as safe. In addition to being expensive and dangerous to conduct, conditions that could not be tested can result in limits on the flight operations that can be cleared. There is therefore considerable interest in the use of flight simulation to assist in the definition of Ship Helicopter Operating Limits [8]. Forrest et al. [85] describe a technique to study landing operations around several ship designs. Employing detached eddy simulations (DES), the time varying distribution in air velocities around the ship deck can be obtained and recorded. Combined with ship motion time histories, these precomputed airwakes were then integrated at The University of Liverpool's HELIFLIGHT-R flight simulator [86].

A series of simulated landing approaches to a Royal Navy type 23 frigate and a Wave class auxiliary oiler were conducted with a FLIGHTLAB model representative of an SH-60 helicopter under a range of wind over deck velocities. The deck recovery procedure was defined as three MTEs: lateral displacement to landing spot, hover for ten seconds and vertical descent. Pilot ratings awarded in the simulation trials were used to define a virtual SHOL envelope for both ships (Figure 2-24).

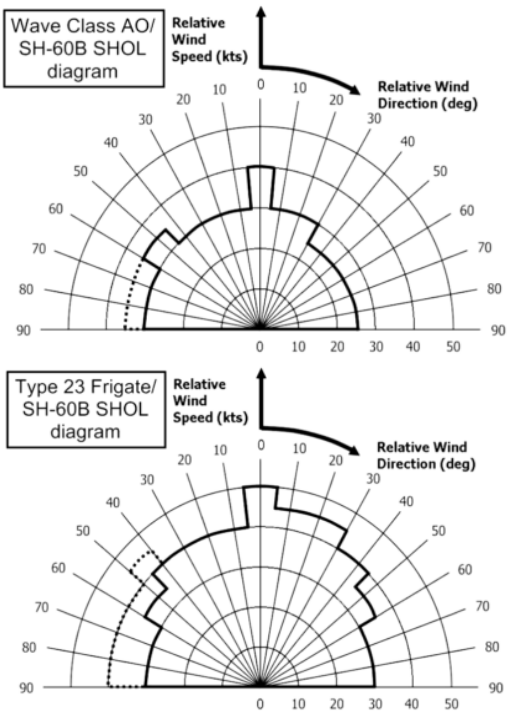

Figure 2-24: SHOL diagrams for top) Type 23 frigate, down) Wave class auxiliary oiler, defined using awarded pilot ratings on the DIPES scale. [85]

Results show a significantly lower limit on lateral wind velocities than for headwinds. For all directions, the larger auxiliary oiler also shows a narrower SHOL envelope. Analysis of the CFD results show that, especially under winds from oblique directions, turbulence resulting from the flow shed at the edges of the ship's superstructure can affect the rotorcraft during the lateral translation and station keeping over the spot (Figure 2-25). This effect is more pronounced for larger ships, whose superstructure sheds larger vortices at lower frequencies but which generate larger upsets. This results in larger flow velocity oscillations which require a greater effort from the pilot to counteract. Power spectral density analysis of pilot control inputs during the deck landings to a Type 23 frigate confirm larger Power Spectral Density (PSD) levels for lateral and pedal control inputs under oblique wind conditions (Figure 2-26). This metric is used in this thesis to examine pilot workload in different MTEs and application of turbulence models.

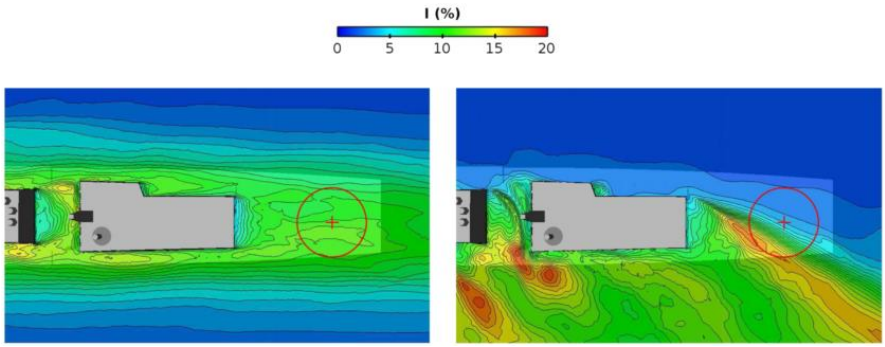

Figure 2-25: turbulence intensity over flight deck of Type 23 frigate under 40kt headwind (left) and 40kt wind 45deg azimuth (green 45) (right). Circle indicates approximate position of rotor during station keeping. [85]

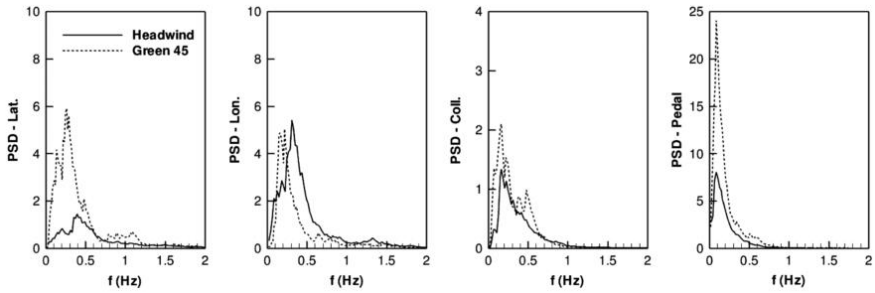

Figure 2-26: PSD of pilot control metrics during station keeping over the Type 23 flight deck under 40kt headwind and green 45.[85]

2.7 Case studies of wind turbine airwake encounters

2.7.1 Airplane encounters with wind turbine wakes

Research on airplane encounters with wind turbine airwakes is limited but is becoming more common as an increase in the number of wind energy installations near airfields has led to the need to assess their influence on general aviation safety. Three main studies, each of them employing a different methodology and metrics, have been found during this literature review, and their findings can inform how to analyse rotorcraft operations in similar environments.

2.7.1.1 Kansas department of transportation 2014

A 2014 project commissioned by the Kansas Department of Transportation [87] studied the influence of proposed wind farm installations near Rooks County regional airport and Pratt regional airport on general aviation. The vortex airwake of a 91.4m-diameter wind turbine was estimated by directly scaling the radius and wind velocity from published wind tunnel test results [88], and a prescribed helical vortex model combined with a vortex decay model was employed to estimate the velocities induced by the airwake downstream of the wind turbine.

The maximum horizontal and vertical velocities induced by the blade tip vortices were estimated for wind speeds between 10mph to 40mph, resulting in crosswind speeds of almost 100ft/s in regions near the wind turbines. The derived velocity distributions were then employed to estimate maximum lateral crosswind and rolling moment coefficients induced on a 10m wingspan general aviation aircraft and compared against FAA limits.

From the results, the report concludes that an aircraft can experience dangerously high roll moment coefficients (see Eq. 2-1) of around 0.5 and lateral crosswinds of up to 30 mph at distances of over two miles covering almost the entire approach area for both airports analysed (Figure 2-27).

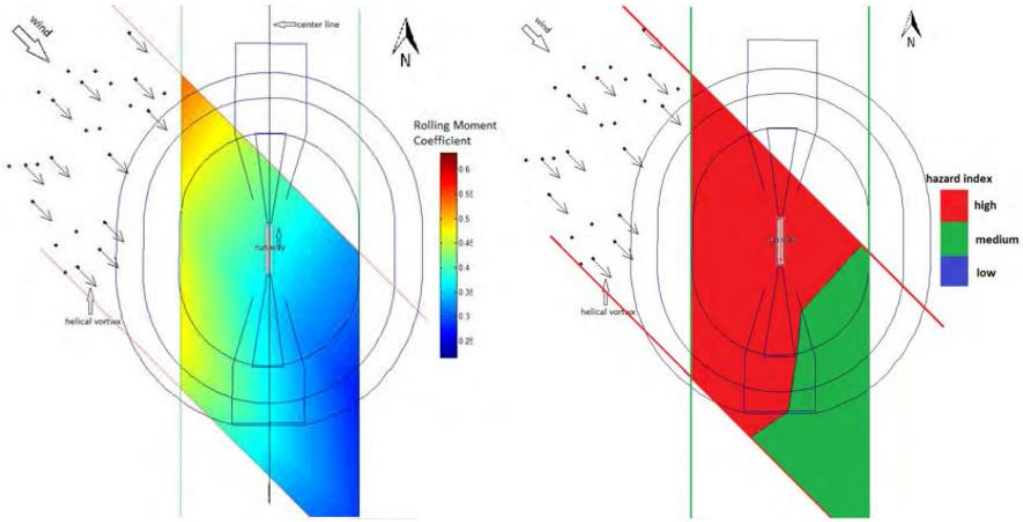

Figure 2-27: Roll moment coefficient induced from wind turbine wakes at Pratt Regional Airport (Kansas, US) under 40mph wind. [87]

2.7.1.2 University of Liverpool 2015

A more recent study was conducted in 2015 at the University of Liverpool for the CAA [11] to assess the impact of wind turbine wakes from two WTN 250kW 30m diameter wind turbines installed near East Midland Airport, UK. Offline and piloted real-time flight simulations were employed to study the effect of disturbances on a light general aviation aircraft when encountering the airwake of a wind turbine during a landing approach and the resulting pilot response.

Kocurek's prescribed vortex wake model [89], combined with a Beddoes vortex decay model [90], was used to precompute a steady velocity field generated by the airwake. The resulting velocity distribution was validated against CFD simulations and wind

tunnel measurements by Wang et al. and Carrion et al. [44] [35] as well as LIDAR field measurements performed at the East Midlands Airport site for these tests (Figure 2-28).

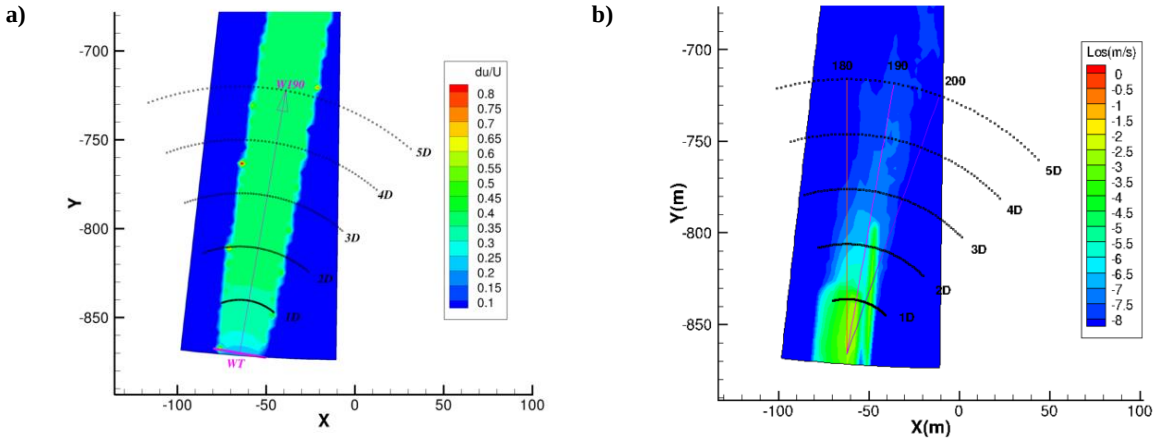

Figure 2-28: Comparison between a) Kocurek's wake axial velocity deficit estimations and b) one hour averaged LIDAR measurements of Line Of Sight (LOS) velocities. Wind speeds averaged around 10m/s. [11]

The computed flow velocity field was then integrated with a flight dynamics model of a generic light general aviation airplane, with dimensions and performance similar to those of a Grob Tutor. Pilots performed simulated landing approaches during which they would cross the wind turbine wake either perpendicularly or obliquely at a 45 degree angle. Aircraft responses and pilot control inputs during each flight were recorded and pilot feedback and ratings on the wake vortex encounter severity scale [9] (see Section 2.5.2) were collected after each flight.

Even at small distances from the wind turbine, recorded aircraft upsets were minor, mainly in the yaw and roll axis (Figure 2-29) as a consequence of the velocity deficit in the direction of the wind turbine axis. All encounters were rated by pilot as either A or B on the WVE rating scale (see Section 2.5.2), implying minor to minimal aircraft excursions demanding corrective actions with minimal urgency or none at all.

A further series of offline simulations were performed in an attempt to reproduce the results obtained by the Kansas report. Applying Kocurek's airwake model, combined with a Beddoes decay model, resulted in significantly smaller vorticity circulation values and therefore induced wake velocities than the values obtained in the Kansas report by directly scaling with wind velocity. The velocity fields of the airwake of a 250kW 30m diameter wind turbine and for a 3MW, 90m diameter wind turbine were computed for a wind velocity of 20m/s. At this velocity the wind turbine regulates its

pitch in order to limit its total power output, something not considered in the Kansas report.

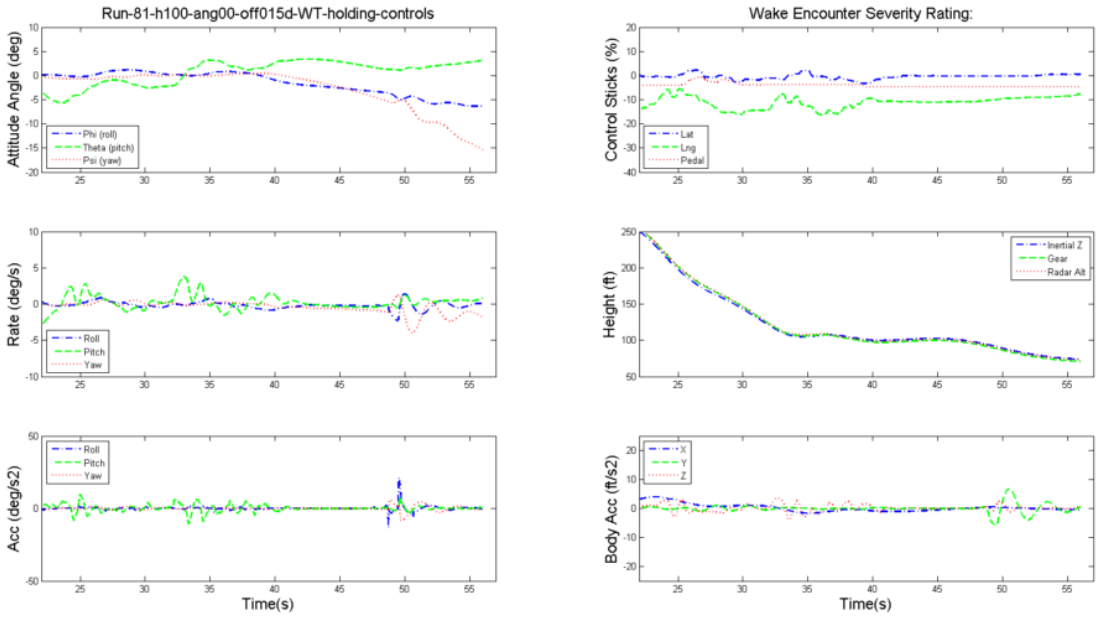

Figure 2-29: Airplane upsets resulting from perpendicular crossing of the wake at 1.5diameters distance and 10m/s flight speed. [11]

The aircraft was flown through the computed airwakes with all the body states frozen. Variations in forces and moments experienced by the aircraft model during the encounter were recorded and compared. The impact of crossing the Beddoes wake (Figure 2-30) and the Kansas wake (Figure 2-31) was qualitatively similar, but the magnitude of the effect was much larger. The most important effect was noticed in lateral force and rolling moment components, as well as a smaller induced yaw moment, which acted on the aircraft during the entire duration of the encounter. Smaller variations in vertical in vertical forces could also be detected when entering and exiting the airwake.

Increasing the distance to the wind turbine at which the airwake was encountered from three diameters to five and ten resulted in small reductions in induced moments but did not change the nature of the encounter qualitatively. However, crossing the airwake with an angle of 45 degrees to the airwake resulted in much larger upward force components appearing, which lasted for the entire duration of the encounter, as well as in a change in the direction of induced lateral forces and roll and yaw moments. The effects were similar, although of a larger magnitude for the airwake of the larger wind turbine and induced vertical forces were present during the entire encounter even when crossing perpendicularly to the airwake.

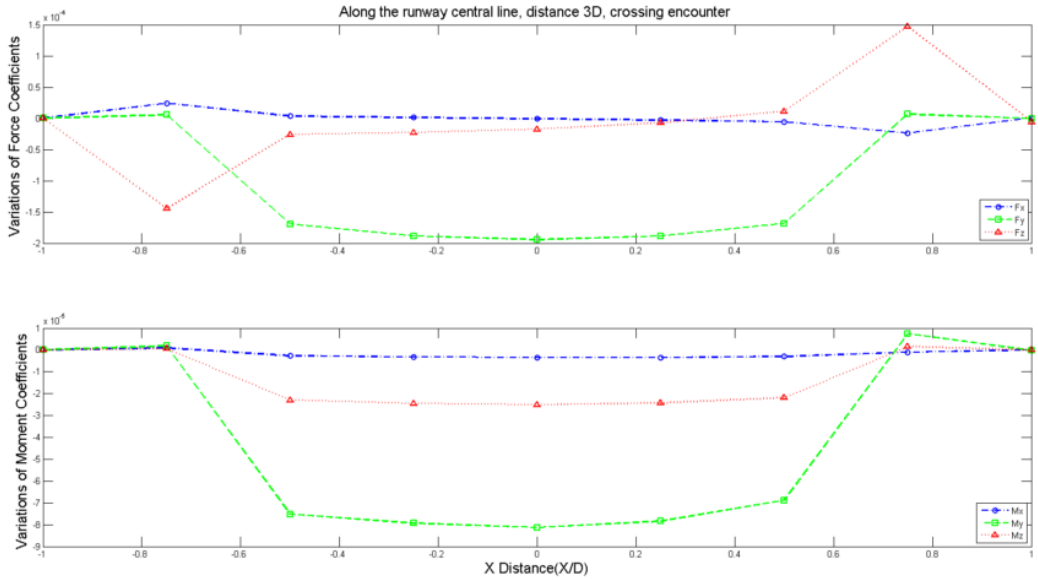

Figure 2-30: Variations in forces and moments experienced by the aircraft during the encounter with WT vortex wake using Kocurek's and Beddoe's wake model.

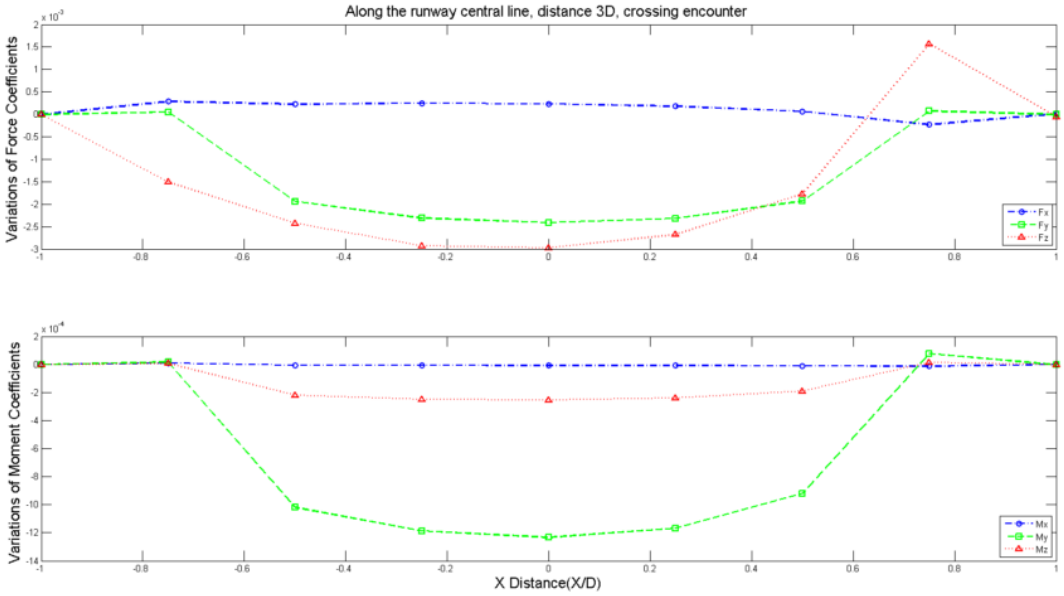

Figure 2-31: Variations in forces and moments experienced by the aircraft during the encounter with WT vortex wake, using the Kansas wake model. [11]

2.7.1.3 University of Naples and Fraunhofer Institute 2014

A collaboration project between the department of industrial engineering at the University of Naples and the Fraunhofer Institute for Wind Energy and Energy Systems conducted research into the dangers presented by wind turbine wakes to general aviation aircraft.

An initial analysis was published by the Fraunhofer Institute in 2014 [91]. The airwakes of four different wind turbines with diameters in the range between 110m to

120m and nominal power output between 2MW and 3MW was researched. The velocity field behind an actuator disk was computed using a RANS solver with a k-ε turbulence model. Turbulence velocities, *U'*, were averaged and added to total wind velocities, w, to produce a static steady airwake:

$$\begin{aligned} \boldsymbol{\Delta w} &= \boldsymbol{w - w_0} \\ \boldsymbol{w_{gust}} &= \boldsymbol{|\Delta w| + w'} \end{aligned} \qquad \textit{2-42}$$

An estimation of changes in aircraft load factor, *n*, was used to evaluate the severity of an encounter at different points of the airwake. The load factor is calculated based on the EASA Certification Specifications for Very Light Aeroplanes and compared against operational boundaries of an Ikarus C-22 ultralight aircraft:

$$\boldsymbol{n = 1 + \frac{\Delta L}{W}} \qquad \textit{2-43}$$

$$\begin{aligned} \boldsymbol{\Delta L} &= \boldsymbol{\frac{1}{2} k \rho_0 S w_{gust} U_{Cruise} Cl_\alpha} \\ \boldsymbol{k} &= \boldsymbol{\frac{0.88\mu}{5.3 + \mu}} \\ \boldsymbol{\mu} &= \boldsymbol{\frac{\frac{2M}{S}}{\rho_0 \bar{c} Cl_\alpha}} \end{aligned} \qquad \textit{2-44}$$

with ρ_0 the air density at sea level, M the airplane's mass, W its weight, S the wing surface, U_{cruise} its cruise speed, Cl_α its lift slope, and $\bar{c}$ its average chord.

Based on the flight envelope of the Ikarus C-22, the following limits for operational cruise velocity under vertical gust were defined:

$$\begin{aligned} \boldsymbol{a_n} &= \boldsymbol{\frac{k \rho_0 S Cl_\alpha}{2Mg} w_{gust}} \\ \boldsymbol{U_{min}} &= \boldsymbol{\frac{U_A}{2}\left(\frac{1}{4} a_n U_A + \sqrt{\frac{1}{16} a_n^2 U_A^2 + 1}\right)} \\ \boldsymbol{U_{max}} &= \boldsymbol{\frac{1}{a_n}} \end{aligned} \qquad \textit{2-45}$$

The flight envelope diagram defines U_A = 36.5m/s and a no exceed velocity U_D = 46.6m/s. The precomputed steady airwake velocity field was used to obtain U_{min} and U_{max} to maintain flight envelope, against downstream distance to the wind turbine for wind velocities of 16mph and 30mph (Figure 2-32, Figure 2-33):

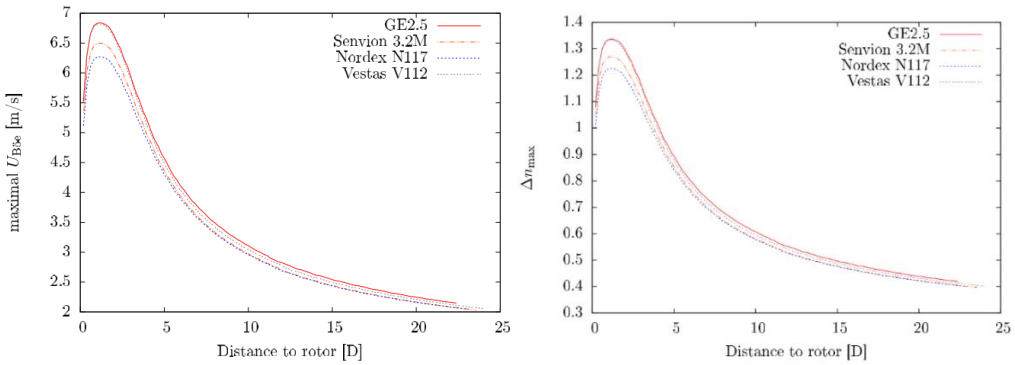

Figure 2-32: Left: Maximum vertical gust velocities (U_{Boe}) for 13.3 wind speed. Right: Maximal loads for flight speed V_C = 33m/s. [91]

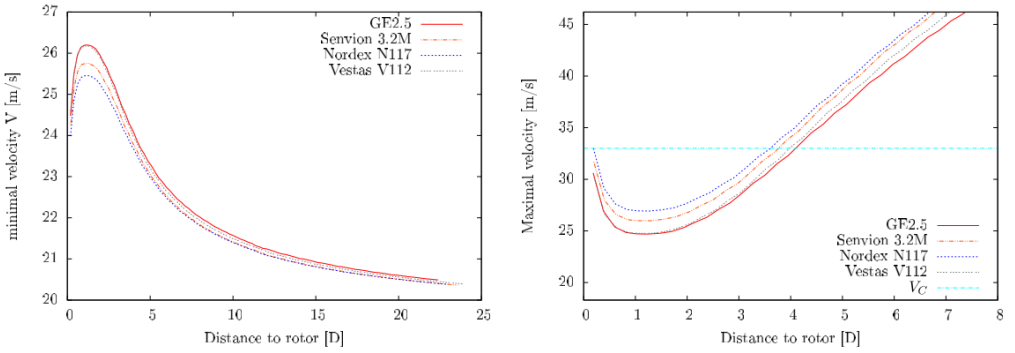

Figure 2-33: Maximum and minimum cruise flight velocities against distance to wind turbine for 13.3m/s wind speed. [91]

Minimum separation distances for intermediate wind velocities were obtained by interpolation. A minimal separation of 2 diameters which increases at higher wind velocities was recommended.

More recent research in collaboration with the University of Naples [92] applies the same load factor criteria to assess the hazards when crossing the airwake of a 126m diameter, 5MW wind turbine. Static turbulent airwakes extending up to 2800m downstream were generated for wind velocities of 5m/s and 12m/s and incidence angles on the turbine rotor of 0deg and 15deg.

A generic ultralight aircraft model of similar size and mass as an Ikarus C-42 was obtained by modifying the model of a Cessna C-172. Using an automatic pilot model, offline simulations of landing approaches at 50kts and 100kts flight speeds were conducted. During each run, the aircraft would cross the airwake through its centre at different downstream distances from the wind turbine. A further set of encounters were run with initial position, flight velocity and descent path randomly determined, so as to generate a distribution of possible encounter scenarios (Figure 2-34).

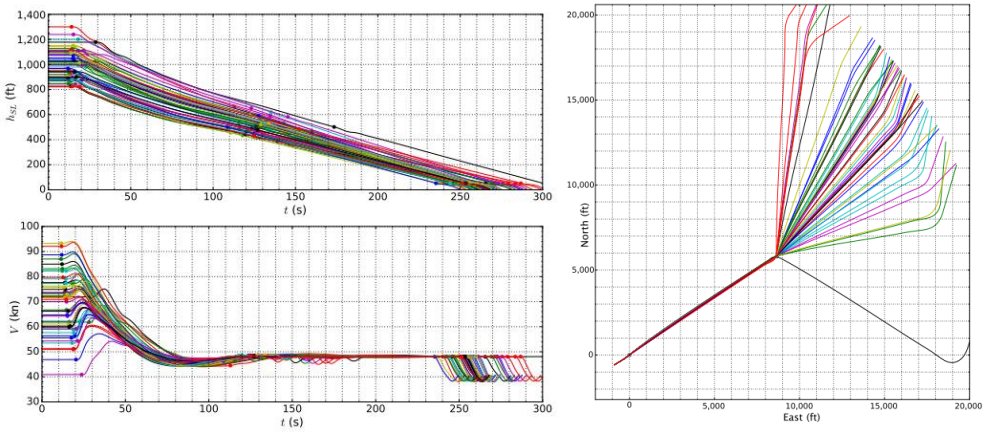

Figure 2-34: Top left: Altitude profile of simulated approach flights. Bottom left: Velocity profiles of approach flights. Right: ground track of approach flights. [92]

Results show that limits of the flight envelope were not exceeded (Figure 2-35). However, there were important differences in the nature of the encounter depending on whether they occurred within the near or the far wake region. The far wake is the region that extends downstream for a distance beyond 6 diameters and where vortex breakdown leads to a region dominated by small scale turbulence. Higher increases in load factor occur when entering the far wake and are much milder near the wind turbine. The frequency of the resulting upsets is also much higher in the turbulent regions. Encounters at higher aircraft speeds also present higher upsets.

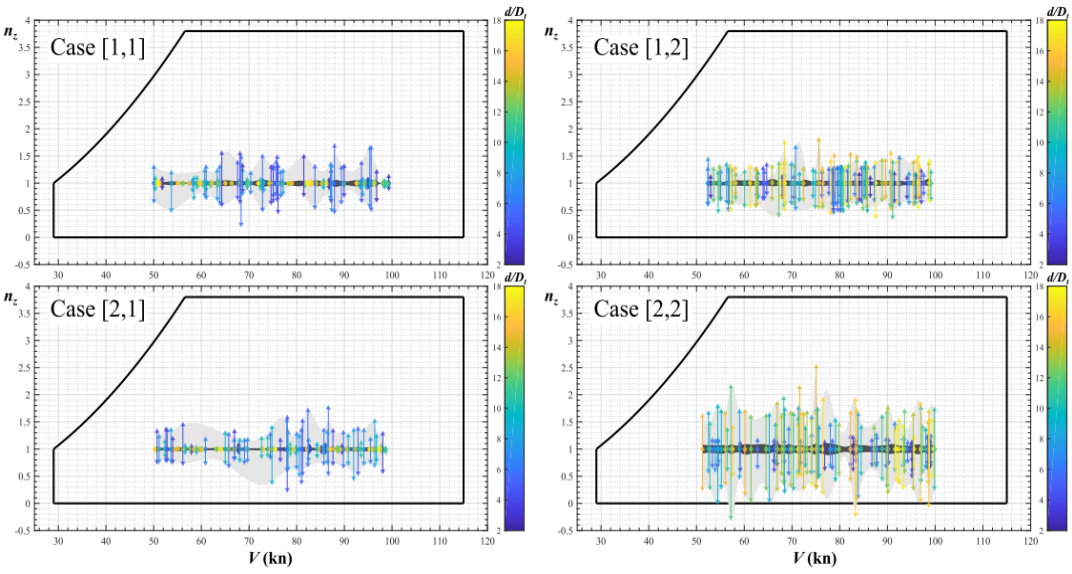

Figure 2-35: Increase in aircraft loads during the encounter. Top left: 5m/s wind aligned with wind turbine axis. Bottom left: 12m/s wind aligned with wind turbine axis. Top Right: 5m/s wind with 15 deg yaw to wind turbine axis. Bottom right: 12m/s wind with 15 deg yaw to wind turbine axis. [92]

Wakes at higher wind speeds also present higher induced load factors on the aircraft and a longer turbulent zone behind the turbine. Wind velocities not aligned with the wind turbine axis result in the formation of a turbulent airwake nearer to the wind

turbine. At lower wind speeds, this results in an earlier dissipation of the wake, at higher wind speeds on the other hand this results in a longer turbulent region, leading to increased probability of encountering greater normal loads during the encounter.

2.7.2 Helicopter encounters with wind turbine wakes

There is limited knowledge on the effects on helicopters encountering a wind turbine wake. The main research was conducted by the Group for Aeronautical Research and Technology in Europe (GARTEUR) action group, HC-AG23 [93] consisting of several European universities and aerospace research institutes including among others the Universities of Glasgow and Liverpool, the Technical University of Delft and the NLR who are also members of the NITROS project.

The work was divided into several work packages: a survey of available wind turbine airwake data was conducted to identify characteristics that result in relevant effects on helicopter dynamics, the application of airwake modelling techniques for flight dynamics analysis and flight simulation, and a series of offline and piloted flight simulation experiments were conducted to assess helicopter upsets and demands on the pilot during a wake encounter. The results have been published in conference papers and are summarized below.

2.7.2.1 Helicopter encounters with wind turbine wake vortices

Van der Wall and Lehman [94], [95] applied an analytical model to study steady state interactions between a helicopter rotor and wake vortexes. The assumption was made that compared to the size of the helicopter rotor, wind turbine blade tip vortices can be approximated as a straight vortex line. The first paper studied cases in which helicopter heading during the encounter is parallel to the vortex line (Figure 2-36).

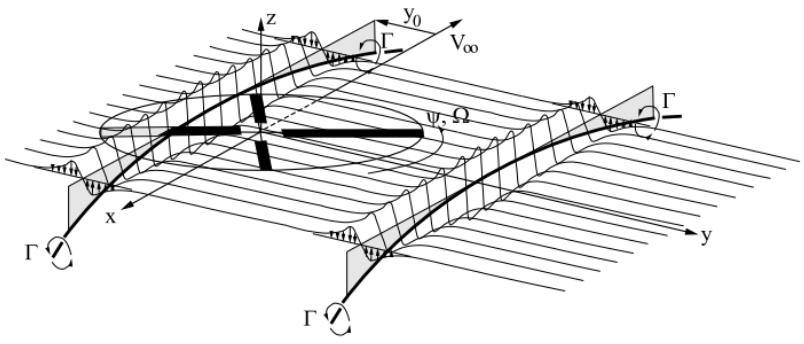

Figure 2-36: Geometry of rotor encounter with wind turbine vortices.[94]

A vortex induced velocity model is applied to estimate a static field of perturbations in rotor inflow λ_V induced by a vortex of strength Γ and core radius r_c at a distance $y - y_0$. A decay model was applied to determine vortex strength and core radius downstream from the wind turbine.

$$\boldsymbol{\lambda_V = \frac{\Gamma}{2\pi\Omega R^2} * \frac{\sqrt{(x-x_0)^2 + (y-y_0)^2}}{(x-x_0)^2 + (y-y_0)^2 + r_c^2}} \qquad 2\text{-}46$$

Blade element momentum theory is applied to relate alterations in total rotor lift and blade flapping moments to changes in flow velocity induced by the vortex over the rotor.

$$\begin{gathered} \boldsymbol{V_T = r + \mu * sin(\psi) + \Delta V_T} \\ \boldsymbol{V_P = \mu_z + \lambda_{i0} + \mu\beta\, cos(\psi) + r\frac{d\beta}{d\psi} + \Delta V_P} \end{gathered} \qquad 2\text{-}47$$

$$\boldsymbol{\frac{d^2\beta}{d\psi^2} + \nu_\beta^2\beta = \gamma\overline{M_\beta}} \qquad 2\text{-}48$$

$$\boldsymbol{\bar{L} = \frac{1}{2}\int_0^1 V_T^2\left(\theta - \frac{V_P}{V_T}\right)dr} \qquad 2\text{-}49$$

$$\boldsymbol{\overline{M_\beta} = \int_0^1 r\, d\bar{L}} \qquad 2\text{-}50$$

Changes in flow velocities around the rotor blade are given by vortex induced velocities and resulting changes in rotor inflow and blade flapping:

$$\begin{gathered} \boldsymbol{\Delta V_T = 0} \\ \boldsymbol{\Delta V_P = \Delta\lambda_i + \lambda_V + \mu\Delta\beta\, cos(\psi) + r\frac{d\Delta\beta}{d\psi}} \end{gathered} \qquad 2\text{-}51$$

Required control inputs to compensate for vortex induced upsets were approximated by differences in rotor trimming required to maintain total rotor thrust and blade flapping moments constant when the vortex axis is located at different distances from the rotor centre. By maintaining blade pitch controls constant, changes in blade flapping angles induced by the vortex can also be studied.

Results are similar to the encounters with aircraft vortex wakes described in Section 2.4, although the strength of vortices shed by a 3MW wind turbine are around one tenth of the vortex of a Boeing B747 aircraft (Γ_0 = 63.7m^2/s, R_c = 0.05m. and Γ_0 = 660m^2/s, R_c = 0.25m respectively). They also show good correlation with those

obtained by DLR's S4 isolated rotor simulation model and HOST helicopter flight dynamics model [96]. As the vortex approaches the helicopter rotor from the side it induces longitudinal blade flapping, producing changes in thrust and reduced rotor power requirements. Encounters during forward flight also induce lateral blade flapping. The sign of these changes depends on the geometry of the encounter with induced longitudinal flapping moments reversing sign as the vortex enters and exits the rotor disk and changes in thrust reverses as the vortex crosses the rotor centre (see Figure 2-37).

If longitudinal and collective blade pitch are changed to maintain constant attitude and thrust, changes in rotor power demand will alter its sign as the vortex crosses the rotor. This will lead to yaw moments due to changes in main rotor mast torque and power availability for the tail rotor, although only effects on the main rotor have been considered in this study.

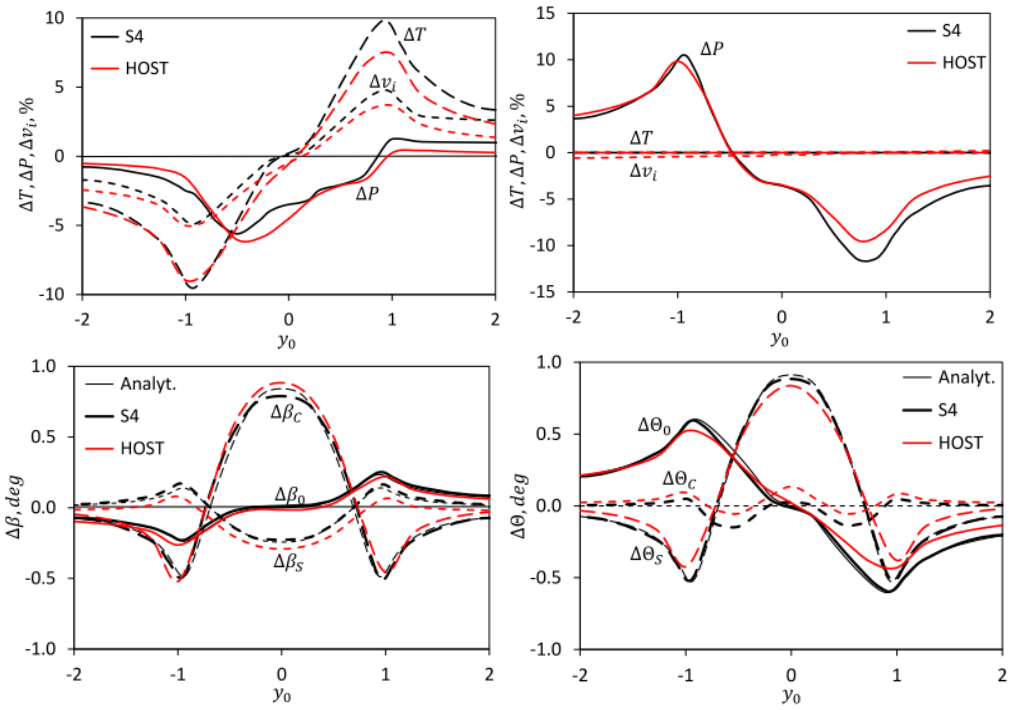

Figure 2-37: Upper row: vortex induced rotor flapping and changes in rotor thrust and power requirements. Lower row: required control trimming to compensate for vortex upset and resulting changes in rotor power requirements. [94]

Two wake encounter severity metrics were proposed, the Rotor Control Ratio (*RCR*), relating required control inputs to the maximum available control power, while the Rotor Flapping Ratio (*RFR*) relates the vortex induced flapping to the maximum allowed flapping angle of the helicopter:

$$RCR = \frac{|\Delta\theta_0| + \sqrt{\Delta\theta_{1s}^2 + \Delta\theta_{1c}^2}}{\Delta\theta_{max}} \quad 2\text{-}52$$

$$RFR = \frac{|\Delta\beta_0| + \sqrt{\Delta\beta_{1s}^2 + \Delta\beta_{1c}^2}}{\Delta\beta_{max}} \quad 2\text{-}53$$

The methodology was applied for several rotor models, representing the rotors of an ultralight coaxial helicopter, a Bo 105 light helicopter, a UH-60 medium helicopter and a CH-53 heavy helicopter. RCR and RFR values were obtained when the rotors encountered vortices of different strengths, representative of wakes of 3MW and 7MW wind turbines (Γ_0 = 63.7m^2/s, R_c = 0.05m and Γ_0 = 98.6m^2/s, R_c = 0.068m respectively) and the vortex wake of a B-747 airplane (Γ_0 = 660m^2/s, R_c = 0.25m).

Results show that medium (Figure 2-38) and heavy rotorcraft encounters with a wind turbine airwake leave sufficient control and blade flapping margin for safe helicopter flight. For light rotorcraft, like the Bo 105 (Figure 2-39) and ultralight coaxial rotorcraft (Figure 2-40), there is enough control power available to counteract an encounter with a wind turbine wake. But in the case of an encounter with the vortex wake of a heavy airliner, a light helicopter will have very little margin in control power to recover. An ultralight rotorcraft will require more control power than available and experience induced flapping angles above the maximum permitted for safe flight. Since the limit does not consider initial trim inputs and rotor tilt during the encounter, the implication is that the encounter leaves very little margin for compensating action. (Figure 2-39, Figure 2-40)

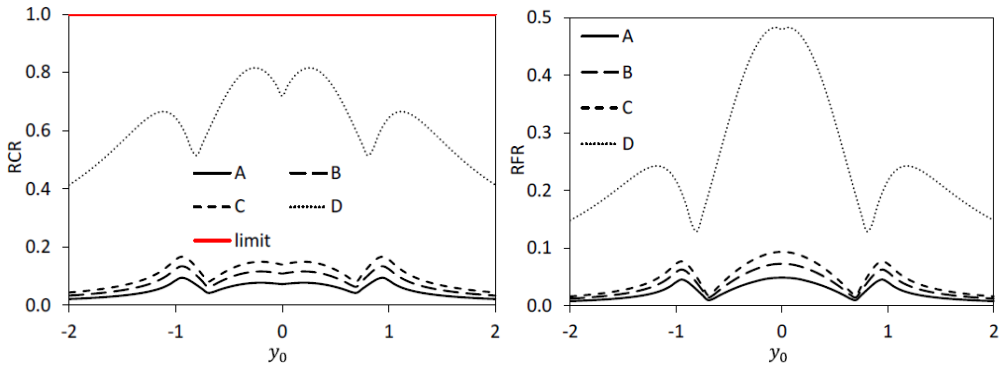

Figure 2-38: RCR and RFR for a UH-1D rotor encountering the vortex of: A) a 3MW wind turbine, B) a 5MW wind turbine, C) a 10MW wind turbine, D) a B-747 airplane. [94]

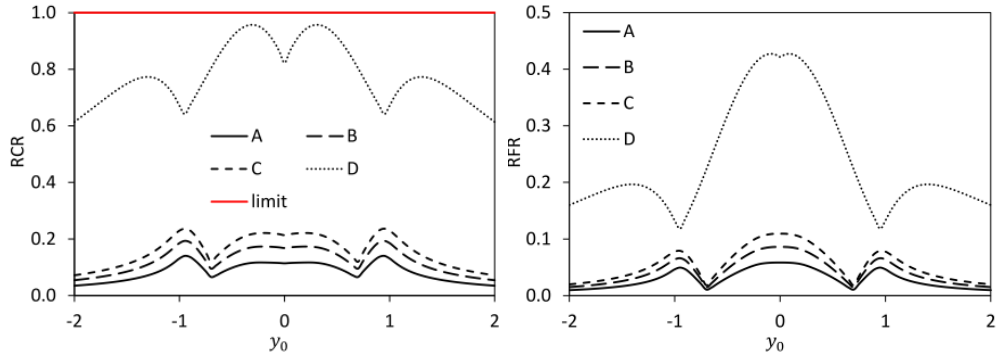

Figure 2-39: RCR and RFR for a Bo 105 rotor encountering the vortex of: A) a 3MW wind turbine, B) a 5MW wind turbine, C) a 10MW wind turbine, D) a B-747 airplane. [94]

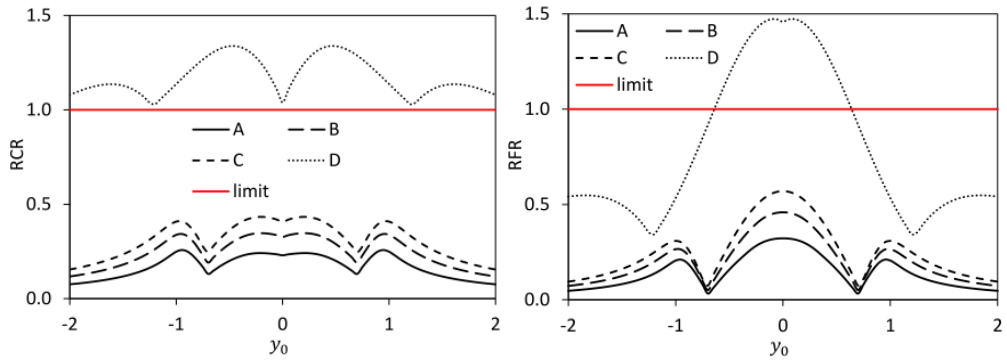

Figure 2-40: RCR and RFR for the rotor of an ultralight coaxial helicopter encountering the vortex of: A) a 3MW wind turbine, B) a 5MW wind turbine, C) a 10MW wind turbine, D) a B-747 airplane. [94]

A later conference paper applies the same model to study effects of a vortex orthogonal to the rotor plane crossing the rotor through its centre [95]. In this case perturbation velocities are given by:

$$\Delta \boldsymbol{V_T} = \boldsymbol{\lambda_V}\, \boldsymbol{cos}(\boldsymbol{\psi} - \boldsymbol{\psi_V})$$
$$\Delta \boldsymbol{V_P} = \boldsymbol{\Delta\lambda_i} + \boldsymbol{r}\frac{\boldsymbol{d\Delta\beta}}{\boldsymbol{d\psi}} \qquad \textit{2-54}$$

Overall, induced upsets are of smaller magnitude to those induced by parallel vortices of similar strength. For a vortex spinning in the opposite direction as the rotor, the encounter results in an increase in rotor thrust, rotor coning and power consumption, as well as induced longitudinal blade flapping, which change in orientation as the vortex enters and leaves the rotor disk and crosses its centre. If control inputs are applied to nullify moments and maintain rotor thrust constant, rotor power requirements fall and a slight reduction in rotor coning ensues (see Figure 2-41).

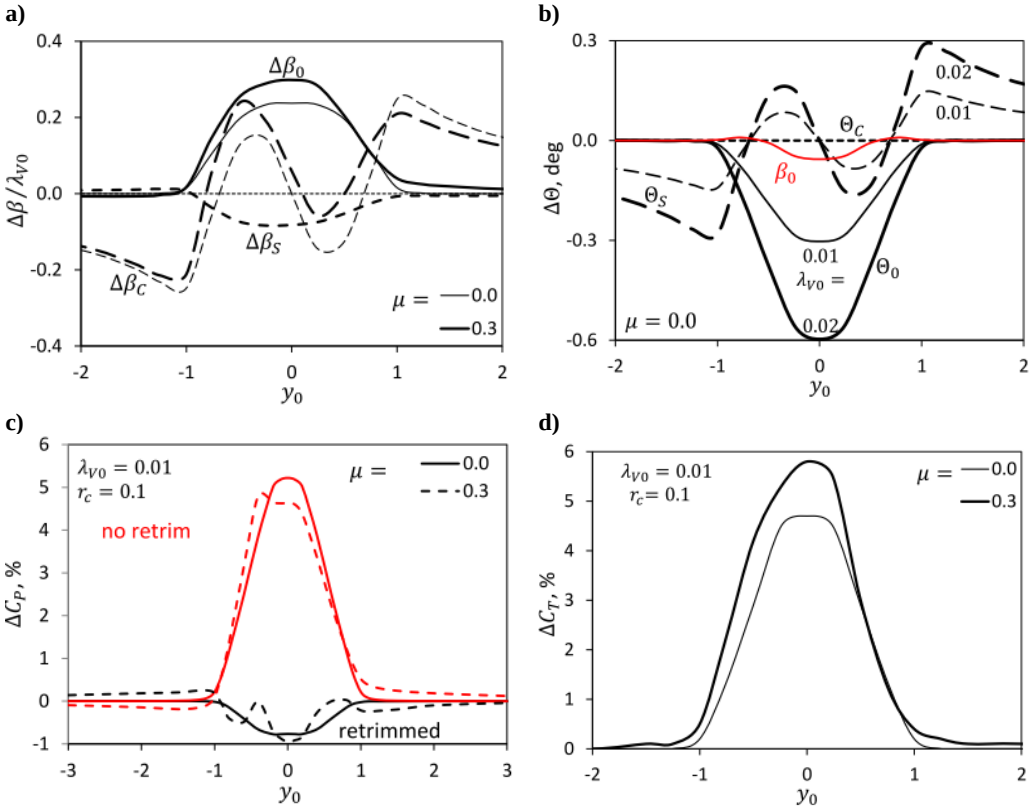

Figure 2-41: Upper row: a) vortex induced changes in rotor flapping and b) required compensating control trim. Lower row: c) Vortex induced changes in rotor power coefficient and d) thrust coefficient in case of no retrim. [95]

Changes in thrust requirement were compared to experimental results measuring the effect of an orthogonal vortex on thrust output and power requirements of a propeller showing a good agreement.

2.7.2.2 Interaction between helicopter rotor and wind turbine airwake

Visingardi and Pavel [97] made use of a blade element momentum model to compute the wake aerodynamics of an NREL 5MW wind turbine [98] and a Bo 105 helicopter rotor. An atmospheric boundary layer was also taken into account for the solution of the wind turbine blade.

The much higher speed of the helicopter rotor blade compared with the speed of the wind turbine blades leads to important differences in characteristic times, making a coupled simulation computationally expensive. A decoupled approach was therefore followed, solving first the aerodynamics of the wind turbine wake and storing a time averaged solution. Aerodynamic simulations of the helicopter rotor within this steady state flow velocity field were then performed.

The rotor was trimmed for hover and forward flight under no wind conditions. Different aerodynamic simulations were performed under the conditions of uniform side wind and at different fixed locations within the time averaged airwake flow field. Estimations of induced blade flapping and resulting changes in rotor moments on the hub were estimated through the application of equation [2-48].

Results (see Figure 2-42) show that the effect of uniform side wind on the rotor changes the incident tangential velocity on the blades around the longitudinal axis (azimuth positions 90 and 270deg) and, due to rotor coning, the incident perpendicular velocity on the blades around the lateral axis (azimuth positions 0 and 180deg) changing the effective bade angle of attack. Resulting rotor loads lead to pitch up and right roll moments for flight under port wind conditions (and opposite for starboard wind conditions).

Solving the rotor inside the wind turbine wake shows alterations in the effective angle of attack of the blades, $\Delta\alpha$, a slight increase in the forward half of the rotor and a change in the 270deg azimuth positions that decreases the effects of side wind. Changes in effective angle of attack at the 90deg azimuth position however increase the effects of port side wind and decrease them in case of starboard side wind.

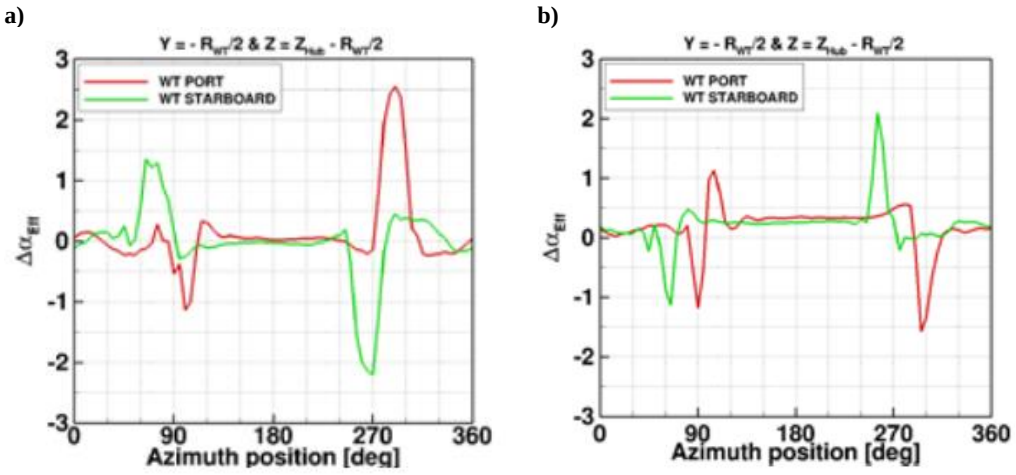

Figure 2-42: a) Changes in blade angle of attack due to uniform wind, b) changes in angle of attack within airwake (differences from conditions of uniform wind).[97]

These changes manifest themselves in rolling moments against the direction of the wind turbine, slight pitch down moments under conditions of port wind and strong pitch up moments under conditions of starboard wind. Overall effects on rotor thrust, torque and yaw moments are limited (Figure 2-43).

The solution of the wake vortex strength has been used to estimate instantaneous upsets from an orthogonal encounter between the rotor and a wake vortex and compared them against control quickness requirements of ADS-33, which provides an idea on whether aircraft satisfying level – 1 or level – 2 requirements would be able to counteract resulting disturbances. The results show that for a left to right crossing upsets in pitch and roll can exceed Level 1 quickness requirements (Figure 2-44).

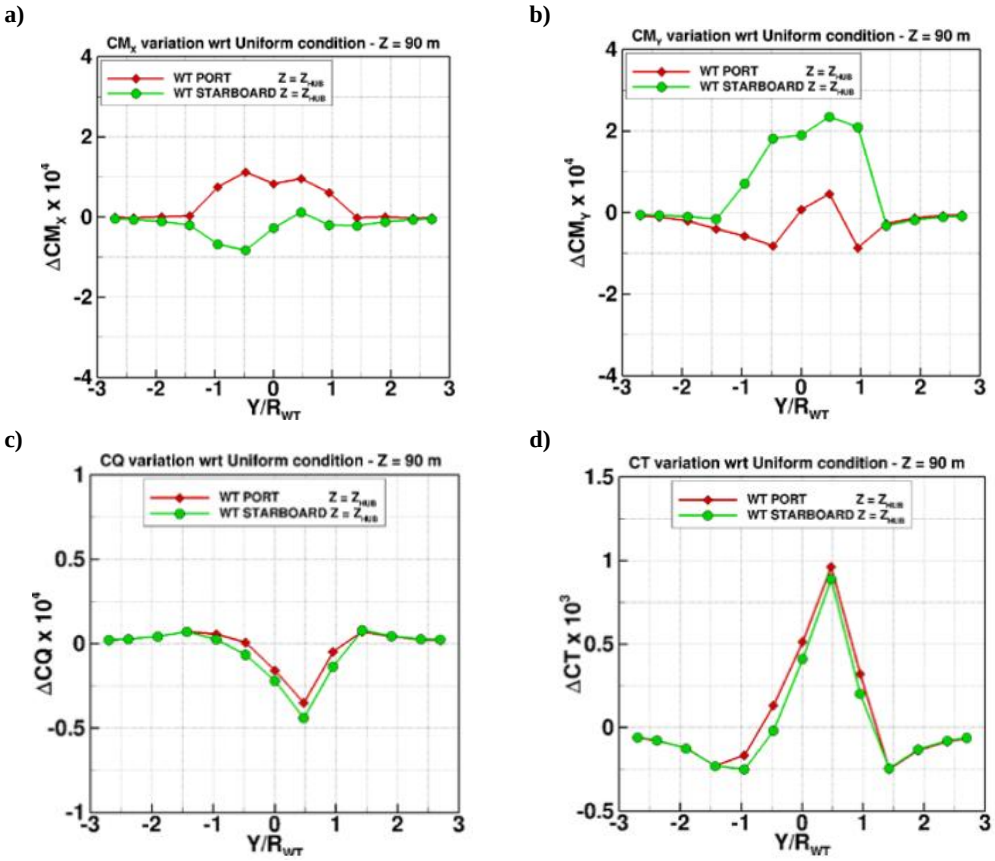

Figure 2-43: Clockwise from upper left: Changes in rotor rolling moment coefficient, pitch moment coefficient, torque coefficient and thrust coefficient when operating inside the airwake. [97]

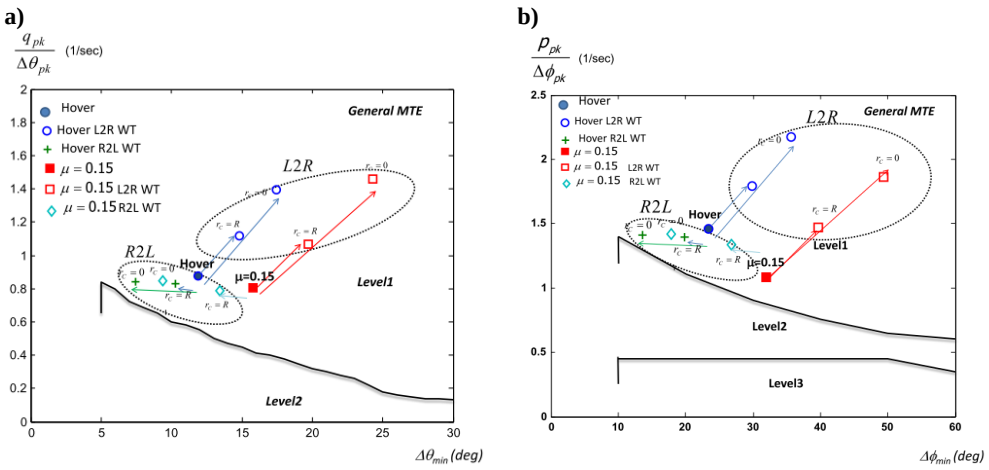

Figure 2-44: Quickness of a) pitch and b) roll upsets from a rotor encountering an orthogonal axis. [97]

Androkinos et al. [99] followed a similar procedure to decouple the wind turbine aerodynamics simulation from the helicopter rotor. A prescribed wake lifting line model was employed for the generation of the wake flow and a free wake vortex particle model for the aerodynamic simulation of the helicopter rotor. Both models showed good agreement when applied to the simulation of the wind turbine wake.

Aerodynamic analysis of the helicopter rotor under uniform port wind and on fixed positions within the time averaged airwake flow field are performed. A trim analysis of the helicopter rotor is also performed. Results are qualitatively similar to those obtained by Visingardi et al. [97] described earlier. For right to left crossings, main effect seems to be due to the velocity deficit on the wake acting against the effect of a uniform side wind and leading to pitch down moments and roll moments towards the left side of the rotorcraft (Figure 2-45).

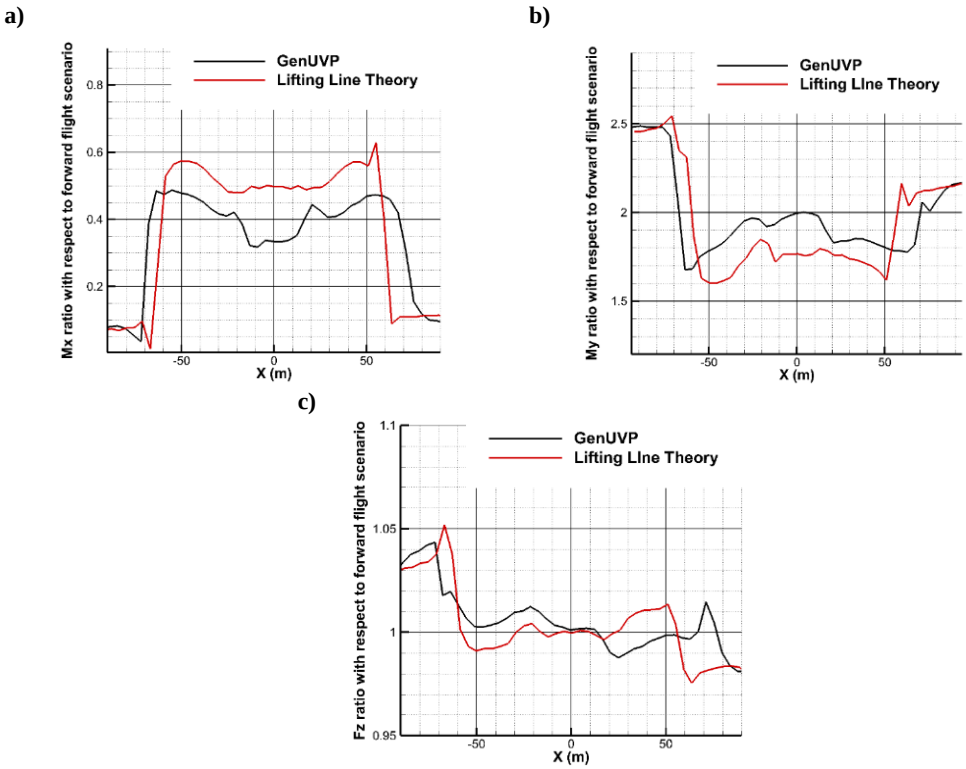

Figure 2-45: Ratio with respect to no wind forward flight conditions of: a) roll moment, b) pitch moment and c) vertical forces of the rotor within the airwake. [99]

2.8 Summary of the literature review

This chapter has provided a review of the of the literature related to the modelling and simulation of rotorcraft operations in turbulent environments. At the time of writing, there is a lack of informed regulatory guidance for rotorcraft operations when at risk

of encountering airwakes or turbulence. Further, the literature regarding the impact of wind turbine wakes on rotorcraft is also very limited and warrants further research.

The wind turbine wake encounter literature has focussed on offline simulations of a helicopter main rotor operating within a wind turbine wake or crossing a blade tip vortex. Results point towards a low severity for vortex encounters even for large wind turbines, but crossing the lower flow velocity deficit region within the wake results in pitch and roll upsets which can require pilot compensation. There is however no real-world flight data or results from piloted flight simulation trials available that would allow verification of these initial findings, and addressing the simulation element of rotorcraft turbine wake encounters is the first step of the Thesis.

A wider literature review study was performed related to rotorcraft operations in turbulent environments, covering areas where existing research and methods could inform the Thesis. Topics reviewed included research into wind turbine wake encounters by fixed-wing airplanes, encounters of large fixed-wing airwakes by rotorcraft, and rotorcraft shipborne and offshore deck landings within a turbulent airwake.

Offline and piloted simulations of fixed wing aircraft encountering wind turbine wakes, and initial offline assessments of rotorcraft response during such encounters, suggest the main effect is a single large disturbance due to the wind velocity deficit inside the wake. Compared to wake vortices from large airplanes, wind turbine blade tip vortices are much weaker. Helicopters tend to be less susceptible than fixed wing aircraft of the same weight to such disturbances, so overall upsets are expected to be smaller. Nevertheless, wind turbine wake encounters might occur under conditions, such as lower altitude or closer proximity to obstacles, that might contribute to a larger safety hazard.

Accidental crossings of wind turbine wakes will probably be relatively quick, similar to encounters with wing wake vortices. Wake modelling methods applied in flight simulation for these encounters, such as the use of steady time-averaged wakes or prescribed wakes, might also be suitable for hazard assessments. Regarding encounter severity assessments, a suitable hazard metric might be related to absolute peak deviations of attitudes and/or flightpath and needs further investigation.

Some offline studies suggest that light airplanes crossing the far field turbulent wake of the wind turbine might experience larger upsets than crossing the more uniform

region near the turbine. Given that most flying should occur at a significant distance from operating wind turbines, such encounters might be more common.

Helicopters can be involved in operations requiring precision manoeuvring and divided crew attention, such as SAR operations. During these operations turbulence levels can vary significantly when winching personnel to wind turbines, which should be turned-off, but where the aircraft is still subjected to the turbulence from the wind turbine structure. In these circumstances, the steady state and prescribed wake models employed in the literature of wind turbine wake encounters might not be representative of the situation encountered in real-word operations.

Such missions share some similarities with helicopter ship and offshore deck landings. There has been significant research in helicopter ship dynamic interface modelling for real-time piloted flight simulation. Results point to unsteady turbulence, especially low frequency upsets in heave, as the main contributor to workload and degraded handling qualities in these conditions. In addition, modelling of unsteady airwake effects is required to accurately capture the impact these airwakes can have on pilot workload during such operations.

Wake and turbulence modelling methods employed for flight simulation of wake encounters were also examined. There is no established standard for modelling of aerodynamic disturbances and assessing the impact they can have on flight safety. Instead, a variety of different approaches are used depending on the situations being studied.

Precomputed time accurate CFD solutions which are reproduced during trials represent the current highest fidelity models but are complex to implement, and storage requirements mean that only short time periods can be stored and need to be repeated in a periodic manner. Potential or prescribed formulations can be used to rapidly precompute a structured flow field, such as an aircraft or wind turbine wake, but would not reproduce the turbulence when the wake breaks down or behind obstacles such as a ship deck or wind turbine nacelle. Stochastic turbulence models are usually easy to implement and provide completely random disturbances, but models developed for fixed wing aircraft applications have limitations to represent the wide range of environmental and flight conditions helicopters operate in and do not account for varying spatial conditions and low speeds. Control equivalent turbulence methods

solve this by using flight test data to calibrate random control inputs but are limited to the specific aircraft and flight conditions for which such data is available.

There is a need for using flight simulation to assess the impact of turbulence and airwakes on the safety of rotorcraft operations in support of the offshore wind energy sector. A simple, fast turnaround method that can generate realistic disturbances applicable to such situations is required and is the focus of this research.

The objectives of the thesis are laid out in the following chapter.

3 Research Objectives:

The literature review presented in the previous chapter showed that there are no unified criteria or procedures for assessing and minimizing the impact of wind turbine turbulence or accidental wake encounters on rotorcraft flight safety. Despite the growth of rotorcraft operations in support of the offshore wind energy sector there is a paucity of 'real-world' data on the impact of rotorcraft encounters with wind turbine wakes. Hence a tool which could be used to assess the potential safety issues associated with such encounters would be very useful for developing new safety criteria that can be used for planning, certification, training and mitigation of these hazards.

The aim of this research is to address some of these shortcomings.

The research objectives of the thesis, are divided in three parts:

- **Identification of hazards:**

Use offline and piloted flight simulation testing to explore possible wake hazard scenarios to identify hazard performance metrics. Through piloted flight simulation, examine the effect of accidental encounters with wind turbine wakes on flight safety as part of the University of Liverpool's contribution to GARTEUR HC/AG-23 action group using a steady airwake. Develop simulation trials to investigate how the aircraft and pilot would respond to these encounters and to find a relationship between environmental and flight conditions, aircraft handling qualities and determine the resulting impact on encounter severity and workload.

Examine the suitability of using a steady airwake on hazard assessment and determine whether including a more realistic unsteady atmospheric or airwake turbulence would result in a similar outcome.

- **Identify fidelity requirements and modelling techniques:**

Realistic flight simulation for wake hazard assessment requires reproduction of unsteady and time – varying disturbances. This leads to the requirement to develop a simple turbulence model, that provides 'random' but representative turbulence which is spatially accurate, that could be employed for real-time piloted simulation studies. It

should also provide an intermediate solution between high fidelity but computationally expensive models provided by CFD wakes and low fidelity stochastic models.

An examination of currently used tools for turbulence modelling which provide accurate spatial turbulence effects, while having reduced computational requirements and can be utilised in real-time simulations is required and, where necessary, develop new tools to provide that capability. To this end, examine the utility of a synthetic eddy model, which tracks the location of turbulence relative to an aircraft, as a candidate method for producing 'realistic' disturbances for real-time piloted simulations.

- **Test feasibility of new tools to explore criteria and requirements for mitigation of hazards**:

Identification and development of new wake modelling techniques that can be employed in real-time piloted flight simulation; real-time operation is a key requirement. Development of a calibration methodology so that resulting turbulence results in realistic disturbances as judged by the pilot and objective metrics. Examination and assessment of the wake fidelity requirements for flight conditions from hover to forward flight is needed.

Evaluation of the model will be based on whether resulting turbulence produces aircraft disturbances and leads to pilot responses and impact on workload that are representative of real-world conditions. Ideally, evaluation against flight test data would be desired, however such data was not available to the project. As a surrogate, reproduce turbulence from other currently employed models and use them to calibrate new methods to aid in the assessment of the sensitivity the new model's parameters for disturbance generation. Based on this this initial calibration further examine the effect of the model parameters on the subjective and objective assessments of pilot workload. Develop a new, 'realistic' turbulence generator that can be utilised in future wake hazard assessment studies.

These results provide a basis to calibrate the model against real world data, should it be available for future development.

4 Simulation tests of Wind Turbine Airwake Encounters

4.1 Introduction

This chapter describes offline and piloted flight simulation trials performed for an initial hazard assessment of a helicopter encountering a wind turbine wake. Trials were conducted as part of the GARTEUR HC-AG/23 work [93]. The test objectives are presented in Section 4.2 whilst the University of Liverpool's flight simulator used for the study is described in Section 4.3. Section 4.4 describes the steady wind turbine wake from the NREL wind turbine [98] used for the trials and its integration with the flight simulation scenario. Section 4.5 describes the Bo 105 helicopter flight dynamics model [100] and provides an overview of relevant handling qualities. Offline gust response and wake encounter simulations are described in 4.6. The airwake and aircraft models were used as a common database source amongst GARTEUR partners due to their open access in the literature. The planning of the piloted flight simulation trials is described in Section 4.7 and trial results are reported in 4.8. Finally, a discussion of the results and a summary of the chapter is provided in Sections 4.9 and 4.10 respectively.

4.2 Objectives

Offline and piloted flight simulation tests were performed to study the effects on rotorcraft flight and handling as well as pilot response during the crossing of the airwake of a 5MW 126m diameter NREL wind turbine. The aim was to identify resulting helicopter upsets from crossing wind turbine airwakes and, with the help of pilot feedback, relate them to hazards.

The objectives of the test can be summarized as follows:

- Measure upsets in rotorcraft dynamics resulting from the encounter with the airwake of a wind turbine.
- Study pilot reaction to the identified upsets.
- Identify which upsets results in workload increases for the pilot and greater encounter severity.

It was anticipated that the results would enable the development of guidance regarding upsets from rotorcraft-wind turbine wake encounters that is currently lacking in the literature [13].

4.3 Flight simulator

The studies reported in this thesis were conducted using the HELIFLIGT-R simulator at the University of Liverpool [86]. HELIFLIGHT – R (Figure 4-1) is a 6 degree of freedom, configurable flight simulator for training and research applications. It is employed in conjunction with Advanced Rotorcraft Technology's (ART) FLIGHTLAB multi-body dynamics software designed for aircraft modelling and analysis [101]. FLIGHTLAB's aircraft models are based around a reconfigurable library of parameters and control models which can be altered to suit the currently studied flight vehicle. The cockpit controls includes basic rotorcraft controls (stick, collective and pedals) and a series of displays used as reconfigurable instrument panels.

Figure 4-1: Left: HELIFLIGHT-R Flight simulator. Right: Cockpit interior and wind turbine farm scenario.

4.4 Airwake and integration within FLIGHTLAB

The NREL 5MW offshore baseline wind turbine [98] is a model representative of utility scale wind turbines intended to be used as a conceptual model for wind energy studies and analyses. Open access to the data makes it well suited to be used as a common airwake for GARTEUR activities. Relevant specifications of the wind turbine model are summarised in Table 4-1.

The airwake used for the trials described in this chapter was modelled and validated by Leble and Barakos [102] using the helicopter multiblock flow solver (HMB) [37] with a $k-\omega$ turbulence model. The grid consisted of 9.3M cells with a size at the blade surface of 10^{-5} times the maximum blade chord of 0.737m. A uniform inflow was defined 2 diameters upstream and the domain extended up to eight diameters downstream. The original disturbance velocities across the airwake were non-dimensionalised by blade tip velocity. Due to data transfer and storage limitations the obtained flowfield was time averaged for implementation in the simulator, producing a steady airwake. Axial flow velocities are represented in Figure 4-2, while values of flow velocities when crossing the wake perpendicular to its axis are shown in Figure 4-3.

Table 4-1: Main characteristics of the NREL 5MW reference wind turbine [98].

NREL 5MW wind Turbine specifications	
Rating	5 MW
Rotor Orientation, Configuration	Upwind, 3 Blades
Control	Variable Speed, Collective Pitch
Rotor, Hub Diameter	126 m, 3 m
Cut-In, Rated, Cut-Out Wind Speed	3 m/s, 11.4 m/s, 25 m/s
Cut-In, Rated Rotor Speed	6.9 rpm, 12.1 rpm
Rated Tip Speed	80 m/s
Overhang, Shaft Tilt, Precone	5 m, 5º, 2.5º

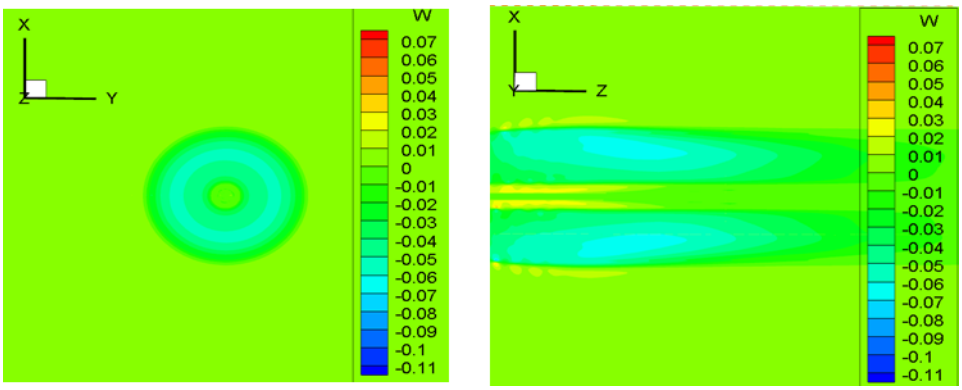

Figure 4-2: Non-dimensional axial velocity distribution of airwake. Coordinates are: z downstream along the wind turbine axis, x is upwards, perpendicular to z, and y is defined using the right hand coordinate system. Coordinate system of the original flow data is independent of flight simulation scenario.

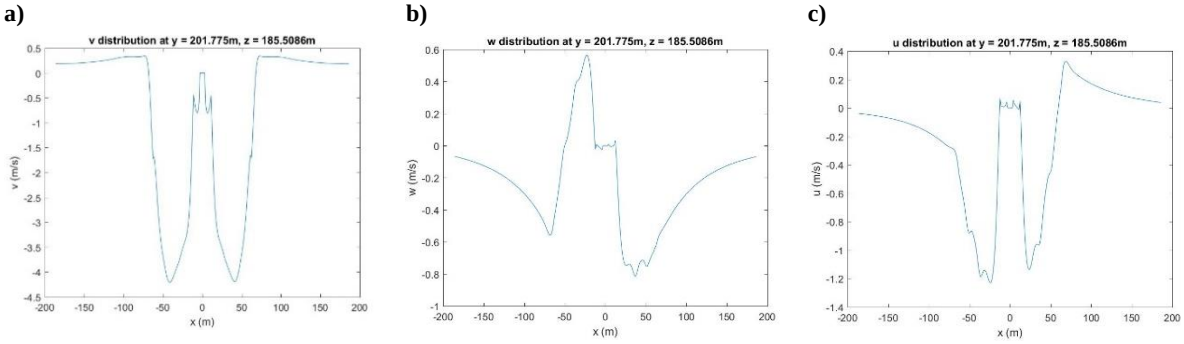

Figure 4-3: Velocity perturbations induced by the wind turbine 202m downstream at hub height in wake box axis. Coordinates of the wake box data are: a) v, downstream along wind turbine axis, b) w (down) vertical, upwards and c) u oriented according to the right hand coordinate system.

The airwake was integrated with the FLIGHTLAB flight mechanics model using the VirAirDyn module, a Simulink lookup table developed at the University of Liverpool [103], and is shown schematically in Figure 4-4. The lookup table stores the interpolated flow velocity disturbances on all three axes of the wake flow domain across a uniform grid distributed along a right prismatic control volume with rectangular sides.

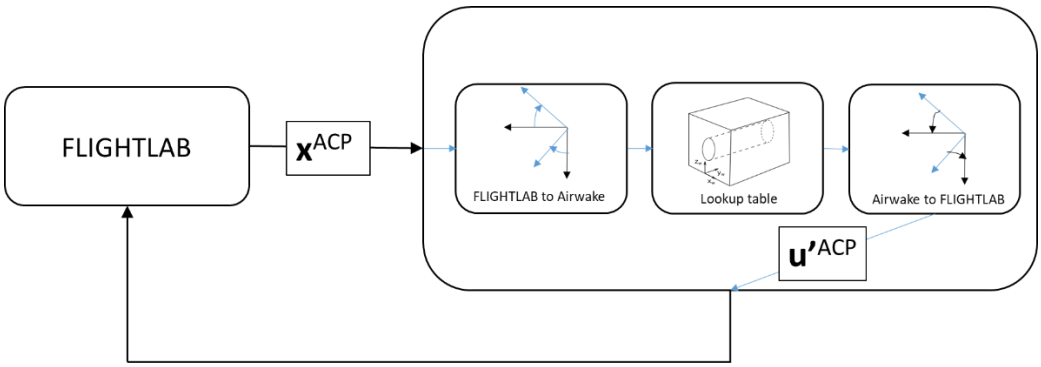

Figure 4-4: Flow diagram of Lookup table for airwake integration.

For each simulator run, the magnitudes of the velocities were scaled according to the environmental wind velocity. Maintaining the velocity deficit proportional to the wind velocity is a reasonable approximation for wind strengths between the cut in and rated wind speed, but not applicable for stronger winds. According to Betz's law [104], assuming no other mechanical inefficiencies, optimum energy output is obtained when the resulting axial velocity deficit is one third of the wind velocity. All simulations performed for this case have been calculated under a 20kts wind. This results in axial velocity deficits of about 4.5m/s (15ft/s) and induced rotational velocities of around 0.8m/s (2.6ft/s) at a downstream distance to the wind turbine of around 2 diameters. Magnitudes comparable to results obtained by GARTEUR partners [97], [99].

There is also a distortion in horizontal velocities perpendicular to the wind turbine axis of around 1m/s (3ft/s). When crossing the airwake, this will manifest itself as a perturbation in forward airspeed for the aircraft.

Cell locations and flow velocity components are stored in their own coordinate system (independent of the CFD and the wind simulator coordinate systems). For each time step, FLIGHTLAB transfers the location of all aircraft ACPs to the VirAirDyn module, which translates them to airwake coordinates. If the ACP is located within the airwake box, the corresponding disturbance flow velocities are obtained by interpolation between cells. After translating them to airwake coordinates the velocity components are transferred back to FLIGHTLAB and added to the flow velocities computed by FLIGHTLAB for this location (see Figure 4-4).

4.5 Bo 105 FLIGHTLAB model

The Messerschmitt Bolkow–Bohn Bo 105 is a light, twin–engine, multipurpose utility helicopter with a four bladed hingeless rotor (Figure 4-5). This feature provides the rotorcraft with high response bandwidth manoeuvrability and control power. This might also make the rotorcraft more susceptible to wake encounters. Table 4-2 presents a summary of the aircraft's main specifications.

The helicopter is still operational in many parts of the world and has been used extensively in research projects across Europe. As a result, there is ample information available on flight performance for the Bo 105 [105] and most partners involved in GARTEUR HC/AG-23 or NITROS had access to flight simulation models or are familiar with the aircraft.

The FLIGHTLAB model of the Bo 105 employed at the University of Liverpool is a medium fidelity model [106] of the Messerschmitt Bolkow – Bohn Bo 105 based on the following features:

- Rigid body fuselage model.
- Blade element theory main rotor model with quasi-steady airloads.
- Bailey rotor tail model.
- Aerodynamic models for stabiliser and fin.
- A simplified engine model.

Aerodynamic forces and moments on the model are calculated from the flow velocities at 25 Aerodynamic Computation Points or ACPs. Five are located on each blade of the rotor, while the other five are located at the aircraft centre of gravity, the tail rotor's hub and at the vertical and horizontal tails.

In its current implementation, the model features no SCAS system and response delays due to the actuators are not considered during the simulation.

Table 4-2: Main specifications of the MBB Bo 105 helicopter. [105]

Geometry			**Power plant**		
			2 × Allison 250-C20B turboshaft engines		
Length	11.86 m	38 ft 11 in	Take off power	298 kW	400 shp
Fuselage length	8.56 m	28 ft 1in	Max continuous power	287 kW	385 shp
Fuselage width	1.58 m	5 ft 2.2 in			
Height rotor hub	3.00 m	9 ft 1.1 in			
Empty mass	1400 kg	3086.5 lb			
Max take off mass	2300 kg	5070.6 lb	**Main Rotor**		
Performance			Rotor diameter	9.84 m	32 ft 3.5 in
Max cruise speed	136 kts		Normal rpm	424 rpm	
Never exceed speed	145 kts		Hinge offset	14% (aprox)	
Service ceiling	17000 ft		**Tail Rotor**		
max rate of climb (60kts)	1600 fpm		Diameter	1.90 m	6 ft 2.8 in
max rate of climb (hover)	400 fpm		Normal RPM	2200 rpm	

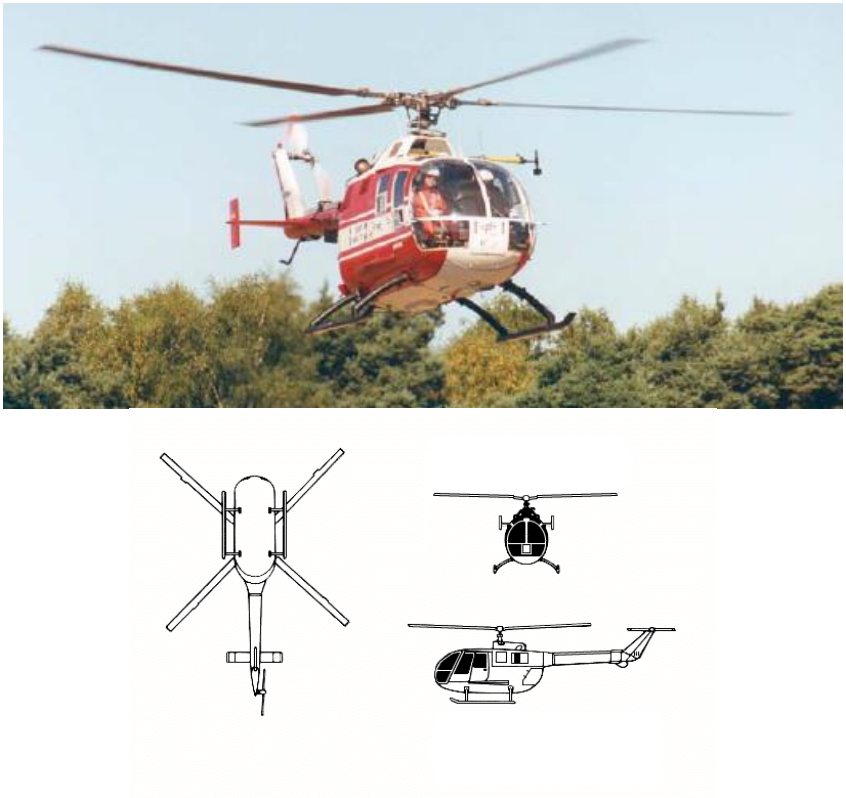

Figure 4-5: Above: DLRs Bo 105 flight test helicopter [105]. *Below: Schematics of the Bo 105 helicopter. Source: Public Domain, https://commons.wikimedia.org/w/index.php?curid=131824*

4.5.1 Bo 105 simulation model, Flight Handling Qualities

In preparation for a previous round of testing, an off line simulation study of handlings qualities at hover and low speeds was performed for the Bo 105 model [100]. Results were measured against ADS -33 criteria and compared to published results from handling qualities flight tests performed by the DLR [105].

Overall, the Bo 105 model presents good handling qualities but has considerable inter-axis couplings due to the design of the rotor hub. Responses to control inputs satisfy Level 1 requirements for bandwidth, quickness and control power in pitch and roll and Level 2 in yaw. Small amplitude mid-term response (stability) falls between Level 2 and 3 in the phugoid mode (divided attention criteria), with a tendency towards instability as flight speed increases, and Level 1 and 2 for the Dutch roll mode (divided attention criteria), becoming more stable as flight speed increases (Figure 4-6). Inter-axis couplings present the main handling qualities deficiencies for the model and the real-world Bo 105 with yaw–collective and pitch-roll couplings falling well within Level 3 (Figure 4-8). The Bo 105 is also particularly susceptible to lateral gusts (Figure 4-10).

Published flight test data [105] differs in available yaw bandwidth compared with the results predicted by the software model and falls into Levels 2 and 3 according to ADS-33 criteria. Otherwise, flight test data results while, slightly less optimistic about the predicted rotorcraft handling qualities, seem to be in reasonable agreement with the software model (Figure 4-7, Figure 4-9).

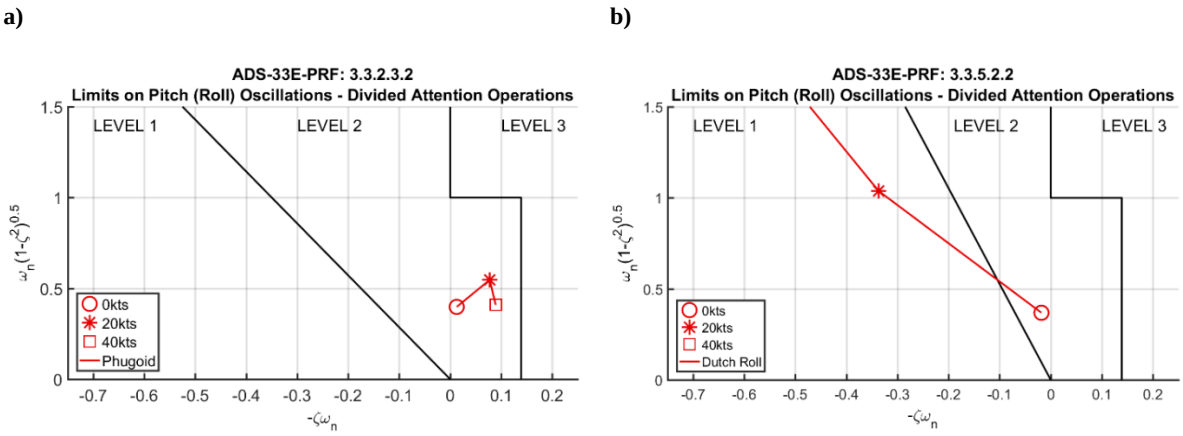

Figure 4-6: Bo 105 FLIGHTLAB model, a) Longitudinal and b) Lateral modes. Ref: Neil Cameron Hover and low speeds flight handling qualities. Internal report.

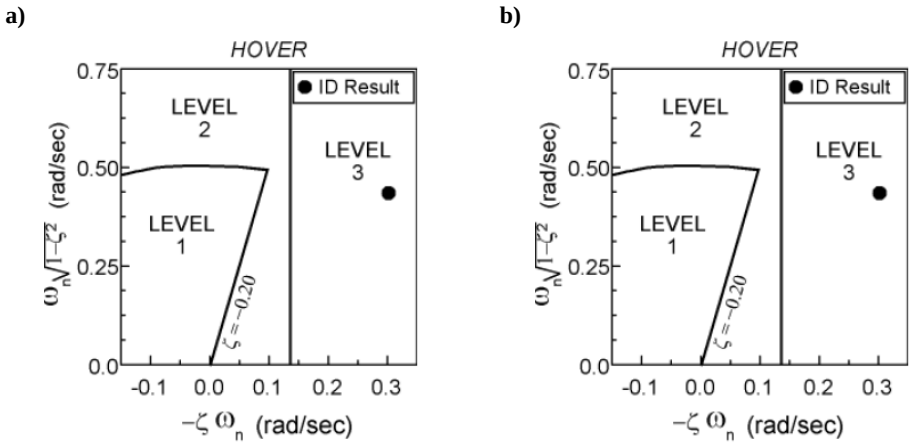

Figure 4-7: Bo 105 Flight test results: a) longitudinal and b) lateral modes in hover. [105]

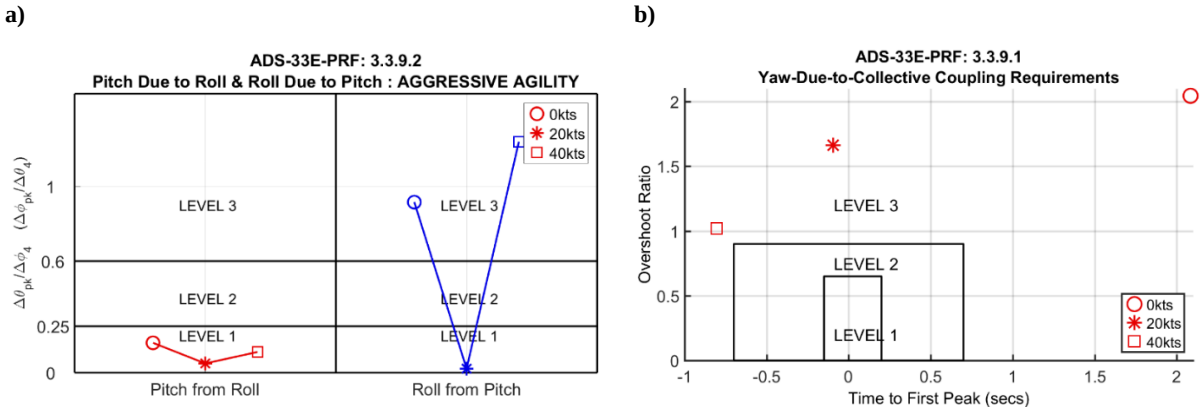

Figure 4-8: Bo 105 FLIGHTLAB model: control axis cross- couplings in a) Pitch–roll and b) yaw – collective. Ref: Neil Cameron. Bo 105 Helicopter Model Hover and low speeds flight handling qualities. Internal report.

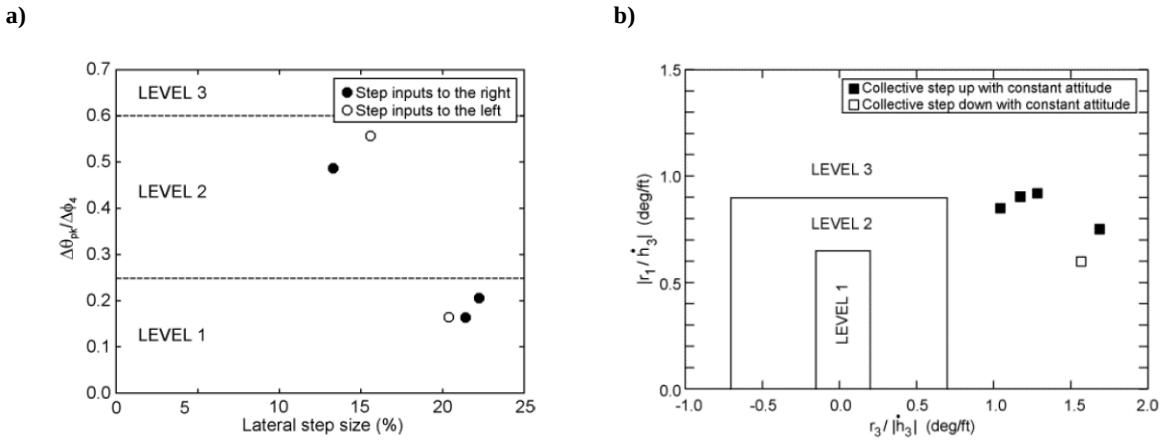

Figure 4-9: Bo 105 Flight test results: control axis cross- couplings during hover in a) Pitch–roll and b) yaw–collective. [105]

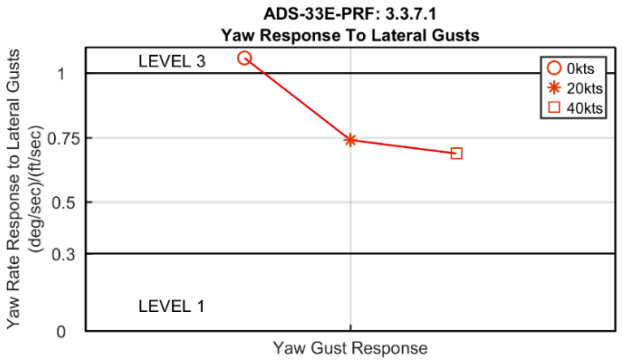

Figure 4-10: Bo 105 FLIGHTLAB model. Yaw responses to lateral Gust and collective input. Ref: Neil Cameron. Bo 105 Helicopter Model Hover and low speeds flight handling qualities. Internal report.

To select between the most critical test scenarios and flight conditions, a trim analysis was performed for the rotorcraft model under different flight conditions. These

included hover and slow speed forward flight at 20kts and 40kts ground speed subjected to winds of up to 30kts impinging on the aircraft from different directions between 0deg to 360deg Azimuth.

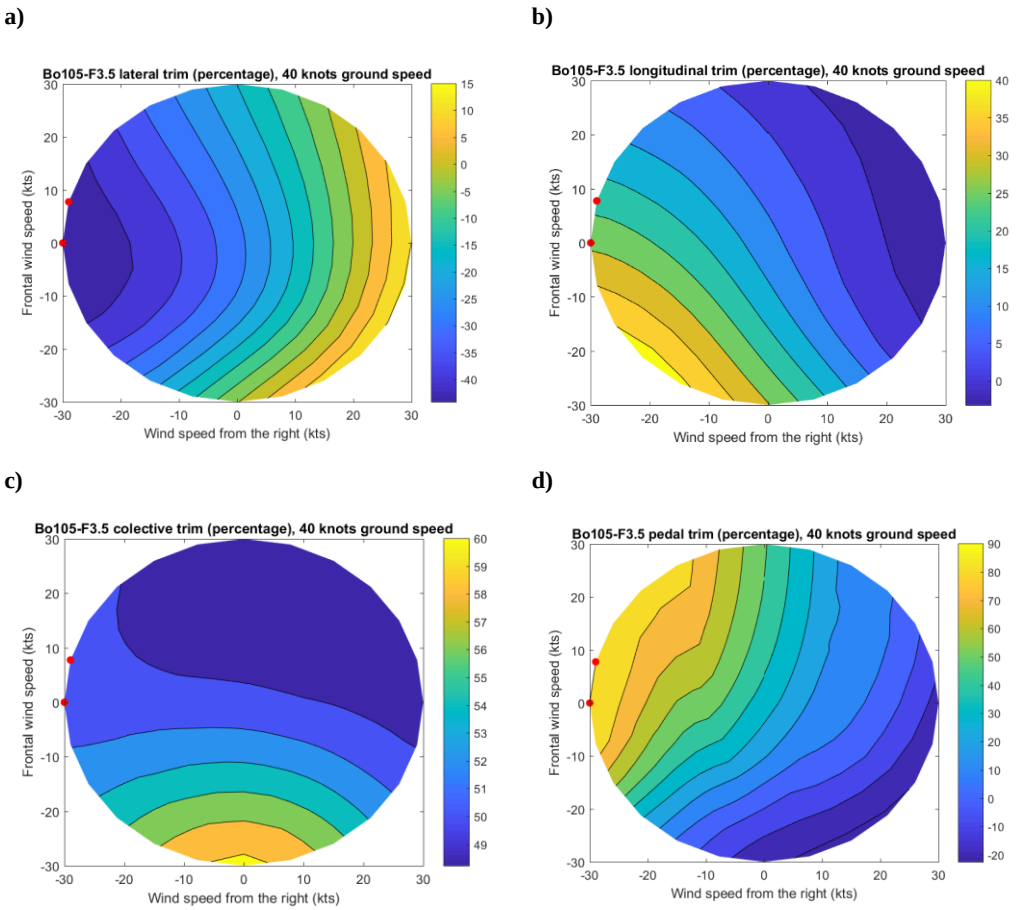

Figure 4-11: Bo – 105 model: Required control inputs in a) lateral stick, b) longitudinal stick, c) collective, d) pedal, for trim at 40kts flight speed, red dots indicate conditions at which trimming conditions could not be achieved

Results for 40kts flight speed are shown in Figure 4-11. Values in the vertical axis indicate wind velocity component along the aircraft's longitudinal axis, positive values, corresponds to wind coming from the frontal sector (azimuth of ± 90 deg). Horizontal axis represents lateral wind velocity components with positive values corresponding to wind coming from the green sector (right side, azimuths of 0 – 180 deg). The colour of the field indicates the control trim position as a percentage of total available control range (with the neutral position being 0). Under conditions of rightwards wind, required pedal input to maintain helicopter heading and flight path increases with forward flight speed to the point that when flying at 40kts groundspeed the model cannot be trimmed for certain wind velocities and azimuths (Figure 4-11).

Results are consistent with those published by the other members of the GARTEUR group for the rotor of the Bo 105 under conditions of uniform side wind (See Section 2.7.2.2).

4.6 Offline simulations:

4.6.1 Gust response:

Further analyses were performed of helicopter attitude upsets following a gust. The flight conditions chosen were hover and low-speed forward flight at 20kts and 40kts with a 20kts lateral wind with either 90deg (green wind) or -90deg (red wind) azimuth (aircraft is trimmed using ground speed, *Vgn*).

The helicopter was subjected to step inputs in wind velocity of a similar magnitude that might expected for an encounter with a wind turbine airwake. Lateral gusts of around 4.5m/s (15ft/s) opposite to the wind direction and vertical upward and downward gusts of 1.3m/s (4ft/s) were tested, comparable to the axial velocity deficit and rotational velocities the aircraft will encounter while crossing the NREL 5MW wind turbine wake (see Section 4.4).

Results (Figure 4-12) show that maximum attitude upsets and attitude rates might result mainly from lateral wind velocity deficits along the wake when the helicopter flies under portside wind (azimuth = 90deg red). At hover, yaw and roll upsets are the most significant and can reach over 20deg in the first three seconds, well within Level 3 according to the ADS-33 transient following a failure criteria (see Section 2.5.2). Increasing the helicopter flight speed decreases the magnitude of pitch and roll upsets. At 20kts, yaw upsets increase, but reduce significantly at 40kts.

Upsets resulting from vertical gusts (Figure 4-13), while small compared to those from a lateral gust, present a very different behaviour. Roll and yaw attitude upsets and rates tend to increase with aircraft flight speed. And when flying in a portside wind (azimuth of 90 deg) resulting upsets in roll and yaw are of opposite sign in hover than in forward flight.

It is important to realize that the encounter with the airwake will be as a result of simultaneous gusts upsets in the lateral, longitudinal and vertical axes and therefore the helicopter response might differ considerably from the results presented here.

a)

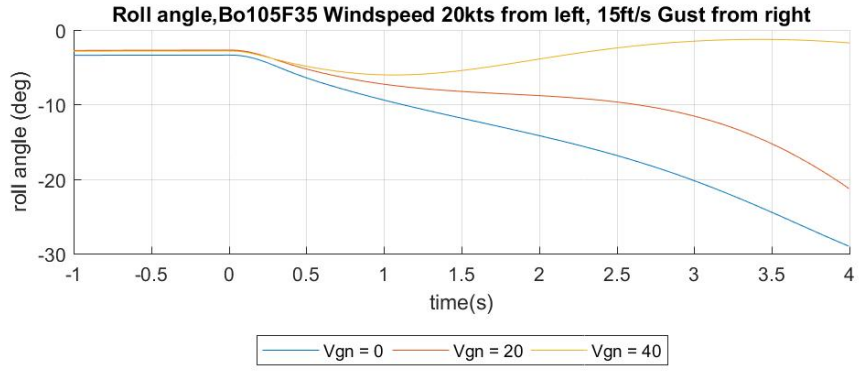

b)

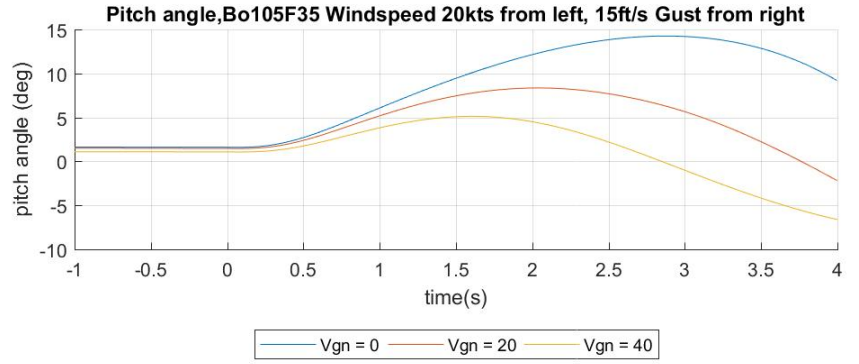

c)

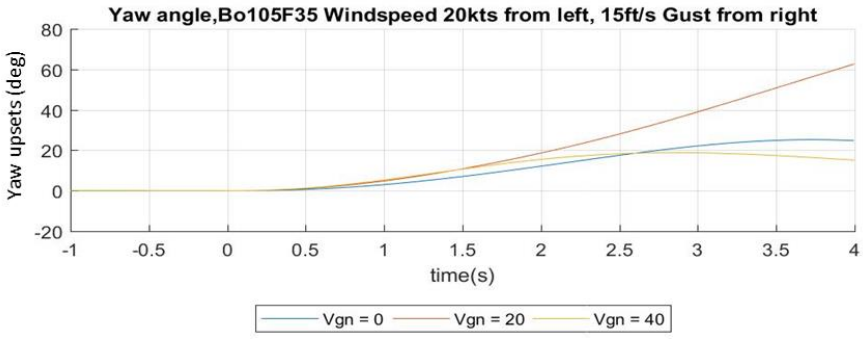

Figure 4-12: Bo 105, 20kts wind speed, azimuth 270deg. 15ft/s gust step with 90deg azimuth. Attitudes after upset (at t = 0s)

a)

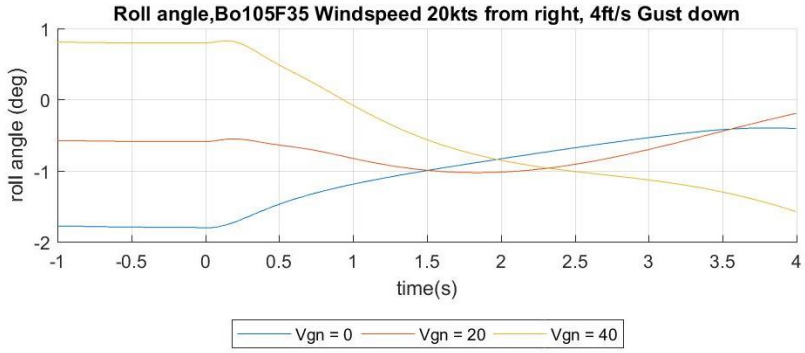

b)

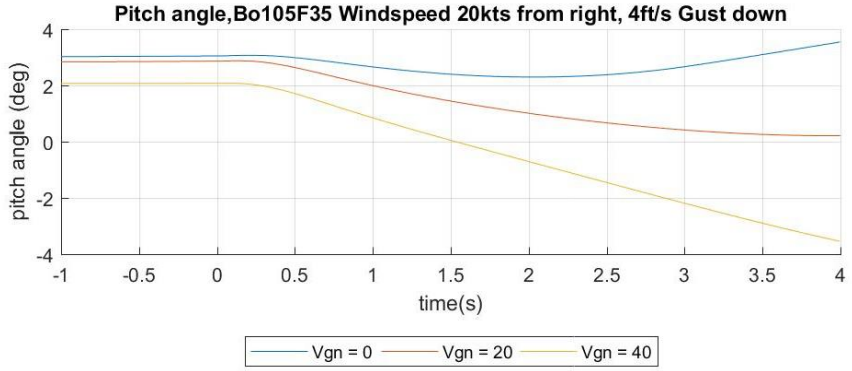

c)

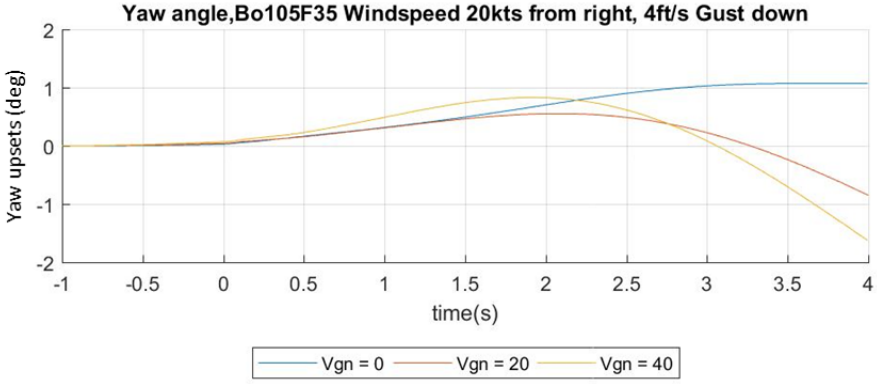

Figure 4-13: Bo 105, 40kts ground speed, 20kts wind speed, azimuth 90deg. 4ft/s gust step from above. Attitudes and angular velocities after upset (at t = 0s)

4.6.2 Wake crossings

To identify cases of interest for piloted flight simulation tests, offline simulations of wake encounters were conducted. The rotorcraft model was trimmed outside the airwake and allowed to fly freely through the precomputed airwake. No corrective action was performed, so while the simulation lasts, resulting upsets will build up and attitude deviations can reach values larger than those which a pilot would allow to happen during online flight simulation. Results are still useful to inform about the nature of initial upsets just after the encounter and how these might evolve in case the pilot might not be able to correct them, (for example due to the need to focus on correcting upsets in more critical axes).

Results show a multiaxial response with attitude upsets of similar magnitude in all axes and a loss of flight altitude and helicopter airspeed. The nature and magnitudes of resulting upsets are similar to those obtained in offline simulations of the helicopter gust response study (see Section 4.6.1). Two main upsets in yaw and smaller ones in roll can be observed when entering and exiting the wake. Afterwards, the aircraft's attitude in roll and yaw tends to oscillate within a limited range until it finally diverges after some seconds; at higher airspeeds, the aircraft might already have left the airwake behind explaining the attitude changes observed. The direction of long-term roll response seems to change with increasing helicopter flight speed, a phenomenon already observed in offline gust response tests. Upsets in the pitch axis tend to start with a delay but start growing immediately. Encounters at higher helicopter flight speeds tended to result in higher maximum attitude upsets; this was particularly noticeably for upsets in the pitch axis (Figure 4-14). On the other hand, a limited effect was noticed for encounters at higher wind velocities or for reducing the distance to the wind turbine below two diameters (Figure 4-15).

Changes in forces and moments on the different components of the rotorcraft are shown in Figure 4-16. Vertical forces and forces in the direction of flight do not change substantially during the encounter. However, there are changes in the lateral force components which seem to stem mainly from the tail rotor and the aerodynamic forces on the fuselage. The main rotor seems to be the main source of pitch moments and, together with the tail rotor, an important contributor of roll moments. Meanwhile, yaw moments during the wake crossing originate mainly from changes in tail rotor thrust during crossing.

a)

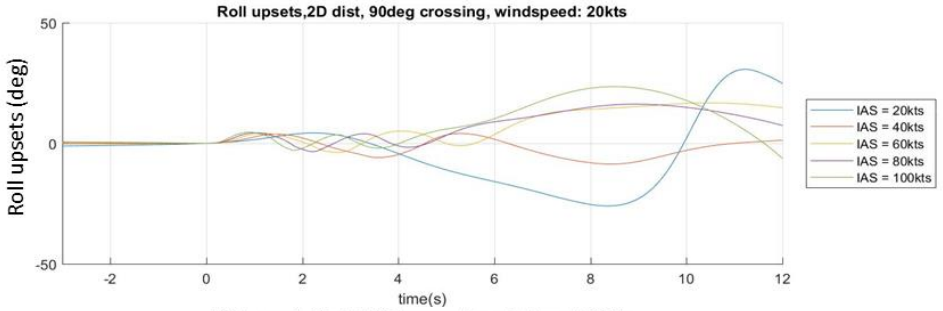

b)

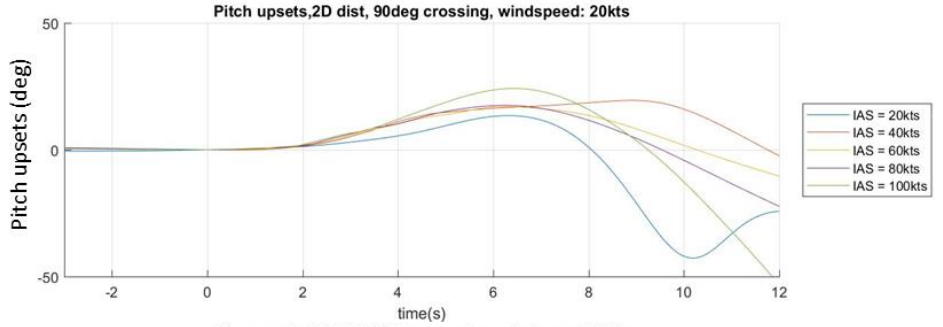

c)

Figure 4-14: Offline simulation results. Helicopter attitude upsets when crossing the airwake (at t = 0s) without pilot control inputs.

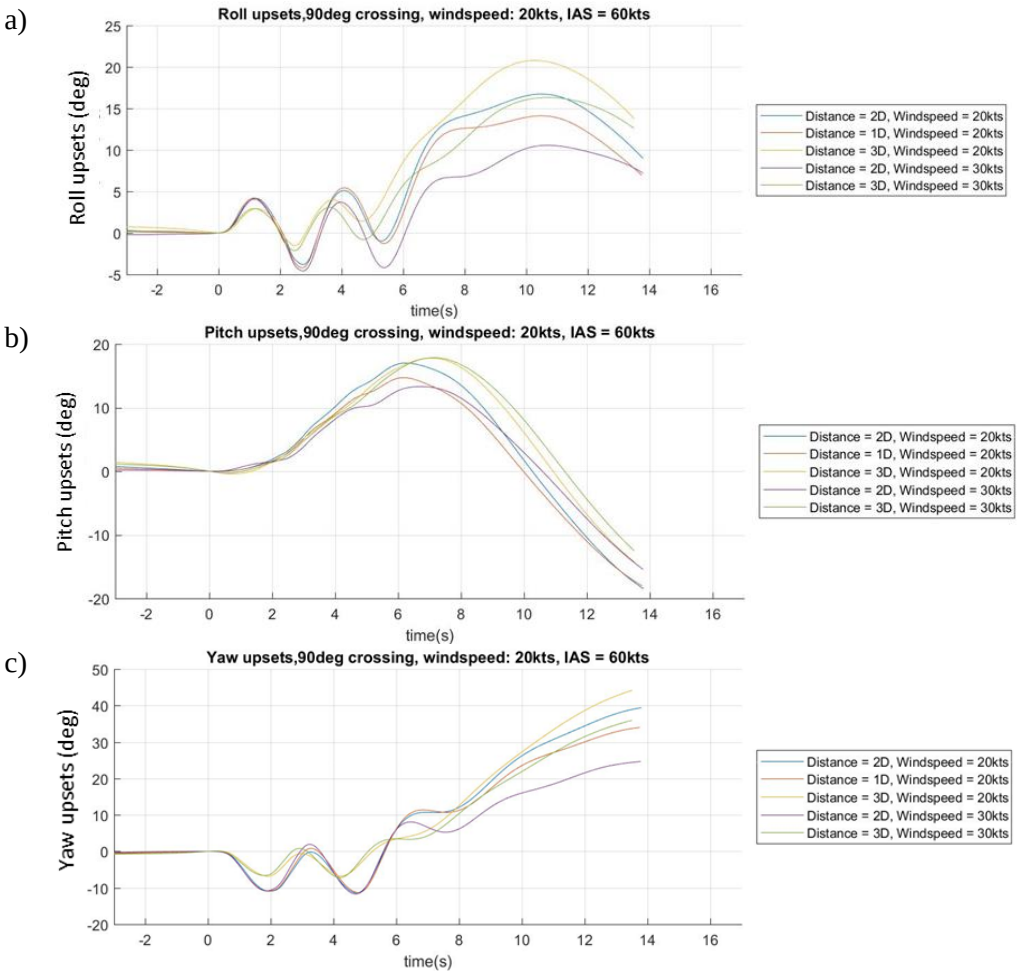

Figure 4-15: Offline simulations. Attitude upsets resulting from airwake encounters at different distances or under different wind speeds.

a)

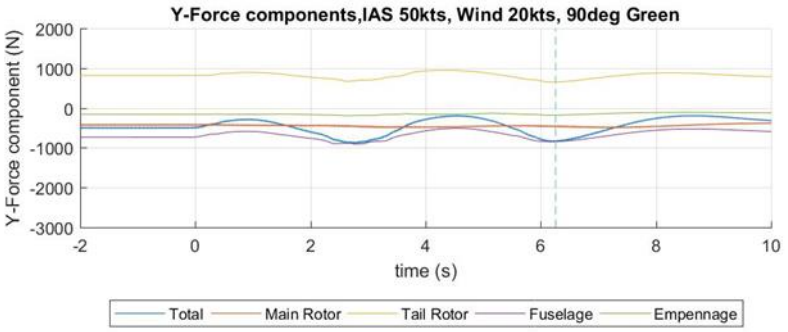

b)

c)

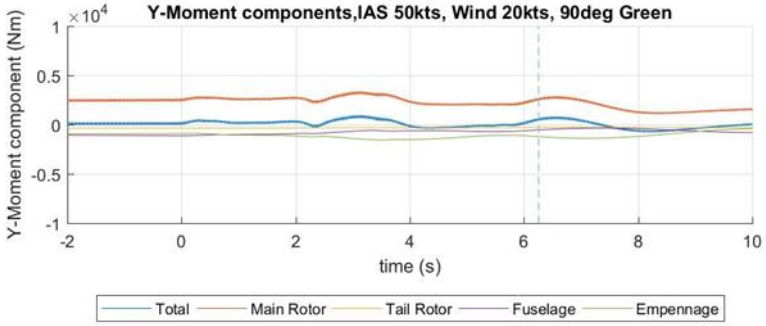

d)

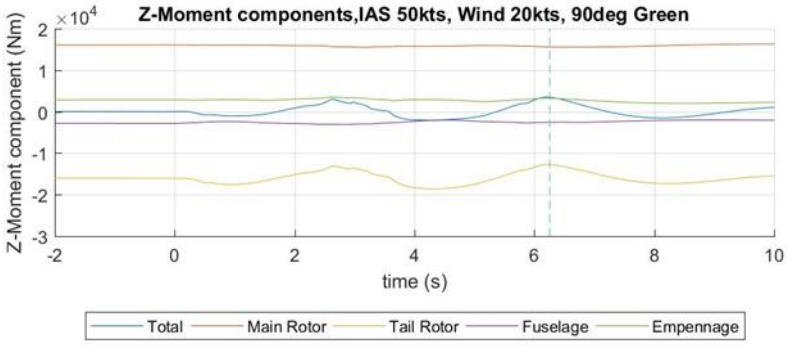

Figure 4-16: Induced lateral forces (Fy), and roll (Mx), pitch (My) and yaw (Mz) moments when crossing the airwake.

4.7 Piloted flight simulation trials

A series of piloted test flights were performed to study effects of a wind turbine wake encounter on rotorcraft handling and the subsequent pilot responses to correct for aircraft deviations from the original flightpath. The tests were conducted by an experienced former Royal Navy test pilot at the University of Liverpool using the HELIFLIGHT-R flight simulator, flying a series of airwake encounters with a simulated Bo 105. Several simulator runs were performed at different helicopter airspeeds and under different wind directions (see Table 4-3). Rotorcraft dynamic parameters and pilot control inputs were recorded together with pilot subjective ratings and valuation of different parameters. Pilot feedback also provided further insight into the hazard assessment and contributors to workload during an encounter.

4.7.1 Test Matrix

Test parameters were selected looking for possible critical encounter conditions that can present themselves under realistic flight conditions.

Flight handling qualities analysis and offline simulation show that overall the Bo 105 model shows better stability than the actual aircraft but has stronger inter-axis couplings. It has difficulties trimming under red winds at high flight speeds, so most runs were performed using green winds. The aircraft exhibits a strong yaw response to lateral gust in offline airwake crossings which then results in secondary roll and pitch upsets. Upsets are stronger under conditions of red winds or high flight velocities.

All test flights were conducted using a wind strength of 20kts which is slightly lower than the 22kts rated wind speed of the NREL wind turbine [98]. It is assumed that under normal circumstances and missions, low altitude flights between wind turbines will be performed at low speeds. Offline testing of the rotorcraft shows that it is particularly sensitive to changes in wind orientation, especially from wind coming from portside (see 3.3.3) and that it might present difficulties in control at higher flight speeds. To study these effects, 14 test runs were conducted. A series of runs were performed at 30kts true airspeed under different wind orientations and another series of runs at varying flight speed between 20kts and 100kts. Two runs were performed in which there was no airwake present in order to provide a benchmark against which to compare results. In addition, a first run was conducted without wind or airwake to allow the pilot to familiarize themselves with the rotorcraft model and the scenario. The complete test matrix is shown in Table 4-3.

Table 4-3: Simulator runs performed. Azimuth angles are given in aircraft body axis.

Run	Airwake	Wind Speed (kts)	TAS (kts)	Wind Azimuth (deg)	IAS (kts)
1	NO	0	30	N/A	30
2	NO	20	30	-90	30
3	YES	20	30	-90	30
4	YES	20	30	90	30
5	YES	20	50	90	50
6	YES	20	100	90	100
7	YES	20	80	90	80
8	YES	20	20	-90	20
9	NO	20	50	90	50
10	YES	20	30	-135	15.86
12	YES	20	30	45	44.14
13	YES	20	30	-45	44.14
14	YES	20	30	135	15.86

4.7.2 Scenario

A scenario for an offshore wind turbine farm was developed for the trials (see Figure 4-17). Each wind turbine has a diameter of 126m and a hub height of 137m. The wind turbine farm consists of two parallel rows of five wind turbines forming a straight corridor oriented along the west – east axis. The wind turbines face the wind from the south, south-west or south-east, resulting in wind azimuths of -45deg, -90deg or -135deg when the aircraft was flying east to west and 45deg, 90deg or 135deg, when flying west to east (see Table 4-4).

Table 4-4: Wind azimuth relative to aircraft depending on wind and flight direction.

Wind Azimuth (deg)	Flight direction	
Wind direction	**E -> W**	**W -> E**
SW -> NE	-45	45
S -> N	-90	90
SE -> NW	-135	135

Wind turbines and cone models were implemented from commercially available software, Presagis' Creator Pro, which was used for scaling the objects and developing the visual scene. They were then added to a custom made ocean scenario using Presagis' VEGA scenario editor.

There is no indication regarding the size of the safe lanes within the CAA guidelines [13], so wind turbines were placed in rows with a lateral separation of 3 diameters (378m) between them and a separation between rows of 4 diameters (504m) and oriented towards the incoming wind direction. The separation distances are typical of those that are used in existing offshore wind farms [34]. A path along the corridor was marked with buoys (cones) for the pilot to follow.

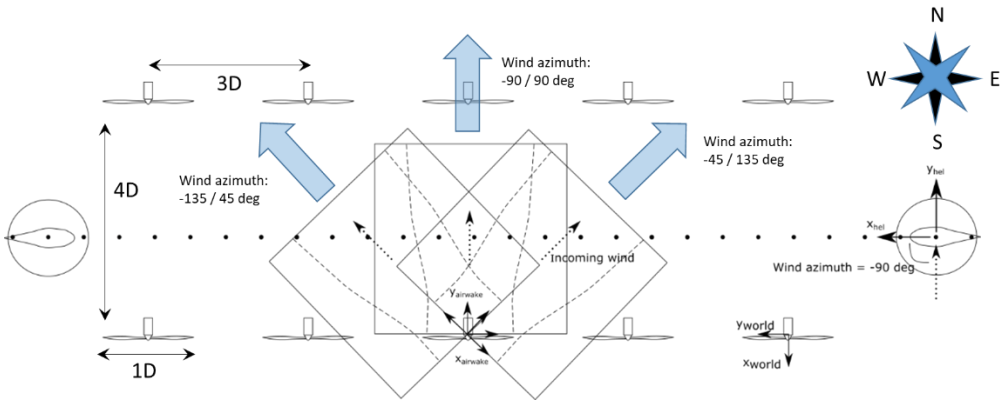

Figure 4-17: Schematic of the flight simulation scenario and object orientations.

For each run, a single NREL computed wind turbine wake was placed 5m downstream from the rotor plane of a wind turbine and oriented according to the incoming wind direction. To prevent the pilot from anticipating when the encounter would take place, the wind turbine behind which the wake was placed was randomly chosen among the turbines in the first (southern) row, using an Excel random function, during the trials planning phase. The total dimensions of the airwake box are 372m wide x 395m long x 372 high. The flightpath was located so that it always crosses the axis of the airwake at a distance of 1.5 diameters from the generating wind turbine. This means the flight path was nearer to the wind turbines when flying under oblique wind conditions (+/-45deg and +/-135deg wind angle to helicopter flightpath), but at the same distance downstream from the wind turbine.

4.7.3 Mission

The helicopter was placed at the starting point in this scenario and the pilot was instructed to perform the following mission:

- Fly straight along the wind turbine corridor, maintaining initial heading, altitude and orientation until reaching the end of the wind turbine farm.

- If an upset is encountered, recover control and return to original flight path as soon as possible without compromising safety.
- Communicate when control of the aircraft has been recovered.
- Mission ends:
    - If an upset in encountered and flightpath is recovered.
    - If an upset in encountered and flightpath control is not recovered and the pilot decides to abort.
    - If no upset is encountered: Once the helicopter reaches the end of the wind farm.

4.7.4 Data recording

During each test, aircraft parameters related to attitude, flight conditions and performance as well as pilot control inputs were recorded for post-test analysis. Video and audio recordings of each flight were made. The pilot was asked to provide their ratings regarding workload requirements for the mission using the Bedford workload rating scale [107] (see Appendix - A), severity of the encounter (see Section 2.5.2) and main reasons influencing their rating by answering a questionnaire (see Appendix - C).

4.8 Piloted simulation results

4.8.1 Overall pilot ratings:

The severity and workload ratings awarded by the pilot for each run are presented on Table 4-5.

Pilot workload and encounter severity ratings against initial helicopter IAS and wind azimuth are presented in Figure 4-18 and Figure 4-19 respectively. Overall, runs awarded a higher severity rating were also considered to have a higher impact on workload. With the exception of one run conducted at 50kts IAS under a starboard wind condition (severity rating C, workload rating 3), all runs were assigned severity ratings (WVE) between A and C and BWR between 2 and 4.

Table 4-5: Severity and workload ratings awarded on each run.

Run	Airwake	IAS (kts)	Wind Speed (kts)	Wind Azimuth (deg)	WVE rating	BWR
2	NO	30	20	N/A	N/A	2
3	YES	30	20	-90	B	3
4	YES	30	20	-90	B	3
5	YES	50	20	90	C	3
6	YES	100	20	90	C	4
7	YES	80	20	90	B	3
8	YES	20	20	-90	B	3
9	NO	50	20	-90	N/A	2
10	YES	30	20	-135	A	2
12	YES	30	20	45	A	2
13	YES	30	20	-45	A	2
14	YES	30	20	135	B	3

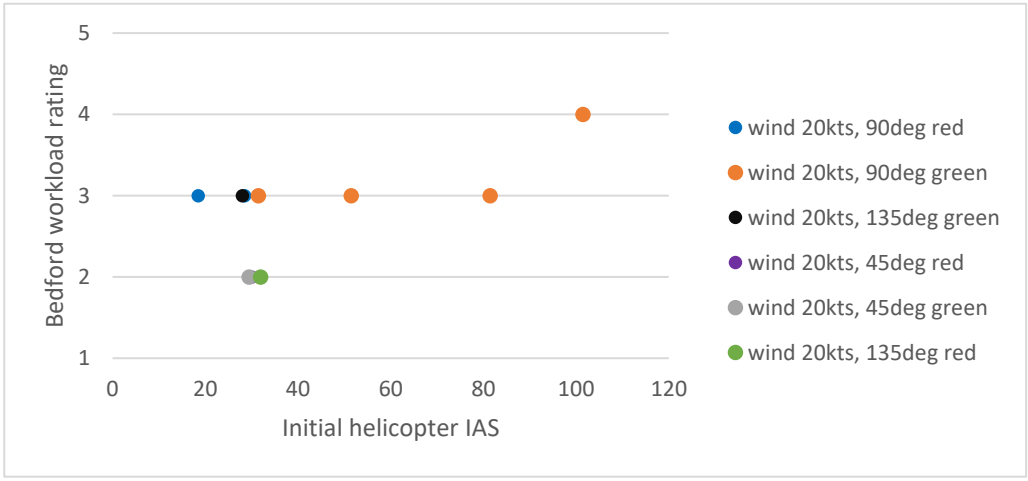

Figure 4-18: BWRs against IAS and wind azimuth.

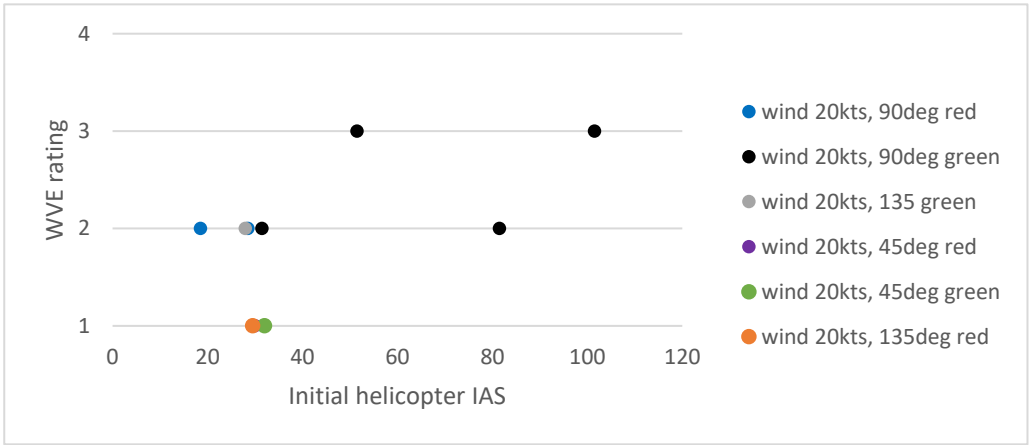

Figure 4-19: Encounter severity ratings against IAS and wind azimuth. (Numbers correspond to a letter rating: 1=A, 2=B, 3=C)

Overall workload and severity ratings were low, usually within Level 1 for a WVE rating. For most conditions, the pilot awarded a severity rating of B, indicating minimal or minor excursions in aircraft states requiring minimal or no urgency for corrective actions and a workload rating of 3, indicating that managing the encounter still left enough spare capacity for additional tasks. Only the encounter at a helicopter IAS of 100kts was awarded higher workload and encounter severity ratings. The WVE severity was reported as C, indicating moderate excursions requiring corrective action with moderate urgency, and workload requirements as 4, leaving little pilot spare capacity for additional tasks. Another run performed at 50kts was also awarded an encounter rating of C, but the effect on workload was still considered low and rated as 2.

In general, encounters crossing the airwake diagonally (wind azimuths of -135deg, -45deg, 45deg, 135deg) were considered less severe by the pilot than encounters crossing the airwake perpendicularly at the same airspeed.

The pilot was asked to complete a questionnaire (see Appendix - C) indicating which aircraft upsets resulted required the most attention. The ratings were awarded according to:

Table 4-6: Pilot awarded focus ratings. See Appendix C.

Rating	Significance:
0	Parameter was not important. Has not been monitored and/or required no pilot effort to control.
1	Parameter was not important. Has been monitored and/or required limited pilot effort to control.
2	Parameter was important. Required frequent monitoring and/or important pilot effort to control.
3	Parameter was very relevant. Dominated pilot's attention and effort during the encounter.

Responses are summarized in Figure 4-20 indicating how often each parameter was given each rating. It should be noted that the ratings are relative to each other, i.e. a high focus rating suggests that this parameter is driving workload demands for the task, but does not imply that that demand is high or low.

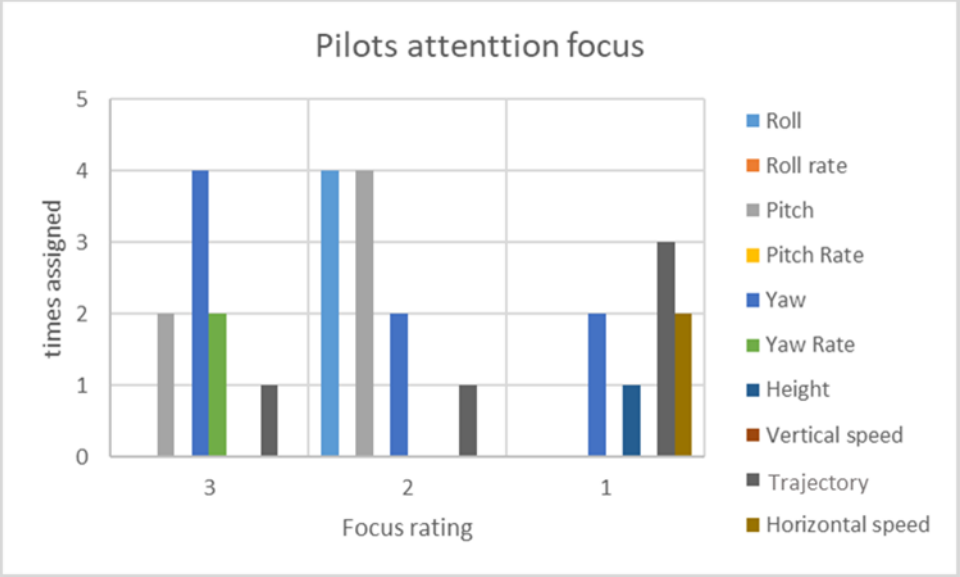

Figure 4-20: Pilot awarded rating for attention focus.

The pilot mentioned upsets in aircraft attitude generated the greatest demand in attention and corrective actions. Yaw attitude was most often mentioned as the main focus of pilot attention and actions, followed by pitch. Often when pitch was rated as requiring the most pilot attention, roll tended to be rated second or equal to pitch. A trend of focus shifting from yaw to pitch and roll exists with higher helicopter airspeeds. Focus on flight path and horizontal speed were mentioned as requiring partial focus because they are dependent on aircraft attitude, while vertical speed or aircraft altitude were never mentioned as parameters demanding special focus or pilot attention.

Finally, in almost all occasions the pilot mentioned difficulty in stabilizing the aircraft in the yaw axis as a relevant factor in their ratings. There were only two exceptions, corresponding to an encounter at 30kts IAS under portside wind and an encounter at 100kts IAS with a starboard wind, in which aircraft stability in pitch was rated as having the highest relevance.

4.8.2 Helicopter response and pilot control actions

Table 4-7 summarizes the highest achieved helicopter attitude rates on each rated run.

Table 4-7: Maximum attitude rates achieved during rated runs.

Run	Airwake	IAS (kts)	Wind Speed (kts)	Wind Azimuth (deg)	Max roll rate (deg/s)	Max pitch rate (deg/s)	Max yaw rate (deg/s)
2	NO	30	20	N/A	4.5	6.5	5.3
3	YES	30	20	-90	9.4	6.3	12.8
4	YES	30	20	-90	4.6	5.1	9.2
5	YES	50	20	90	9.4	4.3	14.5
6	YES	100	20	90	10.4	14.7	10.0
7	YES	80	20	90	11.2	8.1	9.4
8	YES	20	20	90	7.1	7.9	10.0
9	NO	50	20	-90	5.4	4.3	4.1
10	YES	30	20	90	5.1	3.1	5.6
12	YES	30	20	-135	3.8	4.5	6.1
13	YES	30	20	45	6.1	3.8	4.9
14	YES	30	20	-45	5.0	5.0	8.7

Figure 4-21, Figure 4-22 and Figure 4-23 compare aircraft attitudes, attitude rates and pilot control actions between two runs with and without wake encounter, which is indicated by the vertical dashed lines. Both runs were performed at 30kts airspeed in a 20kts port side wind.

As can be seen in Figure 4-21 and in Figure 4-22, piloted wake encounters present a very similar profile as initial disturbances seen in offline simulations. Initially, oscillations in aircraft attitude and attitude rates present a similar amplitude for both runs. While entering and leaving the airwake, the aircraft experiences upsets in the roll and pitch axes, while yaw upsets become dominant during the actual crossing of the airwake. Effects of the encounter still manifest themselves after leaving the airwake as increased amplitude of oscillations in aircraft attitudes and rates.

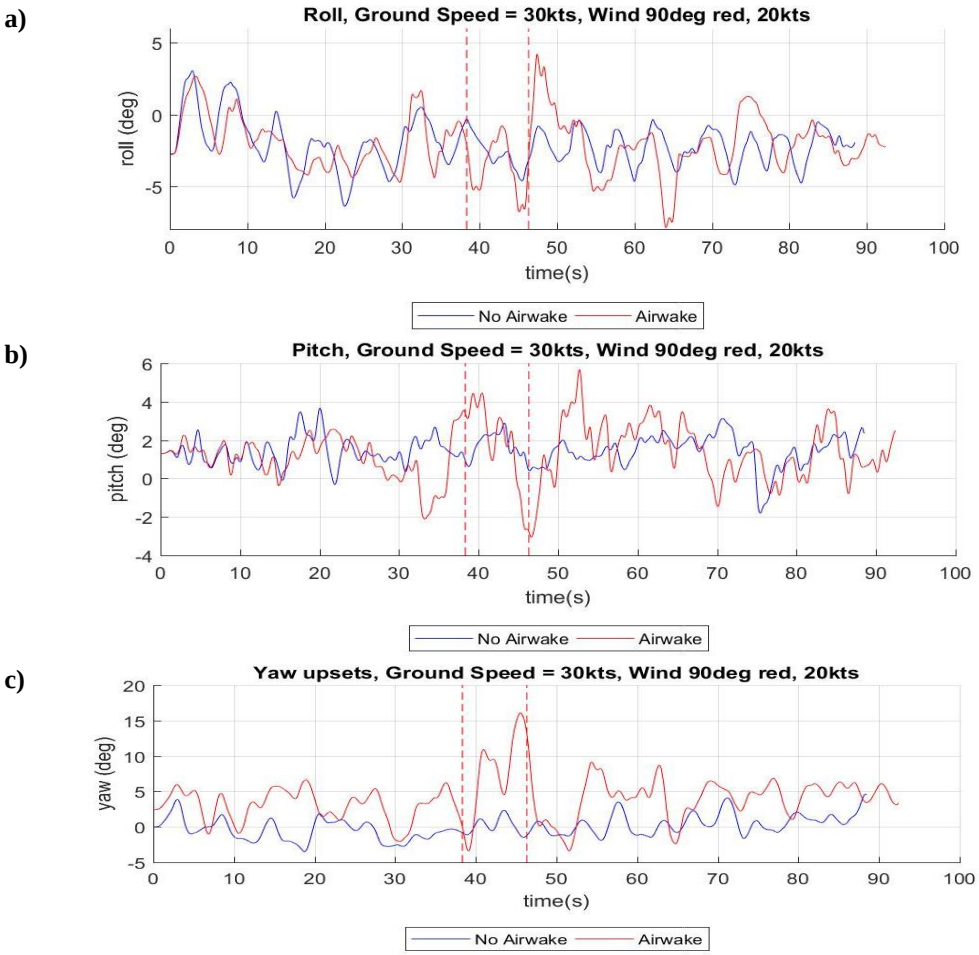

Figure 4-21: Aircraft attitude in a) roll, b) pitch, c) yaw, during a flight at 30kts IAS under a 90deg red 20kts wind with and without airwake. Airwake start and end points are marked by the vertical dashed lines.

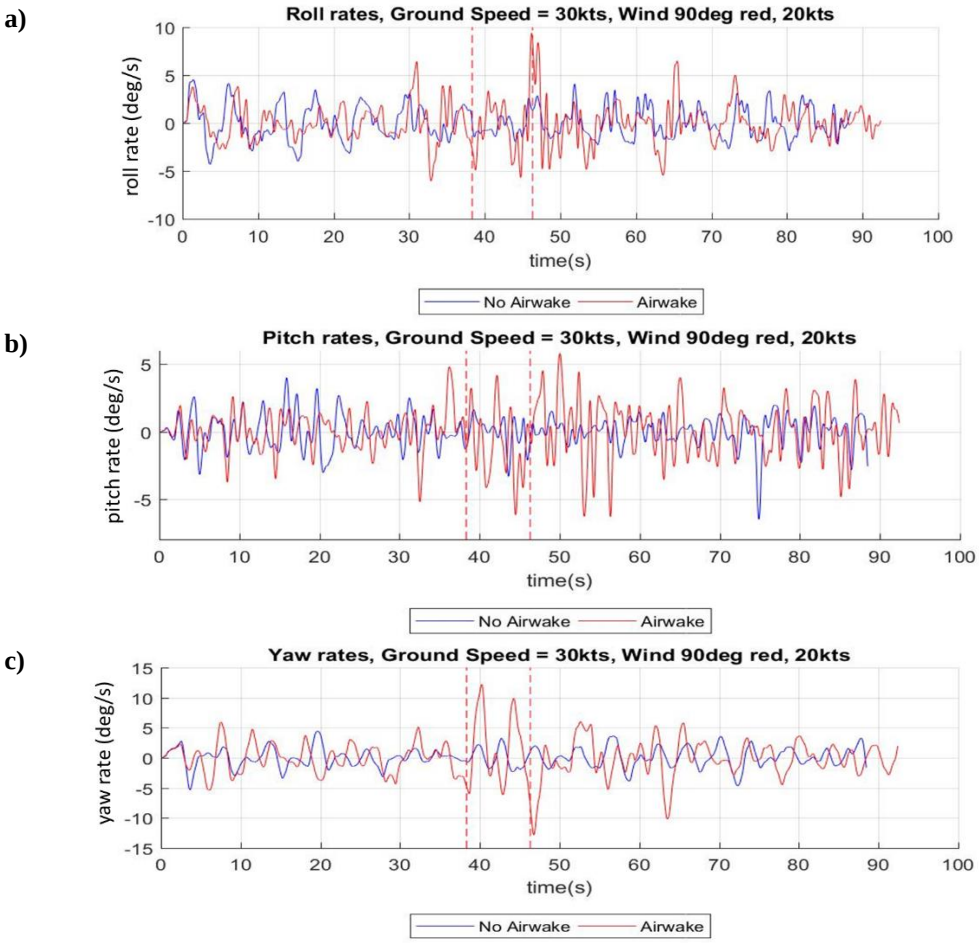

Figure 4-22: Aircraft attitude rates in a) roll, b) pitch, c) yaw, during a flight at 30kts IAS under a 90deg red 20kts wind with and without airwake. Airwake start and end points are marked by the vertical dashed lines.

Pilot corrective activity prevents the long – term deviation in aircraft states observed in offline simulations. Plots of pilot actions (Figure 4-23) show a similar pattern, showing that crossing the airwake requires rapid pilot corrective inputs in pedal and collective, followed by longitudinal and lateral inputs when leaving the airwake. An increase in the amplitude of pilot control inputs persists for some time after the encounter.

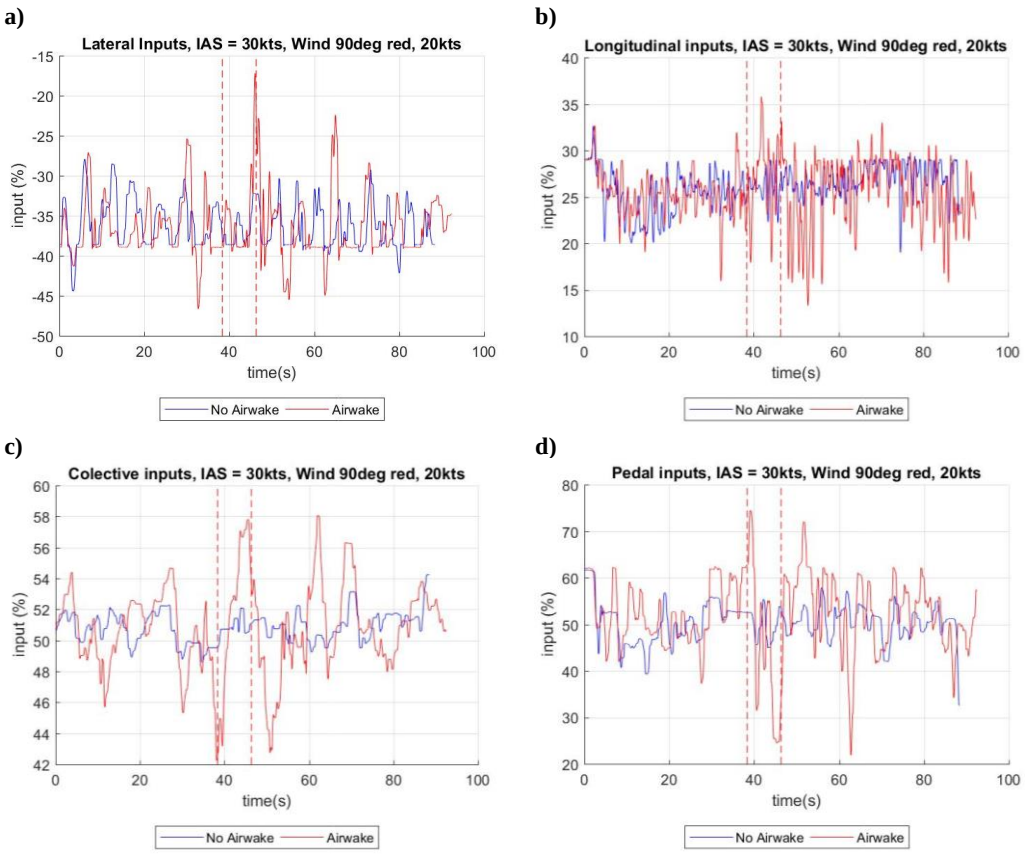

Figure 4-23: Pilot control inputs in a) lateral, b) longitudinal, c) collective and d) pedal, during a flight at 30kts IAS under a 90deg red 20kts wind with and without airwake. Airwake start and end points are marked by the vertical dashed lines.

Flow velocity disturbances in the airwake manifest themselves as oscillations in helicopter airspeed when crossing and collective inputs by the pilot during the encounter might be an attempt to compensate. The effect on altitude is less clear, altitude losses and pilot inputs in collective in this run clearly start before the encounter, suggesting that another factor might also have been involved (Figure 4-24). Overall in all runs, perturbations in airspeed and altitude seem to be contained and relatively low when compared to other upsets.

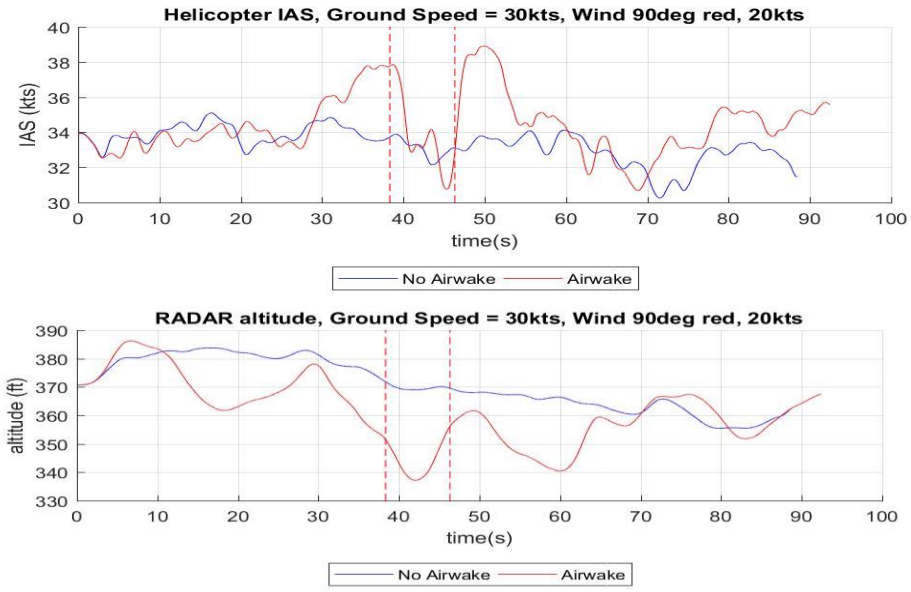

Figure 4-24: forward IAS and aircraft altitude during a flight at 30kts IAS under a 90deg red 20kts wind with and without airwake. Airwake start and end points are marked by the vertical dashed lines.

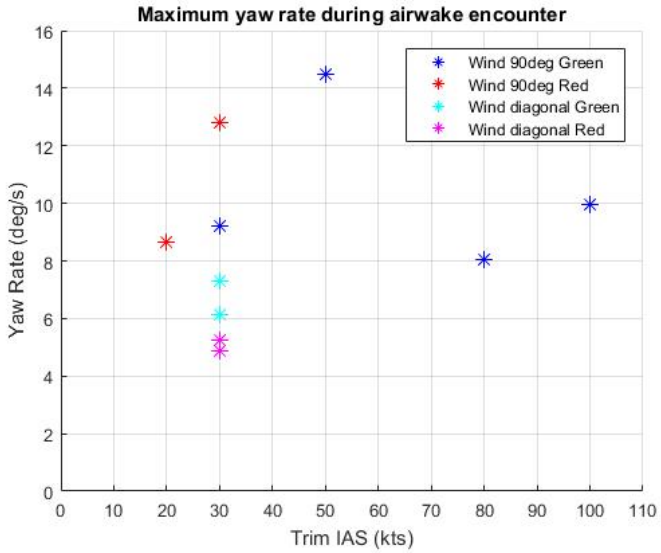

Figure 4-25: Maximum yaw rates achieved while crossing the airwake.

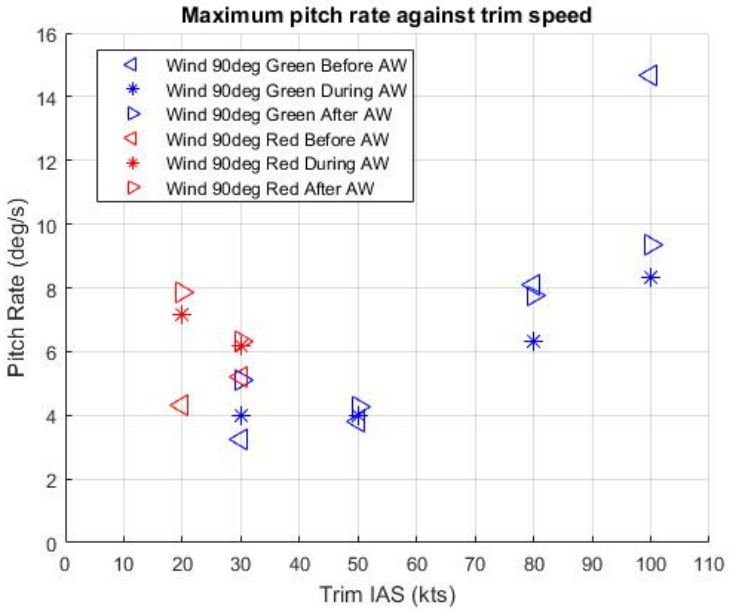

Figure 4-26: Maximum pitch rates achieved before during and after the encounter for perpendicular airwake crossings.

Most of the test runs present a similar outline as the one presented in Figure 4-22 to Figure 4-24: yaw upsets seem to be the largest in magnitude and require large inputs to compensate but are mainly confined to the brief period of crossing the airwake. Only the runs at 20kts and 80kts helicopter speed present larger yaw rates outside than inside the airwake. Roll and pitch upsets are strongest immediately before entering or after leaving the airwake and pilot inputs at those times can be appreciated.

The flight speed at which the encounter takes place has a noticeable effect on the magnitude of the upsets. Yaw rates peak at 50kts (see Figure 4-25) and then become lower as airspeed increases. The pilot mentioned a sense of urgency that this upset creates as the main driver for the higher severity rating of C awarded on this particular run. At the same time, this test run presents smaller pitch and roll oscillations than runs at higher or lower flight speeds.

At 80kts and 100kts flight speeds, the magnitude of the pitch and roll rates increases significantly before crossing the airwake (see Figure 4-26), which might be due to the pilot attempting to counteract the impact of a lateral wind that leads to a pitch – roll cross couplings. At these higher speeds, it becomes difficult to identify any particular effect of the airwake on aircraft pitch and roll attitude (see Figure 4-27 and Figure 4-28). A similar trend can be appreciated when observing pilot control inputs (Figure 4-29).

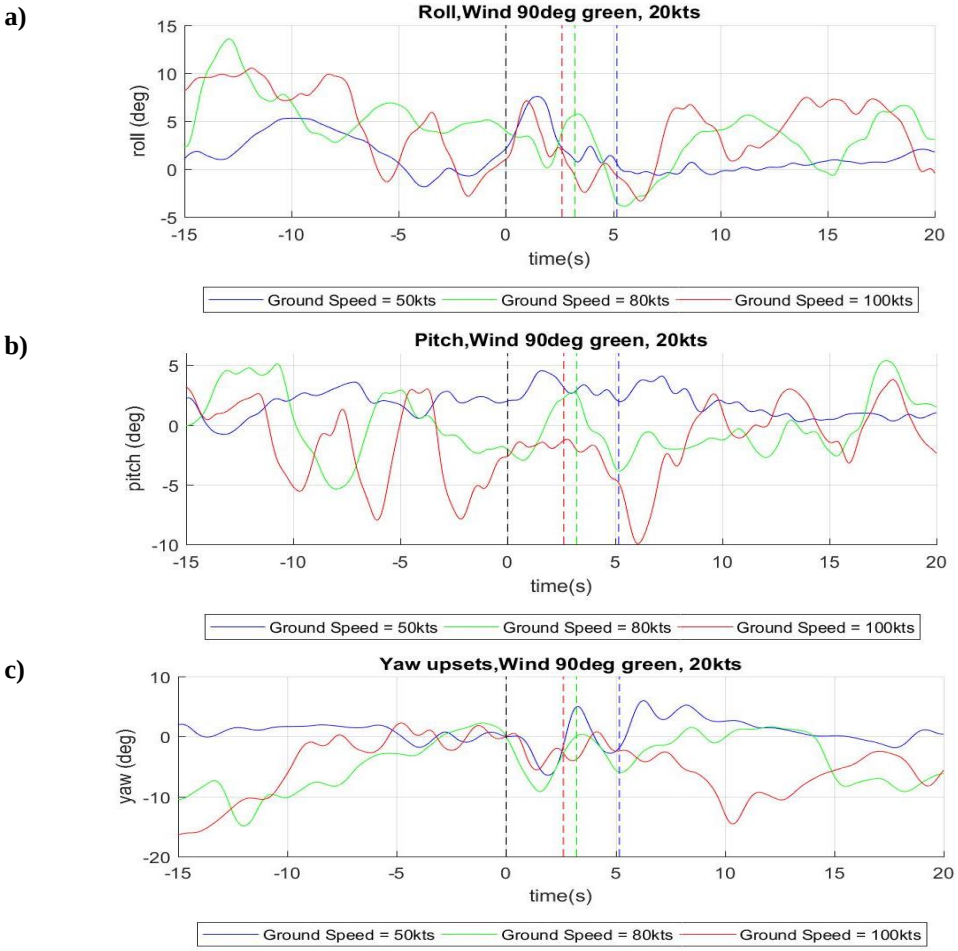

Figure 4-27: Aircraft attitude upsets for encounters at higher airspeeds. Airwake encounter starts at t = 0s and ends with coloured dashed vertical lines.

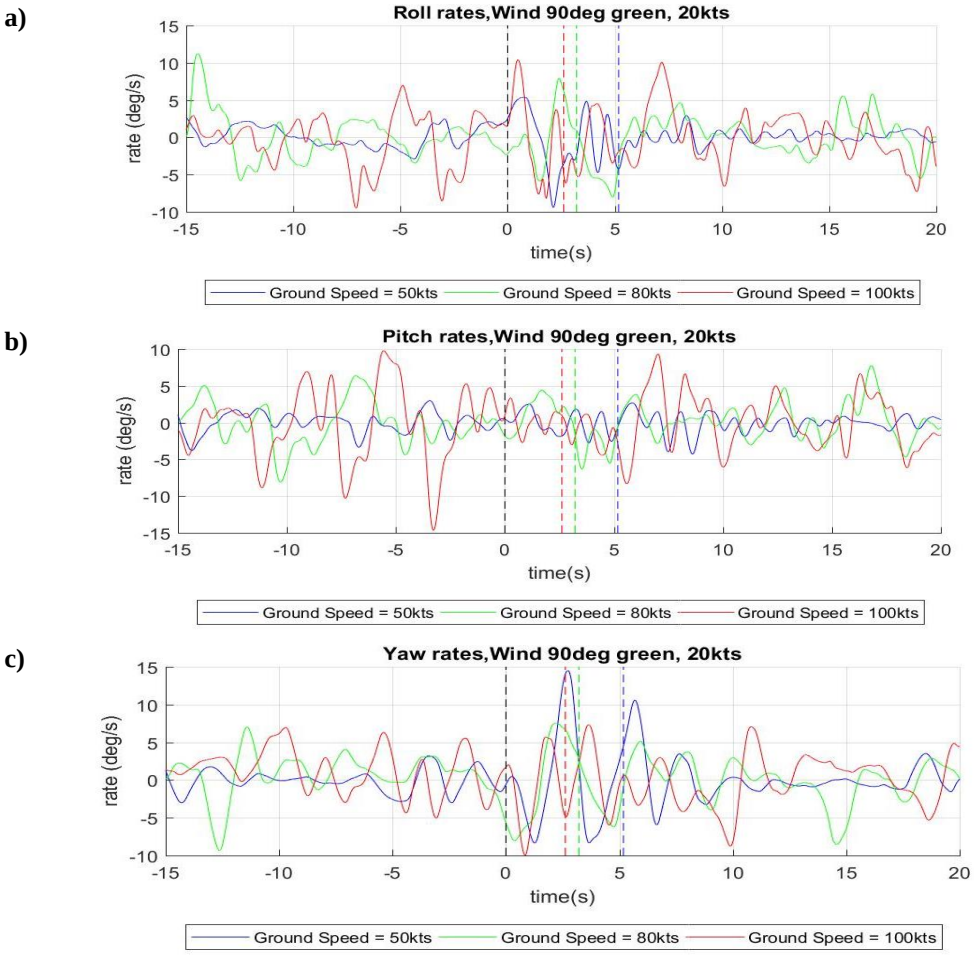

Figure 4-28: Aircraft attitude rates for encounters at higher airspeeds. Airwake encounter starts at t = 0s and ends at dashed vertical lines of the corresponding colour.

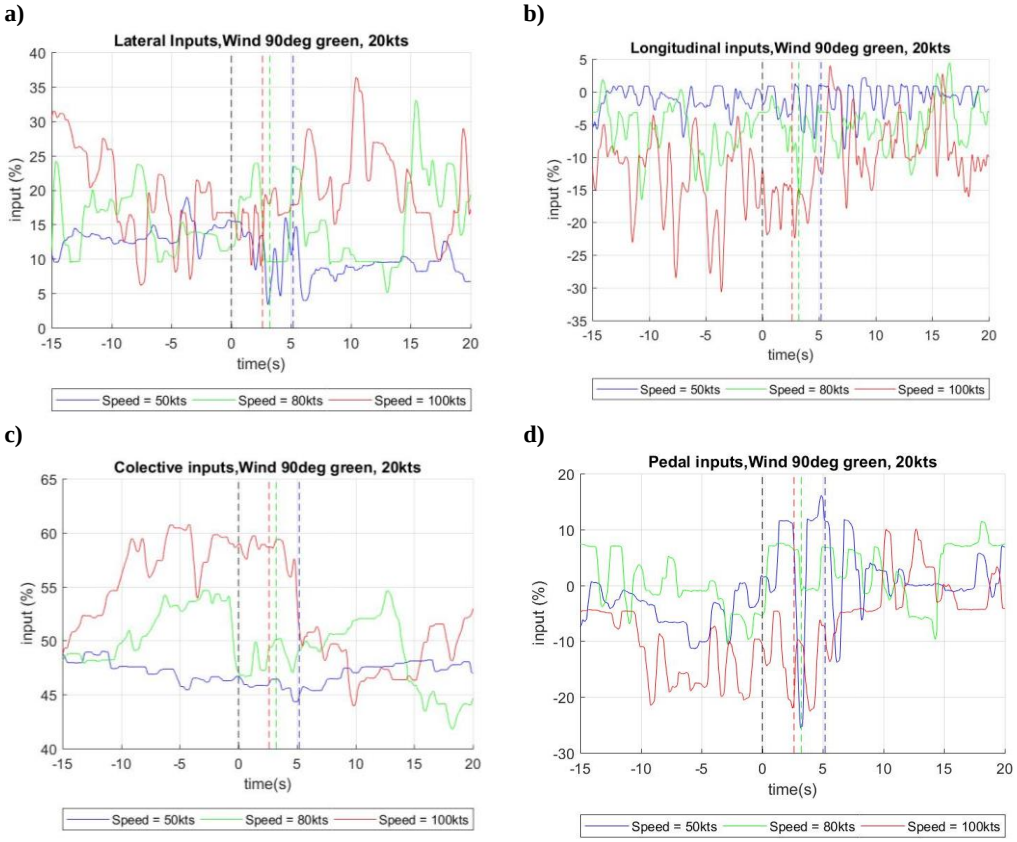

Figure 4-29: Piot control inputs for encounters at higher airspeeds in a) longitudinal, b) lateral, c) collective, d) pedal. Airwake encounter starts at t = 0s and ends at dashed vertical lines of the corresponding colour.

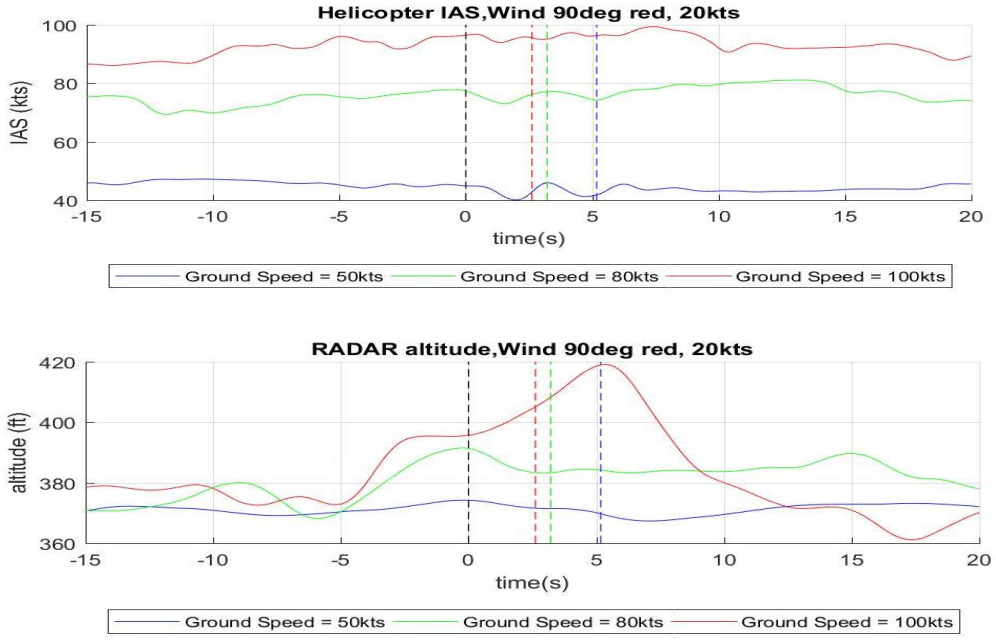

Figure 4-30: Aircraft IAS and altitude for encounters at higher airspeeds. Airwake encounter starts at t = 0s and ends at dashed vertical lines of the corresponding colour.

Upsets in airspeed also seem to be comparatively smaller at higher flight speeds and there is a tendency of altitude gains at higher airspeeds (Figure 4-30). Pilot collective inputs at 80kts and 100kts follow a slow but relatively constant reduction.

The angle at which the wake is crossed also affects the outcome of the wake encounter. When crossing the airwake diagonally, resulting aircraft yaw rates tend to be smaller than during perpendicular encounters (Figure 4-31). Upsets in attitude rates due to the airwake under conditions of port side wind also seem to be of slightly greater magnitude than those resulting from crossing under starboard wind, although this difference was not enough to significantly affect pilot ratings.

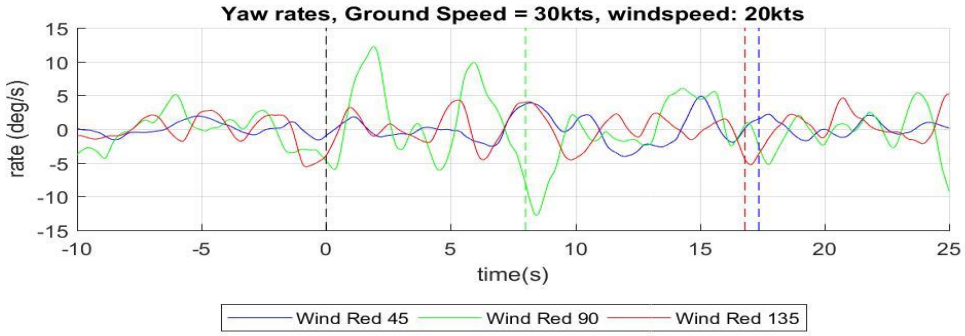

Figure 4-31: Aircraft Yaw rates for encounters at 30kts airspeed under a 20kts wind under different directions. Airwake encounter starts at t = 0s and ends with coloured dashed vertical lines.

4.8.3 Analysis of yaw to pitch and yaw to roll cross couplings.

Pilot comments and analysis of aircraft responses and pilot activity show the existence of pitch to yaw couplings in runs at high speed. Analysis of which explains the large upsets in pitch experienced by the aircraft outside the airwake and led to higher pilot workload for those runs.

ADS–33 provides no requirements and test criteria in this regard, so the following new criteria were developed by adapting the ADS - 33 requirements for pitch–roll couplings: Peak attitude changes in the coupled axis during the first four seconds after an input has been introduced and compared against the attitude changes in the resulting axes after the first four seconds (see Eq 4-1 and Eq 4-2).

$$\boldsymbol{Pitch\ from\ yaw\ ratio} = \frac{\Delta\boldsymbol{\theta}_{\boldsymbol{pk}_{\boldsymbol{t\leq 4s}}}}{\Delta\boldsymbol{\psi}(\boldsymbol{4s})} \qquad \textit{4-1}$$

$$\boldsymbol{Yaw\ from\ pitch\ ratio} = \frac{\Delta\boldsymbol{\psi}_{\boldsymbol{pk}_{\boldsymbol{t\leq 4s}}}}{\Delta\boldsymbol{\theta}(\boldsymbol{4s})} \qquad \textit{4-2}$$

Results are shown in Figure 4-32 and show that the Bo 105 exhibits a significant yaw to pitch coupling. With a tendency of stronger couplings with higher airspeed, reaching the point at 100kts in which pedal inputs command produce a greater response in pitch than in yaw.

a) **b)**

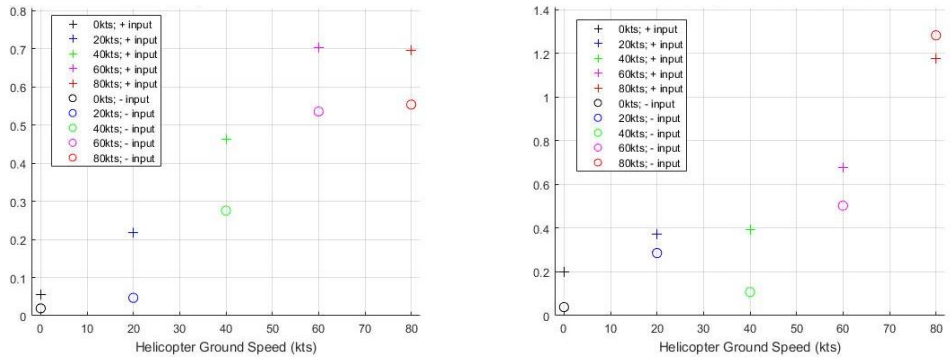

Figure 4-32: Couplings in a) yaw to pitch, b) pitch to yaw for the Bo 105 model.

4.9 Discussion of results

A series of offline and piloted flight simulation tests have been performed to study the effect of a Bo 105 helicopter crossing the airwake of a 5MW 126m diameter wind turbine. The encounter results in aircraft upsets in all three rotational axes. By magnitude, the largest upsets occur mainly in the yaw axis followed by roll. It appears that the leading factor is the effect of lateral velocity deficits on tail rotor thrust and main rotor rolling moments. Upsets in the pitch axis tend to manifest with a delay and could be a consequence of long-term dynamics of the helicopter or caused by the previous upsets in roll and yaw.

Portside wind encounters result in greater upsets. Trimming the helicopter under conditions of uniform portside wind has a greater requirement on available control margins, especially for pedal, than under starboard winds of similar strength. A sudden decay in lateral wind velocity will “reduce” these requirements and, in the absence of corrective inputs, result in greater disturbances than for starboard wind conditions.

Piloted flight simulations show similar upsets to those encountered during offline analysis, although the pilot’s response prevented deviations to build up to the level observed in offline simulations. Pilot ratings and feedback indicate that the severity of

the wake encounters was generally low, requiring pilot response with low to moderate urgency and did not result in significant increases in workload. Encounters at greater airspeed were awarded higher ratings, but lower end Level 2 workload and severity ratings were never exceeded. Aircraft yaw attitude changes were most often mentioned by the pilot as the main focus of their attention and actions, with combined pitch and roll upsets coming a close second.

The pilot also indicated that the flight handling qualities of the non-augmented Bo 105 model, especially the strong yaw–pitch and pitch–roll couplings, were a major cause of increased workload during recovery after the initial aircraft upset. This was more evident at the higher airspeeds. A later flight handling qualities analysis of the Bo 105 model reveals that couplings between the different axes become stronger with increased flight speed.

Plots of aircraft response and pilot control inputs show that, yaw upsets were usually dominant at lower IAS requiring larger pilot inputs, compared to the roll and pitch axes, to be utilised to counteract the effect of the disturbance. But they tended to occur only during the actual wake encounter. By contrast, aircraft oscillations and pilot inputs in the longitudinal axis, prior to encountering the airwake, tended to increase in amplitude with higher airspeed as the pilot's attempts to counteract the impact of lateral wind led to pitch – roll cross couplings. Heading upsets when crossing the airwake require pedal inputs from the pilot which will lead to additional pitch and roll upsets from yaw – pitch cross couplings, which become stronger with increased flight speed.

These results seem to suggest that increases in workload from an encounter are driven by large yaw deviations at lower flight speeds and by the difficulty in maintaining and recovering pitch control at higher airspeeds due to strong inter-axis couplings, especially yaw to pitch coupling, a criterion not covered by ADS-33. The severity of the encounters is a consequence of the poor predicted handling qualities of this aircraft, something that should be considered in all aircraft hazard assessments.

4.10 Chapter Summary

This chapter has described how offline and piloted flight simulations have been used to study the possible impact of encounters of rotorcraft with wind turbine wakes. A precomputed steady airwake from a NREL 5MW wind turbine was integrated with a FLIGHTLAB flight dynamics model of a MBB Bo 105 helicopter. Offline simulations

were used to select test conditions for piloted simulation trials which were conducted with a six degree of motion flight simulator using an offshore wind farm scenario developed for the trials. The test pilot was instructed to perform a level and steady flight during which he would encounter the wake of a wind turbine at a random location. If the encounter resulted in an upset, the pilot was instructed to perform a recovery to the initial flight condition as fast as he deemed possible to do safely. Encounters were tested at different flight speeds and under different wind azimuths. After each run, the pilot was asked to provide a workload and severity rating and feedback about the impact of the encounter. Pilot inputs and helicopter dynamic parameters were also recorded during the trials.

These trials show the potential for flight simulation for planning and training for offshore wind support and potential handling qualities issues that might arise during such scenarios, especially in cases of SAS failures. However, the use of steady wake models for the simulation, whilst useful for initial safety evaluations, limits the applicability of these results, mainly to the study of accidental crossings which spend a short time period inside the wake.

5 Turbulence modelling for flight simulation

5.1 Introduction

The previous chapter described a series of flight simulation trials performed to assess the severity of accidental encounters between a rotorcraft and wind turbine wakes. The trials made use of a precomputed, time averaged, steady airwake, which did not consider the impact of unsteady turbulence on pilot workload. This was an important limitation of the previously reported results.

There is a wide range of 'unsteady' environmental conditions a helicopter might encounter within a wind farm ranging from atmospheric turbulence, turbulence induced by the nacelle and locked blades during winching operations, as well as the turbulent region of the wind turbine far-wake. A question arises if the trials would generate similar results should these unsteady effects be included.

However, at this point in the thesis, no time accurate wind turbine wakes were readily available for further trials and the generation of a new database was judged as too time consuming for the project. Stochastic turbulence models can be adapted for use in rotorcraft simulation (see Section 2.4.2), but their modification to reproduce a non-uniform turbulence field from an airwake is complex and was considered too time consuming.

To address these limitations a new synthetic turbulence model for flight simulation based on a Synthetic Eddy Method (SEM) was developed. This chapter details the theoretical background of the SEM model (Section 5.2.1), and the integration of the generator with a helicopter flight simulation model (detailed in Sections 5.2.2 and 5.2.3). Offline simulations performed to verify the turbulence generator, and its impact on the aircraft, are described in 5.2.4 and 5.2.5, and a brief flight simulation trial is presented, in Section 5.3, in which the real-time capability and feasibility of the concept was demonstrated. Finally, a discussion of the results and a summary of the chapter is provided in Section 5.4.

5.2 Synthetic Eddy Method

The SEM proposed by Jarrin [54] provides a simple and computationally cheap algorithm that is widely used to generate random turbulent oscillations at the inflow of LES based CFD simulations.

Inflow turbulence generators need to satisfy some important requirements that are also relevant for real-time flight simulation turbulence modelling: low computational costs, realistic representation of turbulence, flexible adjustment to reproduce a variety of turbulence conditions and ease of implementation.

5.2.1 Theoretical Background:

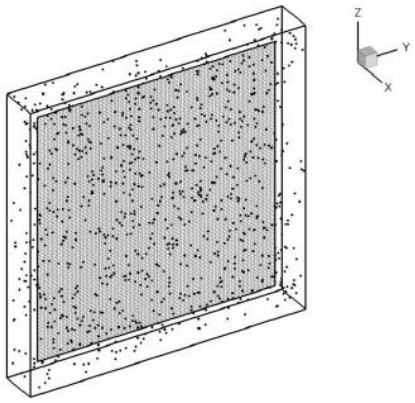

Figure 5-1: Control volume filled by eddies surrounding inflow grid.[49]

A control volume surrounding the area of interest, usually the inflow of the simulation domain, is populated by a uniform random distribution of *N* eddies (see Figure 5-1). The number is chosen so that the volume is completely filled by eddies. At each time step, an eddy located on $\boldsymbol{x}^k$ generates a turbulent velocity perturbation at location $\boldsymbol{x}$ characterized by**:**

$$\boldsymbol{u'}_i^{\,k} = \frac{\mathbf{1}}{\sqrt{\boldsymbol{N}}} \boldsymbol{A}_{ij} \boldsymbol{\varepsilon}_j^k \boldsymbol{f}_\sigma\left(\boldsymbol{x} - \boldsymbol{x}^k\right) \qquad 5\text{-}1$$

where ε_j^k is a randomly assigned sign and $\boldsymbol{A}$ is the Cholesky decomposition of the Reynolds stress tensor ($Re_{ij} = \langle u'_i u'_j \rangle$):

$$A = \begin{bmatrix} \sqrt{Re_{11}} & 0 & 0 \\ \frac{Re_{21}}{A_{11}} & \sqrt{Re_{22} - A_{21}^2} & 0 \\ \frac{Re_{31}}{A_{11}} & \frac{Re_{32} - A_{21}A_{31}}{A_{22}} & \sqrt{Re_{33} - A_{31}^2 - A_{32}^2} \end{bmatrix} \quad 5\text{-}2$$

The velocity distribution of each eddy across the control volume is defined by $f_{\sigma(x)}(x - x^k)$ and depends on the shape of the eddies, defined by a characteristic length in each direction σ:

$$f_{\sigma(x)}(x - x^k) = \sqrt{\frac{V_B}{\sigma^3}} * f\left(\frac{x - x^k}{\sigma_x}\right) f\left(\frac{y - y^k}{\sigma_y}\right) f\left(\frac{z - z^k}{\sigma_z}\right) \quad 5\text{-}3$$

where each component fulfils the normalization condition:

$$\int_{-\infty}^{+\infty} f^2(x) = \int_{-\sigma}^{+\sigma} f^2(x) = 1 \quad 5\text{-}4$$

The resulting velocity on each cell is obtained by adding the contribution of each eddy to the inflow velocity:

$$u_i = \bar{u}_i + \sum_{k=1}^{N} {u'}_i^k \quad 5\text{-}5$$

After each time step the population of eddies is displaced following the flow velocity:

$$x^k(t + dt) = x^k(t) + \bar{u} * dt \quad 5\text{-}6$$

Should an eddy leave the control volume, it is regenerated at the control volume's inflow at a location selected by a uniform random distribution.

The SEM can be adapted to model different environmental turbulence conditions. The values of R_{ij} determine the resulting standard deviation in turbulent velocities generated for each axis, while the shape of the eddies determines the length scale of turbulence and therefore spatial correlation, $R_{ij}(r)$, between turbulent velocities at two different locations x and $x + r$.

$$R_{ij}(r) = Re_{ij} \prod_{l=1}^{3} [f * f]\left(\frac{r_l}{\sigma_l}\right) \quad 5\text{-}7$$

By adjusting the number of eddies so that they completely fill the control volume, $N = \frac{V_B}{\sigma_x \sigma_y \sigma_z}$, adjusting the shape of eddies also defines the resulting frequency spectra:

$$\boldsymbol{\phi_{ij}(x,\omega) = Re_{ij} \frac{\sigma}{|\overline{u}|} \left| \mathcal{F}_{\frac{\sigma\omega}{|\overline{u}|}}\{f\} \right|^2} \quad \textit{5-8}$$

where $\mathcal{F}_{\frac{\sigma\omega}{|\overline{u}|}}\{f\}$ is the Fourier transform of function f at a frequency scaled by $\frac{\sigma\omega}{|\overline{u}|}$.

Randomly placing recycled eddies following a uniform distribution implies that, after enough time has passed, the resulting turbulence is unrelated to previous states. As a result the cumulative time averaged values of generated turbulent velocities should tend to their statistical mean as time passes [49]. Time averaged values of turbulent flow velocities tend to zero and Reynolds stresses tend to their initially defined values, skewness tends to zero and kurtosis (or flatness) tends to a fixed value dependent on the number of eddies, the ratio between their size and the control volume and the velocity and intensity distributions (Eq. [5-9] to [5-12]).

$$\boldsymbol{\langle u_i' \rangle = 0} \quad \textit{5-9}$$

$$\boldsymbol{\langle u_i' u_j' \rangle = A_{im} A_{jm} = Re_{ij}} \quad \textit{5-10}$$

$$\boldsymbol{S_{u_i} = \frac{\langle u_i'^3 \rangle}{\langle u_i'^2 \rangle^{\frac{3}{2}}} = 0} \quad \textit{5-11}$$

$$\boldsymbol{F_{u_i} = \frac{\langle u_i'^4 \rangle}{\langle u_i'^2 \rangle^2} = 3 + \frac{1}{N}\left(4 * {F_f}^3 * F_\varepsilon * \frac{V_B}{\sigma^3} - 3\right)} \quad \textit{5-12}$$

with F_f and F_ε being the kurtosis of the velocity and intensity distribution functions respectively.

5.2.2 Development of Synthetic Eddy Method for Flight Simulation

The SEM method has been applied to generate random turbulent distributions to the aerodynamic computation points (ACPs) of FLIGHTLAB aircraft models. The module has been built using MATLAB's Simulink modelling tool and coupled using FLIGHTLABs *flcomms* function for integration with Simulink.

A box–shaped control volume is defined around the aircraft and populated by a random distribution of eddies (see Figure 5-2). The size of the control volume is

sufficient to contain all ACPs of the aircraft in all directions. On each time step, eddies will be displaced according to the ambient wind velocity.

In its current implementation the eddies represent a geometric distribution of a randomly generated frozen turbulence field which displaces itself with ambient wind velocity, a reasonable assumption for fast flight or wind velocities. Preserving the location of the eddies near the aircraft ensures that the turbulence induced on each of the ACPs is coherent with the effects on the rest of the aircraft even if there are large changes in the orientation of the aircraft velocities.

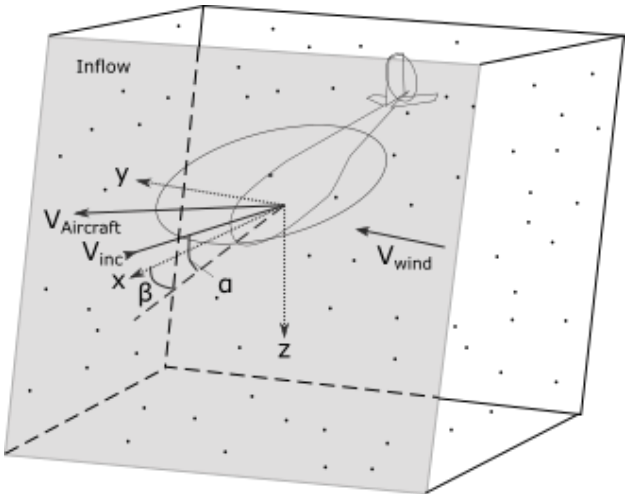

Figure 5-2: Diagram of the control volume used for the SEM.

To regenerate the eddies in the path of the aircraft, on each time step the location of the control volume is defined to account for the movement of the aircraft and its orientation updated in order to orient the inflow towards the incoming eddies:

$$\boldsymbol{V_{inc} = V_{wind} - V_{aircraft}} \qquad 5\text{-}13$$

which can be oriented with respect to the inertial axis of reference by defining the following angles.

$$\boldsymbol{\alpha_{inc} = sin^{-1}\left(\frac{V_{inc_z}}{|V_{inc}|}\right)} \qquad 5\text{-}14$$

$$\boldsymbol{\beta_{inc} = cos^{-1}\left(\frac{V_{inc_x}}{\sqrt{V_{inc_x}^2 + V_{inc_y}^2}}\right) * sign\left(V_{inc_y}\right)} \qquad 5\text{-}15$$

By performing a change of coordinates, the inflow can be defined as parallel to the y-z plane and located at negative values of *x*.

Once the control volume has been defined, eddies falling outside the control volume at the start of the time step are regenerated at a random location between the inflow and the distance covered by the incoming velocity during the last time step, $|\boldsymbol{V}_{inc}| * dt$.

The turbulent velocities induced by each eddy on each ACP are computed as described in the previous chapter:

$$\boldsymbol{u}_i'^{ACP} = \frac{\mathbf{1}}{\sqrt{\boldsymbol{N}}} \sum_{k=1}^{N} \boldsymbol{A}_{ij} \boldsymbol{\varepsilon}_j^{Eddie} \boldsymbol{f}_\sigma \left(\boldsymbol{x}^{ACP} - \boldsymbol{x}^{Eddie} \right) \qquad 5\text{-}16$$

5.2.3 Coupling of Synthetic Eddy Method with FLIGHTLAB

The SEM turbulence module has been coupled with two FLIGHTLAB helicopter models which had been developed at the University of Liverpool for previous research projects. A Bo 105 simulation model (Refs. [108] and [109]) and a Bell 412 variant [110] based on the helicopter operated by the Canadian National Research Council (NRC) [111]. Both models were developed at the University of Liverpool for previous research activities.

At each time step, the SEM module passes generated turbulent flow velocities at each of the aircraft ACPs to FLIGHTLAB, which adds them to the external flow velocities. FLIGHTLAB computes the resulting aerodynamic forces at each ACP and solves the aircraft's dynamics to obtain the new position of each ACP for the next time step. These values are then passed on to the SEM module which uses them to update the current distribution of eddies and the resulting turbulent velocities.

In the current implementation, the synthetic eddy turbulence component has been built as a Simulink model connected to FLIGHTLAB. A test model unconnected to FLIGHTLAB has also been built for testing and validating the algorithm. This model uses stored FLIGHTLAB outputs of the position of the aircraft's ACPs as inputs for the SEM module to generate the resulting turbulent velocities on each ACP. However, there is no aircraft model connected to be affected by them.

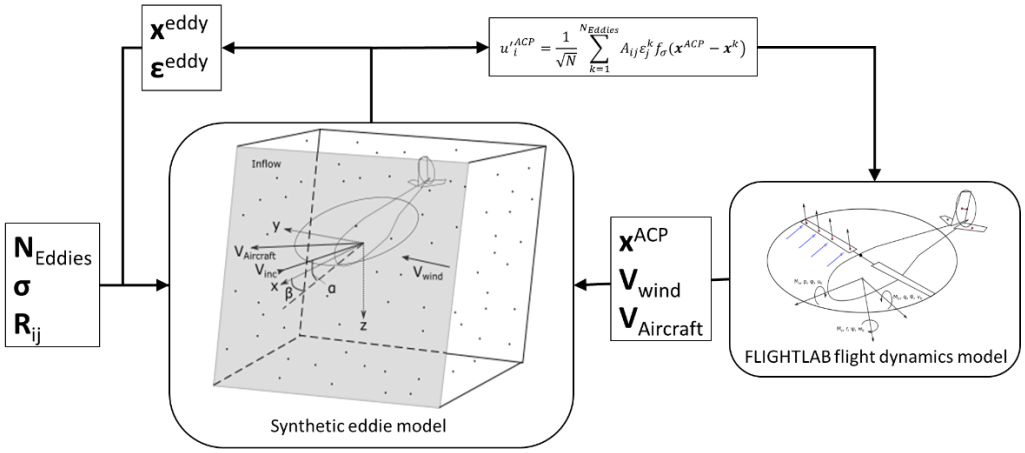

Figure 5-3: Flow chart of data exchanged between the SEM module and FLIGHTLAB.

Exchange of data between FLIGHTLAB and the Simulink turbulence model is performed via FLIGHTLAB's communications protocol, *flcomms*. To ensure that the flight model operates in real-time even if the Simulink model freezes, FLIGHTLAB needs to operate independently from the turbulence model. It always uses the most recent data sent to it from the turbulence model independently even if the time-step does not correspond. Therefore, the task of ensuring synchronization between flight and turbulence model falls completely on the turbulence model. A trigger within the model ensures that the SEM module always waits for FLIGHTLAB to perform a time step before updating the turbulence field. It is also necessary to ensure that the time required for this is always lower than the duration of a FLIGHTLAB model solution time step.

The spectrum of the induced turbulence is a function of the wind speed and eddy size (Eq. [5-8]). Since the control volume needs to be completely filled by eddies, the average frequency of turbulent velocity components scales with the cubic root of the number of eddies. For computational performance of the model, the number of eddies is the most important parameter. Given the size of the control volume surrounding the helicopter, the limit for real-time simulation was found at some 300 to 400 eddies which could generate disturbances within a frequency range of up to 1Hz under a uniform wind of 20kts (see Section 5.2.4).

To allow for real time simulation in the HELIFLIGHT-R flight simulator at the University of Liverpool, the time step of the employed helicopter models had to be modified. FLIGHTLAB defines the time step of an aircraft model as a fraction of the main rotor period under nominal conditions. The default time step duration was extended from $\frac{1}{24}th$ to $\frac{1}{12}th$ of the main rotor period. Correct behaviour of the aircraft

model was checked by comparing the aircraft response to a step input in all controls, finding no difference in the aircraft responses (see Figure 5-4) and through piloted simulation, where pilots were also not able to distinguish any effects from changes in the timestep. This process was performed for the University of Liverpool's FLIGHTLAB models of the MBB Bo 105 and the Bell 412. These modifications allow the model to run smoothly with over 400 eddies.

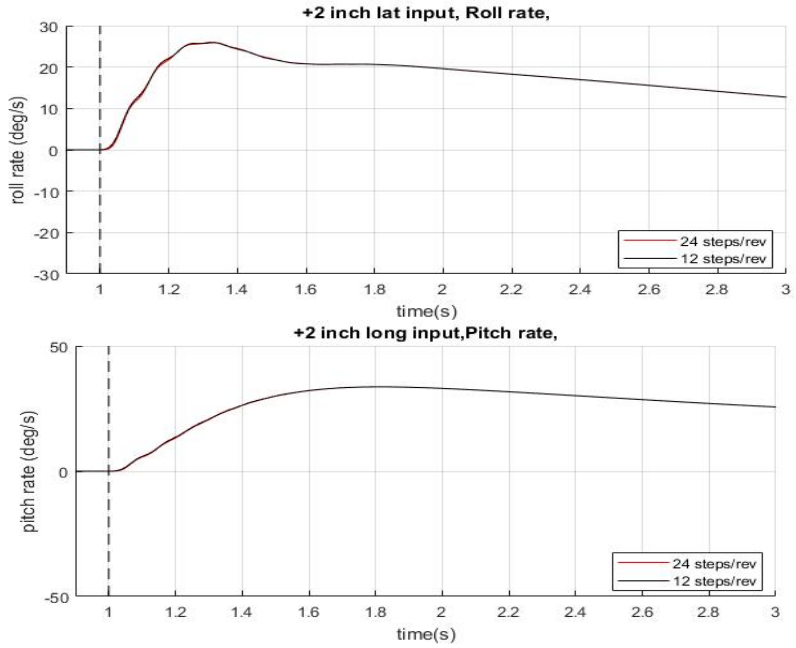

Figure 5-4: Comparison of Bo-105 model response to step input for two different time steps.

Testing of real time capability was performed by comparing the number of time steps performed by FLIGHTLAB and the turbulence model (see Table 5-1, missed time steps are characterized as jumps). Even under ideal conditions the possibility exists that the Simulink model slows down and a step is missed. To ensure that the number and placement of new eddies covers the required fraction of the control box to ensure a uniform distribution, eddies leaving the control volume are regenerated at a random location between the inflow and a distance equal to $d = \boldsymbol{V}_{inc} * \Delta t * Steps$.

Table 5-1: Comparison of time steps missed by the turbulence model during real time simulation.

No of Eddies	FLIGHTLAB Steps	Simulink Steps	Jumps/Steps
296	2566	2566	0,0000
305	2325	2325	0,0000
314	2580	2580	0,0000
342	2707	2706	0,0004
394	2084	2084	0,0000
406	6148	6108	0,0065
495	6217	6175	0,0068
543	2642	2599	0,0163

Upgrades to the PCs used to run FLIGHTLAB and improvements to the network, performed at the laboratory throughout the period of the research resulted in real time simulation capabilities with around 2200 eddies. This became especially useful for the implementation of multiple series of eddies in Chapter 6 and the use of non – isotropic eddies in Chapter 7 to reproduce a pre-generated turbulence field. Nevertheless, the process employed to test and ensure real-time capabilities of the model remained unchanged from the one described here.

5.2.4 Validation and characterization:

In the current implementation, a uniform distribution of $\boldsymbol{\varepsilon}$ has been employed. All diagonal values of the Reynolds Stress Tensor have been maintained as equal and the off–diagonal values have been kept as zero. All three components of eddy size are also equal in all runs and the number of eddies is set as the ratio between control volume and eddy volume in order to completely fill the control volume with a distribution of eddies of uniform density:

$$\begin{gathered} \boldsymbol{Re_{xx} = Re_{yy} = Re_{zz} = Re_{St}} \\ \boldsymbol{Re_{ij} = 0 \; for \; i \neq j} \\ \boldsymbol{\sigma_x = \sigma_y = \sigma_z = \sigma} \\ \boldsymbol{N_{Eddies} = \frac{V_B}{\sigma_x * \sigma_y * \sigma_z} = \frac{V_B}{\sigma^3}} \end{gathered} \qquad \textit{5-17}$$

The eddy shape function, *f(x)*, describes the velocity distribution for each eddy (see Eq. [5-3]). For purposes of validation, the flight simulation SEM was tested using two of the shape functions applied by Jarrin, a tent shape function and a gaussian shape function. The tent shape function was used for initial implementation and testing:

$$\boldsymbol{f(x)} = \begin{cases} \boldsymbol{\sqrt{\frac{3}{2}} * (1 - |x|), \quad if \; |x| < 1} \\ \boldsymbol{0, \quad if \; |x| > 1} \end{cases} \qquad \textit{5-18}$$

The tent shape function has been used to test the behaviour of the SEM model against changes in the different parameters and initial assessment of rotorcraft response for the Bo 105 helicopter model as well as for preliminary flight simulation tests. The resulting PSD of the induced turbulence follows the equation:

$$\boldsymbol{\phi_{ij}(x,\omega) = Re_{ij}\frac{\sigma}{|U|}\left|\frac{e^{-i\frac{\sigma}{|U|}\omega}\left(-1-e^{i\frac{\sigma}{|U|}\omega}\right)^2}{\left(\frac{\sigma}{|U|}\omega\right)^2}\right|^2} \qquad 5\text{-}19$$

The other eddy shape being studied is represented by the following Gaussian function:

$$\boldsymbol{f(x) = \begin{cases} C * e^{-k*x^2}, & if\ |x| < 1 \\ 0, & if\ |x| > 1 \end{cases}} \qquad 5\text{-}20$$

with the value of C, chosen in order to comply with the normalization condition (see Equation 5-4):

$$\boldsymbol{C^2 = \frac{\sqrt{2*k}}{\sqrt{\pi}*\int_{-\sqrt{2k}}^{\sqrt{2k}} e^{-x^2}\,dx}} \qquad 5\text{-}21$$

The Gaussian shape function has been used for the implementation of the multi-scale eddy SEM and has been used for simulations with the Bell 412 helicopter model. Its PSD follows the function:

$$\boldsymbol{\phi_{ij}(x,\omega) = Re_{ij}\frac{\sigma}{|\overline{u}|}|\mathcal{F}_{\frac{\sigma\omega}{|\overline{u}|}}\{f\}|^2}$$

$$\boldsymbol{\mathcal{F}_{\frac{\sigma\omega}{|\overline{u}|}}\{f\} = C * \frac{\sqrt{\pi}e^{-\frac{\left(2\pi*\frac{\sigma}{|\overline{u}|}*\omega\right)^2}{4k}} * \left(erf\left(\sqrt{k} - 2\pi*\frac{\sigma}{|\overline{u}|}\frac{\omega}{2\sqrt{k}}i\right) + erf\left(\sqrt{k} + 2\pi*\frac{\sigma}{|\overline{u}|}\frac{\omega}{2\sqrt{k}}i\right)\right)}{2\sqrt{k}}} \qquad 5\text{-}22$$

with $\mathrm{erf}(z)$being the error function: $\mathrm{erf}(z) = \frac{2}{\sqrt{\pi}}\int_0^z e^{-t^2}dt$.

As the shape function of each eddy is truncated to the region of distance 2σ from its centre along all axes, the Fourier transform presents a similar pattern to the spectral leakage of a window function. This pattern, which is also seen when analytically computing the PSD of the function, as shown in Figure 5-5, consists of a main lobe with a repetition of secondary lobes of decreasing amplitude. The width and amplitude of the lobes is dependent on the shape function, with Gaussian-shaped eddies producing higher frequency lobes than tent-shaped ones. These high frequency disturbances are unrealistic but are a product of the SEM model.

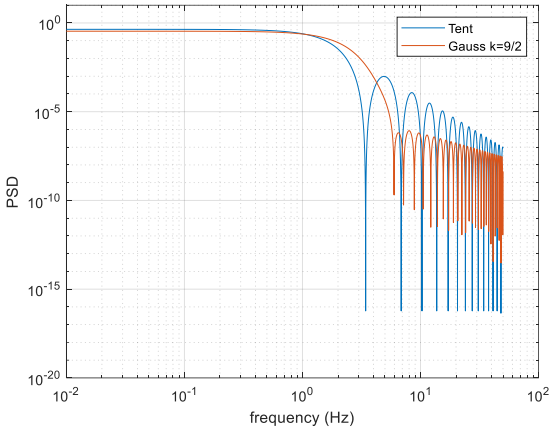

Figure 5-5: Analytically predicted PSD plots of SEM generated turbulence for tent and gaussian shape function. Eddy properties are: Re_{ii} = 1 m^2/s^2, σ = 3m.

A series of offline simulations have been performed using the Bo 105 FLIGHTLAB model (see Section 4.4) to validate it and assess its capabilities for offline and piloted simulations. The conditions tested are shown in Table 5-2, they correspond to the aircraft in hover and forward flight of 30kts and 50kts under a 90deg green wind (from the right) of 10 or 20kts. No pilot model was employed, and no control inputs were given. To ensure that the aircraft maintains a correct orientation and does not crash during the simulation, altitude over ground, aircraft attitude and attitude rates have been frozen for all simulations. For simulations in hover, the horizontal position of the aircraft has also been frozen. Flow velocities and rotor response have been recorded for all simulations.

Table 5-2: Summary of Turbulence parameters of Bo 105 model offline simulations.

Case	Shape	k	Re_{ii} (m^2/s^2)	σ (m)	Wind (kts)	Aircraft IAS (kts)
1	Tent	--	1	3	20	0
2	Tent	--	3	3	20	0
3	Tent	--	3	5	20	0
4	Tent	--	3	3	20	0
5	Tent	--	3	3	10	0
6	Tent	--	3	3	20	30
7	Tent	--	3	3	20	50
9	Gaussian	4,5	3	3	20	0
10	Gaussian	9	3	3	20	0

All cases correspond to homogeneous, isotropic turbulence (see Eq 5-17), therefore, the turbulent velocities induced on a given point for all three axes present the same behaviour, with the value of turbulent velocities standard deviation determined by the diagonal values of the Reynolds Stress Tensor Re_{ii} as seen in Figure 5-6 a. The PSD of the random turbulence obtained from the simulation follows the shape predicted

analytically by Eqs 5-21 and 5-22 and shown in Figure 5-5 with a main lobe whose amplitude falls rapidly for frequencies higher than 1 Hz and secondary lobes of decreasing amplitude at higher frequencies due to the truncated eddy shape function combined with the frequency leakage due to the truncation of a finite time signal.

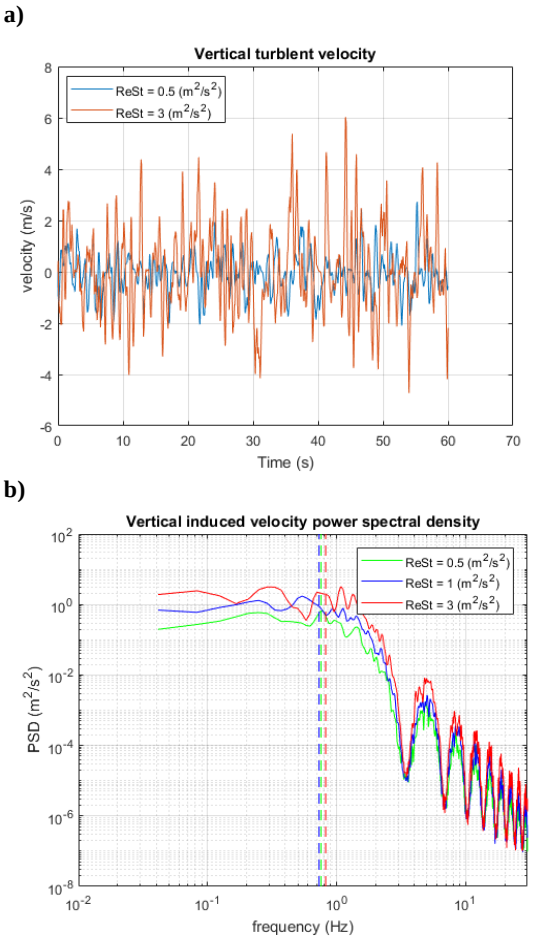

Figure 5-6: a) Time history of vertical component of turbulent velocity against Re_{ii} values, b) Power spectral density of vertical velocity components against Re_{ii}. Vertical dashed lines indicate power spectral density averaged frequency.

The resulting power spectral density (see Eq. [5-8]) and average frequency of induced turbulent velocities depends on the size of eddies, and the relative velocity of eddies to the aircraft, as can be seen in Figure 5-7:

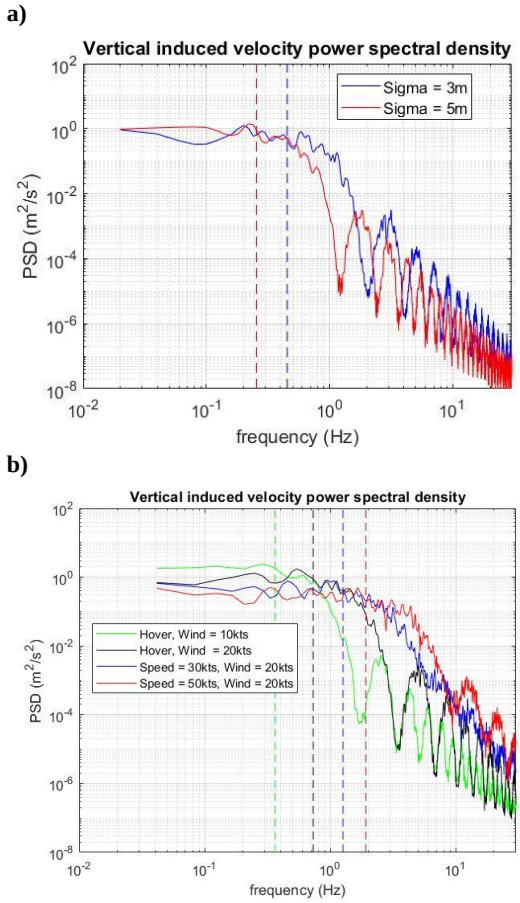

Figure 5-7: a) PSD of vertical induced turbulent velocities against size of eddies, c) PSD of vertical induced turbulent velocities against wind and aircraft speed, computed using Welch method. Vertical dashed lines indicate power spectral density averaged frequency.

Figure 5-8 shows the effect of the eddy shape function on the induced turbulence. Compared with a tent shaped eddy, a Gaussian shape function with a value of $k = 4.5$ shows a shift in the fall of power density towards higher frequencies and a reduction at lower frequencies. Another effect is a reduction in the appearance of low intensity high frequency peaks. This "cleaner" behaviour of the Gaussian function in comparison with the tent shape function should allow for an easier adjustment of the intensity to frequency slope through the use of eddies of multiple sizes. These effects increase with increases in the value of the decay exponential k.

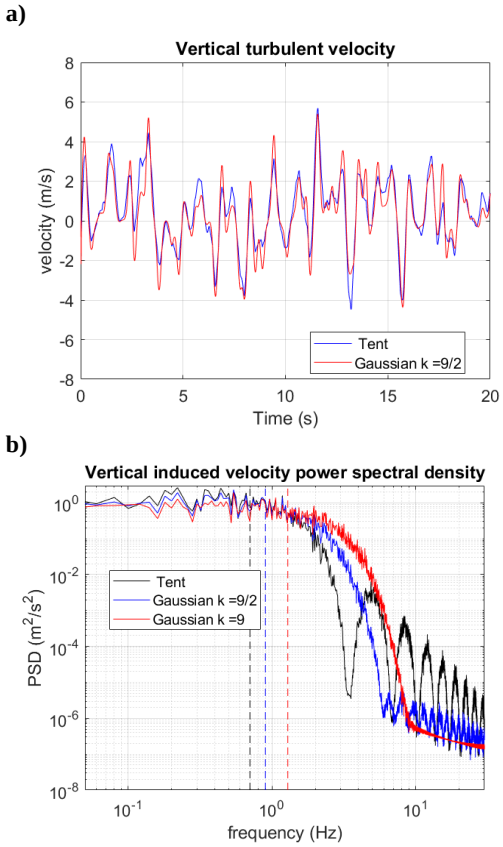

Figure 5-8: Effect of eddy shape function on induced turbulence: a) Time history of induced turbulence for tent and Gaussian shape function, b) Power spectral density of induced turbulence for tent and Gaussian shape, including effect of power decay (k).

Figure 5-9 shows the behaviour of power spectral density averaged frequency obtained from different simulations. As expected from Eq. 5-8, average frequency is proportional to the ratio of incoming flow velocity and characteristic eddy size.

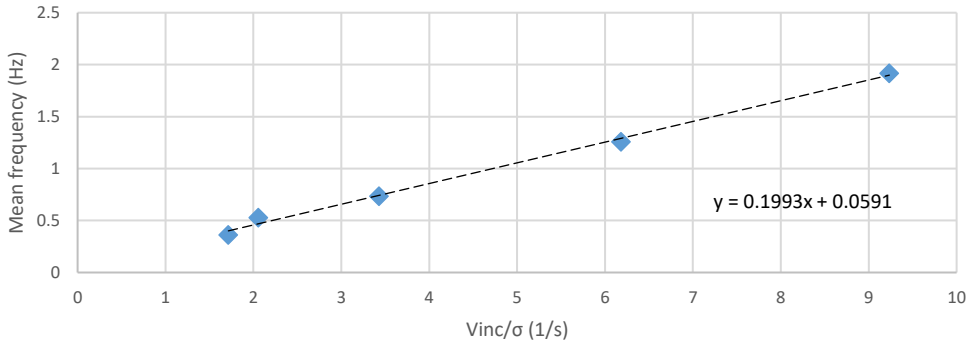

Figure 5-9: Average mean frequency of vertical induced velocity at fuselage against ratio of incoming flow velocity and eddy size. Cases 2, 3, 5, 6 and 7 of Table 5-2

For computational performance of the model, the number of eddies is the most important parameter. Its value is chosen to ensure that the entire control volume (Eq. [5-17]) is completely filled with eddies; this implies that the average frequency of

turbulent velocity components should scale with the cubic root of the number of eddies. In practice a slightly lower scaling was obtained during the tests as can be seen in Figure 5-10:

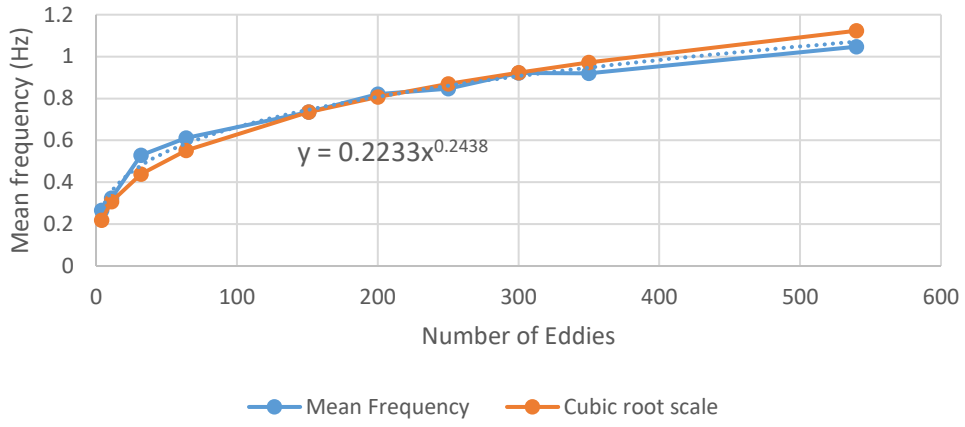

Figure 5-10: Average mean frequency of vertical induced velocity at fuselage against number of eddies. Aircraft fixed in hover under a under 20kts, 90 deg green wind.

Correct implementation of the model has been verified by ensuring that over the long term, cumulative time averaged values of turbulence induced velocities, Reynolds stresses, skewness and flatness (or kurtosis) behave as expected for a stationary, ergodic random process (Ref. [112]) (see eqs. [5-9] to [5-12]). Figure 5-11. depicts the evolution with time of these values for the first case in Table 5-2 (tent shape eddy function, Re_{ii} = 1 m^2/s^2, σ=3m and wind speed of 20kts). Convergence is very fast initially but slows down significantly afterwards, after the first 200s values of Re_{ii} and F_{u_i} oscillate within ± 0.1 of their convergence value, while the average flow velocity oscillations are within ± 0.1 of the square root of Re_{ii}. Skewness trends towards zero at a much lower speed, but after around 5 min, oscillations will stay below an absolute amplitude of 0.5. Simulations performed for a smaller number of eddies, due to larger values of eddy size, will present slower convergence as shown in Figure 5-12. In all cases studied, average lift loads on the blades are fully converged after 180s, as shown in Figure 5-14 in Section 5.2.5, suggesting that the deviations from convergence values are small enough to have a minimal impact during flight simulation trials.

Cumulative time averaged values of turbulent velocity perturbations, Reynolds stresses, skewness and flatness (see equations [5-9] to [5-12]) for the ACP located at the rotorcraft's fuselage of gravity are presented in Figure 5-11, showing that the current implementation does not alter the properties of stationary randomness and independence from the previous history.

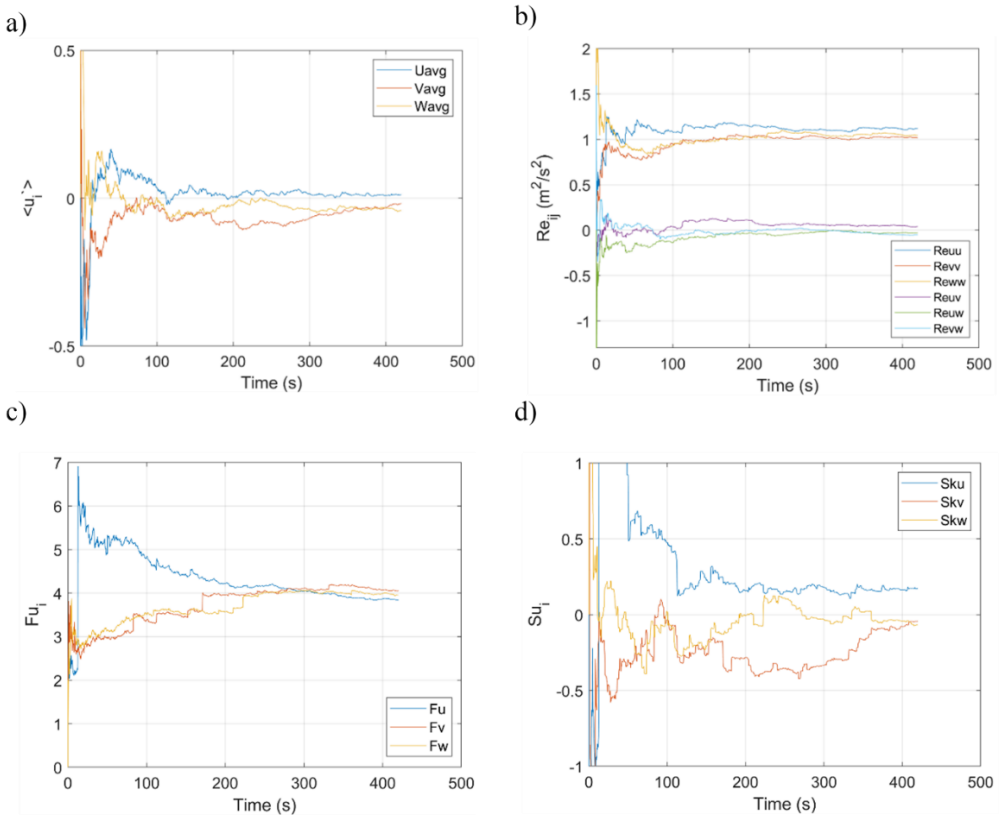

Figure 5-11: Cumulative time averaged values on fuselage ACP of: a) turbulent velocity components, b) Reynolds stresses, c) flatness and d) skewness for σ = 3m (case 1 in Table 5-2).

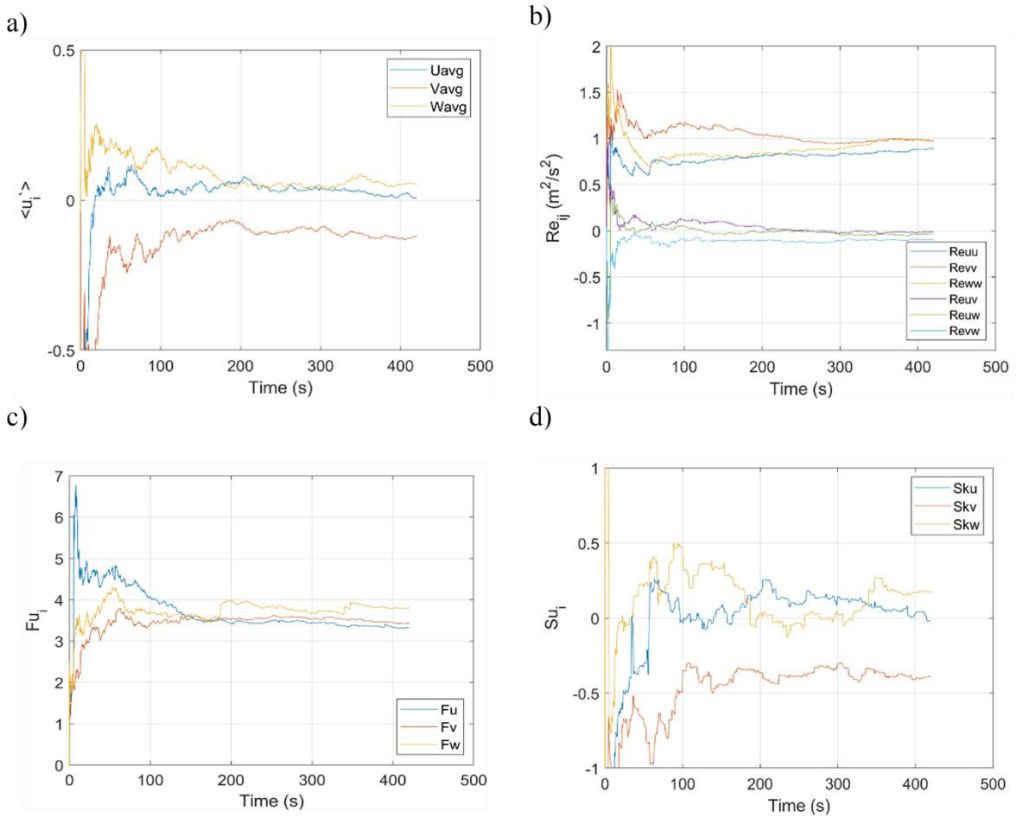

Figure 5-12: Cumulative time averaged values on fuselage ACP of: a) turbulent velocity components, b) Reynolds stresses, c) flatness and d) skewness for σ = 5m (case 3 in Table 5-2).

5.2.5 Offline simulation – Bo 105, rotor response and induced forces and moments

To gain an initial insight into how the synthetic eddy generated turbulence affects rotorcraft handling, the main rotor response as well as aircraft induced forces and moments were recorded for different levels of Re_{ii}. The analysis uses the Virtual Airdyn technique presented by Kääriä et al. in [103] to measure the effect of the turbulence on a rotorcraft's response. The aircraft was trimmed under a uniform wind under no turbulence and then subjected to different turbulence conditions. Given the lack of a SAS and that no pilot model was used, to prevent the helicopter from crashing or attaining unrealistic attitudes, the displacements and rotations in all axes were frozen, with the exception of those tests performed under forward flight, where movement along the longitudinal axis was allowed. The conditions tested are presented in Table 5-3. They correspond to a hover flight under a 90deg green azimuth wind. The size of eddies has been maintained constant at $\sigma_i = 3m$ for all cases. All values for forces and moments presented in the following graphs have been made non-dimensional by dividing with $\pi\rho\Omega^2R^4$ and $\pi\rho\Omega^2R^5$ respectively, including tail rotor thrust and moments in order to allow for comparison with other aircraft elements.

As stated previously the location of all the eddies surrounding the aircraft is preserved across all time steps, this ensures that the turbulence induced on all the aircraft ACPs is coherent with the effects on the rest of the aircraft. This automatic correlation also extends to the induced turbulence seen by all the rotor blade elements (see Figure 5-13).

Table 5-3: Offline simulations performed for the Bo 105

Case	Shape	Re_{ii} (m^2/s^2)	σ (m)	Wind (kts)	AC IAS (kts)
1	--	0	--	20	0 (Frozen)
2	Tent	1	3	20	0 (Frozen)
3	Tent	3	3	20	0 (Frozen)
4	Tent	1	3	10	0 (Frozen)
5	Tent	3	3	10	0 (Frozen)

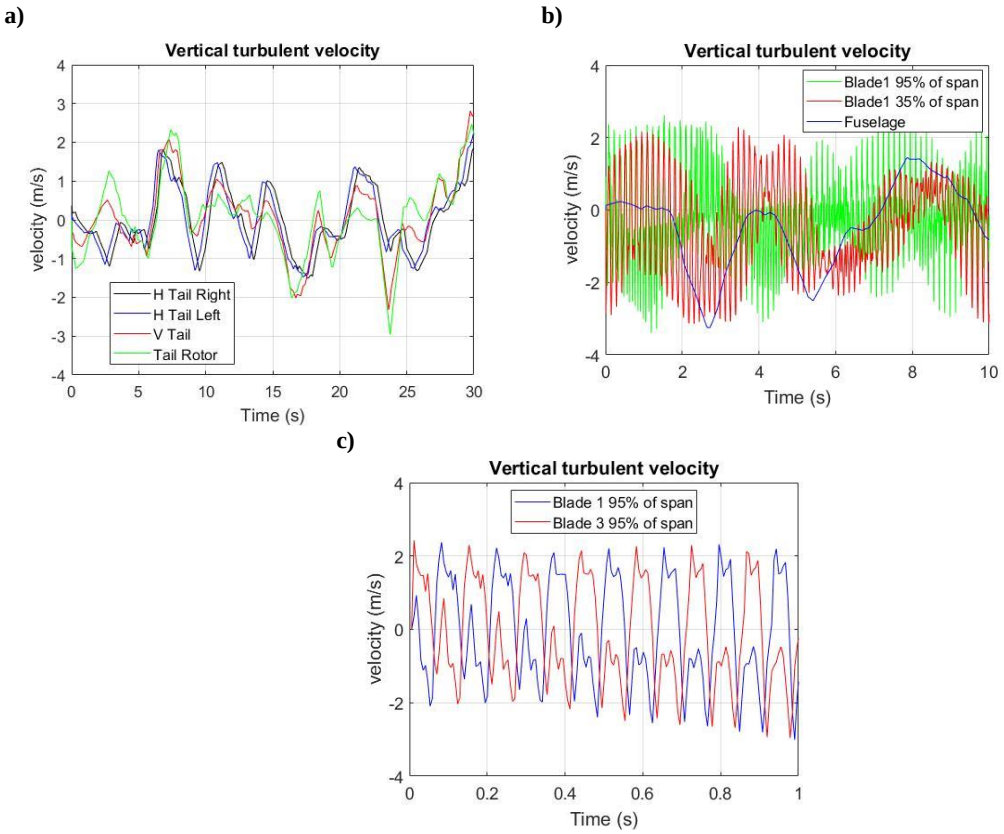

Figure 5-13: Correlation between turbulence induced vertical flow velocities in hover under a 10kts, 90deg green wind (case 4 in Table 5-3): a) At tail and tail rotor, b) At fuselage, blade root and blade tip, c) At the tip of opposite blades.

Despite the time averaged values of $\langle u_i' \rangle$, Re_{ij}, S_{u_i} and F_{u_i} (see Figure 5-11 and Figure 5-12) not achieving full convergence during the simulated time frames, cumulative time averaged values of lift and drag coefficients and their distribution across the blade are fully converged (Figure 5-14 a). As the induced turbulence is of the same intensity and frequency across the entire aircraft, its effects are of greater relevance when compared to the lower relative flow velocities at the blade root. This is evidenced in larger variations of the local angle of attack due to turbulence (Figure 5-14 b) and results in lift coefficient oscillations of greater amplitude and higher frequency near the blade root (Figure 5-14 c).

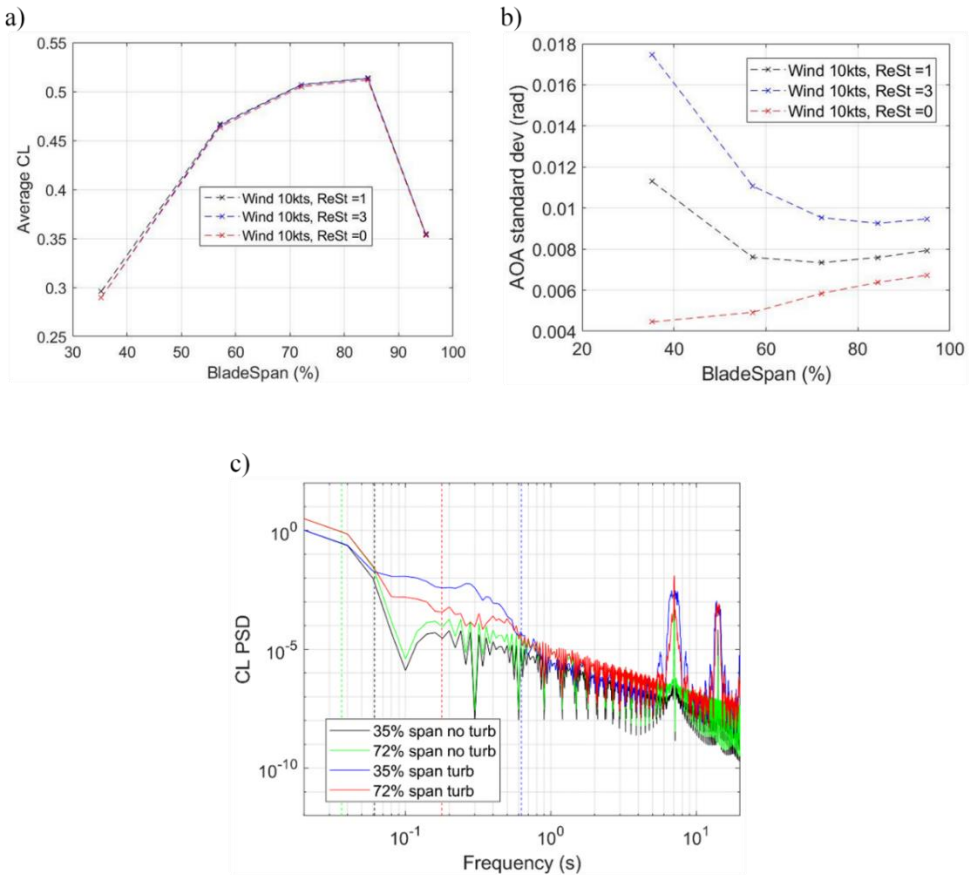

Figure 5-14: Average lift coefficient along main rotor blade span. b) Standard deviation of angle of attack along main rotor blade span. c) Power spectral density at two main rotor blade locations under turbulence with Re_{ii} = 3 m2/s2 and without turbulence. All runs conducted under a 10kts wind (case 4 and 5 in Table 5-3).

Figure 5-15 shows power spectral density plots of main rotor blade flapping angle and thrust in hover for a 20kts 90deg wind under no turbulence and turbulence conditions with values of $Re_{ii} = 1\ m^2/s^2$ and $Re_{ii} = 3\ m^2/s^2$ (cases 1, 2 and 3 in Table 5-3). When not subjected to turbulence, blade flapping occurs mainly at the same frequency as the rotor with minor modes at multiples of rotor frequency. When flying under SEM induced turbulence, blade flapping amplitude increases are appreciable within the 0.1Hz to 1Hz frequency range at which the effect of turbulent induced velocities is the strongest (see Figure 5-6), but the largest effect is seen around frequencies near one and two times the main rotor frequency. Frequencies near multiples of the rotor frequency are also excited. Power spectra of main rotor thrust shows a similar but smaller effect within the 0.1Hz to 1Hz range and a cyclical variation at four times the rotor frequency corresponding to the one per rotor cycle load changes from the four blades.

Since turbulent induced velocities present the same behaviour in all axes, its effects on tail rotor thrust are similar as can be seen in Figure 5-16. Since the tail rotor is

modelled as an actuator disk with a single ACP, no effects due to rotor rotation frequency are modelled.

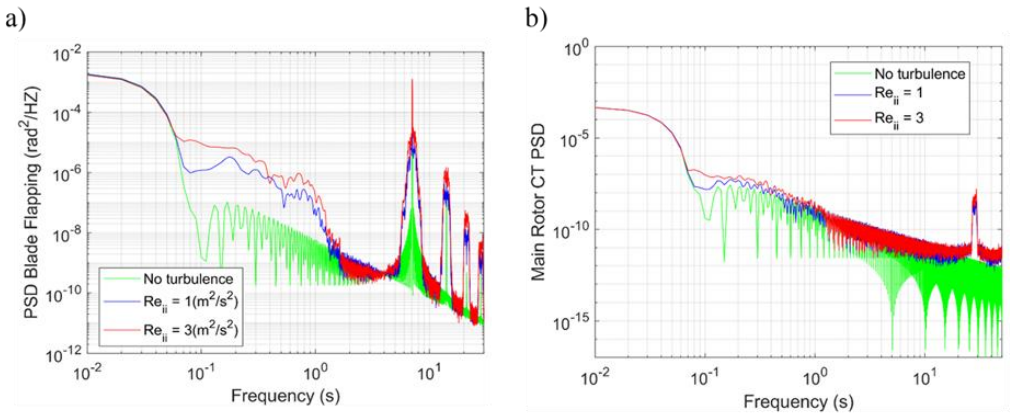

Figure 5-15: a) Power spectral density of main rotor blade flapping. b) Power spectral density of main rotor thrust coefficient.

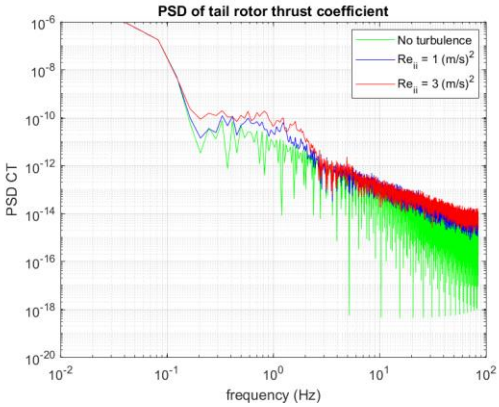

Figure 5-16: Power spectral density of tail rotor thrust non-dimensionalised with main rotor speed and radius.

This effect within the 0.1Hz to 1Hz range can also be observed in the resulting forces and moments acting on the aircraft. Figure 5-17 and Figure 5-18 show a similar behaviour of longitudinal and vertical forces as well as a similar behaviour of rolling and pitch moments, indicating that turbulence effects on the main rotor are the main cause of resulting disturbances.

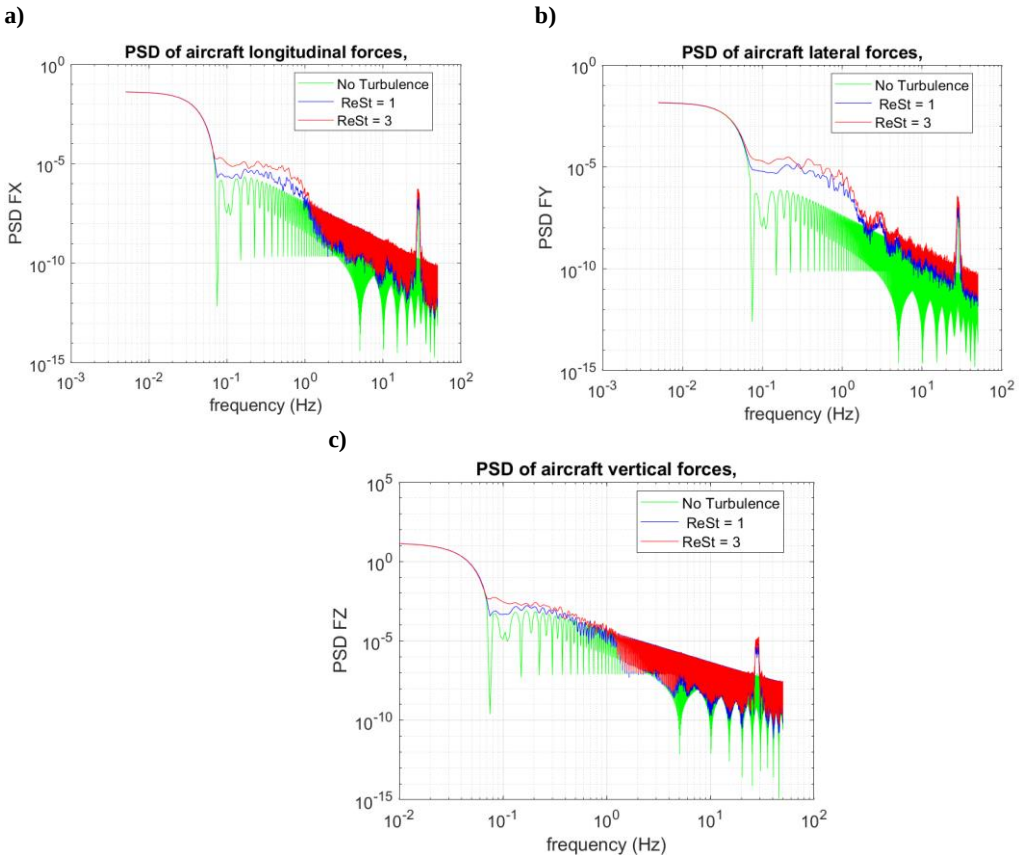

Figure 5-17: a) Power spectral density of longitudinal forces acting on aircraft, b) Power spectral density of lateral forces acting on aircraft, c) Power spectral density of vertical forces acting on aircraft.

At frequencies beyond 2 Hz, the aircraft and rotor behaviour are dominated by the main rotor frequency multiplied by the number of rotor blades, while the low amplitude lobes, especially for simulations without turbulence, are mainly artificial due to frequency leakage from the truncation of a finite time signal. For simulations conducted with turbulence, this signal is amplified by the disturbances caused by the high frequency turbulence component resulting from the eddy shape function and discussed in Section 5.2.4 of this chapter.

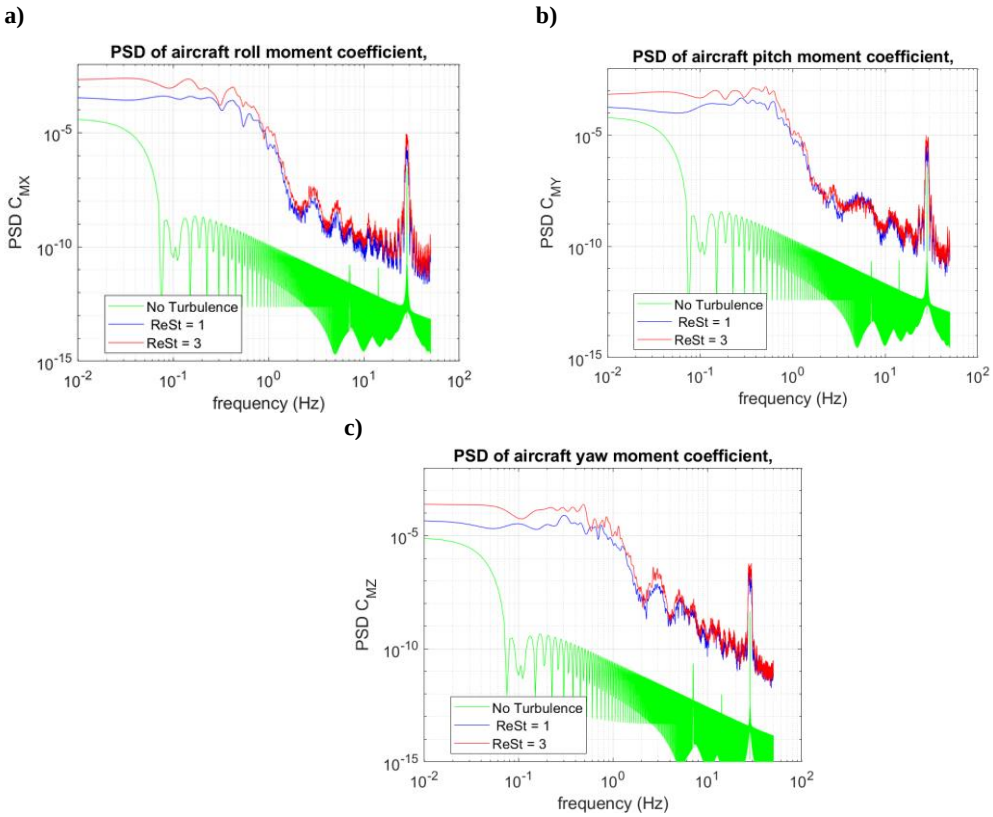

Figure 5-18: a) Power spectral density of roll moments acting on aircraft. b) Power spectral density of pitch moments acting on aircraft. c) Power spectral density yaw moments acting on aircraft.

It is also interesting to analyse the source of lateral forces and yawing moments acting on the aircraft. Figure 5-19 and Figure 5-20 show power spectral densities of lateral forces and yawing moments induced by the main rotor, aircraft tail and tail rotor respectively. It can be seen that the tail rotor generates greater oscillations in lateral force than both the main rotor and the aircraft's tail. However, the effect of turbulence is much stronger on these two, resulting in the appearance of new oscillating lateral forces.

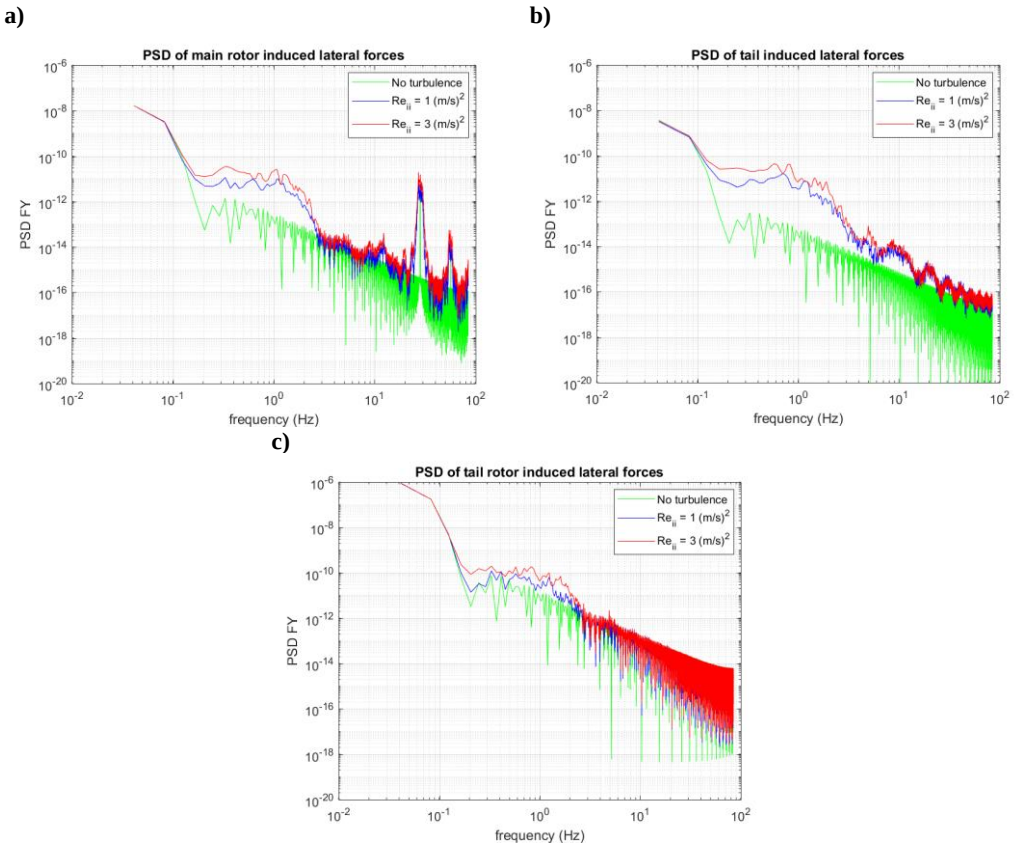

Figure 5-19: a) Power spectral density of main rotor induced lateral forces, b) Power spectral density of tail rotor induced lateral forces, c) Power spectral density of tail induced lateral forces.

A similar effect can be observed when studying the origin of oscillations in yawing moments under turbulence. Again, while the tail rotor and main rotor are the main sources of oscillations in yaw moments acting on the aircraft, the aircraft's vertical tail is the component that presents the largest differences when wind conditions change from no turbulence to higher turbulence conditions.

These results show the need to model the effects of turbulence not only on the main rotor but also on the remaining aircraft elements as their effect on roll and yaw perturbations can be of a similar magnitude as the main rotor.

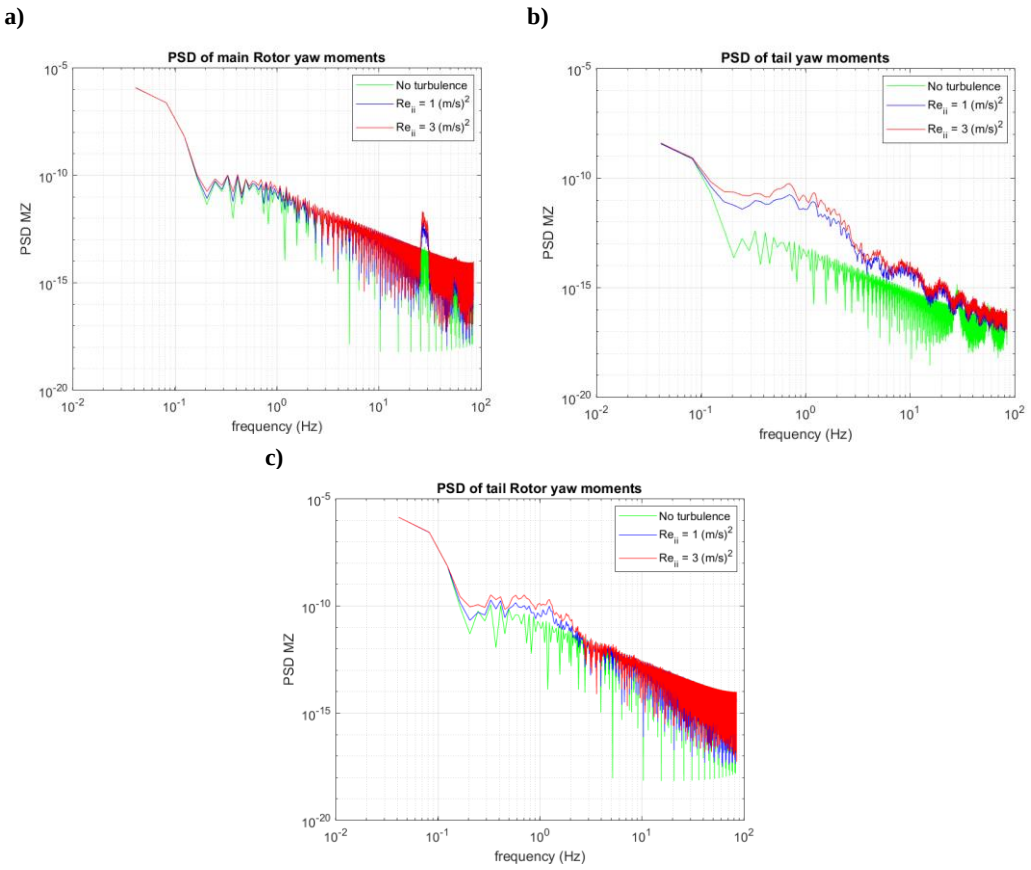

Figure 5-20: a) Power spectral density of main rotor induced yaw moments, b) Power spectral density of tail rotor induced yaw moments, c) Power spectral density of tail induced yaw moments.

5.3 Piloted Flight Simulation Testing of Synthetic Eddy Method

A piloted flight simulation test was performed to assess the feasibility of applying the developed SEM model for piloted flight simulation and provide an initial insight of both its capabilities and the effects of induced turbulence on aircraft handling and pilot workload. The test was conducted in the University of Liverpool's HELIFLIGHT – R flight simulator. The aircraft was a FLIGHTLAB model of a Bo 105 helicopter, with no SAS. The Bo 105 is highly susceptible to external disturbances (see Sections 4.5 and 4.6) and would realistically not operate in a highly turbulent environment, but in this case it allowed the study to start with reduced turbulence intensities and provided a known airframe to assess the turbulence. The pilot was an experienced flight instructor with ample rotorcraft flight simulator experience. Their instructions were to attempt two tasks, both informed by situations that are common during operations to offshore wind farms: a position keeping segment of the ADS-33 precision hover (PH) mission task element (MTE) [21] (see Figure 5-21 and Table 5-4) and a straight and

level (S&L) low speed (30kts) task. The low speed forward flight task was not assessed as an ADS-33 mission task element and no limits on allowed deviations were defined, instead the pilot was instructed to follow a runway (Figure 5-22) while maintaining initial heading altitude, lateral position and velocity and, if disturbed, to return to the original conditions as soon as they deemed feasible for safe flight. All flights were performed at an altitude of 20ft above the ground, under a 10kts, 90deg green (from the right) wind and turbulence with Re_{ii} values of 0, 0.5 m^2/s^2 and 0.75 m^2/s^2, the size of the eddies was kept constant at $\sigma_x = \sigma_y = \sigma_z = 3m$ for all test flights (see Table 5-5), all flights were performed under turbulence produced using the tent based eddy shape.

Figure 5-21: Setup for the Position hover task for the simulator trial.

The Bedford Workload Ratings (BWR) awarded by the pilot [107] (see Appendix - A) show that increases in turbulence intensity lead to increases in required task workload and a reduction in pilot spare capacity for other tasks (see Figure 5-23). Pilot comments indicate that the turbulence resulted in multi-axis disturbances. The disturbances were continuous and too similar between them and the resulting overall impact felt too uniform or bland. The pilot also indicated that due to the lack of an aircraft SAS, even without turbulence, the strong inter-axis couplings of the Bo 105 [105] contribute significantly to the difficulty of the task. This made it difficult to discern between turbulence induced disturbances and aircraft off-axis response to the pilot's own inputs. This was evident during the hover task. Even without turbulence, the pilot awarded a Level 2 BWR rating of 5, indicating a need for considerable pilot compensation to perform the task and reduced spare capacity for additional tasks. Increasing the turbulence resulted in the pilot awarding a BWR of 8, indicating very high workload requirements, difficulty for the pilot in maintaining such level of effort and almost no spare capacity left.

For the S&L task, the effect of adding turbulence on BWRs is not as significant as for the PH case, with the pilot awarding a BWR of 3 (enough spare capacity for all additional tasks) to the runs with and without turbulence, raising the rating to 4

(insufficient spare capacity for easy attention to additional tasks) only for the higher Re_{ii} value of 0.75 m^2/s^2.

Table 5-4: Limits on desired and adequate deviations for the position keeping task.

Parameter	Desired	Adequate
Maintain horizontal position within:	± 3 ft	± 6 ft
Maintain vertical position within:	± 2 ft	± 4 ft

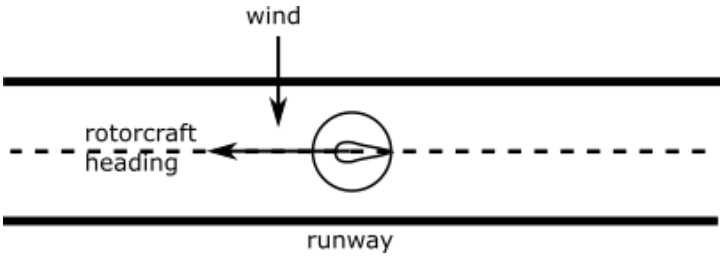

Figure 5-22: Schematics of the steady flight task.

Table 5-5: Piloted simulation runs performed.

Run	MTE	Re_{ii} (m^2/s^2)	σ (m)	Wind (kts)	AC IAS (kts)	BWR
1	PH	0	--	0	0	5
2	PH	0	--	10	0	5
3	PH	0.5	3	10	0	7
4	PH	0.75	3	10	0	8
5	S&L	0	--	10	30	3
6	S&L	0.5	3	10	30	3
7	S&L	0.75	3	10	30	4

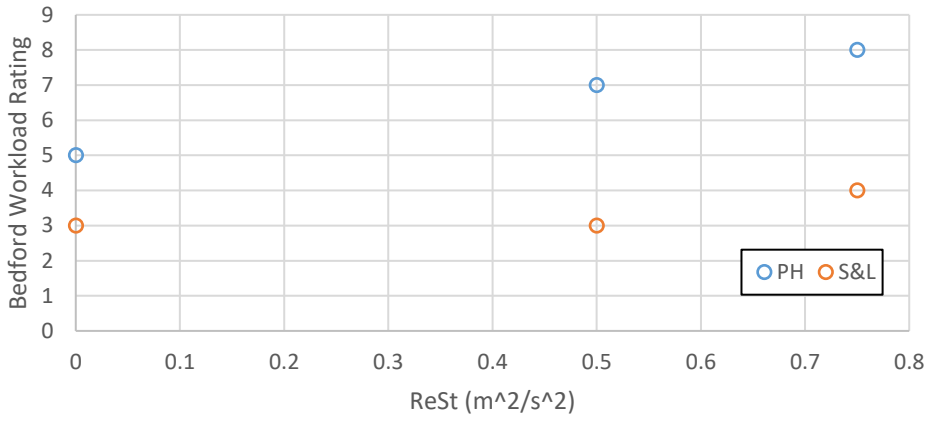

Figure 5-23: Awarded workload ratings against turbulence intensity.

The nature of the hover task requires a greater effort from the pilot in stabilizing the aircraft than for the S&L task which is mainly guidance focused. Upset limits are also much tighter, which also leads to a more difficult task. Recorded test data, however, also suggest a greater susceptibility of aircraft disturbances and pilot activity due to induced turbulence.

Figure 5-24 shows position and heading during the hover task. It can be seen that desired performance is never achieved, with loss of altitude already exceeding adequate boundaries, even under benign environmental conditions. The first run without wind nor turbulence presents somewhat worse performance than the second run undertaken under uniform wind. This might be due to the pilot still requiring some additional practice to accommodate himself to the simulator and the aircraft model. The effects of turbulence are clearly visible in both plots as longitudinal displacements exceeding adequate boundaries, a strong leftward deviation in heading and an increasing loss of altitude. The pilot seems to be able to maintain lateral displacements within adequate boundaries.

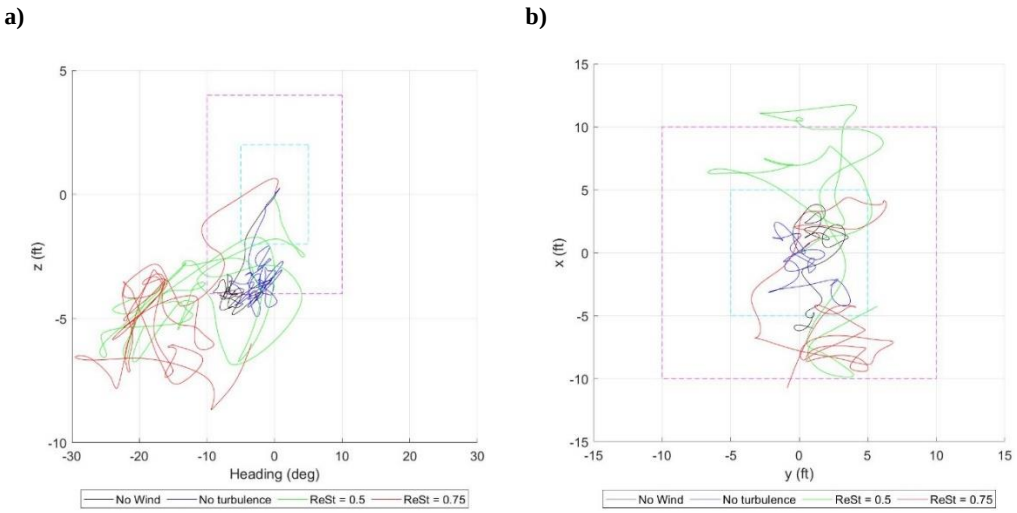

Figure 5-24: Performance of hover task: a) Altitude above ground and Heading, b) Lateral and longitudinal displacements. Dashed lines in cyan and magenta indicate boundaries for adequate and desired deviations respectively.

Analysis of aircraft attitudes show a multi-axis disturbance and a clear influence of turbulence. The amplitude of oscillations in aircraft roll and pitch rates in hover increase with higher levels of turbulence intensity (see Figure 5-25 a and b), requiring an increase in the amplitude of pilot control inputs to counteract them (Figure 5-26). The pilot indicated that they tried to avoid the build-up of large attitudes and in Figure 5-27 a) and b) it can be seen that deviations in roll and pitch do show limited growth with increased values of turbulence. The opposite is true for yaw upsets, with plots (Figure 5-27 c) showing large deviations during hover for both flights, suggesting that the pilot prioritised limiting lateral and longitudinal upsets over maintaining heading.

a)

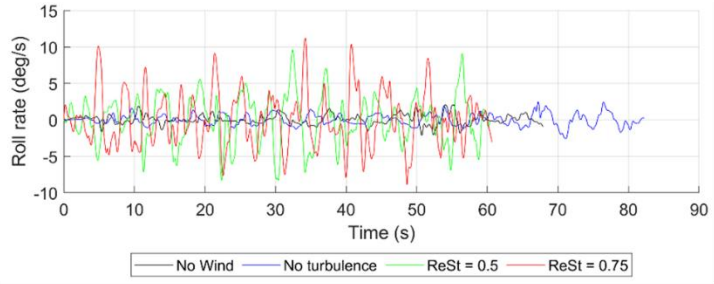

b)

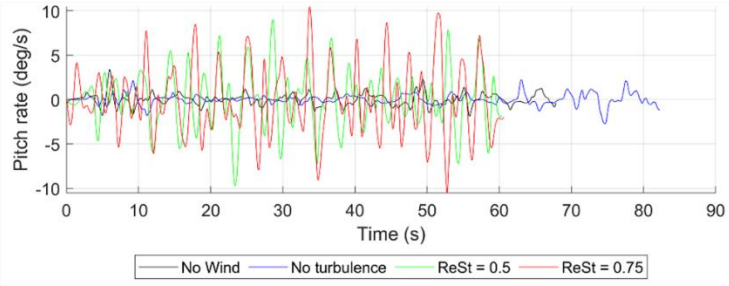

c)

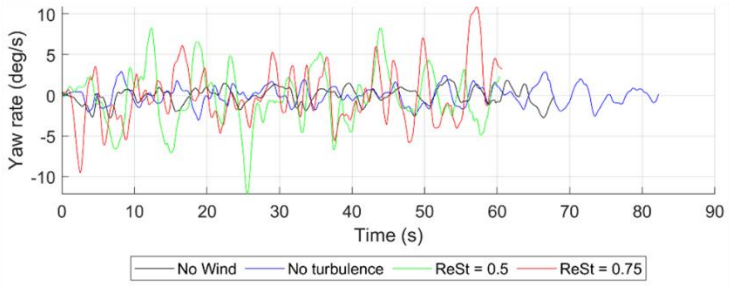

Figure 5-25: Aircraft attitude rates during hover in a) Roll b) Pitch c) Yaw.

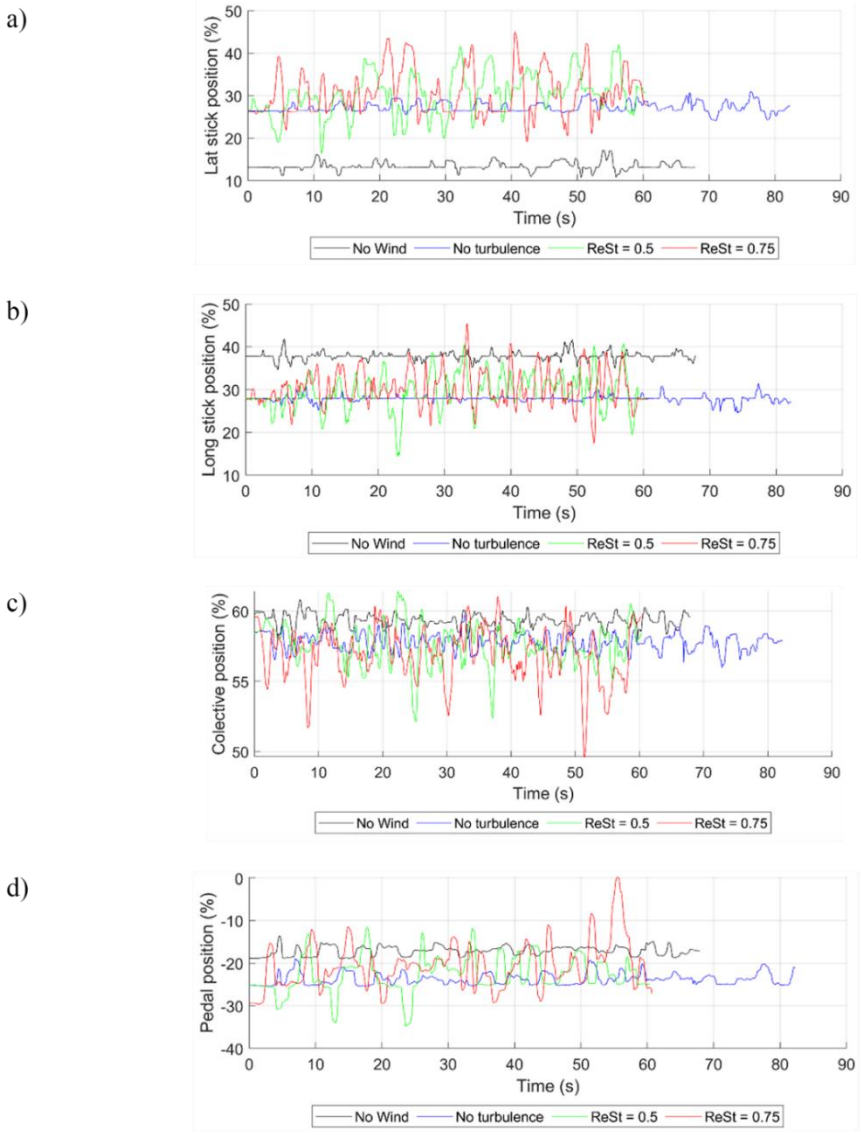

Figure 5-26: Pilot inputs during hover task in a) lateral b) longitudinal c) collective d) pedal.

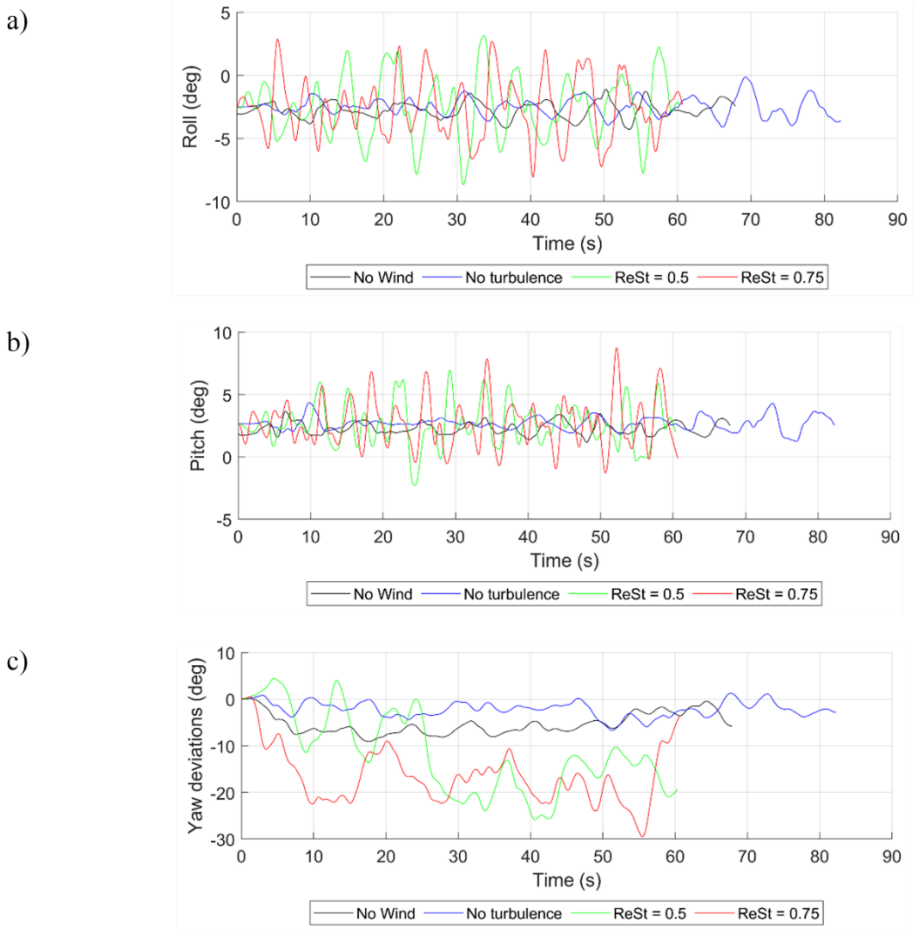

Figure 5-27: Aircraft attitudes in hover a) Roll angle b) Pitch angle c) Deviations in heading.

Figure 5-28 shows height deviations and ground track along the flight path for the S&L task. In contrast with the PH task, turbulence seems to have a more limited effect on task performance. Absolute altitude displacements stay within the ±10ft range and lateral deviations from the flight path of up to ±12ft are appreciable for all runs with or without turbulence. The run under turbulence conditions of Re_{ii} = 0.5 m^2/s^2 shows little appreciable differences when compared to the run without turbulence with deviations taking the form of a continuous drift and the pilot awarding the same workload ratings in both cases. This suggests that the uniform lateral wind has a greater effect on pilot workload than the turbulence. The influence of turbulence becomes evident for the run under Re_{ii} = 0.75 m^2/s^2 as more frequent oscillations in lateral position and especially in altitude.

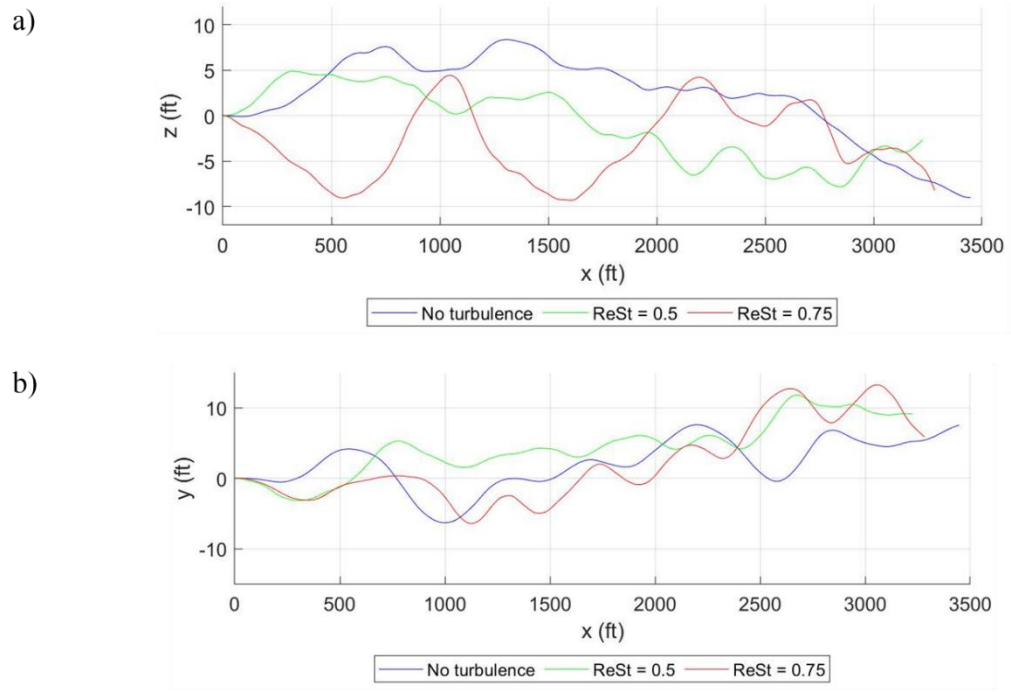

Figure 5-28: Performance during forward flight task a) Deviations in altitude b) Lateral displacement along ground track.

Aircraft deviations in attitude (Figure 5-29) and pilot activity (Figure 5-30) during S&L flight under turbulence of Re_{ii}=0.5 m^2/s^2 show little difference between the with/without turbulence cases. Pilot comments suggest that the relatively uniform nature of the induced disturbances and their higher frequency during S&L flight results in a lower build-up of deviations in aircraft attitudes and position. In the case of Re_{ii} = 0.75 m^2/s^2 however, there seems to be a sudden aircraft upset some 10s within the flight, which might have been caused by a particularly large gust in the longitudinal direction around that same time (Figure 5-31 a). The resulting upsets required large pilot inputs in collective and corresponding inputs in pedal as well as lateral and longitudinal stick inputs to compensate for cross couplings which lasted for most of the remaining run. This seems to be the main reason for the higher workload ratings awarded during the run under Re_{ii} = 0.75 m^2/s^2.

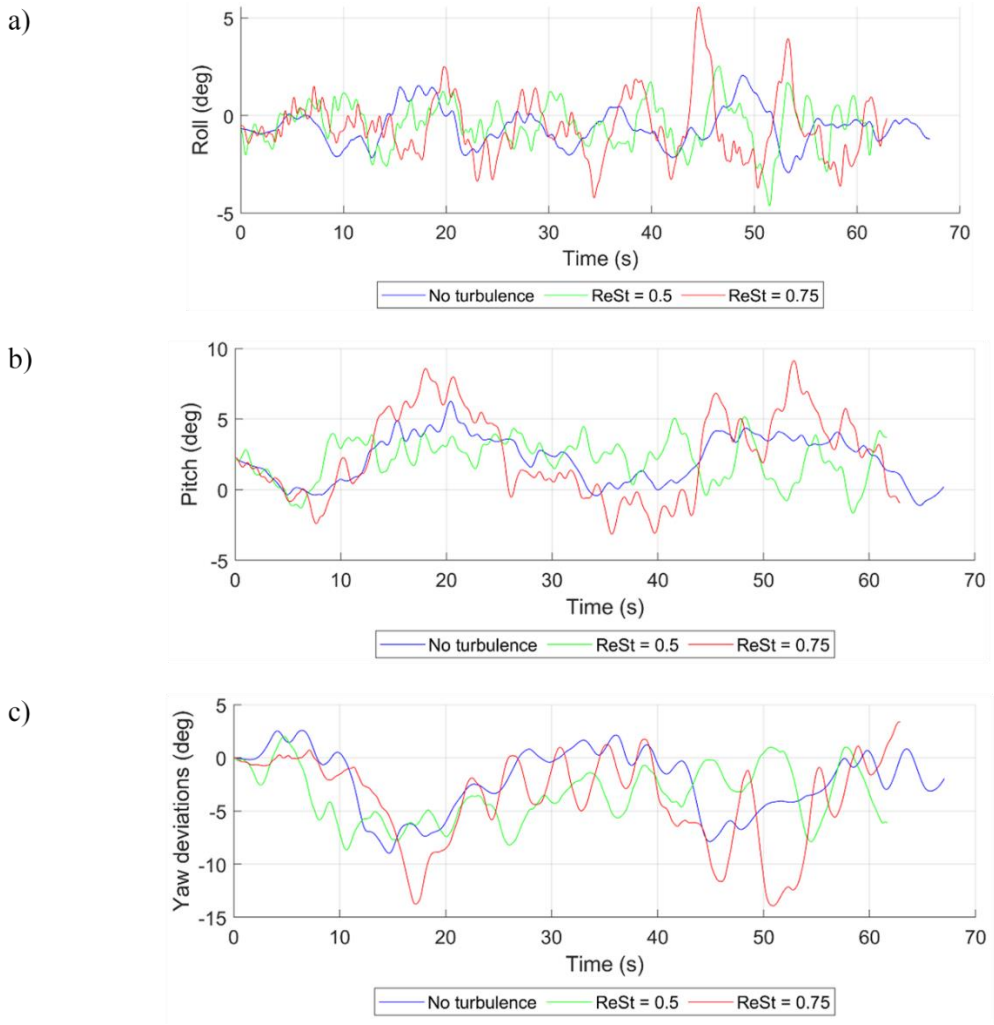

Figure 5-29: Aircraft attitudes during S&L flight a) Roll angle b) Pitch angle c) Deviations in heading.

a)

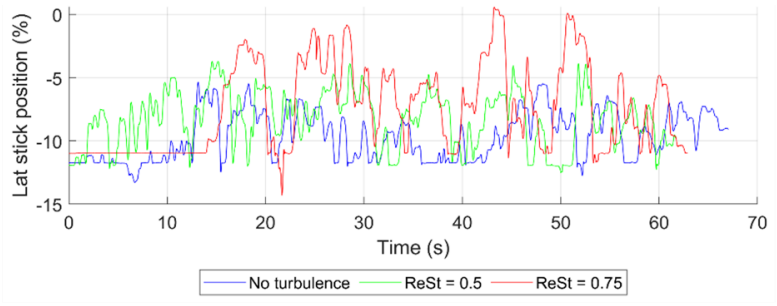

b)

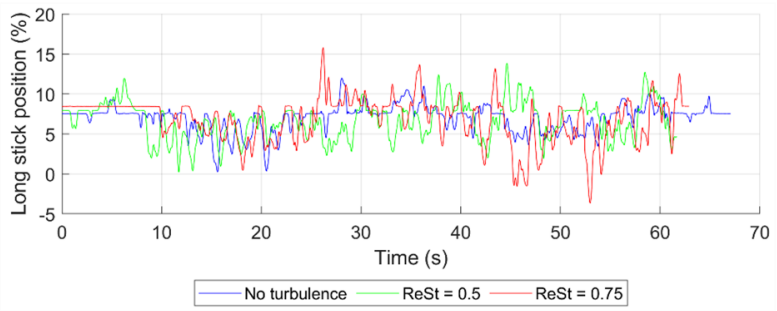

c)

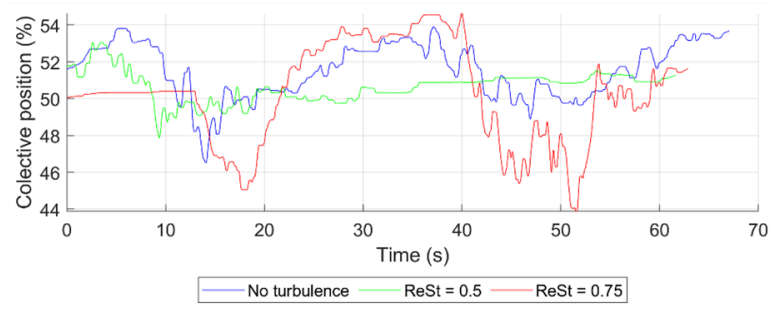

d)

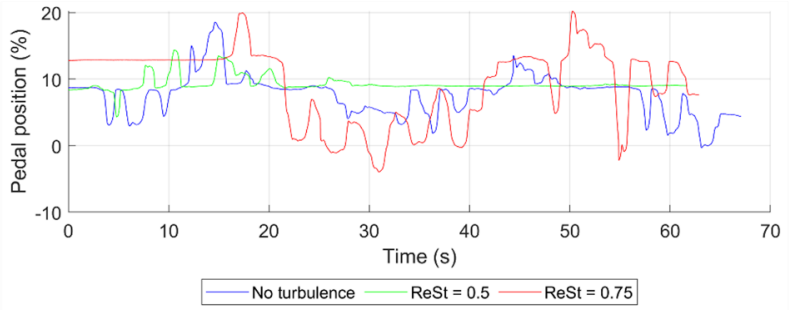

Figure 5-30: Pilot inputs during S&L flight task. a) Lateral b) Longitudinal c) Collective d) Pedal.

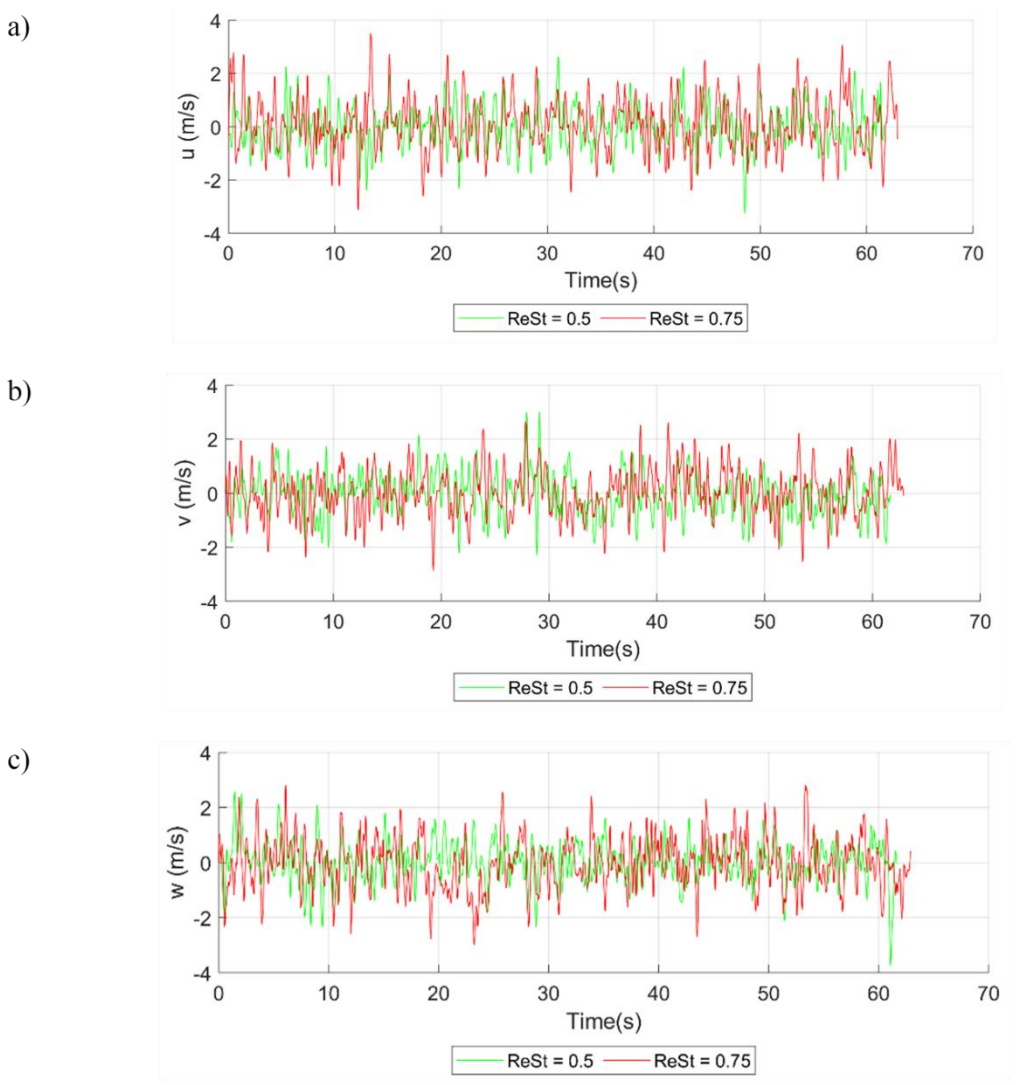

Figure 5-31: Turbulent flow velocities measured at the aircraft's fuselage ACP a) x – component b) y – component c) z - component. Axis in inertial frame of reference. Aircraft flight path was oriented towards positive x-axis.

For helicopter operations, disturbances with a frequency between 0.1Hz to 2Hz are considered to have the largest impact on pilot workload [113]. Disturbances at lower frequencies are low enough not to require any urgency from the pilot to correct for, whilst higher frequencies are often filtered out by the rotor system. The RMS of the PSD of aircraft disturbances within this frequency range (Eq 5-23) have been used in the past to assess the impact of turbulence during simulation of shipboard landings, e.g. by Kääriä et al. [103] and positively correlated with pilot workload during flight simulation trials, e.g. by Watson et al. [61].

$$\int_{0.1Hz}^{2Hz} \sqrt{PSD(f)}\, df \qquad 5\text{-}23$$

Figure 5-32, shows that test conditions where higher BWR were awarded by the pilot, such as PH flight under turbulence of higher values of Re_{ii}, also resulted in higher values of RMS of attitude moments and thrust forces acting on the aircraft.

Figure 5-33 and Figure 5-34, show the standard deviations of attitudes, attitude rates and RMS of the pilot's control inputs against the values of Re_{ii} respectively. The effect of increasing turbulence in producing larger disturbances which result in an increased pilot corrective response in the different axes, as would be expected, is apparent as is the higher susceptibility to disturbances of the PH task compared with the S&L forward flight task. The overall trend suggests that this correlation is also applicable to predicting workload trends from aircraft disturbances and pilot inputs and is explored Chapter 6.

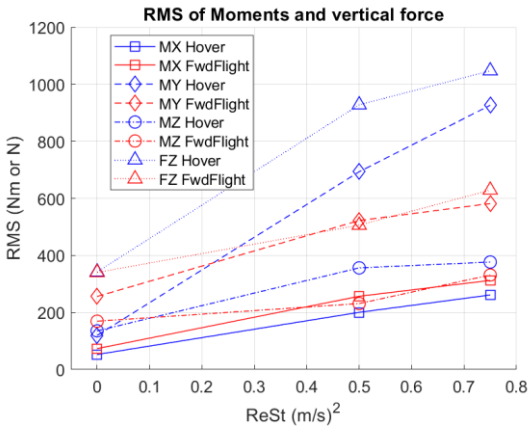

Figure 5-32: RMS of aircraft moments and vertical forces on aircraft.

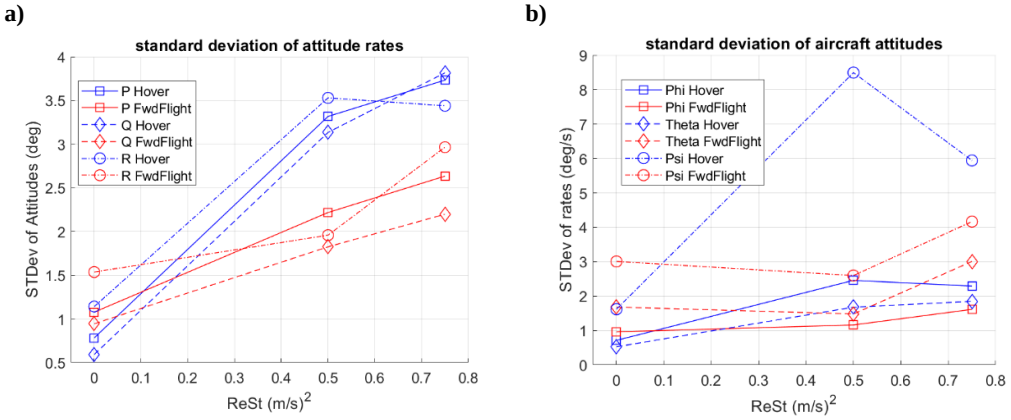

Figure 5-33: Standard deviation of a) aircraft attitude rates and b) attitudes.

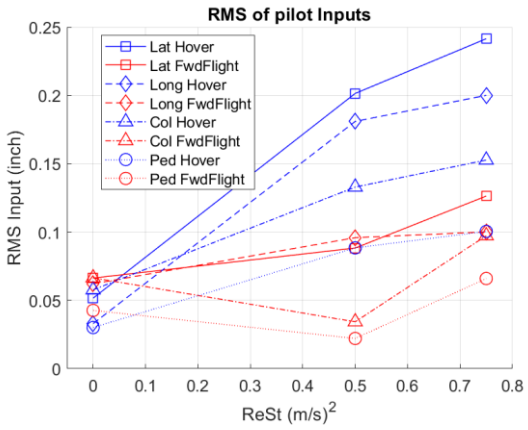

Figure 5-34: RMS of pilot control inputs.

5.4 Chapter Summary

This chapter described the development of a real–time random turbulence generator for flight simulation based on a SEM.

The SEM is based on the generation of a random distribution of turbulence generating eddies within a control volume surrounding the simulated aircraft. Eddies are displaced by environmental wind and regenerated at the inflow as they leave the domain surrounding the aircraft. Changing the values of the Reynolds stress tensor, eddy size and shape, allows for adjustment of the resulting turbulence intensity, average frequency and shape of the frequency spectra of the induced turbulence.

The SEM offers a completely random turbulence model that is easy to implement and can simulate a wide range of turbulence conditions. Among its main advantages is that it preserves the location of the eddies near the aircraft, ensuring that the turbulence induced across the different aircraft locations is automatically coherent with the effects on the rest of the aircraft, also taking into account the rotation of the rotor

blades, even if aircraft flight velocities experience large changes in a small number of time steps.

Its main drawback is that computational costs of the model are directly proportional to the number of eddies, depending on the equipment used and conditions simulated, this can limit the generation of turbulence of very high frequency in real time. By limiting the number of eddies and adjusting the simulation timesteps, the current implementation of the SEM model can work in real time.

The model has been developed in Simulink and coupled with a FLIGHTLAB model of a Bo 105 helicopter. Flight simulation testing was performed and the pilot conducted two tasks in the presence of the SEM generated turbulence: maintaining a hover over a starting point and maintaining steady and level flight along an indicated flight path. Test analysis shows that resulting aircraft disturbances are within the 0.1Hz – 2Hz frequency range that is considered to impact aircraft handling and led to increased pilot workload and degraded task performance. These effects were more apparent during the PH task than the S&L forward flight task. Higher turbulence intensities due to increasing values of Re_{ii} required the pilot to use larger corrective control inputs to compensate for the turbulence and led to higher workload ratings. Increases in turbulence Re_{ii} values also led to increases in the RMS of attitude upsets and forces acting on aircraft as well as the pilot inputs. This relationship will be further explored in the tests discussed in the next chapters.

The trials described in this chapter were performed as a proof of concept without any adjustment of the turbulence to represent realistic conditions. The pilot also commented that the resulting turbulence was too uniform or bland. The next chapters will describe further developments and testing focused on improving the realism of the generated turbulence, calibrating the model to reproduce specific conditions and test its applicability to study the impact of turbulence on aircraft handling.

6 Impact of SEM generated turbulence on flight handling qualities.

6.1 Introduction

In the previous chapter, a new turbulence generator for flight simulation was developed and trials were performed to test the feasibility of the concept, demonstrate real-time capability and examine impact on pilot workload. The following chapter describes improvements to the SEM model and the tests performed to better understand how the model affects aircraft handling and pilot workload when changing SEM input parameters and under different flight conditions.

A comment from pilots about the SEM turbulence model in the previous chapter was that the resulting turbulence felt bland and too uniform (see Section 5.3). To improve this, the SEM module was upgraded to work with multiple series of eddies of different strength and size. By mixing large eddies, with high values of Re_{ii} with smaller, low Re_{ii} ones, the resulting turbulence is a mixture of large amplitude low frequency and low amplitude, high frequency disturbances. Adjustments of the relative eddy properties of each series, allows tuning the power spectral density curve of the resulting turbulence.

The upgraded SEM was coupled to a FLIGHTLAB model of a Bell 412 helicopter, which is equipped with SAS in the roll, pitch and heading axis and has improved handling qualities when compared to the Bo 105 used in the preceding chapter. This should allow a better assessment of the impact of the turbulence on aircraft handling and pilot workload during piloted flight simulation trials. To study a wide range of flight conditions, the pilot performed two MTEs: the ADS-33 PH, and a custom S&L flight task at a 40kts low airspeed and 60kts forward flight condition.

This chapter is structured as follows: Section 6.2, describes the multi-scale upgrade to the SEM model to allow for the use of multiple eddy series. Section 6.3. briefly discusses the Bell 412 FLIGHTLAB model and its most relevant handling qualities. Offline simulations performed to assess the impact of the SAS and the impact of the multi–scale SEM on the aircraft are presented in Section 6.4. Section 6.5 describes the subsequent flight simulation trials that were conducted and discusses the results for the

PH task (Section 6.5.2) and the S&L MTE (Section 6.5.3). Finally, a summary of the chapter and results is presented in Section 6.6.

6.2 Upgrade to the SEM turbulence module: Implementation of multi – scale eddies

Pilot feedback from the initial trials of the SEM turbulence model indicated that the nature of the turbulence was too uniform or bland. Real world turbulence is a mixture of large amplitude, low frequency and low amplitude, high frequency disturbances.

To reproduce such conditions, an upgrade to Jarrin's model has been implemented within the flight simulation SEM module to allow the capability to use multiple scales of eddies.

By defining the strength and size for the eddies in each of these series, it is possible to adjust the slope of the resulting turbulence power density with frequency. The applied algorithm is an adaptation of the one described by Luo [114] for using multiple series of eddies to adjust the turbulence PSD output by the SEM. The control volume surrounding the aircraft is populated by N_{Series} different series of eddies. The size and strength of the eddies in each series are given by:

$$\boldsymbol{\sigma^m = q_m * \sigma} \qquad \boldsymbol{A_m = \sqrt{p_m} * A} \qquad \textit{6-1}$$

where q_m and p_m are scaling values relating eddy size and Reynolds Stress tensor to a reference value.

The total number of eddies in each series is selected so that each of them completely fills the control volume:

$$\boldsymbol{N^m = \frac{V_B}{\sigma_x^m * \sigma_y^m * \sigma_z^m}} \qquad \textit{6-2}$$

The main reason for this implementation, rather than using different control volumes with the same number of eddies for each series as described by Luo, is to keep the total number of eddies as low as possible to limit the increase in computational costs. Filling the control volume with the number of eddies given by Eq. 6-2 and placing them using a normal random distribution, will result in eddies overlapping by a length

of about σ in each direction. As a result of this overlap, the number of eddies of each series that each ACP should be exposed to, at any given time, should average to a value of eight (see Figure 6-1).

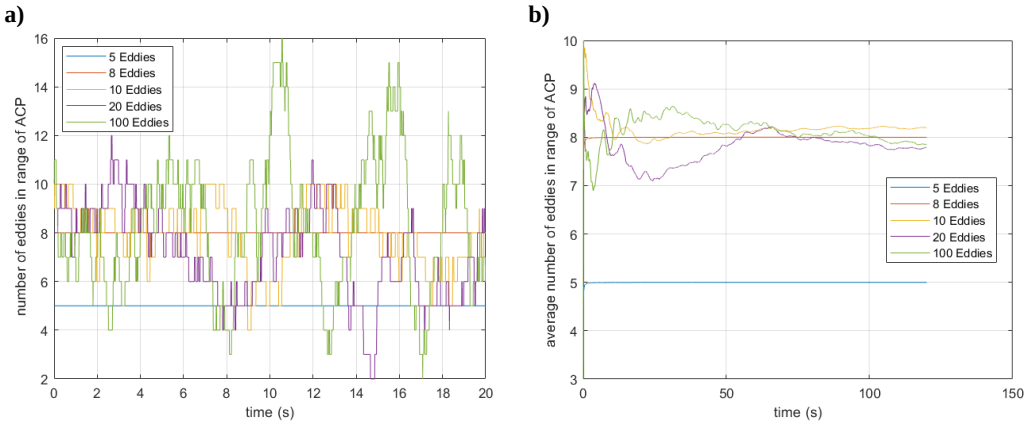

Figure 6-1: a) Number of eddies in range of fuselage ACP, based on the number of eddies for each series, b) time averaged of the number of eddies in range of fuselage ACP

To ensure the same behaviour also for series with very large eddies, an additional larger control volume was used for these series only using 10 eddies, number determined by trial and error, to ensure the control volume was adequately populated.

$$V_B^m = N_{min}^m * \sigma_x^m * \sigma_y^m * \sigma_z^m \qquad 6\text{-}3$$

The resulting turbulence is the sum off the turbulence induced by each of the eddy series:

$$u_i'^{ACP} = \sum_{m=1}^{N_{Series}} \left(\frac{1}{\sqrt{N^m}} \sum_{k=1}^{N_{Eddies}^m} A_{ij}^m \varepsilon_j^k f_{\sigma_m}(x^{ACP} - x^k) \right) \qquad 6\text{-}4$$

and the total turbulence spectra is the total induced for all series:

$$\phi_{ii}(x, \omega) = \sum_{m=1}^{N_{series}} \phi_{ii}^m(x, \omega) \qquad 6\text{-}5$$

The MATLAB code for multi–scale SEM Simulink functions can be found in Appendix - D.

Using multi-scale eddy series offers a new additional option to adjust the induced turbulence spectra. Total induced turbulence is the sum of the turbulence induced by each of the different eddy series (see Figure 6-2). Each individual series presents the

characteristic behaviour and average frequency for its eddy strength and size, including the cumulative time averaged values of induced velocities, skewness, flatness and Reynolds stresses. Time averaged Reynolds stresses of total induced turbulence will tend to the sum of Reynolds stresses induced by each individual series (see Figure 6-3).

Figure 6-4 shows power spectral density of induced vertical turbulence for three different eddy distributions (see Table 6-1). Total turbulence in all the cases results in the same total values of $Re_{ii} = 3\ m^2/s^2$. For simplicity and as a case study, values of Re_{ii}^{m} for each series have been chosen to be proportional to σ^m. The resulting turbulence spectra show a shift of power density towards lower frequencies and a slower fall in power density with increased frequencies. Adjustment of the number of eddy series and the relationship between eddy size and strength should allow adjusting the slope of the turbulence spectra to better match real world conditions.

Table 6-1: Summary of Turbulence parameters tested in Figure 6-2, Figure 6-4 and Figure 6-3 (effect of multi – scale SEM)

Case	Shape	k	No of Series	Re^m_{ii} (m^2/s^2)	σ^m (m)
1 Series	Tent	4,5	1	3	3
2 Series	Gauss	4,5	2	1 , 2	3 , 6
3 Series	Gauss	4,5	3	0.5 , 1 , 1.5	3 , 6 , 9

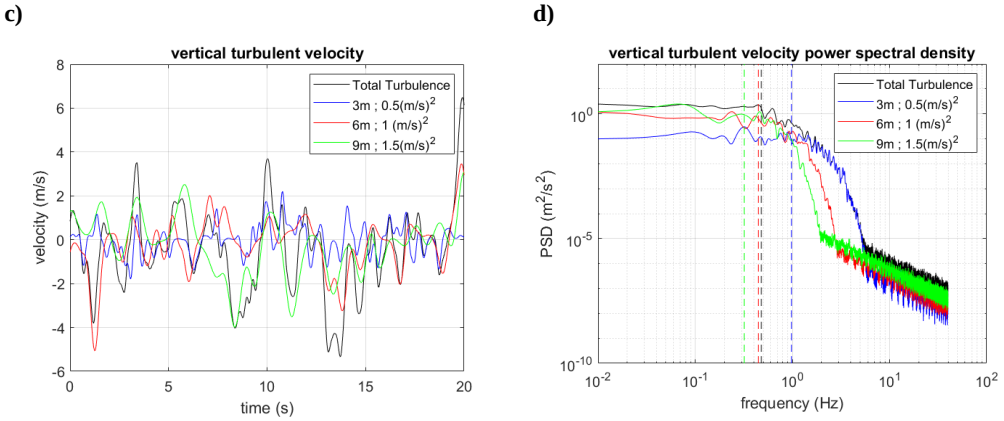

Figure 6-2: Turbulence induced by each of the eddy series and total sum: a) Time history, b) Power spectral density. Vertical dashed lines indicate PSD averaged frequency.

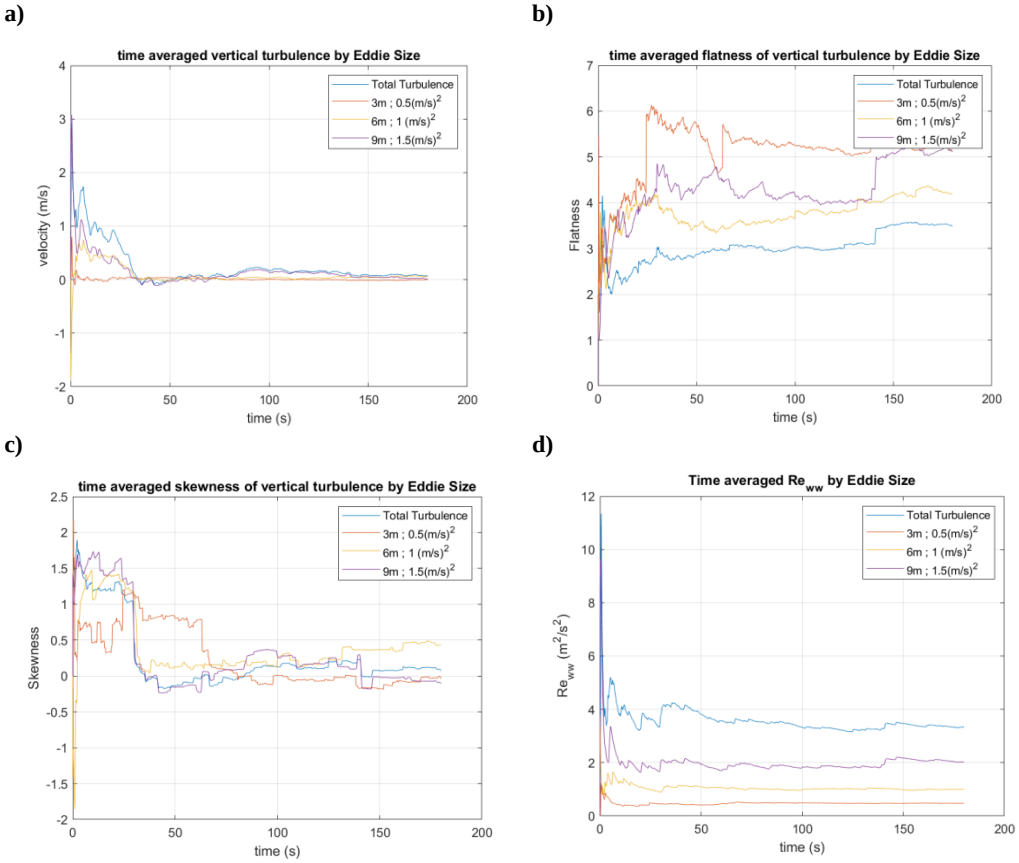

Figure 6-3: Cumulative time averaged values on fuselage ACP of: a) turbulent velocity components, b) Reynolds stresses, c) flatness and d) skewness for each eddy series and of total induced turbulence.

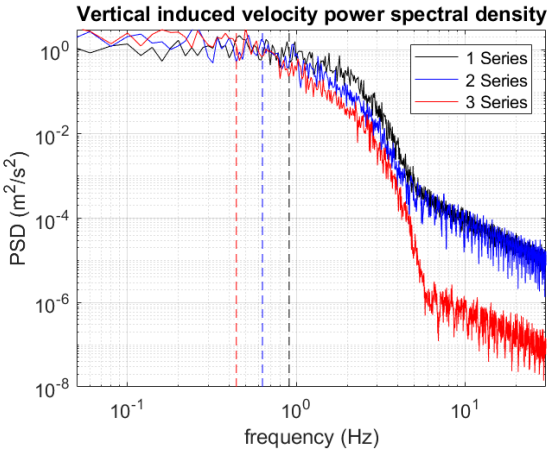

Figure 6-4: Power spectral density of induced turbulence for three different distributions of eddy size and strength. Vertical dashed lines indicate PSD averaged frequency.

6.3 Bell 412 Aircraft model – handling qualities.

The lack of a SAS, combined with strong inter-axis–couplings in the Bo 105 model used for the trials in the previous chapter, made it difficult to discern the impact of the turbulence from the aircraft's own responses to pilot inputs. For further flight

simulation testing, the SEM turbulence model was coupled to the University of Liverpool's Bell 412 FLIGHTLAB model [110] based on the Advanced Systems Research Aircraft (ASRA) operated by the National Research Council (NRC) of Canada [115]. The model includes a variable stability control system that can be configured as rate damping or rate command attitude hold (RCAH) in roll, pitch and yaw or as attitude command attitude hold in roll and pitch but lacks any augmentation in the heave axis.

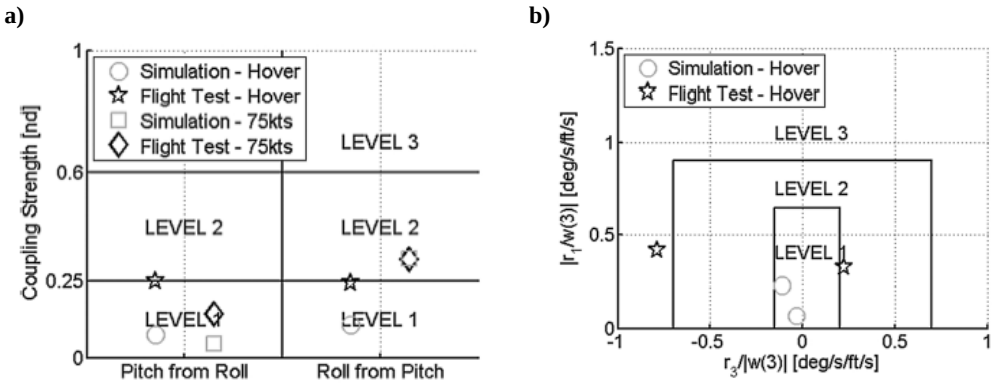

Figure 6-5: Bell 412 model cross couplings evaluated against ADS-33 criteria: a) pitch – roll couplings (3.3.9.1 and 3.4.5.2), b) collective – yaw couplings (3.3.9.2 and 3.4.5.3). [110]

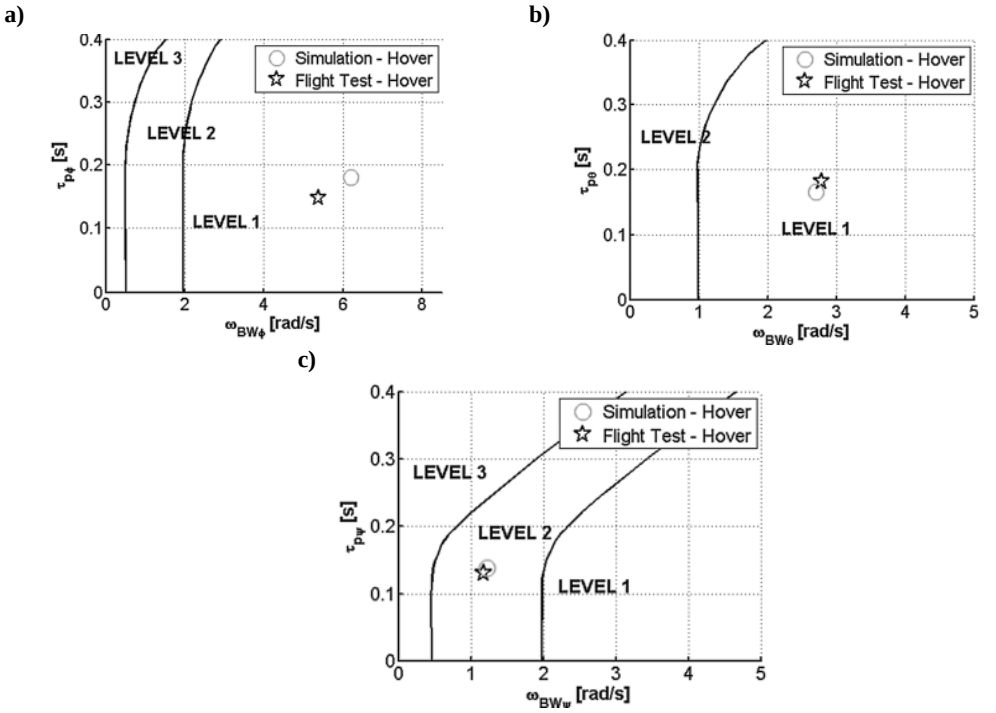

Figure 6-6: Bell 412 model control bandwidth limits evaluated against ADS-33 criteria (3.3.2.1): a) roll, b) pitch, c) yaw. [110]

Compared with Bo 105, the Bell 412 model presents improved handling qualities evaluated against ADS - 33 criteria. This is seen in reduced control cross couplings (Figure 6-5), achieving Level 1 pitch – roll and collective to yaw couplings in hover (3.3.9.1 and 3.3.9.2) and Level 2 during forward flight (3.4.5.2 and 3.4.5.3). While lower than the Bo 105, the Bell 412 has high bandwidth in hover (3.3.2.1), achieving Level 1 for roll and pitch and Level 2 for yaw (Figure 6-6). The main deficiency of the model is its Level 3 longitudinal stability during hover (Figure 6-7), when assessed against the ADS-33 criteria for divided attention (3.3.2.3 and 3.4.1.2) an aspect that negatively affects the ease of the precision hover task.

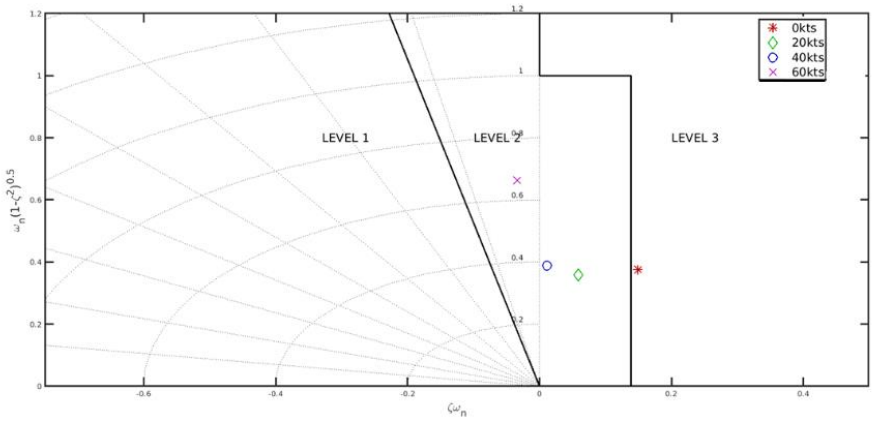

Figure 6-7: Bell 412 model longitudinal stability – phugoid mode, evaluated against ADS-33 criteria for divided attention operations in hover (3.3.2.3) and forward flight (3.4.1.2).

6.4 Offline simulation – Bell 412, SCAS system response and effect of multi–scale SEM

In preparation for piloted simulation tests, offline analysis of the aircraft response to the SEM induced turbulence was performed. The SCAS system was configured in RCAH mode allowing for offline simulations to be performed with aircraft displacement and rotations in all axes allowed, except for the vertical axis to prevent collision with the ground. Simulations presented in this chapter focus on the response of the SCAS system and how the aircraft responds to changes in eddy shape and size and to the use of multi-scale turbulence. All simulations correspond to the aircraft in hover under a 10 kts wind with a 90 deg azimuth from the right (see Table 6-2). Wind velocity was lowered with respect to the previous simulations in order to reduce the probability of the aircraft achieving unrealistic attitudes when aircraft positions and attitudes are allowed to change. Displacements in the vertical axis were left frozen to avoid the aircraft colliding with the ground.

Figure 6-8 shows PSD plots of aircraft roll, pitch and yaw moments in hover, comparing the response to SEM induced turbulence for different aircraft conditions: when the aircraft stability system is deactivated and aircraft movement and rotations in all axes are fixed, and when the stability system is configured for RCAH and free displacement is allowed in all axes except heave. The response to conditions in a uniform wind without turbulence is added for reference. For the SCAS free system and frozen aircraft states, the induced moments follow a similar behaviour to the Bo 105 helicopter model with disturbances being strongest for frequencies up to 1Hz, with pitch response presenting a peak at around 0.3Hz – 0.5Hz. The amplitudes of moment coefficients decay sharply for higher frequencies, but present peaks at multiples of four times the main rotor frequency. As discussed in Section 5.2.5 high frequency data for the rotor and aircraft response PSDs are affected by the frequency leakage caused by truncation of a finite time signal.

Figure 6-8 also shows that the SCAS system is capable of counteracting turbulence induced moments in the low frequency (below 0.5Hz) domain for all three axes, especially in the longitudinal and lateral axes, resulting in an overall decrease in the amplitude of induced disturbances. Above 0.5Hz this reduction becomes less noticeable, resulting in an overall shift of disturbances towards higher frequencies and the appearance of peaks in roll and pitch disturbances at around 1Hz and 0.5Hz. These frequencies are near to the Bell 412 longitudinal and lateral control bandwidth limits in attitude command and attitude hold configuration as discussed in Section 6.3 [110]. The resulting aircraft response can be seen in Figure 6-9, which shows aircraft attitudes in all three axes in the presence of turbulence, showing that the SCAS system reduces roll and pitch attitude deviations, but is not capable of reducing the large yaw deviations.

Table 6-2: Offline simulations performed for the Bell 412

Case	Shape	k	Re_{ii} (m^2/s^2)	σ (m)	SCAS	Mov
1	--	--	0	--	RCAH	free
2	Gauss	4.5	1	3	OFF	frozen
3	Gauss	4.5	3	3	RCAH	free
4	Gauss	9	3	3	RCAH	free
5	Tent	--	3	3	RCAH	free
6	Gauss	4.5	3	6	RCAH	free
7	Gauss	4.5	3	9	RCAH	free
8	Gauss	4.5	[3 , 6]	[3 , 6]	RCAH	free
9	Gauss	4.5	[0.5 , 1 , 1.5]	[3 , 6 , 9]	RCAH	free

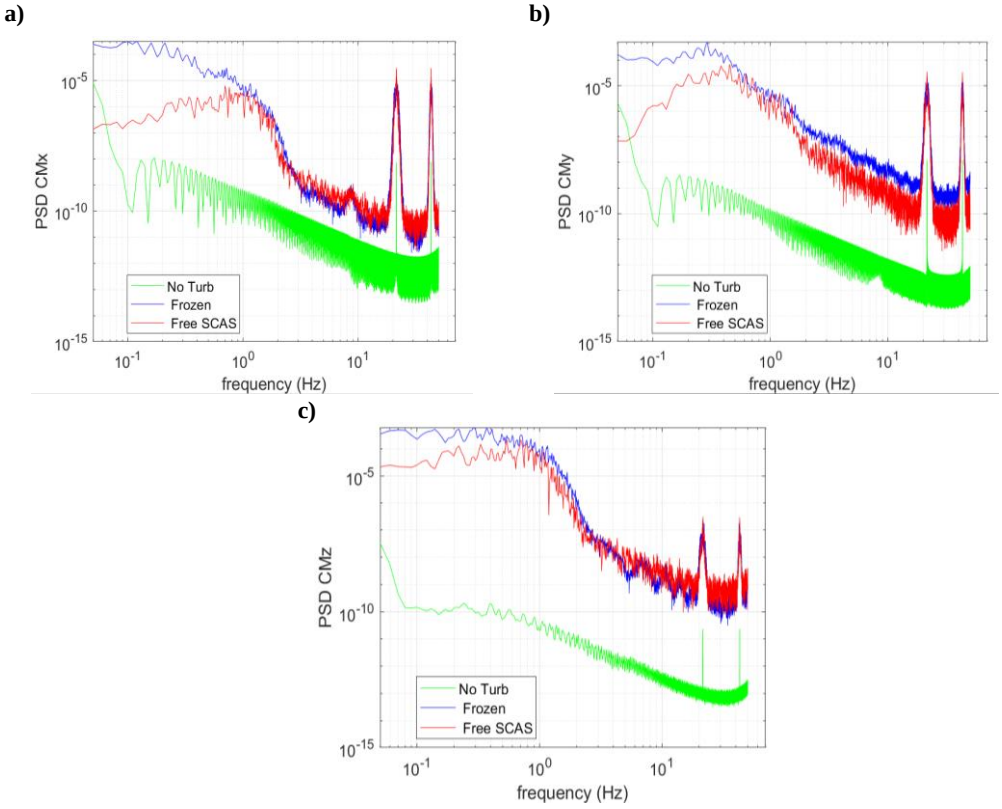

Figure 6-8: Comparison aircraft moment coefficients in hover under uniform wind and SEM generated turbulence in a) roll, b) pitch and c) yaw. Cases include: hover without turbulence, frozen aircraft under turbulence, unfrozen aircraft with stability system activated and configured as RCAH.

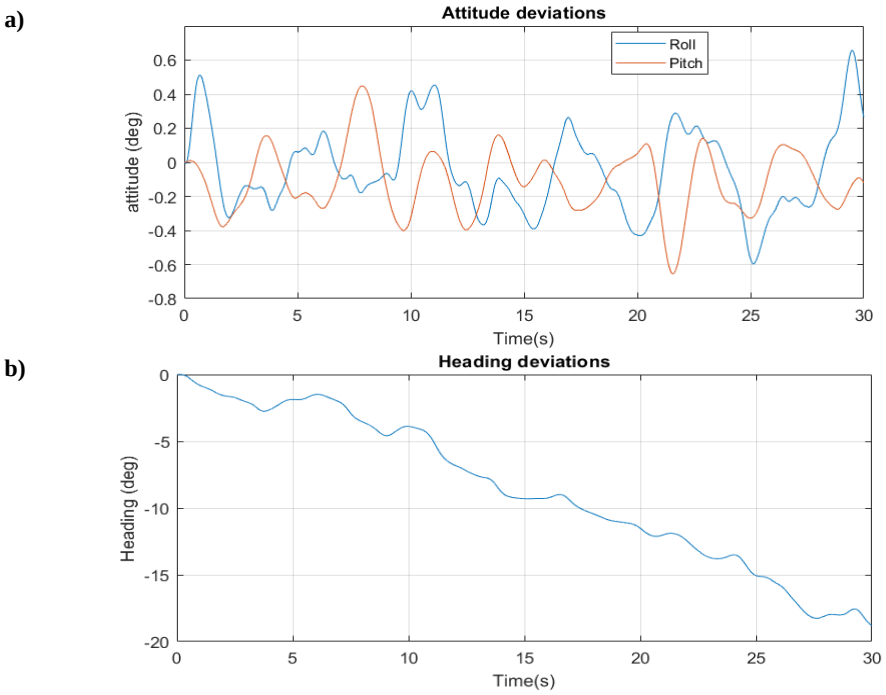

Figure 6-9: Attitude deviations in a) roll and pitch, b) heading, for the first 30s under turbulence with ReSt = 3 m^2/s^2 , eddy size = 3m and k = 4.5

A better insight into the response of the SCAS can be gained from Figure 6-10, which presents PSD plots of main rotor longitudinal and lateral pitch and tail rotor collective pitch under conditions of no turbulence and two different turbulence intensities. Given that no pilot model is used, changes in rotor blade pitch are mainly due to the commands from the SCAS system. As can be seen, the SCAS responds mainly to low frequency disturbances with the response in frequencies above 0.5Hz no longer scaling with turbulence intensity. SCAS input power density decays rapidly for frequencies higher than 1Hz in line with the behaviour of induced turbulence and induced moments.

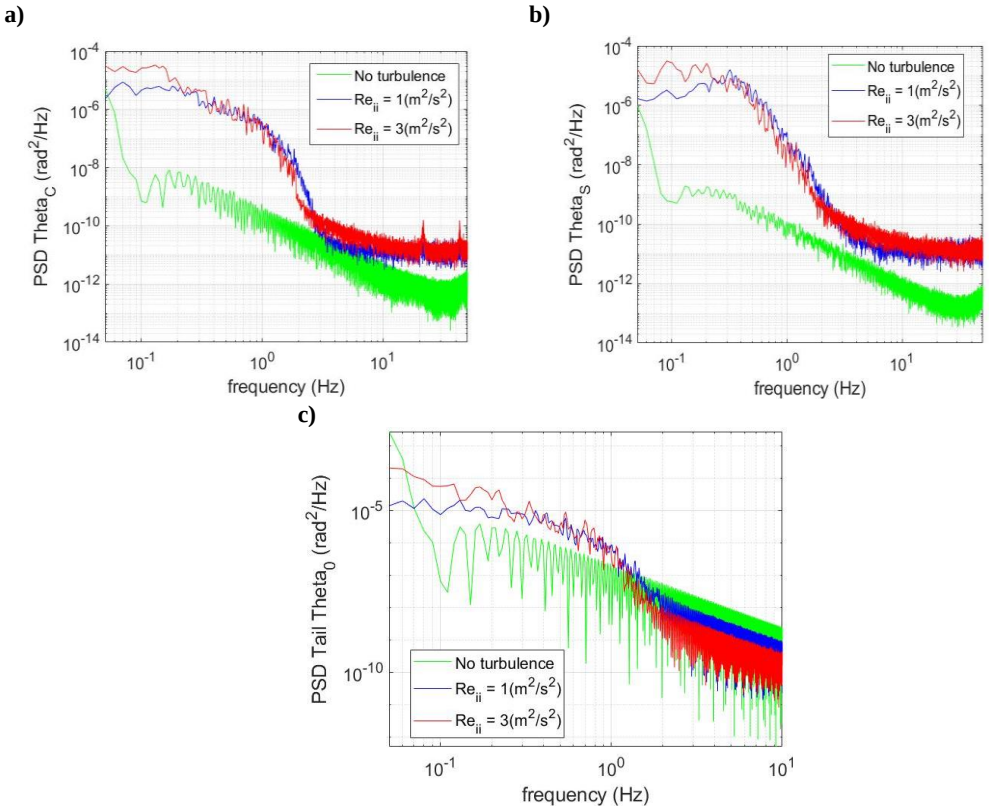

Figure 6-10: Power spectral density of main rotor and tail rotor actuators: a) lateral pitch, b) longitudinal pitch, c) tail rotor collective pitch. Given lack of pilot model, blade response is mainly due to SCAS system commands.

The aircraft response to turbulence resulting from different eddy shapes is shown in Figure 6-11. Amplitude of low frequency disturbances does not seem to be significantly affected by eddy shape, probably as a result of SCAS activity. Differences start to appear in the frequency range between 0.5Hz and 1Hz where induced moments follow a similar shape as the induced turbulence (see Figure 5-8). The effect is most noticeable in the lateral axis, where the higher amplitude of induced turbulence around 1Hz for a value of $k = 9$ (see Eq. 5-20) results in an increase in the amplitude of the aircrafts response. Figure 6-12 shows the effect of differences in eddy

size and of including multiple eddy series of different size. The figures correspond to cases 3, 6, 7, 8 and 9 of Table 6-2. Increasing eddy size decreases the frequency after which power density of disturbances starts to rapidly decay, in line with the behaviour of turbulent flow, resulting in lower average frequencies for induced disturbances. The aircraft's response to multi-scale SEM turbulence presents an intermediate situation that results in turbulence induced disturbances across a wider frequency spectrum than under a single eddy size, despite the total induced turbulence intensity being of the same value. This presents an interesting condition for testing, because while there is evidence that low frequency, large amplitude turbulence has greater effects on pilot workload [85], the Bell 412's SCAS system seems to be better able to mitigate them leaving the high frequency disturbances almost intact.

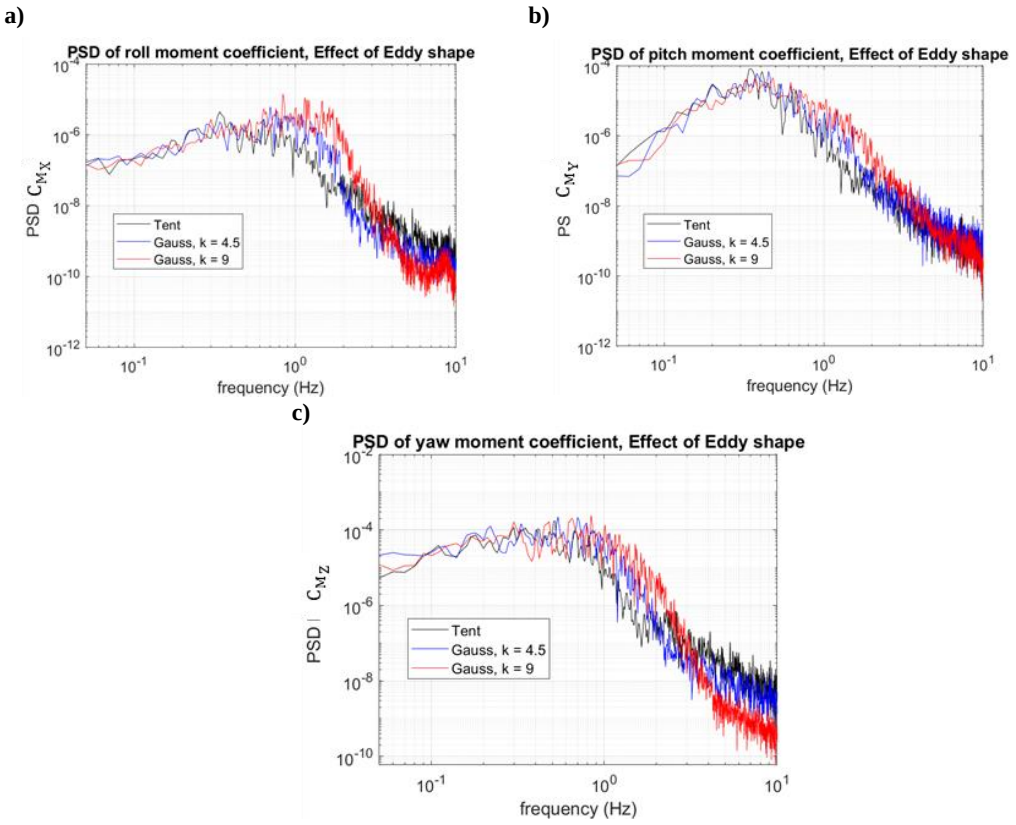

Figure 6-11: Effect of eddy shape on turbulence induced aircraft moments in a) roll, b) pitch, c) yaw.

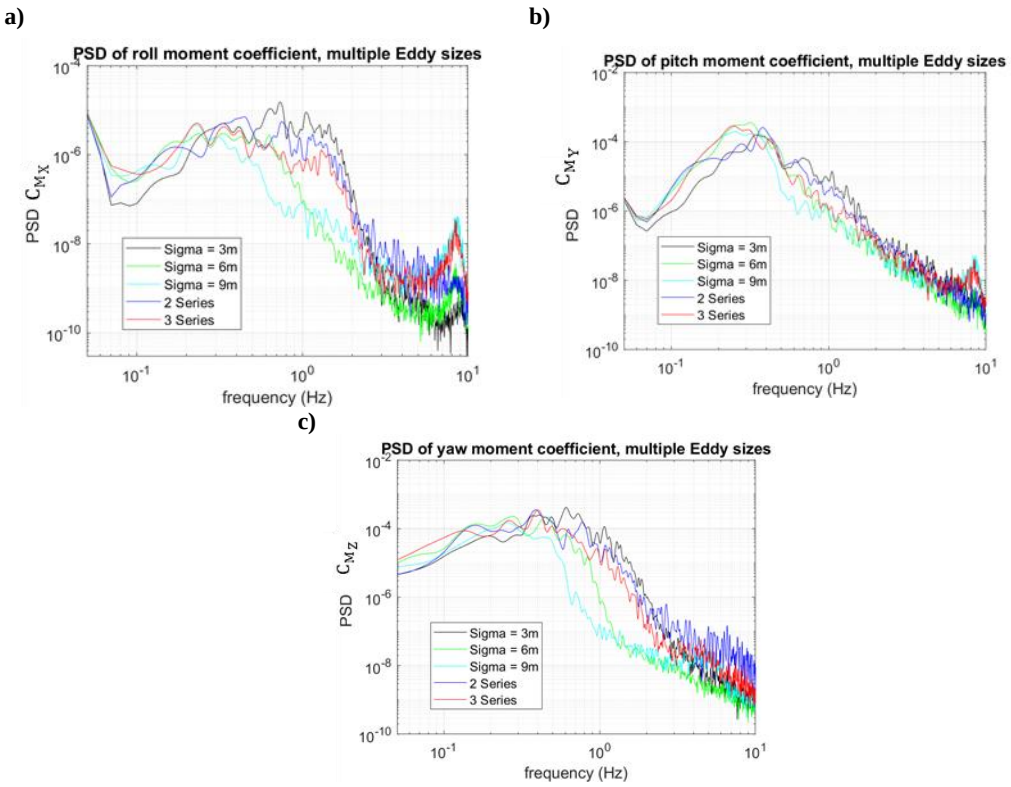

Figure 6-12: Effect of eddy size and multiple eddy sizes on turbulence induced aircraft moments in a) roll, b) pitch, c) yaw.

6.5 Flight simulation testing of Bell 412 and SEM turbulence model:

Initial flight simulation testing of the SEM model reported in Section 5.3 has shown that the current implementation of the SEM model is capable of working in real-time for piloted flight simulation and of generating turbulence that affects pilot workload and task performance. The tests also suggested a relationship between turbulence intensity, RMS of moments and forces on rotorcraft, oscillations in aircraft attitude rates, pilot activity and resulting pilot workload ratings. This is investigated further for multi-scale eddies.

6.5.1 Objectives and methods:

A comprehensive test campaign was performed, using the Bell 412 helicopter model which has improved handling qualities (see Section 6.3), especially in regards to reduced inter-axis coupling of the airframe. The availability of a SCAS made it easier to discern the impact of the turbulence in handling and pilot workload. The motion platform was activated and using a custom motion setup, optimized by Memon for conditions of turbulence as described in [116]. A wide range of flight conditions was

explored to search for limits imposed by the SEM turbulence generator, the aircraft handling qualities or the simulator motion limits.

Tests were flown by an experienced former Royal Air Force test pilot, with experience in the Bell 412 and helicopter operations in support of offshore wind energy.

The pilot performed a precision hover task as defined in ADS-33 [21] (see Figure 6-13 and Table 6-3) to assess how different adjustments of the SEM induced turbulence affects aircraft handling, pilot response and workload. The impact of turbulence at different flight speeds was tested using a newly defined steady and level flight task.

The objectives of the test were the following:

- **Identifying turbulence intensity limits at which aircraft handling or motion based flight simulation is still feasible and identify a suitable value to test other parameters:**
  The pilot was tasked to perform the precision hover task starting from conditions of no turbulence, the value of Reynolds stresses were gradually increased uniformly in all directions to Re_{ii} = 1 m^2/s^2, Re_{ii} = 3 m^2/s^2 and Re_{ii} = 6 m^2/s^2. While keeping the size of the eddies constant at $\sigma_i = 3m$ in all directions. The value of Re_{ii} = 3 m^2/s^2, was chosen to test changes in all other turbulence parameters. At this level, the pilot awarded handling qualities and workload ratings of 4, up from 3 under no turbulence. Which allowed margin in both directions when assessing the impact of other parameters.
- **Assess effects of changing the size of the eddies and using multi – scale eddy series to generate the turbulence:**
  Starting at $\sigma_i = 3\,m$, eddy sizes were increased uniformly in all directions to $\sigma_i = 6\,m$ and to $\sigma_i = 9\,m$. Then combinations of eddy series with these sizes were tried. Values of R_{ii} were scaled with σ_i, while keeping the sum always at Re_{ii} = 3 m^2/s^2.
- **Assess impact of turbulence for different flight conditions:**
  This was examined by performing a custom defined steady and level flight task at 40kts and 60kts under the same turbulence conditions as the hover task.
- **Obtain subjective pilot opinion on the realism of the turbulence model:**
  Pilot feedback was sought during debrief regarding how similar the turbulence and their response to the upsets felt when compared to previous flight experience.

All testing was performed under a 20kts, 90deg azimuth green wind; the wind speed is typical for wind turbine working conditions. The aircraft SCAS system was configured for RCAH in all cases. All runs were performed under isotropic, uniform turbulence conditions with turbulence intensity and eddy size equal for all three axes:

$$\begin{gathered} Re_{xx} = Re_{yy} = Re_{zz} = Re_{ii} \\ Re_{ij} = 0 \; for \; i \neq j \\ \sigma_x = \sigma_y = \sigma_z = \sigma_i \end{gathered} \qquad 6\text{-}6$$

Aircraft dynamics and pilot inputs were recorded and subjective data gathered using the Bedford Workload [107] (BWR) and Cooper Harper Handling Qualities rating scales [117] (HQR) respectively. Additional pilot feedback and comments were also obtained during briefing, test and de-briefing.

Ratings were awarded based on the most demanding segment of the task, which for the hover task, unless otherwise indicated, was the station keeping segment. HQRs were awarded based on achieved task performance, and the accompanying level of pilot compensation required for the task. BWR were based on the pilot's perception of whether they would be able to attempt additional tasks or respond to unexpected events while focused on the main task.

Recorded aircraft parameters and pilot control inputs were analysed with the aim to better understand the impact of turbulence on task performance and pilot workload. The relation between RMS of aircraft upsets and pilot inputs within the 0.1 Hz – 2 Hz range were discussed in the previous chapter as potential workload correlations and are further explored here.

Changes in the size of eddies and the use of multi-scale series of eddies result in changes in the PSD curve of the induced turbulence and resulting disturbances and might lead to changes in pilot control response. It is usual to distinguish between pilot control inputs intended for aircraft navigation, which tend to be of lower frequency and large amplitude from those intended to stabilize the aircraft against external or internal disturbances and which tend to be high frequency inputs of smaller amplitude [118]. Tasks such as the PH MTE, which require accurate positioning of the aircraft, tend to be stabilization dominated tasks. Increases in the frequency or amplitude of stabilization inputs, tend to lead to workload increases reported by the pilot. The use of an RMS analysis might obscure this impact by reducing the entire response in the

0.1 – 2 Hz frequency range to a single parameter. Analysis of the PSD, from which RMS values are derived, is often used in the study and characterization of random phenomena such as turbulence. For this reason, it has also been applied throughout this chapter to study the behaviour of pilot inputs in the frequency domain when responding to the resulting disturbance.

6.5.2 Results - Precision Hover Mission Task Element (MTE)

6.5.2.1 Precision Hover MTE definition:

In this series of tests, the PH MTE was performed as defined in ADS-33, using the desired and adequate performance limits defined for cargo/utility rotorcraft in a good visual environment (Table 6-3). This MTE starts with the aircraft in hover at a distance to a target point oriented 45deg relative to the aircraft's heading (Figure 6-13). The pilot was tasked to perform the following:

- Approach the target point at a ground speed of between 6kts and 10kts and transition to hover in a single smooth manoeuvre. The deceleration manoeuvre should be completed within the desired or adequate time limits indicated in Table 6-3.
- Notify when the deceleration manoeuvre starts and then again when a stabilized hover has been achieved.
- Maintain a stabilized hover over the designated point for at least 30s, or longer should you deem it necessary to provide an HQ evaluation. Maintain deviations in aircraft position, altitude and heading within desired or adequate limits indicated in Table 6-3.

Table 6-3: Desired and adequate limits for the precision hover task.

Parameter	Desired	Adequate
Once the transition to hover has been initiated: attain a stabilized hover before:	5 sec	8 sec
Maintain horizontal position within:	± 3 ft	± 6 ft
Maintain vertical position within:	± 2 ft	± 4 ft
Maintain heading within:	± 5 deg	± 10 deg

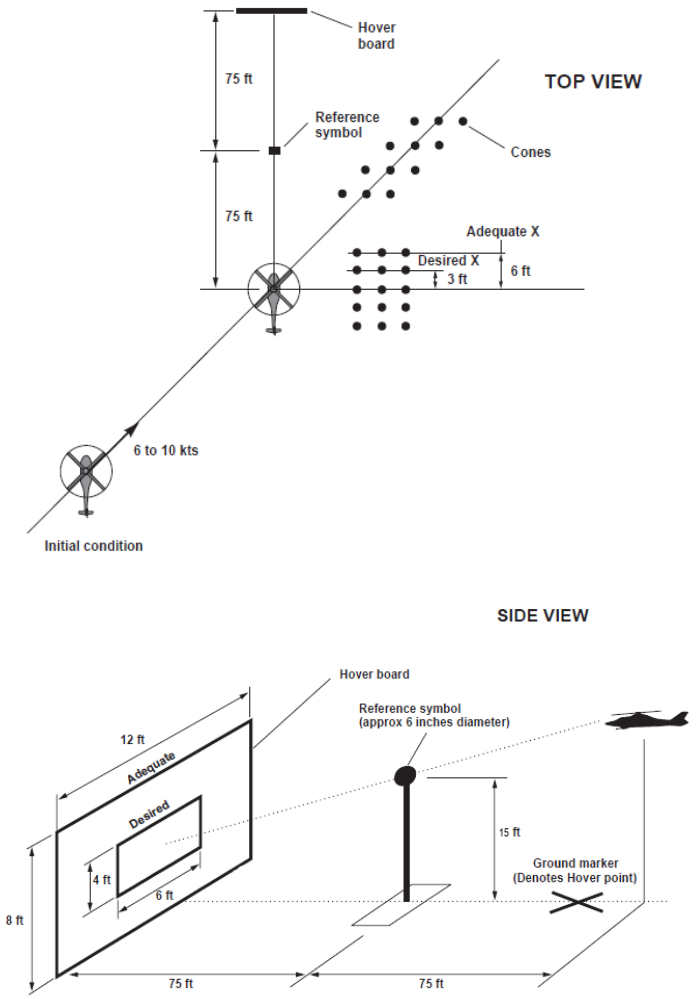

Figure 6-13: Schematic of Precision Hover test course and visual cues

6.5.2.2 Runs performed and pilot ratings:

Table 6-4 reports the performed runs for the hover task, turbulence parameters and pilot ratings for each run. In the first run the pilot flew freely until they could familiarize themselves with the flight simulator, controls and aircraft model. In the second run the pilot performed the task under a 20kts uniform wind without any turbulence. The pilot awarded a BWR and an HQR of 3, indicating some mild deficiencies in handling requiring minimal pilot compensation and allowing sufficient spare workload for additional tasks. According to their comments, roll and pitch control were the main drivers of workload when performing the task under conditions of no turbulence.

Table 6-4: Hover MTE simulation runs performed.

Run		Total Re_{ii} (m^2/s^2)	No of eddy scales	Re_{ii} (m^2/s^2) for each scale	σ (m) for each scale		Stabilization time (s)	HQR	BWR	
1		0	-	-	-		-	-	-	
2		0	-	-	-		0	3	3	
3		1	1	[1]	3		13	3	3	
4		3	1	[1]	3		7	4	4	
5		3	1	[1]	6		0	5	6	
6		6	1	[1]	3		6	5	6	
7		3	1	[1]	9		4	6	7	
8		3	2	[1,2]	[3,6]		5	5	6	
9		3	2	[0.5,1.5]	[3,9]		8	5	5	
10		3	3	[0.5,1,1.5]	[1,3,9]		5	6	6	
11		6	1	1	6		Not recorded	6	7	

6.5.2.3 Effect of turbulence and increases in Reynolds stress magnitude

The presence of turbulence results in handling deteriorations and an increase in workload which become larger under increasing levels of turbulence intensity. HQRs and BWR for different turbulence intensities are shown in Figure 6-14. All runs discussed in this chapter were conducted with the same eddy size of $\sigma_i = 3m$. The effects range from minimal for the lowest turbulence intensity tested, $Re_{ii} = 1\ m^2/s^2$, where the pilot awarded the same handling qualities and workload ratings of 3 as the case without turbulence, up to Level 2 ratings of 5 in HQR and 6 in BWR, indicating a need for considerable pilot compensation and leaving little to no spare capacity for additional tasks.

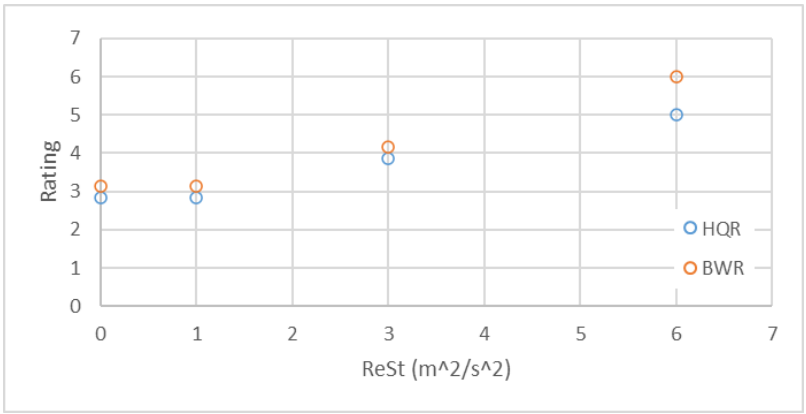

Figure 6-14: HQRs and BWRs for different magnitudes of Reynolds stresses.

According to the pilot, when flying under turbulence, control in the vertical axis was the main driver for workload increases, followed by heading due to the resulting cross couplings. In the run under the highest turbulence intensity (Run 6, Re_{ii} = 6 m^2/s^2), the pilot indicated that lateral control required most of their effort, followed by heave and yaw. Their comments suggest that vertical turbulence was probably too high for the low altitude setting of the precision hover MTE, although it might be more realistic in situations farther away from the ground like wind turbine servicing or hovering near cliffs. It is also worth mentioning that the aircraft lacks any stability augmentation in heave, leaving the task of counteracting vertical disturbances entirely to the pilot. The impact of turbulence was more strongly felt during the hover phase, which on its own is more stabilization focused than the guidance focused translation phase.

Figure 6-15 a) shows aircraft ground track during approach to the hover point, Figure 6-15 b) shows approach rate to the hover point during the entire run (derivative of distance to the hover point with time) and c) shows altitude deviation from hover point during the entire run. Dashed lines are used for the approach phase, dotted lines indicate stabilization over the hover point and continuous lines for the station keeping segment. Magenta and cyan dashed lines indicate adequate and desired limits on deviations from target during hover. The figures show that the pilot was able to maintain course and approach rate with ease, with little deviations along the ground track and only slight oscillations in the approach rate during Run 6 with the highest turbulence intensity of Re_{ii} = 6 m^2/s^2. The case is different when comparing altitude deviations. The pilot started the MTE slightly above the hover point and in all cases starts the approach with a slight climb which he corrects once near the hover point. This climb and the altitude oscillations during the approach become greater with increases in turbulence intensity, confirming pilot comments that put heave control as being the main driver of additional workload.

A smaller effect of the turbulence during the translation phase is consistent with previous findings [119] and again might be a combination of the aircraft being less susceptible to disturbances during forward flight and that there are no requirements set for the translation phase of the hover MTE other than reaching the hover point in a single smooth manoeuvre.

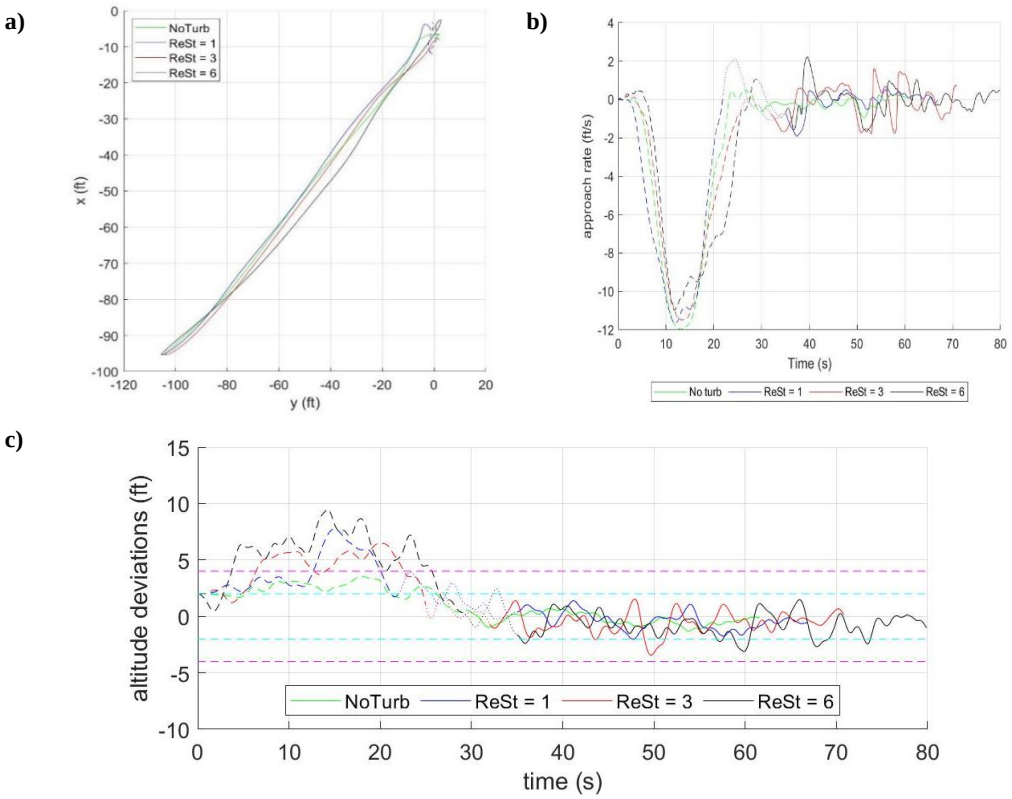

Figure 6-15: Approach to hover point: a) Ground track, b) approach rate to hover point during the entire run, c) altitude deviations from hover altitude during the entire run. Approach, stabilization and hover phase are indicated in b) and c) by dashed, dotted and continuous lines respectively.

Figure 6-16 and Figure 6-17 show the performance achieved during the hover phase (continuous lines) of the MTE and depict deviations in aircraft altitude, heading and ground position against ADS-33 defined adequate and desired performance boundaries. When flying without turbulence, the pilot shows no difficulty in keeping deviations within the desired boundaries. Under conditions of turbulence, amplitude of upsets increases and performance worsens, although deviations are kept within adequate limits most of the time. A rightward shift in heading towards incoming wind (Figure 6-16 a) and b)) and larger oscillations in altitude (Figure 6-16 a) and c)) can be appreciated, although there seems to be a limited effect from increases in turbulence intensity. By contrast, deviations in longitudinal position (Figure 6-17 a) and b)) seem to be affected by the intensity of the turbulence, with adequate boundaries being exceeded in Run 6 under a turbulence of Re_{ii} = 6 m^2/s^2 and deviations in lateral position increasing suddenly for this same run (Figure 6-17 a) and c)).

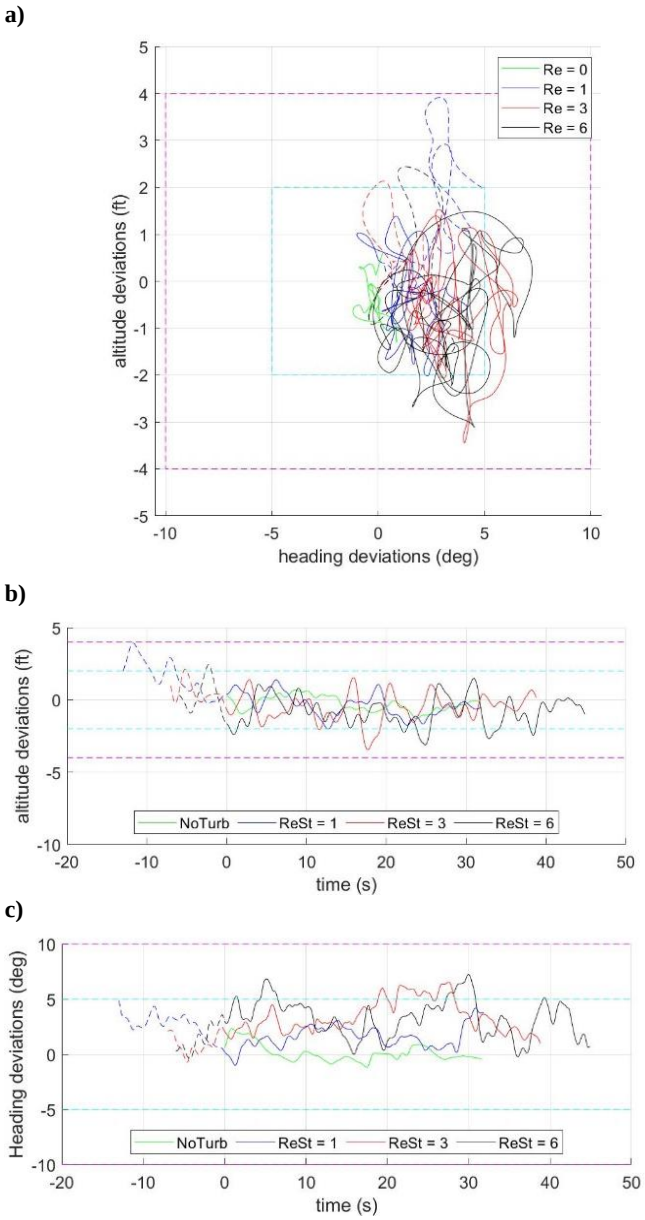

Figure 6-16: Altitude and heading deviations during the hover task for runs 2, 3, 5 and 6. Effect of eddy strength. Dashed lines indicate stabilization phase when applicable. Cyan and magenta dashed lines indicate desired and adequate boundaries. For time plots, 0 is moment when pilot declares aircraft to be stabilized.

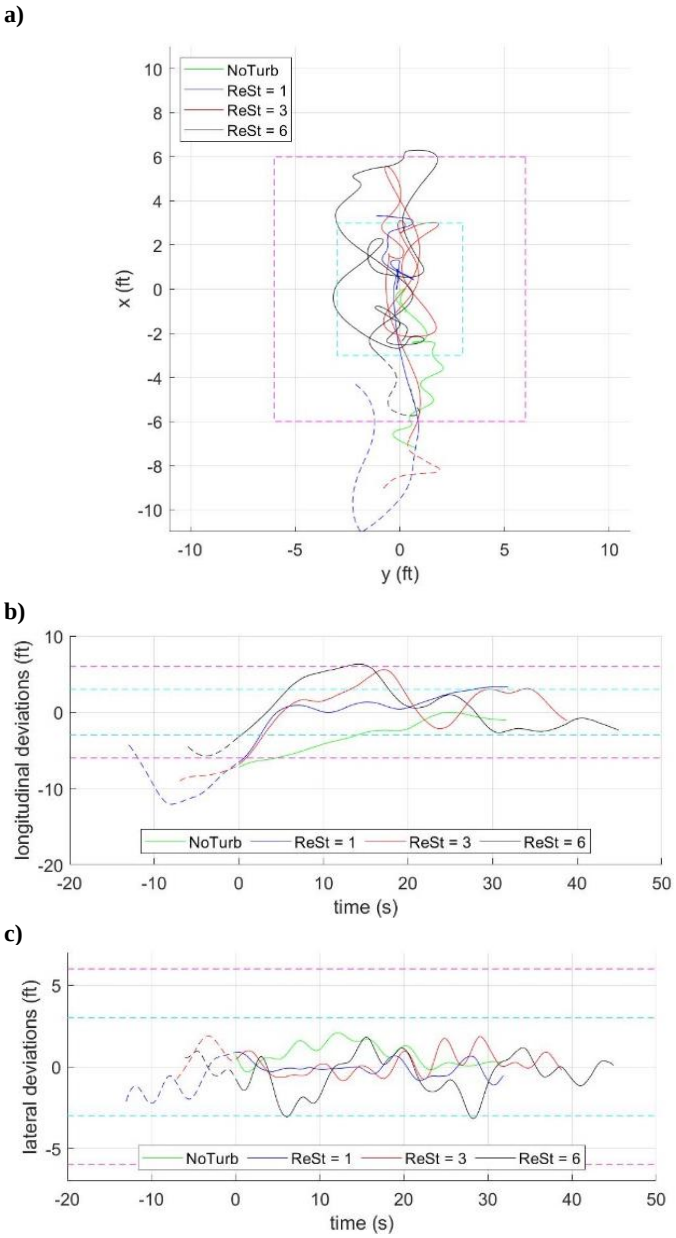

Figure 6-17: Longitudinal and lateral deviations during the hover task for runs 2, 3, 5 and 6. Effect of eddy strength. Dashed lines indicate stabilization phase when applicable. Cyan and magenta dashed lines indicate desired and adequate boundaries. For time plots, 0 is moment when pilot declares aircraft to be stabilized.

Power spectral density plots of pilot inputs during translation and hover are shown in Figure 6-18 and Figure 6-19 respectively. A shift in control activity can also be appreciated between the two MTE phases of translation to the hover point and station keeping or hover. During the run without any turbulence, the translation requires inputs in all axes (Figure 6-18), whilst the hover phase seems to put demands mainly in lateral control (Figure 6-19 a) due to the lateral wind, with amplitude of inputs in all other axes decreasing. There is also a shift towards a higher input frequency, signalling a shift from guidance actions toward stabilization, the exception to this is the lateral axis, probably due to the need to counteract the uniform lateral wind.

The inclusion of turbulence leads to a clear increase in the amplitude of pilot inputs in all axes with increasing levels of turbulence intensity. The large amplitude increase in stick inputs during the translation phase for the lowest turbulence case (run 3, Re_{ii} = 1 m^2/s^2) stands out immediately, but this seems to be an outlier and might be because the pilot still needed to familiarize themselves with the turbulence and resulting aircraft response and the effect seems to subside once the aircraft reaches the hover phase (Figure 6-19).

Turbulence of intermediate intensity (run 4, Re_{ii} = 3 m^2/s^2) seems to have less effect during the translation phase, requiring some stabilization effort in heave (Figure 6-18 c) and larger pedal inputs (Figure 6-18 d) than the case without turbulence. However, there is a strong effect during the hover phase, with all axis requiring inputs of increasing amplitude. This increase in amplitude happens mainly in the 0Hz – 0.25Hz range for most axes. But collective inputs cover a wider frequency range between 0Hz to 0.6Hz already under conditions of no turbulence and the amplitude of pilot inputs grows across this entire range. This supports pilot comments that under the influence of turbulence, the nature of the station keeping phase changes with pilot's effort shifting from stabilizing the aircraft in the longitudinal and lateral axis to the heave and heading axes.

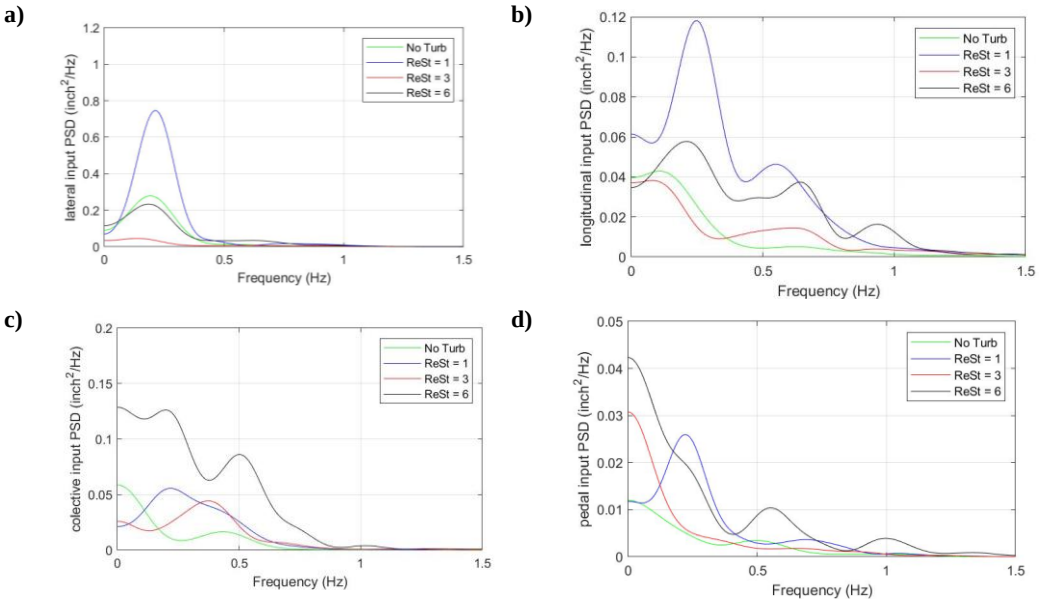

Figure 6-18: Power spectral density of pilot inputs during translation to hover point: in a) lateral, b) longitudinal, c) collective, d) pedal.

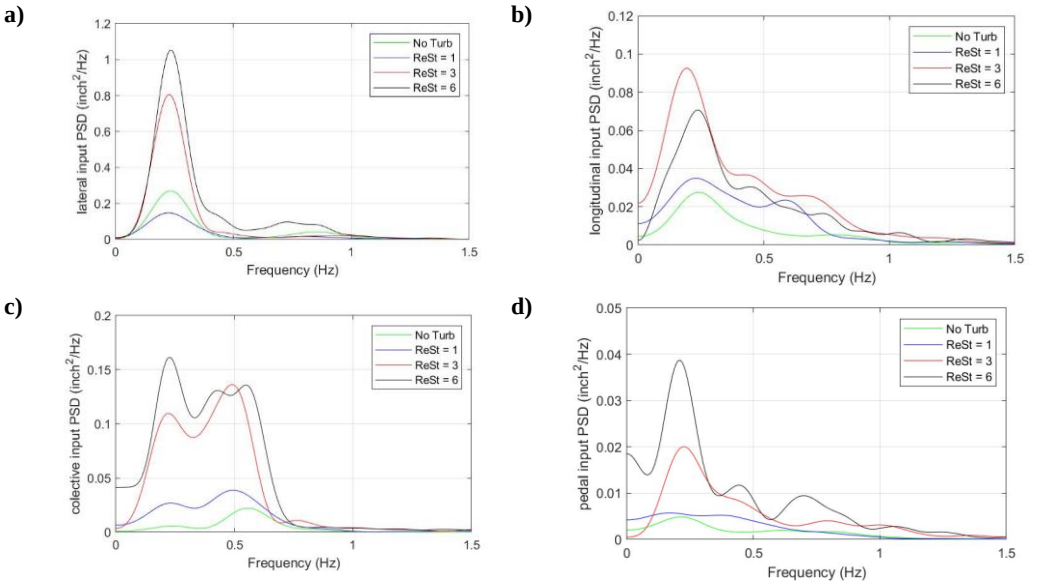

Figure 6-19: Power spectral density of pilot inputs during station keeping over hover point: in a) lateral, b) longitudinal, c) collective, d) pedal.

When flying under the highest turbulence intensity (run 6, Re_{ii} = 6 m^2/s^2), the effect in hover is similar to the previous case, however longitudinal and collective inputs during the translation phase cover a wider range of frequencies, again pointing towards a larger stabilization effort from the pilot.

The stabilization phase of the task was identified during the tests by the pilot announcing when the aircraft had reached the hover point. The time required to stabilize the aircraft over the hover point was measured from the voice recordings taken during the test and varies significantly by case. With the exception of a 13s long stabilization period for run 3 (Re_{ii} = 1 m^2/s^2) which again seems to be an outlier, stabilization was usually achieved within the adequate time limits and was reached immediately upon reaching the hover point for the case without turbulence (run 2, Re_{ii} = 0 m^2/s^2).

There seems to be no strong correlation between the time required for stabilization and pilot ratings for the turbulence parameters in this phase of flight. Figure 6-20 shows pilot inputs for the entirety of runs 3, 4 and 6 (Re_{ii} = 1 m^2/s^2, Re_{ii} = 3 m^2/s^2 and Re_{ii} = 6 m^2/s^2), with discontinuous, dotted and continuous lines indicating the translation, stabilization and hover respectively. Some of the patterns in pilot inputs distinguishing the translation and hover phases identified in the PSD plots of Figure 6-18 and Figure 6-19 can be identified here too, including a trend of larger inputs under turbulence, larger higher frequency inputs during the hover phase and the increased demands for collective and lateral control under turbulence and there seem to be some large single pilot inputs during the transition period or just before or after it (lateral inputs and longitudinal inputs for run 3, Re_{ii} = 1 m^2/s^2, and lateral and collective inputs for run 6, Re_{ii} = 6 m^2/s^2). Which might be associated with maneuvering to reduce flight speed and transition into hover over the target point.

These inputs are of similar size than later inputs during the hover phase, although they might be separated in time from them. This seems to suggest that the presence of turbulence requires a constant stabilization effort on the part of the pilot to compensate for turbulence induced disturbances and that it might not make sense to separate the stabilization phase from hover.

a)

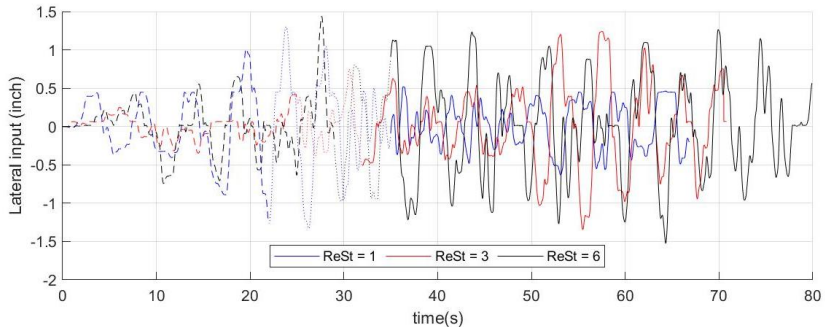

b)

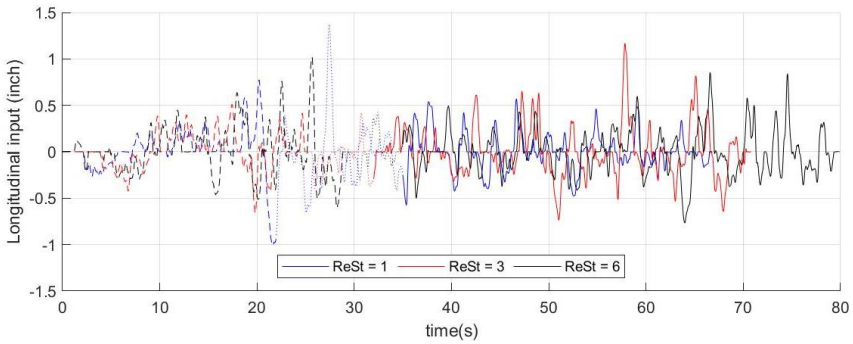

c)

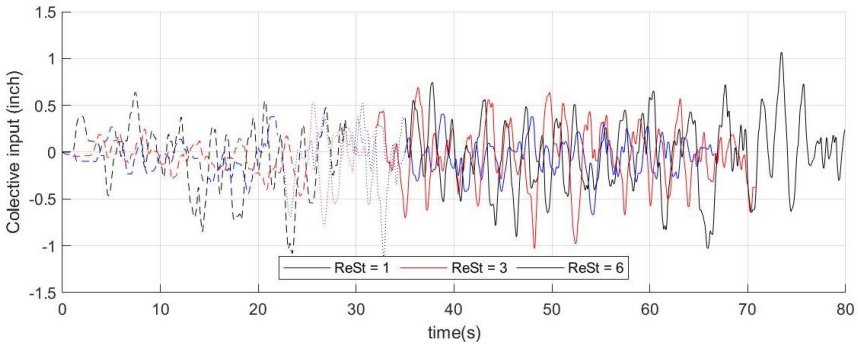

d)

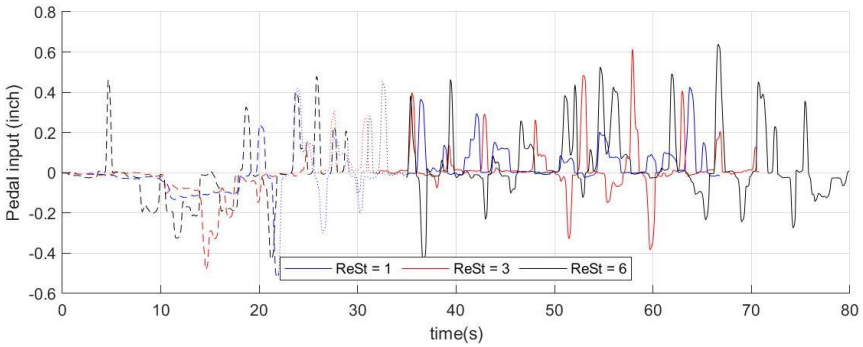

Figure 6-20: Pilot inputs during runs 4 (Re_{ii} = 1), 6 (Re_{ii} = 3) and 7 (Re_{ii} = 6) in a) lateral, b) longitudinal, c) collective and d) pedal. Approach, stabilization and hover phases are given by dashed, dotted and continuous lines respectively.

Figure 6-21 shows RMS values of oscillations in aircraft moments and forces against values of Re_{ii} for the translation and hover phases of the MTE. An increase in RMS values with turbulence intensity can be appreciated, especially for vertical and lateral forces. There is little difference in RMS values between the translation and hover phases except for vertical and lateral forces which seem to be less affected during run 4 of intermediate turbulence intensity, $Re_{ii} = 3\ m^2/s^2$.

RMS of pilot inputs are shown in Figure 6-22 a) for stick inputs and Figure 6-22 b) for collective and pedal inputs. Pilot inputs follow the same trend of increasing RMS values with turbulence intensity as moments and forces, with the already mentioned exception of the translation phase of run 3 ($Re_{ii} = 1\ m^2/s^2$) which was the pilot's first run flown under turbulence and the pilot was still adapting to these conditions. This is a similar trend to the one observed in initial tests performed with this model (see Section 5.3).

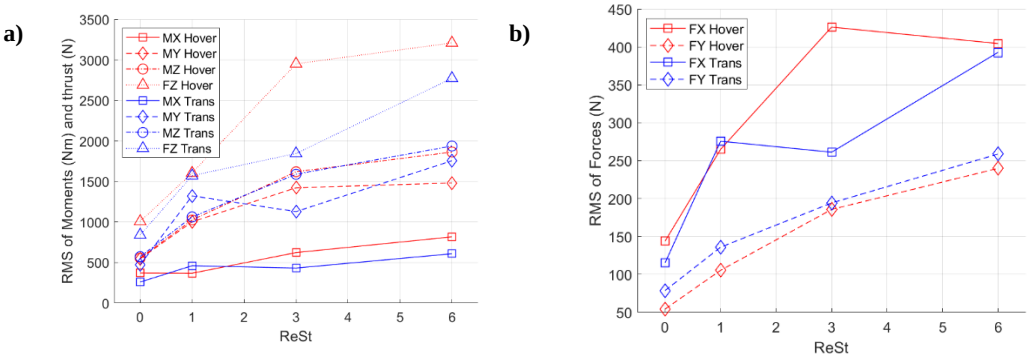

Figure 6-21: RMS of oscillations in aircraft a) moments and vertical force, b) longitudinal and lateral forces

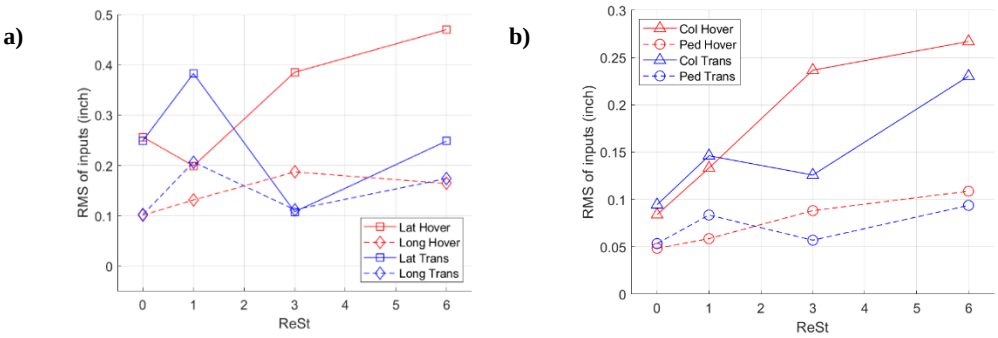

Figure 6-22: RMS of pilot inputs: a) in lateral and longitudinal, b) in collective and pedal.

6.5.2.4 Effect of eddy size

To test the impact on aircraft response and pilot workload of increasing the size of turbulent eddies, runs 5 and 7 were performed with eddy sizes of $\sigma_i = 6m$ and $\sigma_i = 9m$, resulting in turbulence of a lower average frequency. All tests were performed using Reynolds stress values of $Re_{ii} = 3\ m^2/s^2$. The pilot awarded higher HQRs and WLRs when flying within the turbulence resulting from larger eddy sizes, as can be seen in Figure 6-23. For run 7 with eddy size of $\sigma_i = 9m$, the pilot awarded a Level 2 HQR rating of 6 and a Level 3 WLR of 7 implying extensive pilot effort required for the main task and very little spare capacity available, although the primary task of flying the MTE was not in question.

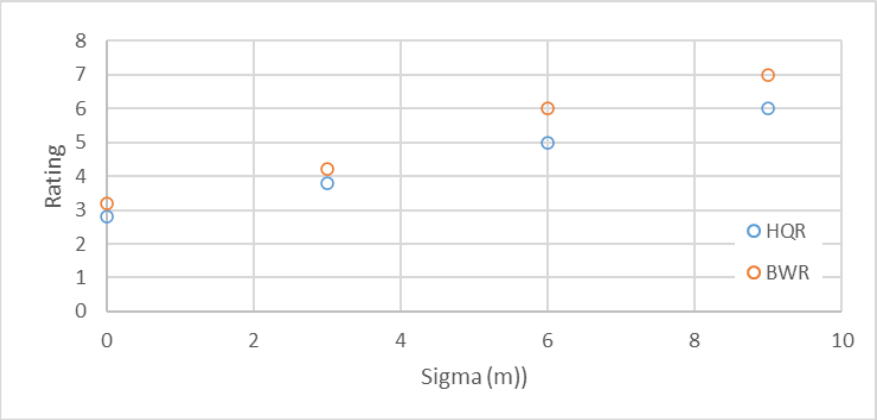

Figure 6-23: HQRs and BWRs for different eddy sizes.

Heave control was again cited by the pilot as the main driver of workload increases in all flights, with compensation of cross couplings in yaw being the secondary cause. The exact character of resulting aircraft disturbances, however, seems to change under different eddy sizes. During run 5, with $\sigma_i = 6m$, the pilot reported difficulty in maintaining a constant approach rate during the translation to hover phase and a reduced predictability of aircraft responses to collective inputs, suggesting a delay in aircraft response leading to excessive inputs. In the case of run 7 with $\sigma_i = 9m$ the pilot reported that the high HQR and BWR ratings were driven by the possible occurrence of pilot induced oscillations (PIO) in the collective axis that occurred during the last 10 seconds. Unfortunately, this was not expected, and no PIO rating was taken. For the entirety of the run before the possible PIO, the pilot considered the most important upsets during the run to be in the heave axis and easily controllable despite a slow aircraft response to collective input.

Ground track during approach to hover, as well as approach rate and altitude over the hover point during the entire run are shown in Figure 6-24 a), b) and c) respectively. The most interesting case is run 5 ($\sigma_i = 6m$). Not only did the translation phase for this run take significantly more time than for other cases, it also shows important oscillations in approach rate and a significant climb during the translation to the hover point of around 5ft in above what is seen for other cases. Run 7 with $\sigma_i = 9m$ shows again a profile similar to the other runs regarding approach rate and altitude oscillations.

Task performance during the hover phase is shown in Figure 6-25 and Figure 6-26. Figure 6-25 depicts altitude and heading deviations during runs 2 (no turbulence), 3 ($\sigma_i = 3m$), 5 ($\sigma_i = 6m$) and 7 ($\sigma_i = 9m$). As can be seen, adequate performance was achieved for most of the time in all runs, with heading deviations drifting rightwards towards the direction of the incoming wind but staying most of the time within the desired range. Oscillations in heave (Figure 6-25 b) present the most interesting trend with one very large descent outside the adequate range evident for run 5 ($\sigma_i = 6m$) and a series of large oscillations between seconds 20 and 30 of run 7 ($\sigma_i = 9m$), which occur in the time period for which the pilot might have encountered a possible PIO. Deviations in longitudinal and lateral position are shown in Figure 6-26. Deviations in longitudinal position (Figure 6-26 b) are kept mainly within adequate boundaries, although all runs present a soft, oscillating forward shift. The pilot manages to keep lateral deviations (Figure 6-26 c) within desired boundaries in all cases, except during the last 10 seconds of run 7 ($\sigma_i = 9m$), when the aircraft drifts slightly to the left.

a)

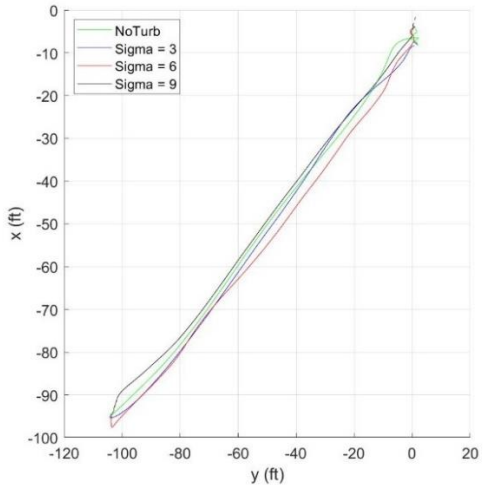

b)

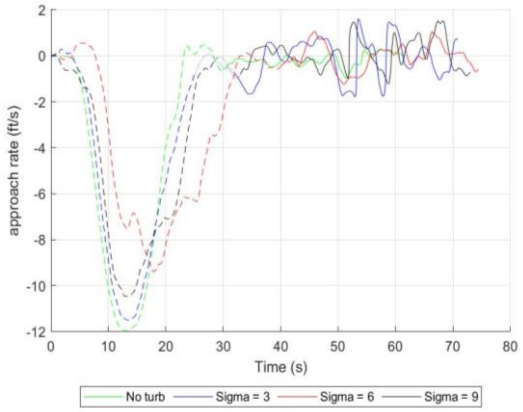

c)

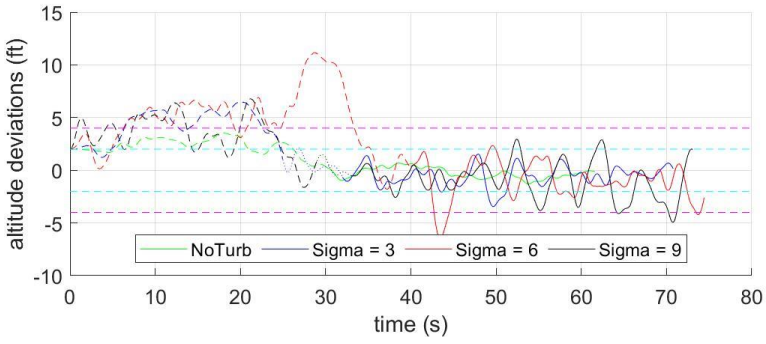

Figure 6-24: Approach to hover point: a) Ground track, b) approach rate to hover point during the entire run, c) altitude deviations from hover altitude during the entire run. Approach, stabilization and hover phase are indicated in b) and c) by dashed, dotted and continuous lines respectively.

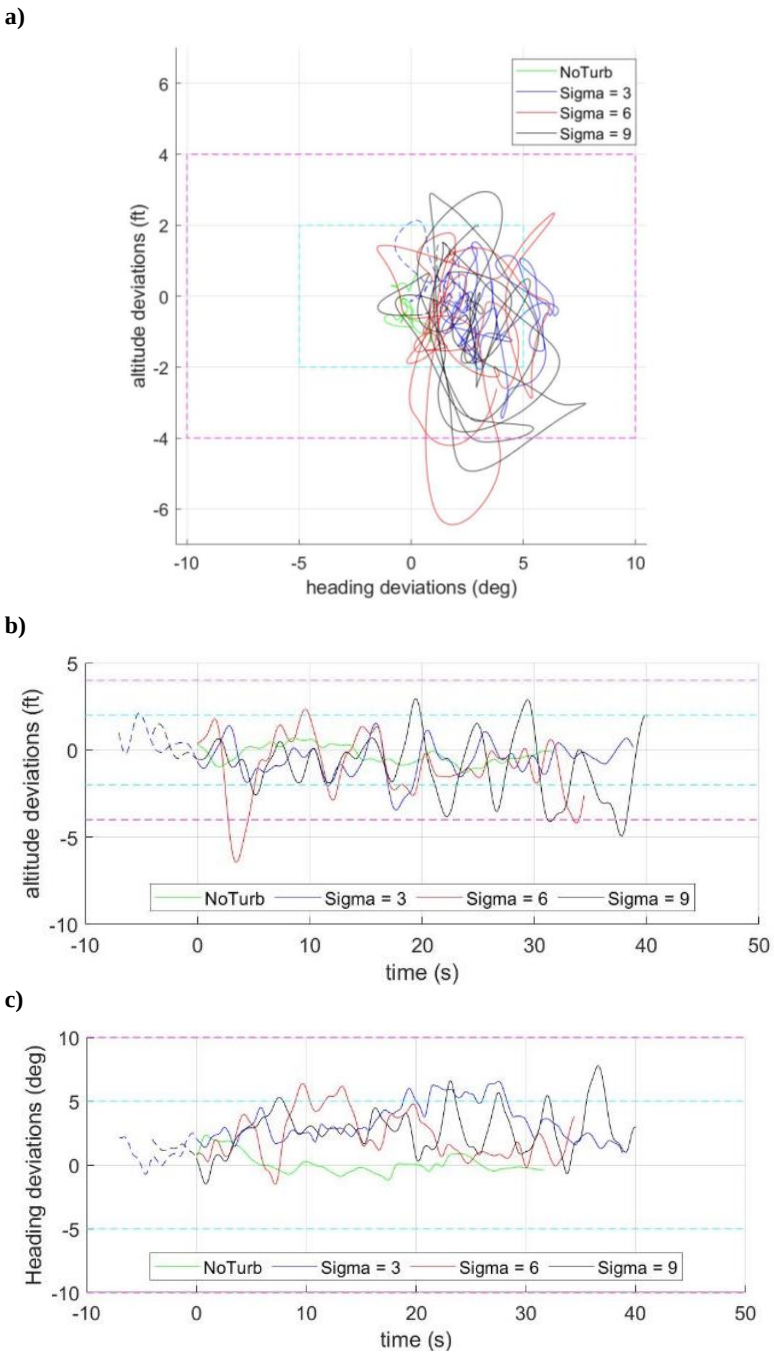

Figure 6-25: Altitude and heading deviations during the hover task for runs 2, 4, 5 and 7. Effect of eddy size. Dashed lines indicate stabilization phase when applicable. Cyan and magenta dashed lines indicate desired and adequate boundaries. For time plots, 0 is moment when pilot declares aircraft to be stabilized.

a)

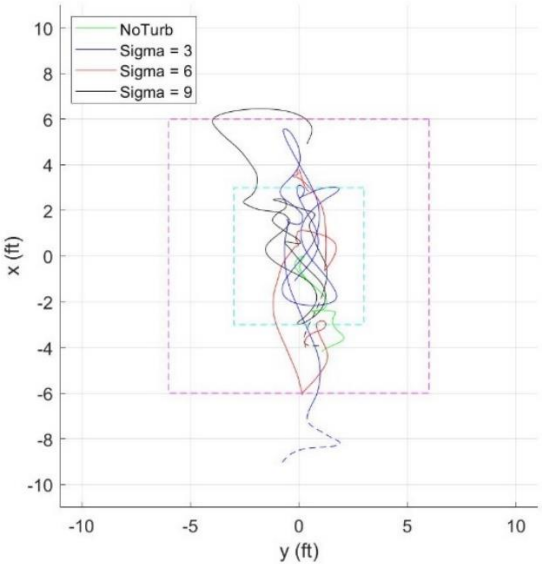

b)

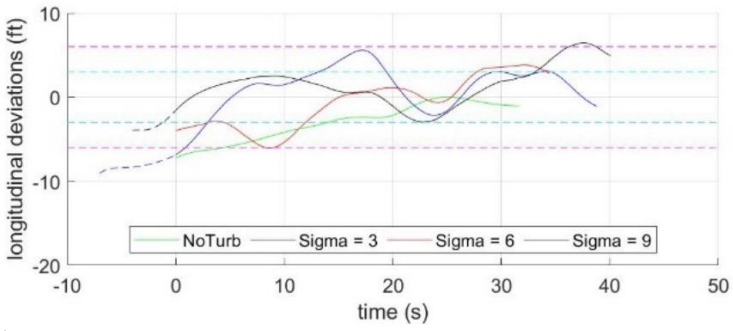

c)

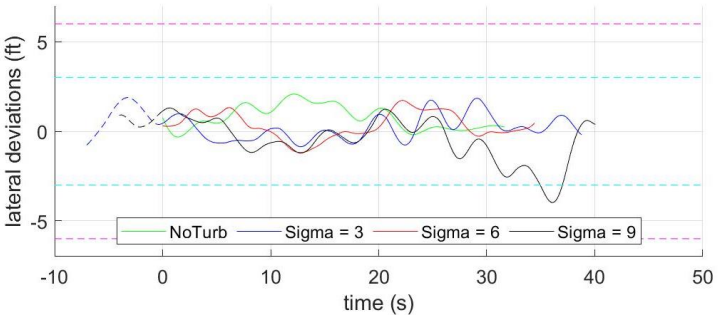

Figure 6-26: Longitudinal and lateral deviations during the hover task for runs 2, 4, 5 and 7. Effect of eddy size. Dashed lines indicate stabilization phase when applicable. Cyan and magenta dashed lines indicate desired and adequate boundaries. For time plots, 0 is moment when pilot declares aircraft to be stabilized.

PSD plots of pilot inputs during the translation and hover phases are shown in Figure 6-27 and Figure 6-28 respectively. During run 5, when flying under turbulence of eddy size $\sigma_i = 6m$, the pilot needed to produce inputs of very large amplitude during the translation phase, mainly in the lateral (Figure 6-27 a) and longitudinal (Figure 6-27 b) axis. Inputs in the longitudinal axis also cover a broad frequency spectrum of 0 to 0.75Hz with peaks at around 0.25Hz and 0.6Hz, suggesting a mixture of guidance and stabilization pilot activity, something often associated with large workload increases [118]. Pilot inputs in collective and pedal also show a small increase in amplitude and cover a wider frequency range of between 0Hz and 0.5Hz than under smaller eddy sizes. By contrast, during run 8, flown under turbulence of eddy size of $\sigma_i = 9m$, pilot stick inputs do not present such large amplitudes and collective and pedal inputs show a very similar behaviour as in the case of $\sigma_i = 6m$.

During the hover phase pilot inputs present a pattern similar to the one observed previously with increases in turbulence intensity. Lateral and longitudinal inputs (Figure 6-28 a) and b) show an increase in amplitude with smaller eddy sizes, while the opposite is true for inputs in collective and pedal (Figure 6-28 a) and b).

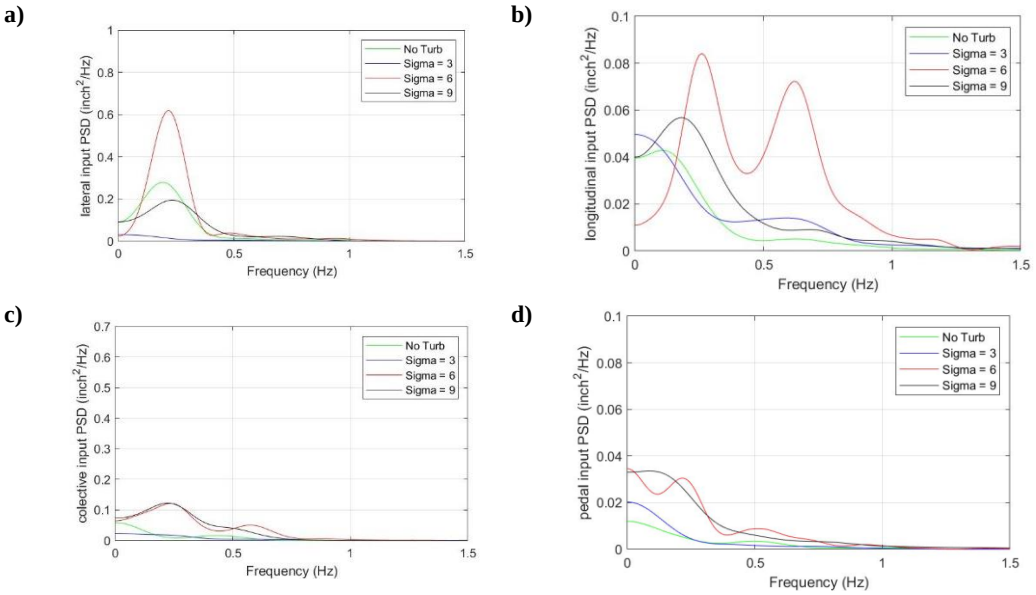

Figure 6-27: Power spectral density of pilot inputs during translation to hover point: in a) lateral, b) longitudinal, c) collective, d) pedal.

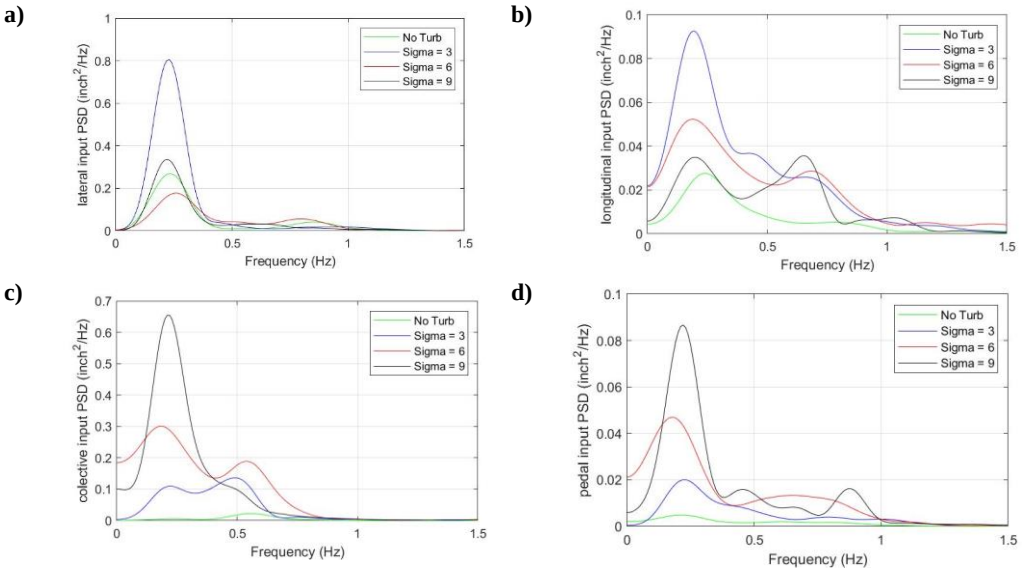

Figure 6-28: Power spectral density of pilot inputs during station keeping over hover point: in a) lateral, b) longitudinal, c) collective, d) pedal.

The pilot commented that they encountered a possible PIO in the heave axis at the end of the station keeping phase of run 7 (eddy size σ_i = 9m), which was confirmed in post-trial analysis. Figure 6-29 depicts pilot inputs in the collective together with altitude deviations over the hover point and seems to confirm this. Some 17 seconds after the start of the hover, the pilot started introducing large inputs into the collective which follow a 180 deg phase delay with large oscillations in altitude occurring during the same time period. This situation lasts until almost 35 seconds into the hover phase. Interestingly, this phase delay seems to be present already from the start of the hover phase, although oscillations are of much smaller amplitude.

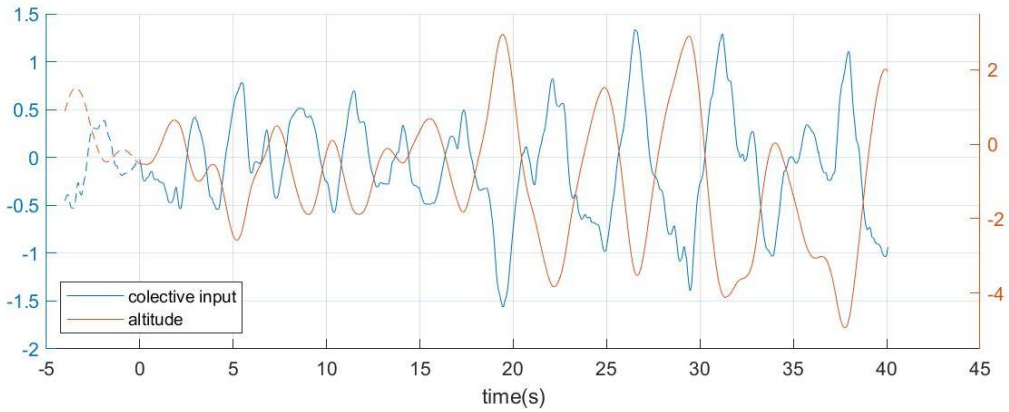

Figure 6-29: Left axis: pilot inputs in collective during the hover phase. Right axis: altitude deviations from hover point during hover phase. Discontinuous lines mark the stabilization phase.

The duration of the stabilization phase during these runs also seems to present little correlation with eddy size or awarded pilot rating and will not be discussed in this chapter.

The RMS of oscillations in moments and forces acting on the aircraft against values of eddy size are shown in Figure 6-30 a) and b) respectively. RMS values of pitch moment as well as vertical and longitudinal forces show a peak at eddy sizes of $\sigma_i = 6m$, while roll and yaw moments as well as lateral forces show little effect from the changes in eddy size. Changes in RMS values when switching from translation to hover can also be seen, the most notable being large increases for vertical forces and longitudinal forces under turbulence of eddy size $\sigma_i = 3m$. An increase in RMS values for lateral forces and a decrease in RMS for pitch moment for eddy sizes $\sigma_i = 6m$ can also be appreciated after transitioning into the hover phase.

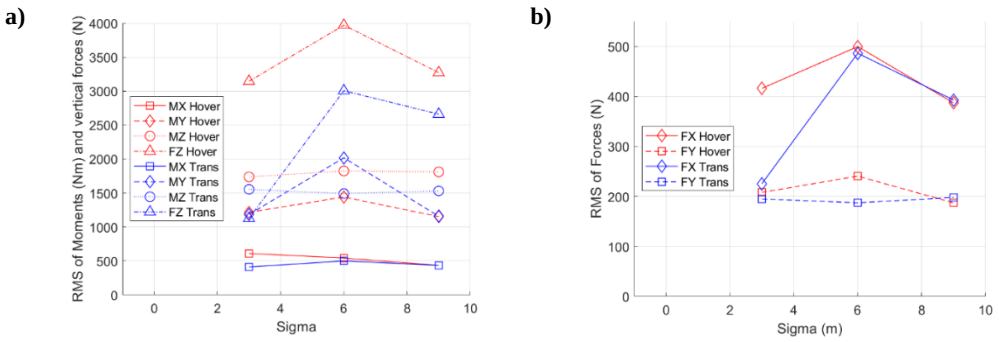

Figure 6-30: Root mean square of oscillations in aircraft a) moments and vertical force, b) longitudinal and lateral

RMS values of pilot inputs are shown Figure 6-31 and do not follow RMS of forces and moments as closely as observed when changing the values of Reynolds stresses (which were shown in Figure 6-22). Stick inputs (Figure 6-31 a) during translation present a peak in RMS value for run 6 at eddy size of $\sigma_i = 6m$, especially in the lateral axis despite there being no such large increases in RMS values of roll moments and lateral forces. During the hover phase, the trend for lateral inputs becomes the inverse with highest RMS values appearing at $\sigma_i = 3m$. Pilot inputs in collective (Figure 6-31 b) seem to follow the same behaviour as oscillations in vertical forces, presenting a large increase during the hover phase and a peak at $\sigma_i = 6m$. Pedal inputs also show an increase with eddy size despite there being little change in RMS values of yaw moment, which might be a consequence of cross couplings with the collective.

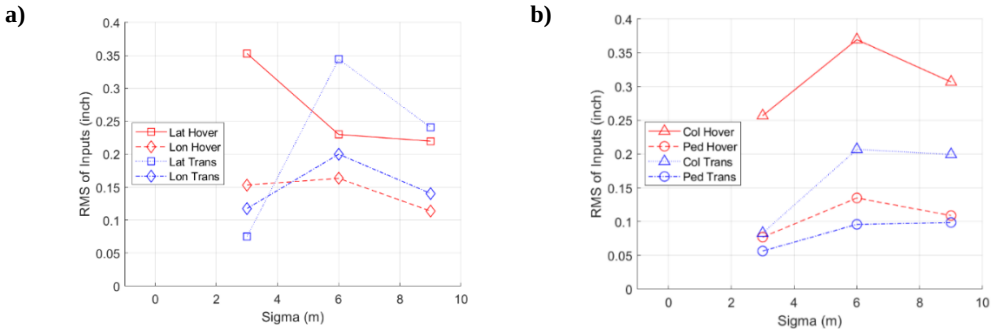

Figure 6-31: Root mean square of pilot inputs: a) in lateral and longitudinal, b) in collective and pedal.

6.5.2.5 Effect of multi-scale eddy series

The last parameter to be tested is the use of multi-scale eddy series. In this case the turbulence is generated by adding the turbulences resulting from multiple eddy series together, having a different size and strength. By scaling the value of Re_{ii} with the size of the eddy, σ_i, the result is a mixture of large amplitude low frequency and low amplitude high frequency disturbances and a smoother decay of the turbulence power density with frequency (see Section 6.2).

To allow for comparison with the previous runs of the trial, the same eddy sizes used in the previous trial were employed and the values of Re_{ii} for each series adjusted so that the total sum is equal to $Re_{ii} = 3\ m^2/s^2$. Table 6-5 shows the runs performed at different eddy sizes and the runs performed using the multi-scale eddies, ordered by the approximate average frequency of the resulting turbulence.

The pilot awarded HQRs and BWRs suggest a similar difficulty of the task for the runs performed under multi-scale eddy series as under single scale turbulence of size $\sigma_i = 6m$, which results in similar average frequency for the induced turbulence. Figure 6-32 shows handling qualities (a) and workload ratings (b) against average turbulence frequency for these runs, suggesting a trend of greater task difficulty when flying under turbulence of equal intensity but lower frequency.

Table 6-5: Runs performed with different eddy sizes and using multi-scale eddy series. Ordered by average frequency of the induced turbulence.

Run	Number of series	Scaling	$Re_{ii}\left(\frac{m^2}{s^2}\right)$	σ (m)	Average frequency (Hz)	HQR	BWR
4	1	1	3	3	0.88	4	4
8	2	1,2	1,2	3, 6	0.6	5	6
9	2	1,3	0.75, 2.25	3, 9	0.45	6	5
10	3	1,2,3	0.5, 1, 1.5	3, 6, 9	0.45	6	6
5	1	1	3	6	0.44	5	6
7	1	1	3	9	0.29	6	7

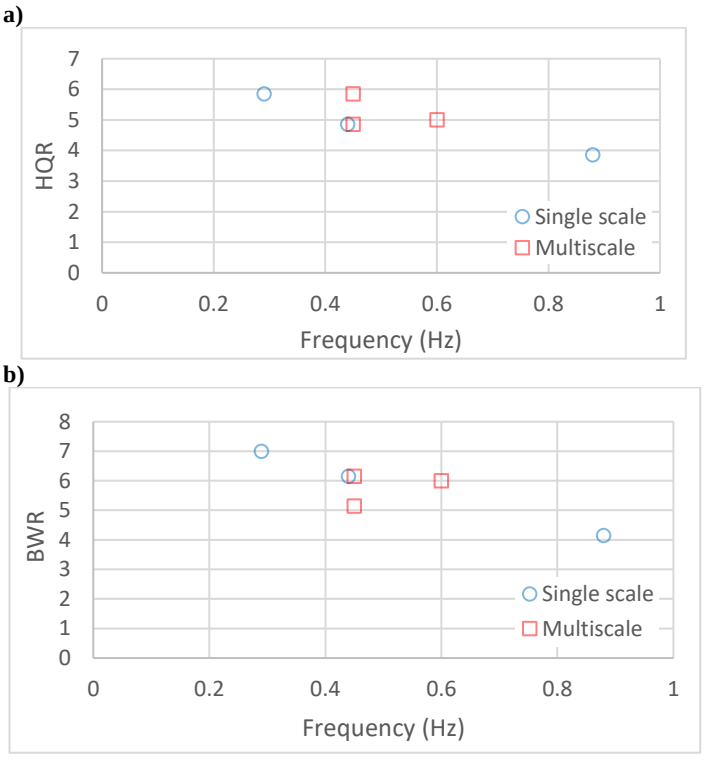

Figure 6-32: Pilot awarded handling qualities (a) and workload (b) ratings against average frequency of induced turbulence.

Figure 6-33 shows ground track, approach rate and altitude during the translation and hover phases. It can be seen that using multiple-scale eddies makes it more difficult for the pilot to maintain a steady approach rate (Figure 6-33 b) and, depending on the distribution of eddy sizes, leads to altitude oscillations (Figure 6-33 c). The impact in flying observed when using multi-scale eddies to generate turbulence is similar to that observed when changing the size of eddies in Section 6.5.2.4. For example, in run 9 (see Figure 6-33), aircraft upsets in altitude and approach rate to the hover point under a turbulence of two series of eddies of size $\sigma^1_i = 3m$ and $\sigma^2_i = 9m$ respectively are of similar amplitude as those experienced for run 5 under turbulence produced by a single series of eddies of size $\sigma_i = 6m$ (see Figure 6-24).

Other than approaching the hover point at a speed between 6kts to 10kts, there are no performance requirements limiting deviations in aircraft position or attitude defined for the approach to the hover point. According to the pilot, this reduced the impact of turbulence during the translation phase on the BWR and HQR that was awarded. These were mainly determined by the hover phase, which was the most demanding part of the MTE. Pilot effort during hover was again focused on counteracting deviations in heave, followed by maintaining heading and longitudinal position, induced in part by cross couplings from inputs in the collective axis. Pilot comments indicated a trend in which, after correcting for deviations in heave, they shifted their attention to heading and longitudinal position which in turn led to large disturbances in heave.

Figure 6-34 and Figure 6-35, show task performance during the hover phase and which shows a similar impact to previous runs of turbulence resulting in deviations in altitude, heading and longitudinal position. These grow larger for runs 9 and 10 which were performed under the series of eddies of sizes $\sigma_i = [3m, 9m]$ and $\sigma_i = [3m, 6m, 9m]$. Time series (Subgraphs b) and c) for each figure) show single large deviations in altitude that exceed adequate limits (at around 15*s*, 20*s* and 25*s* after the start of the hover phase).

a)

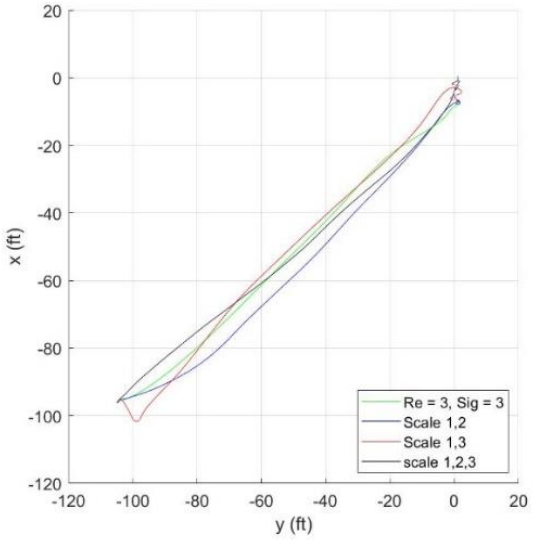

b)

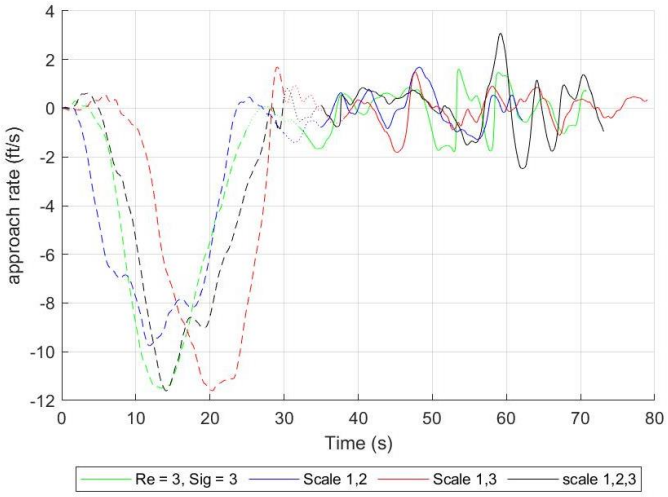

c)

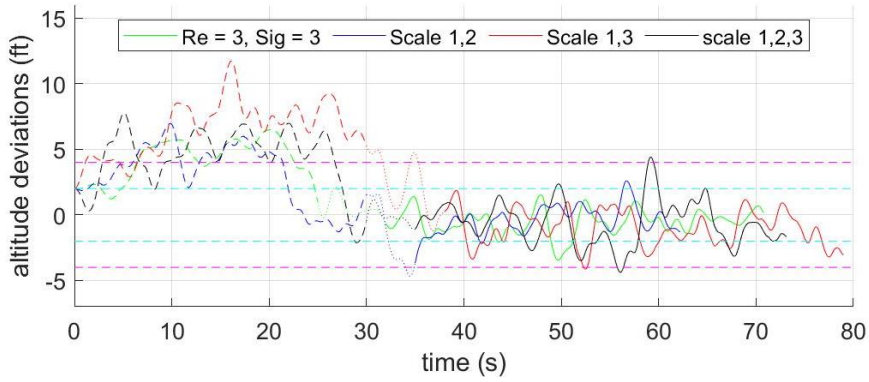

Figure 6-33: Approach to hover point: a) Ground track, b) approach rate to hover point during the entire run, c) altitude deviations from hover altitude during the entire run. Approach, stabilization and hover phase are indicated in b) and c) by dashed, dotted and continuous lines respectively.

a)

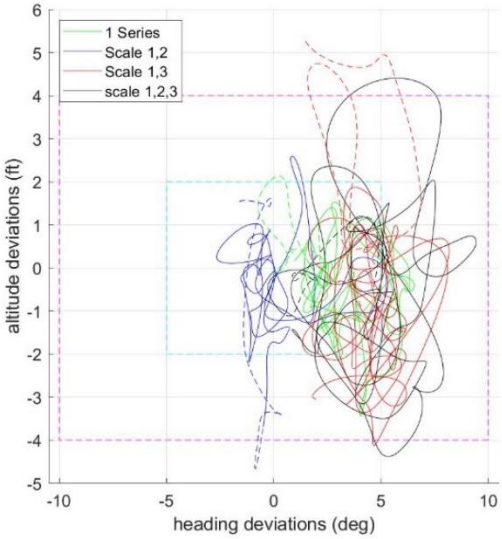

b)

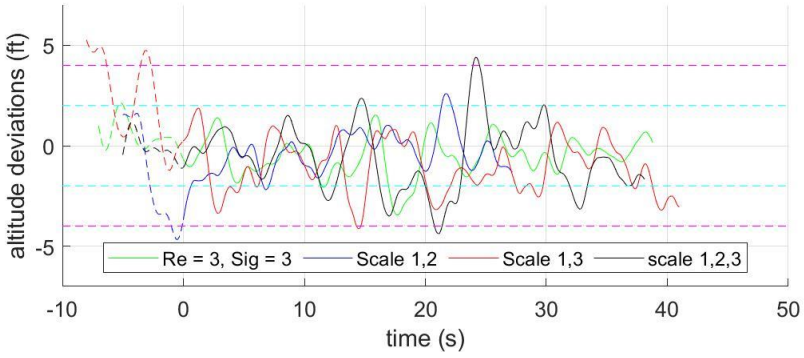

c)

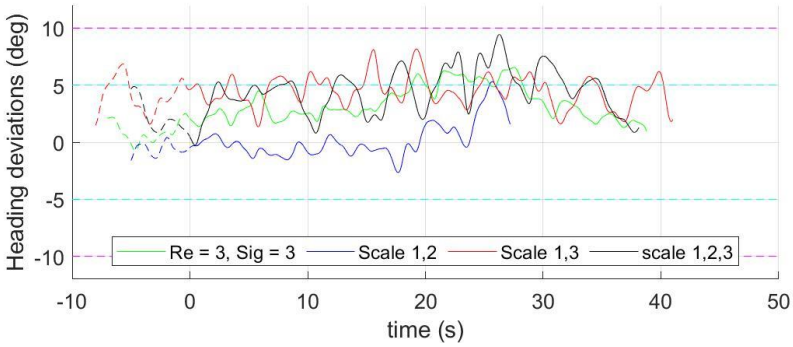

Figure 6-34: Altitude and heading deviations during the hover task for runs 4, 8, 9 and 10. Effect of multi-scale eddies. Dashed lines indicate stabilization phase when applicable. Cyan and magenta dashed lines indicate desired and adequate boundaries. For time plots, 0 is moment when pilot declares aircraft to be stabilized.

a)

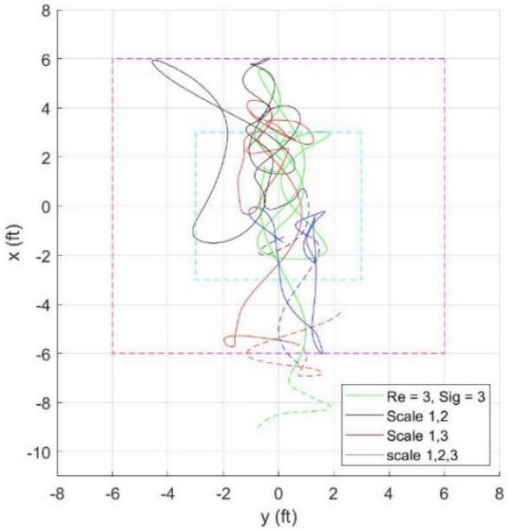

b)

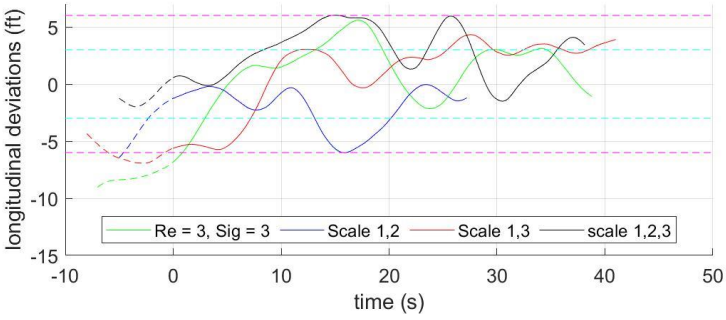

c)

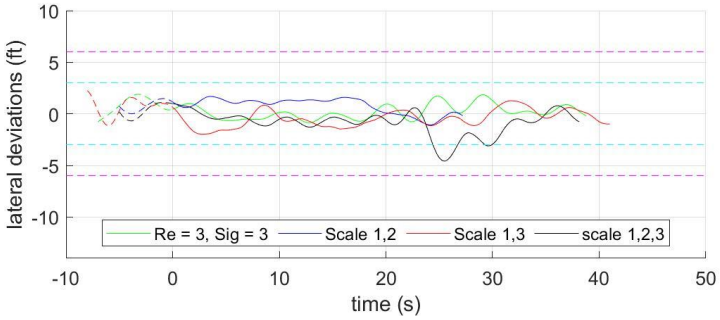

Figure 6-35: Longitudinal and lateral deviations during the hover task for runs 4, 8, 9 and 10. Effect of multi-scale eddies. Dashed lines indicate stabilization phase when applicable. Cyan and magenta dashed lines indicate desired and adequate boundaries. For time plots, 0 is moment when pilot declares aircraft to be stabilized.

PSD plots of pilot control inputs during the hover phase for different series of single eddy sizes and multi-scale series of eddies are shown in Figure 6-36. The figures show a change when the task is performed using turbulence induced by multiple series of eddies. Stick inputs in lateral (graph a) and longitudinal (graph b) follow a similar pattern of increased amplitude for conditions in which the pilot assigned higher workload ratings. Inputs in collective (graph c) and pedal (graph d) show either a distribution of input power density across a wider range of frequencies or additional peaks at a higher frequency for those runs performed under turbulence due to eddies of sizes of σ_i = [3m, 9m] and σ_i = [3m, 6m, 9m]. A combination of large low frequency inputs and smaller large frequency inputs is often associated to increase pilot workload.

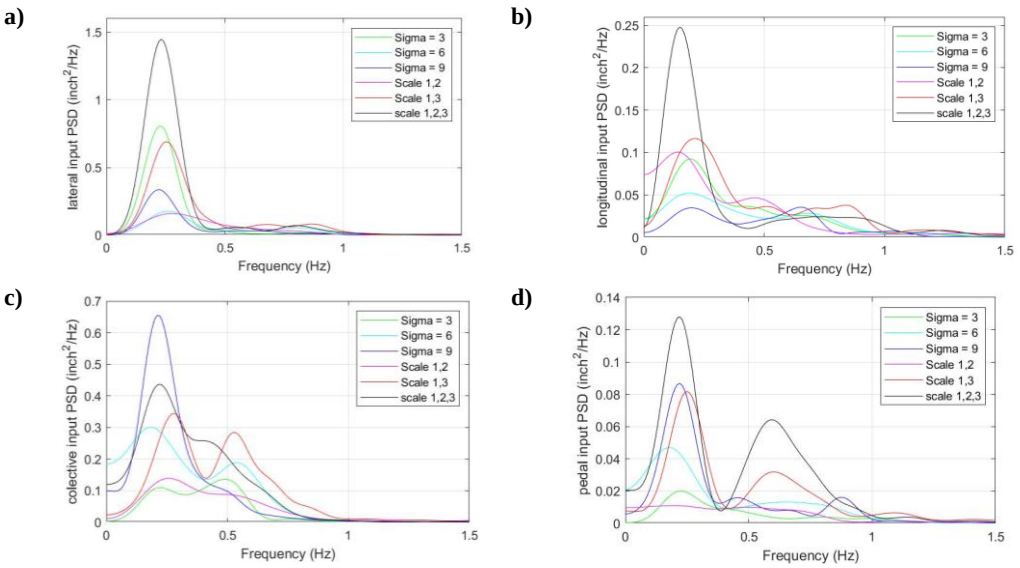

Figure 6-36: Power spectral density of pilot inputs during station keeping over hover point: in a) lateral, b) longitudinal, c) collective, d) pedal.

When seen in context with pilot comments and single large deviations in altitude, the source of pilot workload is due to the pilot simultaneously compensating for disturbances induced by the different series of eddies, although further analysis is necessary to confirm this point.

6.5.2.6 Discussion of the Precision Hover MTE

During the precision hover MTE, the pilot's workload was driven by the station keeping phase as this segment shows the largest deviations in aircraft position and attitude that the pilot had to correct for.

Turbulence impacts task performance and requires the pilot to shift their focus from countering deviations in roll and pitch to focusing mainly on the heave axis, followed by heading and longitudinal position. These effects are manifested by an increased difficulty for the pilot to keep deviations in these parameters within desired or even adequate boundaries. According to the pilot, the main driver for increased workload is the need to constantly stabilize in all axes, especially in collective to maintain altitude. Analysis of power spectral density of the pilot's control inputs indicate that during the hover phase, increased pilot workload tends to manifest itself as an increase in control input amplitude in all axes. Even when the average frequency of the turbulence changes, stick inputs tend to show peaks at a constant frequency of around 0.3Hz, with longitudinal inputs also show secondary peaks up to around 0.8Hz. Collective and pedal inputs tend to present multiple peaks spread across a wider frequency range between 0Hz and 0.8Hz.

Possible causes for this might be the lack of any stability augmentation in the heave axis for the Bell 412 as well as the close proximity to the ground leading the pilot to act with greater urgency to compensate for altitude deviations. The Bell 412 also shows poor longitudinal stability in hover (see Figure 6-7).

Flying under turbulence of increasing values of Reynolds stress tensor while maintaining a small eddy size ($\sigma_i = 3m$), leads to increases in workload requirements and decreasing task performance. Keeping the value of Reynolds stresses constant while increasing the eddy size also leads to an increase in workload requirements and worse task performance, with the largest eddy size tested ($\sigma_i = 9m$) resulting in a possible PIO prone situation. Interestingly, changes in eddy size, which change the average frequency of the induced turbulence, do not seem to change the frequency of pilot inputs, with the pilot responding mainly by increasing or decreasing the amplitude of inputs.

Station keeping under turbulence induced by multiple-scale eddies by contrast does seem to lead the pilot to spread control inputs in the collective and pedal across a wider frequency range. When taking into account pilot feedback, this suggests that the pilot needs to switch their attention between counteracting the high frequency low amplitude oscillations and the occasional large amplitude, low frequency ones.

The trend observed in Section 5.3 where turbulence of higher Re_{ii} values also leads to higher RMS of moments and forces acting on the aircraft and higher RMS of pilot

inputs is also confirmed here when testing with different values of Re_{ii} and same size of eddies (see Figure 6-21 and Figure 6-22). However, when analysing the impact of turbulence from different eddy sizes, the relationship between pilot workload and RMS values of all moments and forces needs further examination. For example, the RMS values for vertical and longitudinal forces, as well as pitch moments during translation, show a peak for the $\sigma_i = 6m$ case and a decrease for the $\sigma_i = 9m$ case. But this does not seem to correlate with the higher BWR and HQR nor for the PIO prone situation reported by the pilot. It should be noted that the RMS metric 'averages' a signal over the full time series and does not highlight possible peaks in pilot compensation that occurs in a PIO situation and this warrants further investigation.

Figure 6-37 shows the RMS of pilot control inputs against RMS of turbulence induced velocities and pilot awarded workload ratings, suggesting a strong correlation between turbulence, pilot inputs in the collective and in pedal and pilot awarded workload ratings. But this correlation seems to breakdown when comparing for pilot stick inputs.

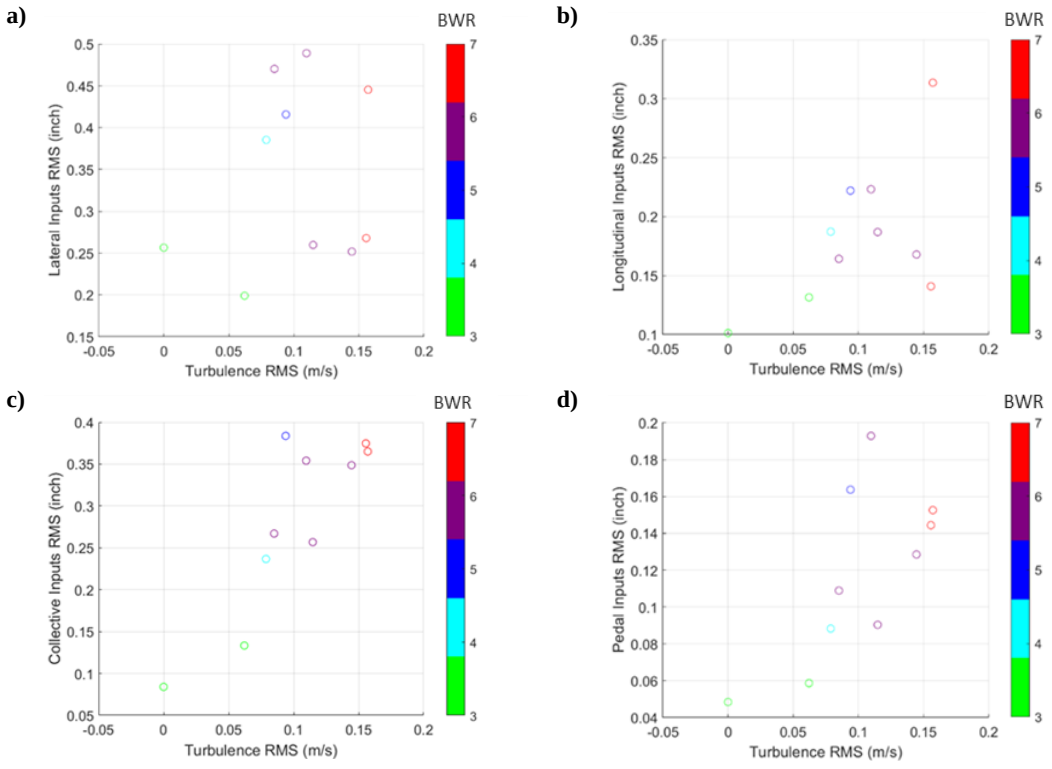

Figure 6-37:Pilot awarded BWRs against RMS of pilot control inputs and RMS of induced turbulence during station keeping phase (measured at aircraft fuselage)

There also appears to be a trend of higher pilot workload and worsening handling qualities as the average frequency of induced turbulence decreases. Figure 6-38 summarizes this trend by presenting pilot awarded workload ratings against standard

deviation and average frequency of turbulent flow velocities as measured at the aircraft's fuselage ACP during the station keeping phase of the runs shown in Section 6.5.2.2.

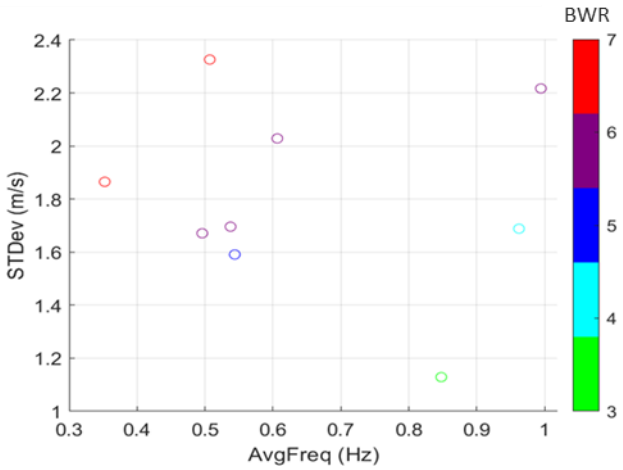

Figure 6-38: Pilot awarded BWRs against standard deviations and average frequency of turbulent flows during station keeping phase (measured at aircraft's fuselage ACP)

Turbulence seems to make less of an impact when the aircraft is displacing itself to the hover point. Increasing the values of Re_{ii} does not seem to lead to large changes in aircraft path (Figure 6-15 a), approach rate (Figure 6-15 b), altitude (Figure 6-15 c) or pilot inputs (Figure 6-18) during this phase.

However, runs conducted under turbulence induced by eddies of sizes $\sigma_i = 6m$ or series with size $\sigma_i = [3m, 9m]$, show large upsets during the translation phase in altitude (Figure 6-24 and Figure 6-33 c) and approach rate (Figure 6-24 and Figure 6-33 b). Pilot control inputs during this phase (Figure 6-27) show a spread of pilot inputs in the longitudinal axis across a wider frequency range, suggesting a mixture of stabilization and guidance inputs. But this does not have an impact on pilot awarded workload and handling qualities ratings as the lack of limits in deviations during this phase means that upsets do not result in degraded task performance.

Assessing transition from translation to hover according to the stabilization time criteria defined in ADS – 33 proved difficult. While there seem to be clear pilot control inputs intended to reduce flight speed and start the transition to hover, it was hard to clearly determine where the stabilization phase ends and station keeping starts. The presence of turbulence requires constant stabilization effort on the part of the pilot and separating the two phases might not make sense when assessing task performance.

6.5.3 Results - Steady and level forward flight task

6.5.3.1 Steady and level forward flight task – MTE definition:

To evaluate the impact of turbulence in a range of flight speeds, a custom steady and level (S&L) forward flight MTE was designed in this thesis. Flights were performed under a 20kts, 90deg wind with varying SEM turbulence conditions. The pilot was instructed to maintain airspeed, staying within lateral boundaries and not to exceed maximum altitude for at least 30 seconds. Limits for lateral, altitude and heading deviations were based on the acceleration – deceleration task as defined by ADS–33 (see Table 6-6 and Figure 6-39). Limits on allowable airspeed deviations were based on the results of previous testing (see Section 5.3).

A custom test track was developed consisting of a runway marked by cones and flat markers to provide a visual reference for desired and adequate lateral deviations, respectively. A series of vertical poles provided an altitude reference with desired limits indicated as blue and adequate as yellow. The central runway line indicated the intended heading, but no other visual reference was provided for absolute heading deviations. The pilot used instrumentation on the control panel to assess airspeed and heading deviations (see Figure 6-40).

The test run ended after 30s, upon call of the pilot or when the end of the test track was reached.

Table 6-6: Desired and adequate limits for the level flight task

Parameter	Desired	Adequate
Maximum altitude equal or lower to:	50 ft	70 ft
Maintain lateral track within:	± 10 ft	± 20 ft
Maintain Heading within:	± 10 deg	± 20 deg
Maintain IAS within:	± 5 kts	± 10 kts

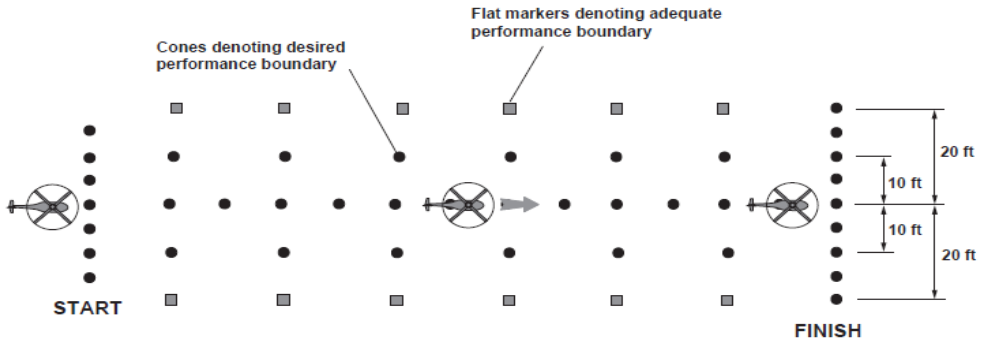

Figure 6-39: Schematic of forward flight test course and visual cues

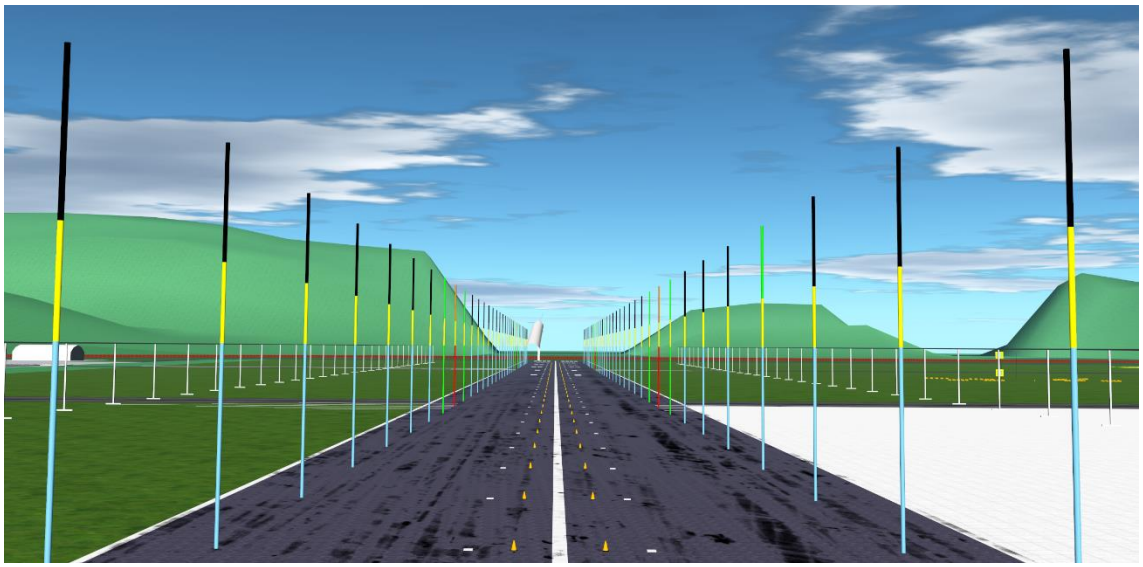

Figure 6-40: Simulator Steady and level flight test track.

6.5.3.2 Runs performed and Pilot ratings:

Table 6-7: Steady and level MTE simulation runs performed.

Run	IAS (kts)	Total Re_{ii} (m^2/s^2)	No of eddy scales	Re_{ii} (m^2/s^2) for each scale	σ (m) for each scale	Average frequency (Hz)		HQR	BWR	
1	40	0	-	-	-			3	3	
2	40	1	1	1	3	1.97		3	3	
3	40	3	1	3	3	1.97		4	4	
4	40	6	1	6	3	1.97		4	5	
5	40	3	1	3	6	0.98		5	5	
6	40	3	1	3	9	0.65		4	4	
7	40	3	2	[1, 2]	[3, 6]	1.34		4	5	
8	40	3	2	[0.75, 2.25]	[3, 9]	1.01		4	4	
9	40	3	3	[0.5, 1, 1.5]	[3, 6, 9]	1.01		4	4	
10										
11	60	0	-	-	-			3	2	
12	60	3	1	3	3	2.78		3	3	
13	60	6	1	6	3	2.78		4	5	
14	60	3	1	3	6	1.39		4	5	
15	60	3	1	3	9	0.92		4	4	
16	60	3	2	[1, 2]	[3, 6]	1.90		3	3	
17	60	3	2	[0.75, 2.25]	[3, 9]	1.42		4	4	
18	60	3	3	[0.5, 1, 1.5]	[3, 6, 9]	1.42		4	5	
19	60	3	1	3	9	0.92		4	5	
20	60	6	1	6	3	2.78		3	4	
21	60	3	1	3	6	1.39		5	6	
22	60	3	1	3	3	2.78		4	4	

Table 6-7 reports the performed runs for the S&L flight task, aircraft trim airspeed, turbulence parameters and pilot ratings for each run. The runs were performed under

the same conditions of the hover task at airspeeds of 40kts and 60kts to enable comparisons to be made.

6.5.3.3 *Impact of turbulence on steady and level flight.*

For the steady and level flight task, the impact of turbulence on task performance and pilot workload was significantly lower than for the hover tasks. Pilot comments indicated maintaining lateral path and heading was the main source of workload and this did not change when flying under conditions of turbulence or at different airspeeds, although under steady wind, the aircraft was easier to fly at higher airspeeds.

a)

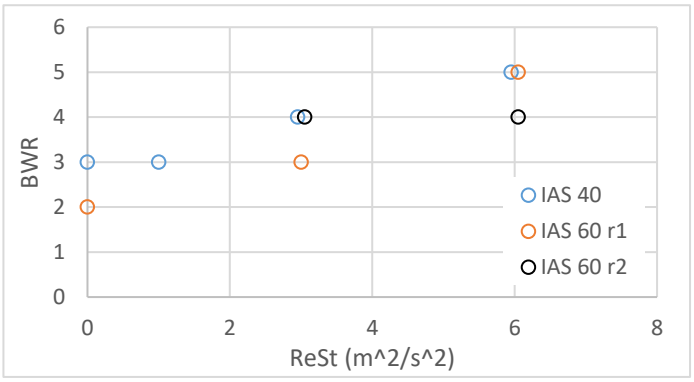

b)

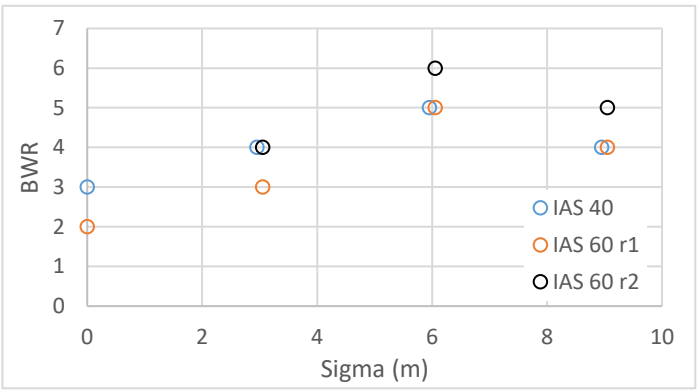

Figure 6-41: pilot awarded BWRs against: a) values of Reynolds stress tensor. b) eddy size.

The same trend of increasing values of Re_{ii} leading to increased workload for the pilot and lower task performance was observed again (see Figure 6-41 a). Aircraft disturbances and pilot control inputs also show a similar behaviour of increased amplitude with increases in levels of Re_{ii} and will not be discussed further in this chapter.

When assessing task performance against turbulence induced by differing eddy sizes (see Figure 6-41 b), a peak at the intermediate eddy size of $\sigma_i = 6m$ becomes evident. This size also presented the largest impact during the translation phase for the hover task.

Figure 6-42 shows the BWR awarded against average frequency of aircraft disturbances for all runs conducted in the steady and level flight condition. A peak in BWR awarded can be distinguished when average frequency of the turbulence stays within the 1Hz to 1.5Hz range.

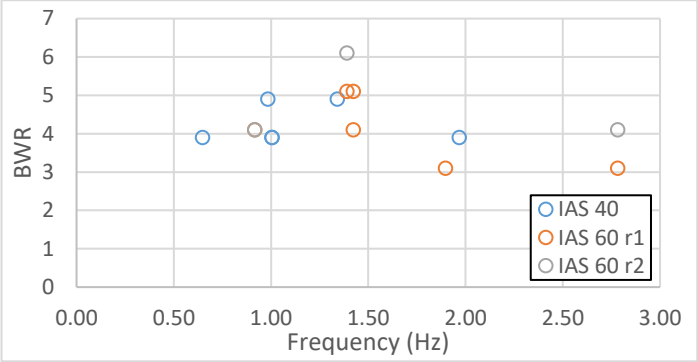

Figure 6-42: Pilot awarded BWRs against average frequency of induced turbulence during steady and level flight

Overall task performance shows the pilot reporting no difficulty in maintaining lateral deviations and airspeed upsets within the desired boundaries, however altitude performance was within the adequate performance standard (see Figure 6-43). In the case of altitude, the aircraft started directly at the desired limits and with an initial tendency to climb due to airspeed. The pilot usually corrected quickly and in most cases was able to stay below desired altitude limits for most of the run.

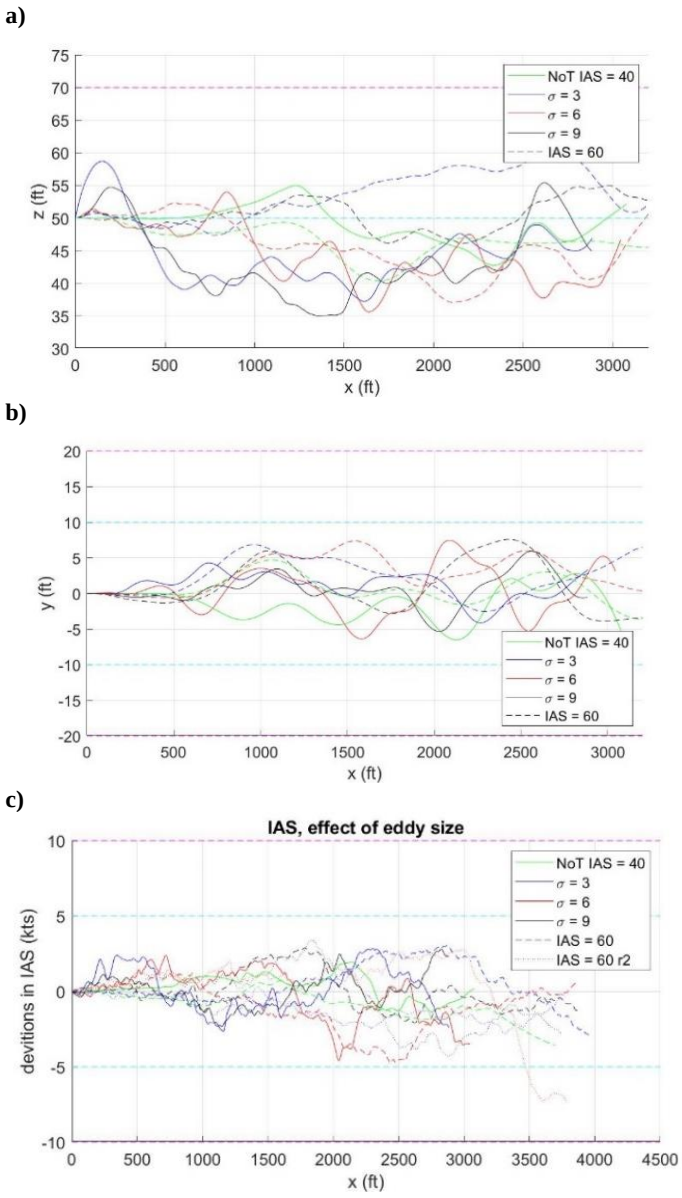

Figure 6-43: Steady and level flight task performance against eddy size: a) altitude deviations. b) lateral deviations from flight path. c) Upsets from initial airspeed. Green and magenta dashed lines indicate desired and adequate limits, respectively.

Figure 6-44 and Figure 6-45 show power spectral analysis of pilot inputs in the presence of turbulence of different eddy sizes and multi-scale series at airspeeds of 40kts and 60kts respectively. Overall, a trend is observed showing an increase in the amplitude of pilot inputs, with inputs in the lateral and pedal peaking around 0.25Hz, in collective at 0Hz and longitudinal inputs showing a main peak at 0.25Hz and multiple secondary peaks spreading up to 1Hz. This correlates with increased pilot workload. Large increases in control amplitude appears for all axes for the particular condition of $\sigma_i = 6m$ for both flight speeds. This turbulence condition seems to be the only one that consistently demands larger amplitude in pilot response across both flight speeds tested.

In contrast to the hover task, multiple series of eddies do not seem to induce the pilot to spread their inputs across a wider range of frequencies and, rather, their effect is limited to increases in amplitude similar as seen when altering the size of single eddy turbulence.

Finally, it is interesting to compare pilot inputs for this particular condition of $\sigma_i = 6m$ across all the different flight conditions tested. These are hover, translation to the hover point and steady and level flight at 40kts and 60kts. It is noted that the flight conditions and task demands are very different between the four cases but it offers some insight into how a specific turbulence condition can impact workload and performance across a range of tasks as might be expected in the real world.

Figure 6-46 shows pilot power spectral density for the baseline case of $\sigma_i = 3m$ and $Re_{ii} = 3\ m^2/s^2$. The pattern shown is common for most conditions tested, where pilot inputs during the hover phase in all axes are of significantly higher amplitude than for all other flight conditions, the exception being longitudinal stick inputs during low speed forward flight. This is consistent with previous results pointing towards the station keeping phase of the hover task MTE being the most demanding of the flight conditions tested and also the most susceptible to be impacted by turbulence.

Figure 6-47 shows pilot power spectral density for the case of $\sigma_i = 6m$ and $Re_{ii} = 3\ m^2/s^2$. Pilot inputs show larger amplitudes under conditions of steady and level flight and translation than during hover for all axes except heave, which still seems to put the greatest pilot demands during the hover phase. This suggests a particular sensitivity of the aircraft in forward flight to this particular turbulence condition.

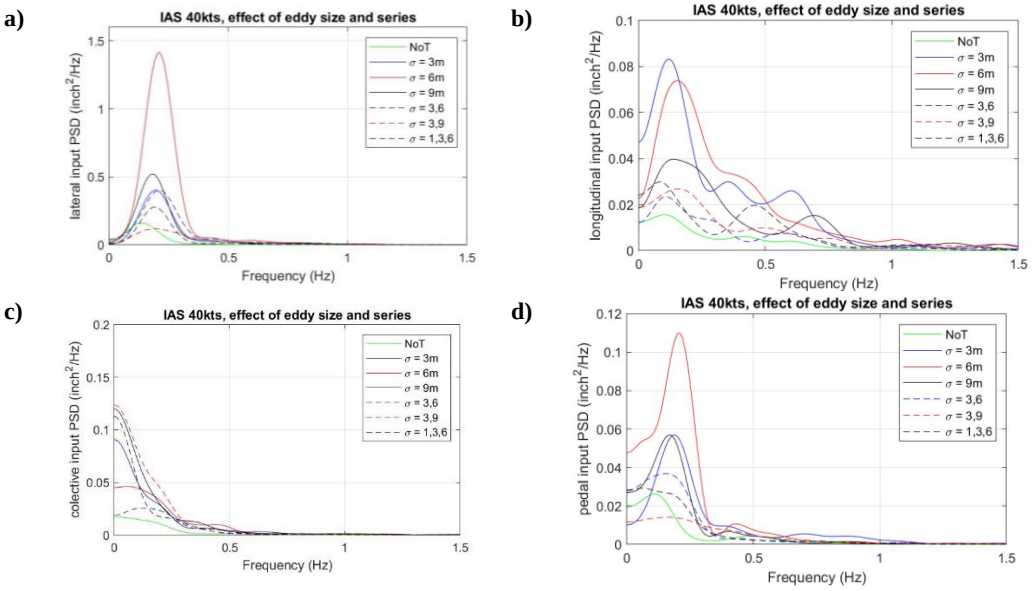

Figure 6-44: Power spectral density of pilot inputs during the steady and level flight task at 40kts for changes in eddy size and series. For a) lateral, b) longitudinal, c) collective, d) pedal

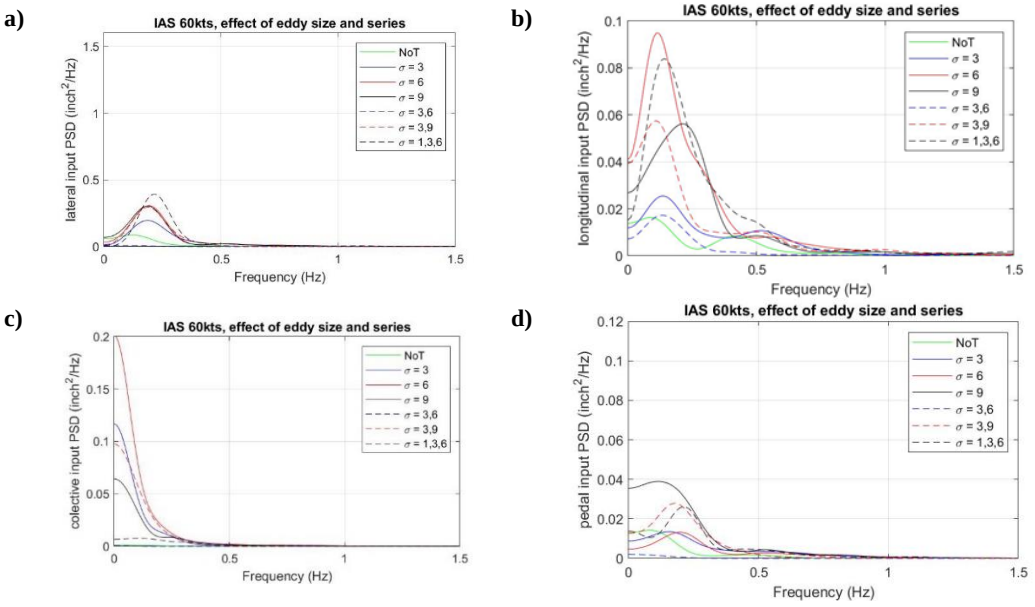

Figure 6-45: Power spectral density of pilot inputs during the steady and level flight task at 60kts for changes in eddy size and series. For a) lateral, b) longitudinal, c) collective, d) pedal.

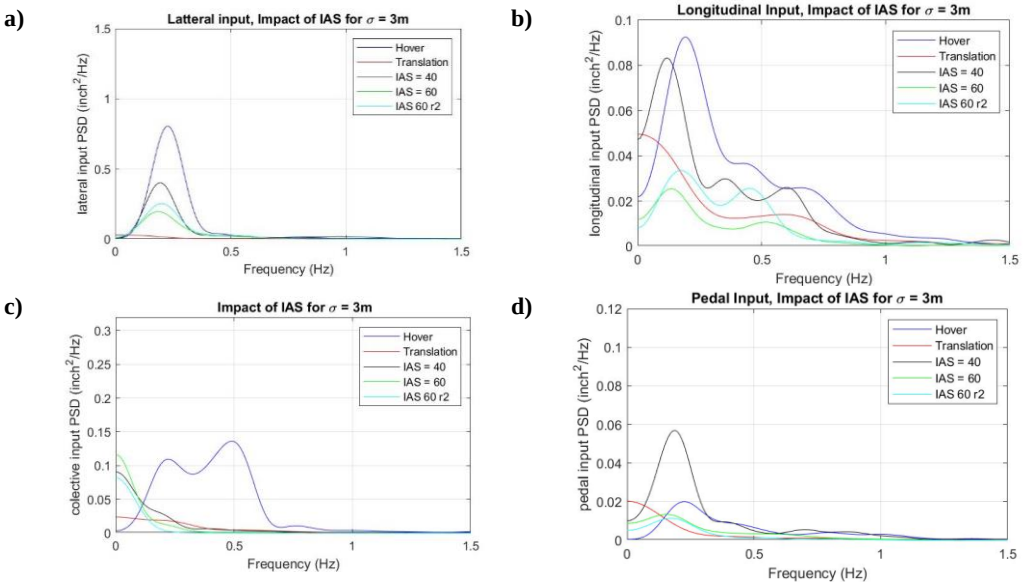

Figure 6-46: Power spectral density of pilot inputs under turbulence of eddy size σ_i = 3m for different flight conditions. For a) lateral, b) longitudinal, c) collective, d) pedal.

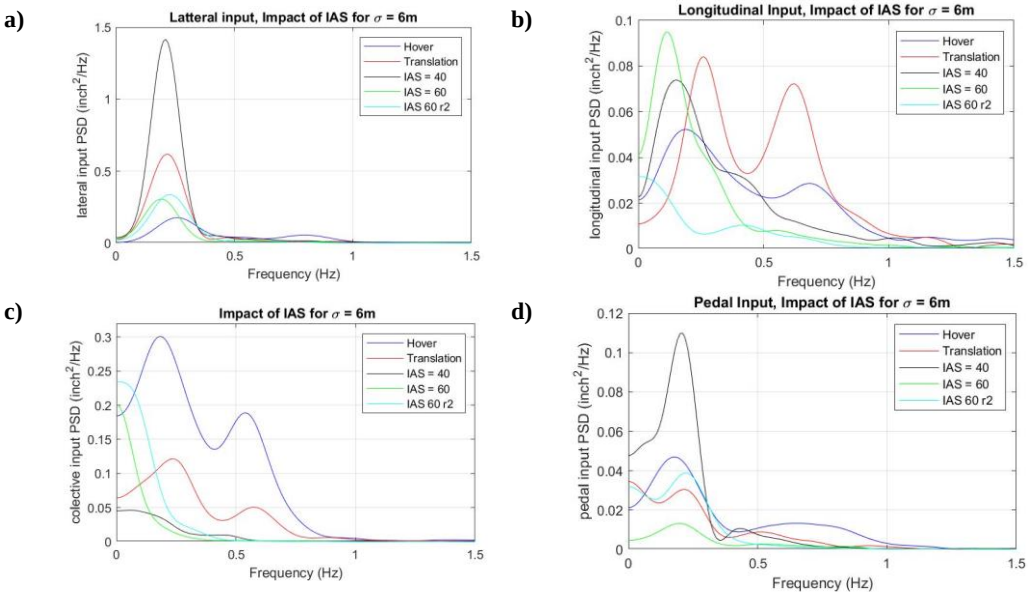

Figure 6-47: Power spectral density of pilot inputs under turbulence of eddy size σ_i = 6m for different flight conditions. For a) lateral, b) longitudinal, c) collective, d) pedal

6.5.3.4 Discussion of Steady and level flight

In contrast with the hover task, the S&L flight task was less demanding for the pilot and this also resulted in a lower overall impact of turbulence. While pilot workload rating shows clear increases when flying under increased turbulence intensity, task performance was less affected with the pilot managing to keep deviations within desired boundaries in most cases and always within adequate. The pilot indicated that maintaining lateral positioning and heading was the main source of workload during steady and level flight.

Impact of different eddy sizes presents an interesting situation were the particular condition of $\sigma_i = 6m$ tested seems to impact pilot workload and task performance more than other eddy sizes or combinations of eddy series. This trend was also visible during the translation phase of the hover task.

For the 40kts and 60kts S&L flights, a turbulence with eddy size $\sigma_i = 6m$ results in turbulence over the aircraft of an average frequency around 1Hz and 1.4Hz respectively. Overall, when taking into account aircraft flight velocity, workload seems to peak when average frequency of the disturbances stays within the 1 to 1.5Hz range (Figure 6-42).

The reasons for the higher workload under turbulence within this frequency range are unclear. Forward flight and translation to the hover point places a greater demand for pilot compensation in the lateral and longitudinal axes, and this does not seem to change significantly under turbulence. Turbulence at this frequency might have a greater effect in roll and pitch (see Figure 6-12) upsets for this aircraft which might be the reason behind pilot workload increases.

Turbulence induced by multiple series of eddies also has an impact in pilot workload, but it does not seem to be fundamentally different to the effects observed when simply altering the size of eddies using a single uniform series, with pilot activity showing mainly changes in input amplitude in response to changes in turbulence conditions.

6.6 Chapter Summary

In this chapter the impact of the turbulence generated by the upgraded SEM model on helicopter handling qualities was studied.

The chapter described an improved version of the SEM which allows the use of multiple series of eddies of different scale and length to be included in the simulations. By mixing large scale, high Re_{ii} eddies with smaller eddies of lower Re_{ii} values, the resulting turbulence is a more realistic mixture of high amplitude, low frequency and low amplitude high frequency disturbances, addressing the issue of a bland or non-uniform turbulence pointed by pilots in previous trials.

Offline simulations performed with the aircraft showed that the RCAH configured SCAS, reduces the amplitude of attitude moment oscillations of the aircraft with frequencies below 1Hz, but shows limited mitigation against disturbances at higher frequencies. As result, the SCAS prevents disturbances in roll and pitch from building up, but not disturbances in yaw which impede precision handling. Using multiple series of eddies to generate turbulence, the resulting disturbances can be spread across a broader frequency range for turbulence of the same total value of Re_{ii}.

As a general trend, the presence of turbulence results in a worsening of aircraft handling, an increase in pilot workload and a reduction in task performance. These effects become more severe as the values of Reynolds stresses, and therefore total turbulence intensity, increase.

The PH MTE puts the greater demand on the pilot and is the most susceptible to be impacted by the presence of turbulence. Disturbances in heave, and the need to counteract them during the station keeping phase, were the main cause of workload increases for the pilot. Turbulence of higher intensity and/or lower frequencies has a larger impact on pilot workload and task performance, with PSD of pilot control inputs showing an increase in the amplitude of pilot inputs in all axes. Station keeping under low frequency turbulence might result in PIO prone conditions in the heave axis, which significantly increases pilot workload and reduces task performance.

When flying under turbulence induced by a single series of eddies, pilot workload manifests itself mainly as an increase in amplitude of control inputs. In contrast, when keeping hover under turbulence induced by multiple series of eddies, pilot control inputs in collective and pedal show a spread across a wider frequency range. Higher RMS values of turbulence also seem to lead to higher RMS of pilot inputs in collective and higher workload ratings during the station keeping phase.

During translation, the aircraft exhibited a distinct behaviour when flying under turbulence induced by eddies of size $\sigma = 6m$. Large variations in approach rate to the

hover point and larger pilot inputs in lateral and longitudinal axis to counter this effect were required, the latter spread across a wider frequency range. Pilot workload was still driven by the station keeping phase.

During S&L flight, the main impact of turbulence on pilot workload were disturbances in lateral positioning and heading, followed by speed control. Highest workload ratings were awarded by the pilot when eddy size and flight speed resulted in turbulence with an average frequency between 1 and 1.5 Hz which are values close to the Bell 412 bandwidth limits in the lateral axis. PSD plots of pilot control inputs also show larger amplitude of inputs in the longitudinal and lateral axis for those runs.

Overall, the pilot workload ratings were lower and task performance higher for the S&L task when compared with the PH MTE. In contrast to the PH MTE, the use of multiple-scale eddies did not seem to lead a wider frequency range of corrective pilot control responses.

The results show that the SEM model can be applied for flight simulation testing. For hovering flight and precision manoeuvres, the use of multiple-scale eddies results in a different pilot response with pilot control inputs covering a wider range of frequency than when subjected to a single size of eddy. This suggests that, at least for hover, the impact of turbulence on flight is not only dependent on its amplitude, but also its frequency distribution.

The next chapters focus on using calibrating the SEM model to reproduce specific turbulence conditions.

7 Calibration of the Synthetic Eddy Model and comparison with turbulence models

7.1 Introduction

From the tests performed in the previous chapter, it was concluded that using multiple series of eddies of different scales and strengths resulted in the pilot changing his response to turbulence induced disturbances during hover.

The focus of this chapter is on the calibration of the multi-scale SEM model to reproduce specific turbulence conditions. This has been done by selecting the values for parameters defining the properties of the eddies for each of the eddy series in the SEM model. The aim has been to find a strategy that draws on turbulence data from a variety of sources, such as precomputed CFD solutions, experiments or real-world measurements. This input will allow the SEM to generate random turbulence in real time that reproduces the most relevant properties of the data, without the need to preload the original dataset for each simulation session.

To rapidly create a dataset to test this concept, a generator that uses Mann's atmospheric turbulence model was used to create a series of turbulence fields which were integrated with the flight simulator. The SEM model was calibrated to reproduce the PSD of the turbulent flow velocities produced by the pre-generated turbulence fields. Three strategies were tested for this calibration which differ in the target PSD towards which the SEM was adjusted: The first is a direct adjustment of the SEM model to the theoretical von Karman spectrum (referred as VK-Fit). The second obtains an approximate curve to the measured PSD at the centre point of the Mann wake and fitting the SEM model to this intermediate curve (Curve – Fit). The third strategy, uses the cross-section average of the Mann wake PSD as the target for fitting the SEM model (Direct – Fit).

The turbulence generated by each model was compared, by evaluating the match to the flow velocity PSD and time averaged convergence of Reynolds stresses as well as RMS and average frequency of generated turbulence for different input values of Reynolds stress tensor and turbulence wavelength.

Offline flight simulation was used to compare the impact of the generated turbulence on the aircraft, focusing on the PSD and RMS values of turbulence induced moments

and forces. For a head wind, whilst experiencing the turbulence conditions generated by the Mann wakes and reproduced by the SEM, the aircraft's SAS was capable of containing disturbances in roll, pitch and also yaw. Therefore, the head wind condition was used for offline and piloted simulations in this chapter to examine the effect of the turbulence without having to take the SAS performance into account.

The chapter is structured in three parts. Section 7.2 describes the theoretical background of the Mann turbulence model (Section 7.2.1) and the integration of the airwakes with FLIGHTLAB (Section 7.2.2). Section 7.3 describes the three strategies which were tested to fit the PSD of SEM generated turbulence to the turbulent PSD of the Mann generated wakes: VK-Fit, Curve-Fit and Direct-Fit, are described in Sections 7.3.1, 7.3.2 and 7.3.3 respectively. Characteristics of the turbulent flow generated by the Mann wakes and the different SEM fitting strategies is described in Section 7.3.4. Offline simulations to assess the fitting and aircraft responses to the different turbulence models are compared in Section 7.4. Finally, Section 7.5 summarizes the chapter and discusses the results.

7.2 Time accurate wakes using a Mann atmospheric turbulence model

7.2.1 Theoretical Background:

To allow for rapid generation of precomputed airwakes for testing of calibration strategies and evaluation of impact on simulated flight, a Mann atmospheric turbulence model [51] was used; the turbulence generator employed was developed by the Technical University of Denmark [120]. Mann's turbulence model generates a turbulence flowfield which allows adjustment of the resulting turbulence to account for atmospheric boundary layer and ground shear effects at low altitude and has been applied in the generation of inflow turbulence for wind turbine CFD simulations [52].

Mann's model uses the spectral tensor for isotropic incompressible turbulence and von Karman's energy spectrum:

$$\boldsymbol{\Phi_{ij}(k) = \frac{E(k)}{4\pi k^4}(\delta_{ij}k^2 - k_i k_j)} \qquad 7\text{-}1$$

where $\boldsymbol{k}$ is the wave number vector and $k = |\boldsymbol{k}| = \sqrt{k_1^2 + k_2^2 + k_3^2}$ its modulus and $E(k)$ is von Karman's energy spectrum:

$$\boldsymbol{E(k) = \alpha \epsilon^{\frac{2}{3}} L^{\frac{5}{3}} \frac{L^4 k^4}{(1 + L^2 k^2)^{\frac{17}{6}}}} \qquad 7\text{-}2$$

where α is the Komolgorov constant, ϵ is the dissipation of kinetic turbulent energy and L is the characteristic wave length of the turbulence.

The resulting flow field is computed from the Fourier transform of the Fourier–Stieltjes vectors, $\boldsymbol{Z(k)}$, over the relevant wave number space:

$$\boldsymbol{u(x) = \int e^{ikx} dZ(k)} \qquad 7\text{-}3$$

where the values for the Fourier–Stieltjes vectors are randomly generated following a Gaussian distribution and are related to the spectral tensor by:

$$\boldsymbol{\langle dZ_i^*(k) dZ_j(k) \rangle = \Phi_{ij}(k) dk_1 dk_2 dk_3} \qquad 7\text{-}4$$

To account for boundary layer shear and resulting anisotropy [121], Mann applies a correction to the isotropic Fourier-Stieltjes vector as follows:

$$\boldsymbol{dZ(k) = \begin{bmatrix} 1 & 0 & C_1(k,\beta) - \frac{k_2}{k_1} C_2(k,\beta) \\ 0 & 1 & \frac{k_2}{k_1} C_1(k,\beta) + C_2(k,\beta) \\ 0 & 0 & \frac{k_0^2}{k^2} \end{bmatrix} * dZ_{ISO}(k)} \qquad 7\text{-}5$$

where $k = |\boldsymbol{k}| = \sqrt{k_1^2 + k_2^2 + k_3^2}$ is the wave number modulus and $k_0 = |\boldsymbol{k_0}| = \sqrt{k_1^2 + k_2^2 + k_{3,0}^2}$ where $k_3 = k_{3,0} + \beta k_1$ accounts for the changes in the wave vector with time due to the dimensionless eddy life time β. This is obtained from the atmospheric boundary layer wind shear, $\frac{d|U|}{dz}$, a parameter defining shear, Γ, due to the boundary layer, the wave number and characteristic turbulence length:

$$\boldsymbol{\beta = \frac{d|U|}{dz} (kL)^{-\frac{2}{3}} \Gamma} \qquad 7\text{-}6$$

An attempt was made to model an atmospheric boundary layer (ABL) within FLIGHTLAB using the same interfaces employed for the airwakes and SEM turbulence. However, during the trimming phase, the change in the flow velocities experienced at an ACP, due to the ABL, are not considered in the current interface implementation. Given the time constraints for developing this trial no further development of the interfaces was undertaken to represent an ABL and hence no shear was implemented for the Mann wakes.

Thus, for cases with no shear, $\Gamma = 0$, the correction coefficients tend towards the isotropic Fourier–Stieltjes vector:

$$\boldsymbol{C_1}(\boldsymbol{k},\boldsymbol{0}) = \boldsymbol{0}\ ;\ \boldsymbol{C_2}(\boldsymbol{k},\boldsymbol{0}) = \boldsymbol{0}\ ;\ \boldsymbol{k_{\beta=0}} = \boldsymbol{k}$$

$$\boldsymbol{dZ}(\boldsymbol{k})_{\boldsymbol{\beta=0}} = \boldsymbol{dZ_{ISO}}(\boldsymbol{k}) \qquad 7\text{-}7$$

and the PSD of the obtained turbulence should tend to the von Karman spectrum (Eq. 7-18).

7.2.2 Implementation of Mann Model within FLIGHTLAB

A series of flowfield domains were computed using a Mann field turbulence generator developed by the Technical University of Denmark [120]. The model takes as input the parameters $\alpha\epsilon^{\frac{2}{3}}$, L and Γ , grid size and resolution in x, y and z axes and a seed number to generate a random turbulence field.

For flight simulation, three wakes were generated with a grid resolution of $dx = dy = dz = 1m$, similar to the minimum distance between ACPs on the main rotor of the helicopter model (0.8m). The total grid size was of $N_x \times \mathrm{N}_y \times N_z = 512 \times 128 \times 64$. This results in a turbulence field large enough to perform a precision hover flying task (test track dimensions of ~ 100ft x 100ft x 25ft) without leaving the wake and which can be generated in a relatively short time (about 30 min each wake). Based on data from measurements [51], [121], 20m to 100m are realistic values for over sea turbulence wavelength. To not exceed half of the wave box width and in order to extend the data set to smaller, high frequency wavelengths, Wake lengths were chosen to be 5m, 15m, 30m, 45m. and 60m.

An adequate value of turbulence strength for flight simulation trials needs to be determined during testing based on pilot performance on the task and pilot feedback.

Therefore, all wakes were pre-generated for a value of $\alpha\epsilon^{\frac{2}{3}} = 1.0$. Once an adequate turbulence strength was found for testing, the resulting flow field velocities were scaled to the intended value of the Reynolds stress tensor without the need of generating new wakes for this specific intensity.

$$\boldsymbol{u_i^{ACP} = u_{i\ wake}^{ACP} \sqrt{\frac{Re_{ii_{Target}}}{0.6388\ \alpha\epsilon^{\frac{2}{3}} L^{\frac{2}{3}}}}} \qquad 7\text{-}8$$

Figure 7-1 depicts this scaling strategy at work with two wakes generated using the same seed and with values of $\alpha\epsilon^{\frac{2}{3}} = 1.0$ and $\alpha\epsilon^{\frac{2}{3}} = 2.0$. Scaling the resulting flow field of the first wake with Eq. 7-8 will generate the same output as the second.

Figure 7-2 schematizes the integration of the Mann generated flow fields with FLIGHTLAB. The setup is similar to the Virtual AirDyn [103], used at the University of Liverpool to implement time-accurate airwakes for flight simulation and offline analysis.

a)

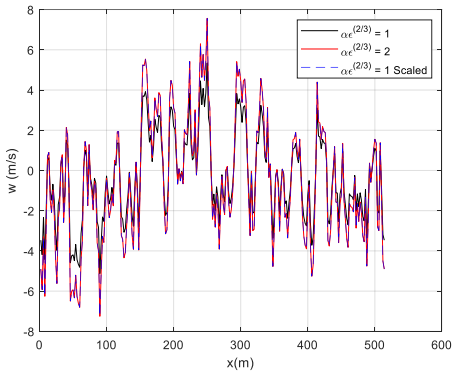

b)

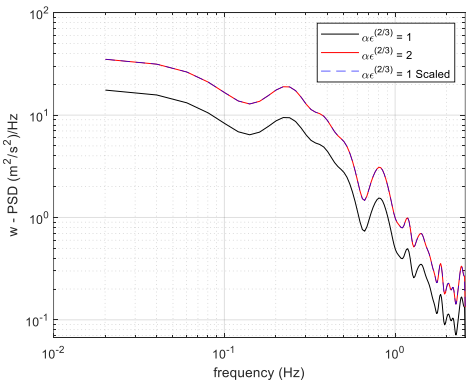

Figure 7-1: Scaling of w flow turbulence velocity to target Reynolds stress tensor: a) Time series, b) PSD

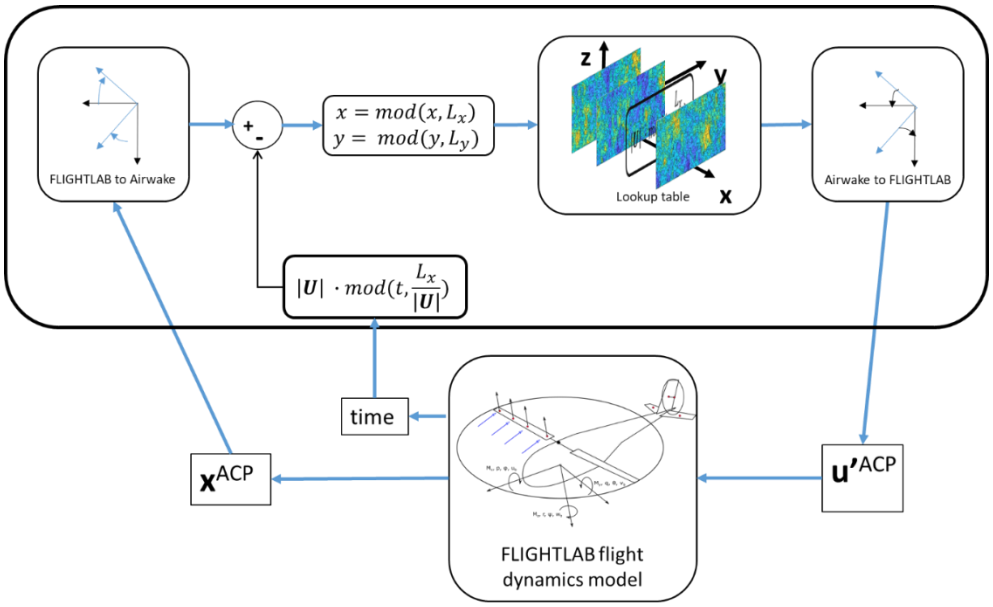

Figure 7-2: Diagram showing the integration of the Mann turbulence field with FLIGHTLAB.

A reference system is defined for positions within the wake box. The direction of the *x* – axis is defined along the main wind direction, the *z* – axis is pointed upwards and the *y* – axis defines a right-hand reference system. Displacement of the turbulence field with time is taken into account by using the frozen flow field hypothesis. *y* – z planes are displaced along the *x* axis with wind velocity. Once a slice reaches the end of the grid, it is returned to the initial position and the process repeats itself during the simulation.

Flow velocity disturbances in all three axes are interpolated across a uniform grid distributed along a right prismatic control volume with rectangular sides and stored as a look up table. At each time step, turbulent flow velocities at each of the aircraft ACPs are computed by interpolating from the flow velocities at the nearest grid points. The resulting flow velocities are sent to FLIGHTLAB which then resolves the resulting aircraft dynamics and the new location of the ACPs for the next time steps.

The current implementation is intended to reproduce atmospheric turbulence rather than disturbances at one specific location. To this aim, the wake is repeated periodically along the *x* and *y* directions. Should the aircraft leave the domain of the wake, the position of the aircraft ACPs relative to the wake box will be shifted to fall within the wake domain of the look up table.

7.3 Adjustment of SEM to turbulence conditions.

To reproduce non–isotropic turbulence, eddy size is modified [49]. For each turbulent velocity component in each axis *i*, an eddy length in each of the three axial directions *j* is defined:

$$\boldsymbol{f_{\sigma_{ij}}(x - x^{eddy}) = \sqrt{\frac{V_B}{\sigma_{i1}\sigma_{i2}\sigma_{i3}}} * \prod_{j=1}^{3} f\left(\frac{x_j - x_j^{eddy}}{\sigma_{ij}}\right)} \qquad 7\text{-}9$$

For multi-scale eddies, the resulting total PSD of SEM generated turbulence is the sum of the PSD produced by each of the individual series of eddies:

$$\boldsymbol{\phi_{ii}(x,\omega) = \sum_{m=1}^{N_{series}} \phi_{ii}^{m}(x,\omega) = \sum_{m=1}^{N_{series}} Re_{ij}^{m} \frac{\sigma_{ij}^{m}}{|U|} \left| \mathcal{F}_{\frac{\sigma_{ij}^{m}\omega}{|\bar{u}|}}\{f\} \right|^2} \qquad 7\text{-}10$$

For adjustment of the SEM generated turbulence, values for these parameters can be obtained from measurements or CFD simulations [122], [123]. The multi-scale SEM can be adjusted to a specific target spectrum. The procedure employed is an adaptation of the one described by Luo [114]. The variables to fit are the scalers for eddy strength, p_m, and eddy size, q_m, for each series:

$$\boldsymbol{\sigma_i^m = q_i^m * L\,;\; Re^m = p_i^m * Re} \qquad 7\text{-}11$$

where L is the wavelength of the spectra to fit. In order to reduce the number of variables to fit, the size scalers are related between them as:

$$\boldsymbol{q_i^{m+1} = \zeta_i q_i^m = \zeta_i^m * q_1^m} \qquad 7\text{-}12$$

Using MATLAB's least squares curve fitting function, the non-dimensional PSD of the SEM induced turbulence is fitted to the target spectra:

$$\boldsymbol{\frac{|U|}{Re_{ii} * L}\,\phi_{ii}^{SEM}(x,\tilde{\omega}) = \widehat{\phi_{ii}^{SEM}}(x,\tilde{\omega}) = \sum_{m=1}^{N_{series}} p_i^m q_i^m |\mathcal{F}\{f\}|^2 = \widehat{\phi_{ii}^{TARGET}}(x,\tilde{\omega})} \qquad 7\text{-}13$$

where $\tilde{\omega}$ is the dimensionless frequency: $\frac{L}{|U|} * \omega$.

To reduce the maximum number of eddies, the constraints defined in equation 7-14 are introduced. A minimum eddy size, σ_{min}, is selected and the size scaler, ζ_i^m, is set as equal or greater than one. And for the solution to make physical sense the minimum value for the scaler for eddy strength, p_i^m, has to be greater or equal to 0:

$$\begin{gathered} \boldsymbol{q_1^m \geq \frac{\sigma_{min}}{L}} \\ \boldsymbol{\zeta_i \geq 1} \\ \boldsymbol{p_i^m \geq 0} \end{gathered} \qquad \textit{7-14}$$

Finally, the resulting spectrum is dimensionalised again, by multiplying by $\frac{Re_{ii}*L}{|U|}$. Luo [114] sets the condition that $\sum_{m=1}^{N_{series}} p_i^m = 1$ to pre select the value of Reynolds stress tensor before solving for the SEM parameters. Here, to simplify the procedure and allow for adjustments after solving the parameters, the intended value of Re_{ii} is set by dividing it by the sum of the Reynolds stress scalers:

$$\boldsymbol{\phi_{ii}^{SEM}(x,\tilde{\omega}) = \frac{1}{\sum_{m=1}^{N_{series}} p_i^m} \frac{Re_{ii} * L}{|U|} \sum_{m=1}^{N_{series}} p_i^m q_i^m |\mathcal{F}\{f\}|^2} \qquad \textit{7-15}$$

Another adaptation used for the cases tested in this study, was the definition of a minimum eddy size of $\sigma_{ii} = 2m$ in order to limit the maximum number of eddies.

The fit was pursued under a wind velocity of $|\boldsymbol{U}| = 20kts$, which is typical of North Sea conditions during which offshore work can be conducted. The target spectrum to fit was defined by 59 points, covering a frequency range of 0.05Hz to 3Hz in intervals of 0.05Hz, which includes the 0.1Hz to 2Hz region in which upsets impact pilot workload. Fitting the turbulence spectrum induced by the Gaussian eddy shape (Eq. 5-22) requires the computation of an error function, leading to long computation times. To avoid this, the calibration study was performed using a cosine eddy shape function:

$$\boldsymbol{f(x) = \begin{cases} \frac{1}{\sqrt{3}}(1 + cos(\pi * x)), & if\ |x| < 1 \\ 0, & if\ |x| > 1 \end{cases}} \qquad \textit{7-16}$$

To simplify the fitting process, the Fourier transform of the shape function has been solved analytically:

$$\mathcal{F}(f) = \frac{1}{\sqrt{3}}\frac{\sigma}{U} sin(2\pi\omega)\left(\frac{4\pi\omega}{\pi^2 - (2\pi\omega)^2} + \frac{2}{2\pi\omega}\right) \quad 7\text{-}17$$

Figure 7-3 shows the shape of the analytically computed PSD of the cosine shaped function, compared to the previously used tent and Gaussian shaped functions. Its high frequency noise from the secondary lobes is initially higher than the gaussian shape function but decays faster with higher frequencies.

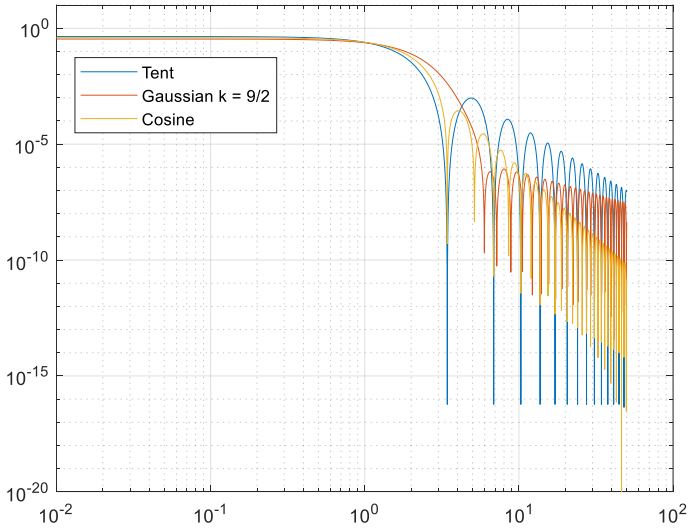

Figure 7-3: Analytically predicted PSD plots of SEM generated turbulence for cosine, tent and gaussian shape function. Eddy properties are: Re_{ii} = 1 m^2/s^2, σ = 3m.

7.3.1 Adjustment of SEM turbulence to von Karman turbulence spectrum

No boundary layer shear was modelled. Therefore, all cases of Mann turbulence considered were for values of $\Gamma = 0$. Under these conditions, the output of the Mann model should approach the von Karman energy spectrum. For turbulence in the direction of the main flow and in the lateral and vertical directions, these are defined as:

$$\phi_{uu}(\omega) = \frac{\pi}{U} * 0.4754 * Re * \frac{L}{\left(1 + \left(\frac{2\pi L}{U}\omega\right)^2\right)^{\frac{5}{6}}}$$

$$\phi_{vv}(\omega) = \phi_{ww}(\omega) = \frac{2\pi}{U} * \frac{1}{12} * 0.4754 * Re * L * \frac{3 + 8\left(\frac{2\pi L}{U}\omega\right)^2}{\left(1 + \left(\frac{2\pi L}{U}\omega\right)\right)^{\frac{11}{6}}} \quad 7\text{-}18$$

In practice the theoretical von Karman spectra appears to underestimate the amplitude of the generated turbulence as can be seen in Figure 7-4.

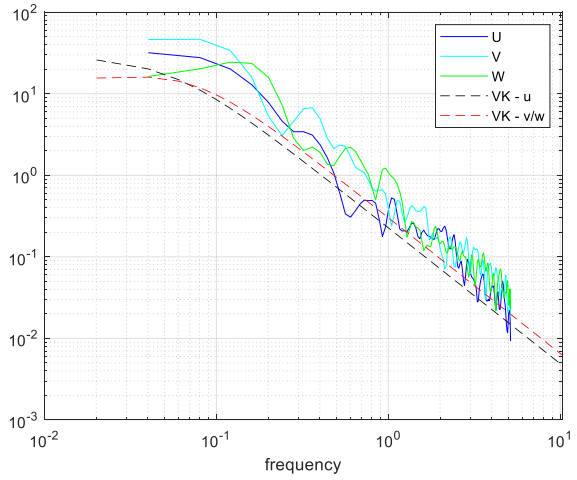

Figure 7-4: PSD of Mann turbulence components (continuous lines) against theoretical Von Karman spectra (dashed lines).

Following the process detailed at the beginning of this Section 7.3, a fit to this condition of the SEM model was performed, for the frequencies between 0.05Hz and 3Hz in increments of 0.05. This includes the range of 0.1Hz to 2Hz which is usually considered to have the largest impact on pilot workload [106], [124]. With a minimum eddy size of 2m and far field wind velocity of 20kts, a reasonable fit can be achieved for frequencies of up to 2Hz as shown in Figure 7-5. PSD values for the SEM model seem to be slightly higher in the range below 1Hz. For higher frequencies, the Mann model decays slower and induces a high frequency turbulence component much higher than the SEM.

Convergence of time averaged values of flow velocities, $\langle u'_i \rangle$, Reynolds stress tensor, Re_{ii}, flatness (or kurtosis), F_{u_i}, and skewness, S_{u_i}, shows a similar behaviour for both models, with rapid convergence initially and then a very slow, almost not existing convergence after the first 150 – 200 seconds (shown in Figure 7-6). Mann-generated wakes have been integrated as a time varying lookup table with a duration of about ~50s after which the turbulence field repeats itself periodically. As a result, no further convergence will occur for this model.

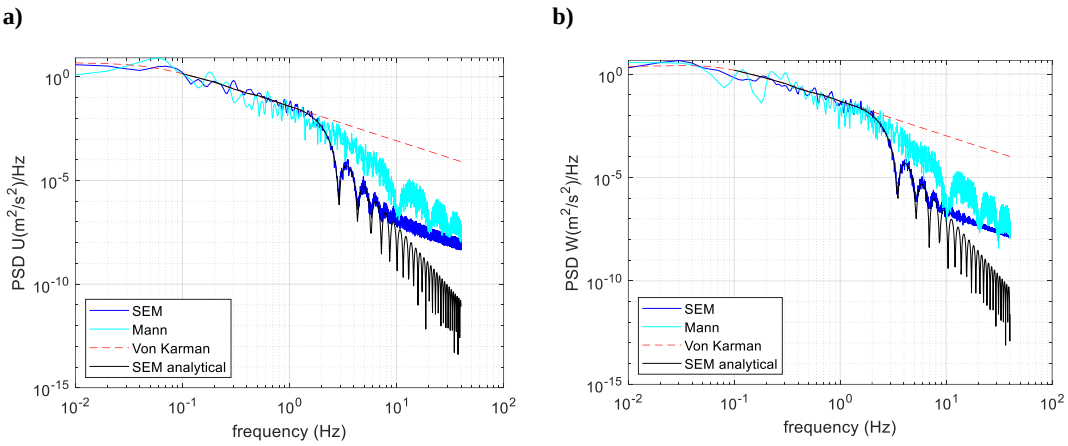

Figure 7-5: PSD fit of SEM turbulence (blue line: result, black line: analytical) to Von Karman flow (red dashed line), compared with Mann turbulence output (cyan line) for main flow direction (a) and lateral and vertical direction (b).

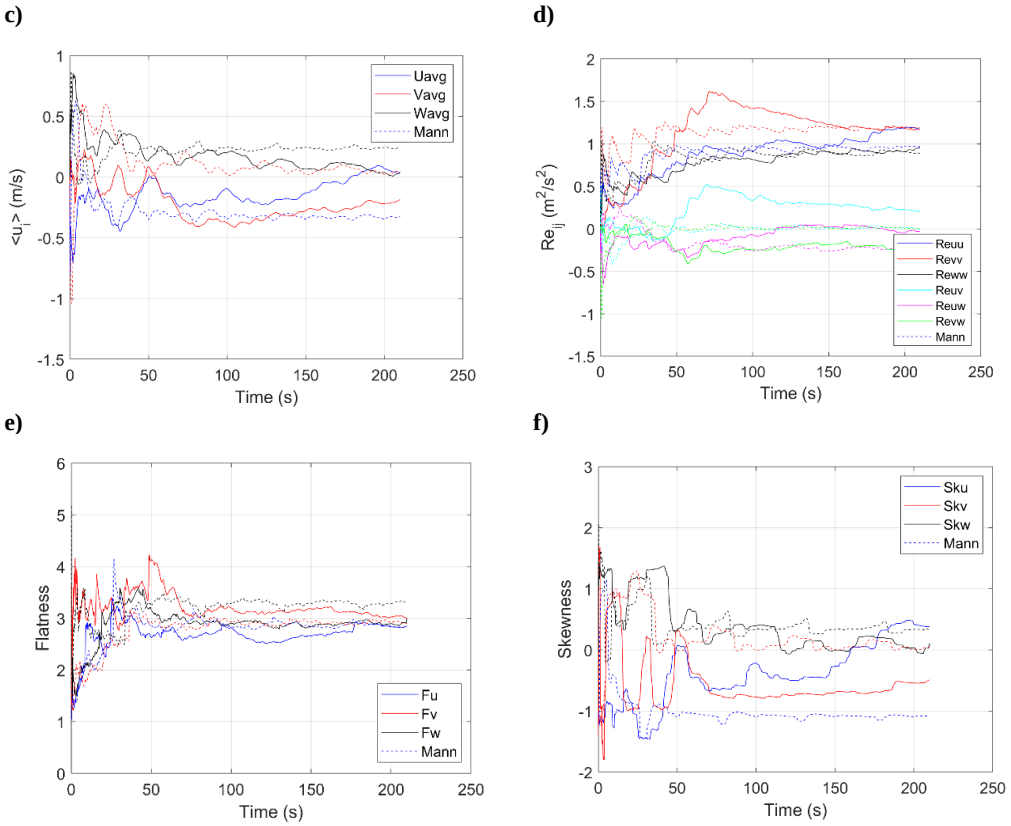

Figure 7-6:Cumulative time averaged values on fuselage ACP of: a) turbulent velocity components, b) Reynolds stresses, c) flatness and d) skewness for σ = 3m.

7.3.2 Intermediate PSD curve fit of local turbulence.

A second strategy was tested in order to fit the SEM model to a simulated or measured turbulence field at a given location rather than to a specific model. In this case, the dimensional PSD of the Mann generated turbulence at the centre of the wake box was approximated by a curve fit of the form:

$$\widetilde{\boldsymbol{\phi}(\widetilde{\boldsymbol{\omega}})} = \boldsymbol{A} * \frac{\boldsymbol{B} + \boldsymbol{C} * \widetilde{\boldsymbol{\omega}^2}}{\left(\boldsymbol{D} + \boldsymbol{E} * \widetilde{\boldsymbol{\omega}^2}\right)^{\boldsymbol{F}}} \qquad 7\text{-}19$$

Using the same MATLAB curve fit function as for the SEM turbulence, the parameters A, B, C, D, E and F were adjusted or set at a fixed value as shown in Table 7-1 in order to account for turbulence in the longitudinal direction (wake box reference, along wind direction) or lateral (perpendicular to main wind direction):

Table 7-1: Coefficients adjusted for curve fit to Mann turbulence spectra

Axis	Fixed	Variable
Longitudinal (u)	$C = 0\ ; F = 5/6$	A, B, D, E
Lateral (v,w)	$F = 11/6$	A, B, C, D, E

The resulting curve seems to provide a good fit at lower frequencies, but over predicts the power content at high frequencies as seen in Figure 7-7.

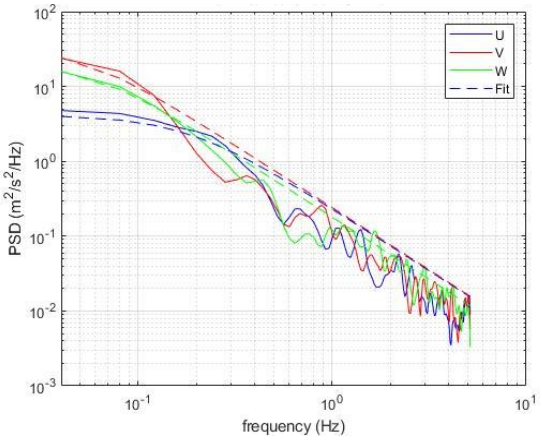

Figure 7-7: PSD of Mann turbulence components against PSD curve fit.

The SEM model was then fitted to this curve approaching the Mann turbulence PSD. At the location at which the Mann turbulence was extracted, a good match for turbulence in the lateral and vertical directions is obtained but large disturbances in the main flow direction are observed for frequencies above 0.1Hz (see Figure 7-8), with

convergence of cumulative time averaged values also showing a similar behaviour to the previous methods (Figure 7-9).

This fitting strategy, however, is sensitive to single large events occurring at the point of measurement. The curve fitting coefficients estimated can vary widely between locations, rendering the approach inadequate for other positions within the wake (see Figure 7-10 and Table 7-2).

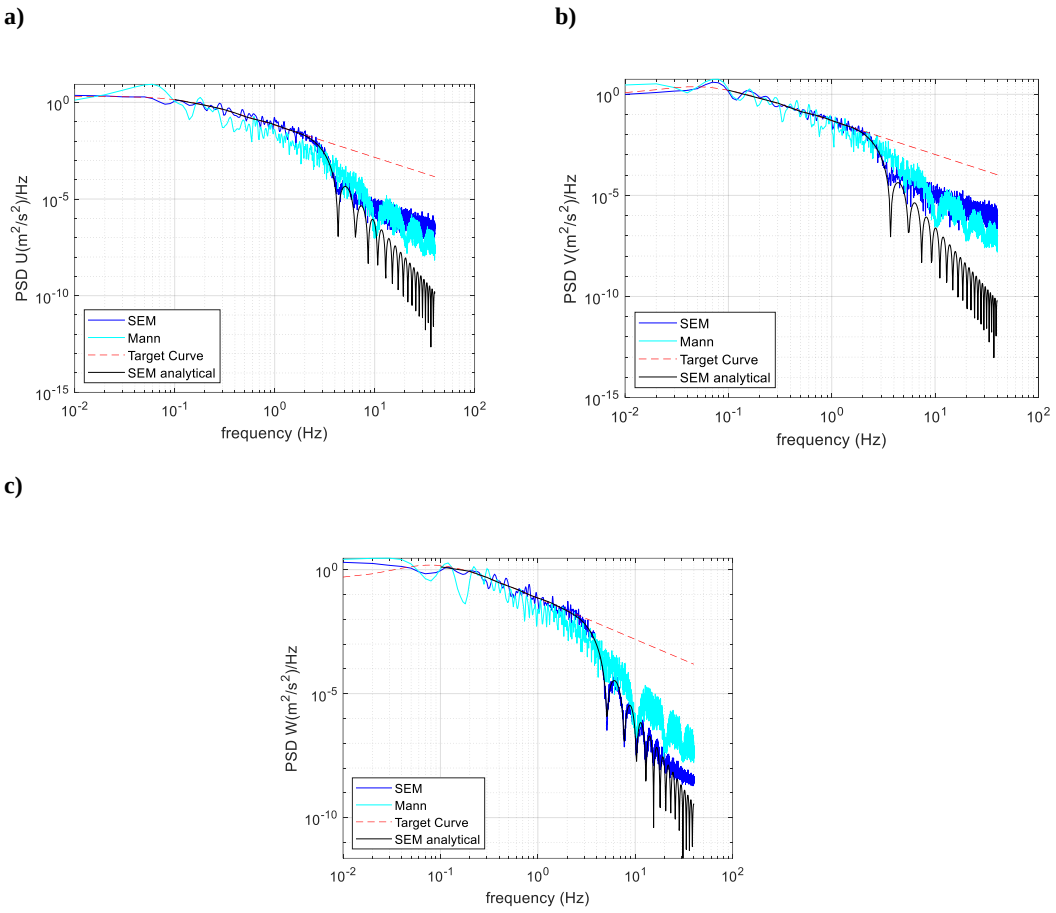

Figure 7-8: PSD fit of SEM turbulence at the centre of the Mann wake (blue line: result, black line: analytical) to Mann turbulence fit (red dashed line), compared with Mann turbulence output (cyan line) for main flow direction (a) and lateral and vertical direction (c).

Table 7-2: Coefficient values for curve fit for vertical Mann turbulence at a location at the centre of the wake and at ¾ of the y and ¼ of the z range.

Y (m)	Z (m)	A	B	C	D	E	F
64	**32**	0.65	2.33	516.39	2.26	43.29	11/6
32	**16**	1.18	2.93	245.56	3.31	40.97	11/6

The use of an intermediate curve approaching the turbulence PSD could be implemented in a future development of the SEM model to reproduce the localised

turbulence at different locations and adjust the resulting parameters of the SEM model according to the position of the aircraft.

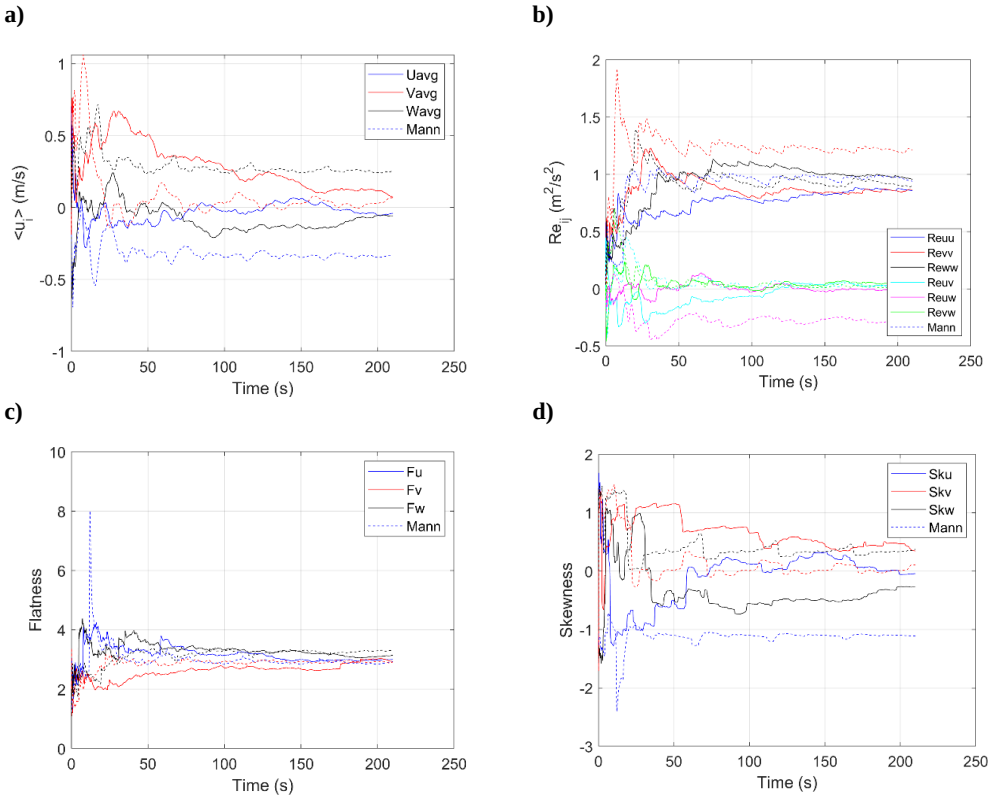

Figure 7-9: Cumulative time averaged values on fuselage ACP of: a) turbulent velocity components, b) Reynolds stresses, c) flatness and d) skewness for σ = 3m.

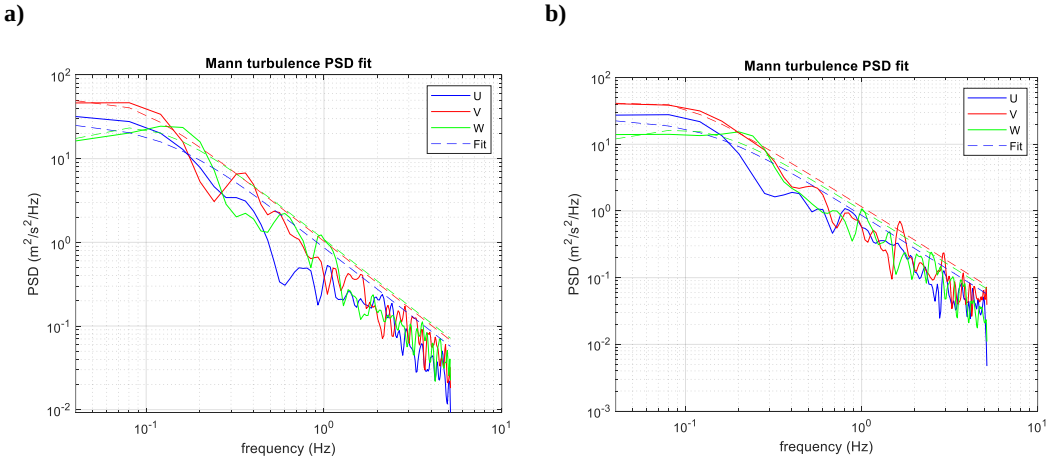

Figure 7-10: PSD of Mann turbulence components against PSD curve fit a) at the centre point of the Mann box, b) at ¼ of the position in y and z.

7.3.3 Direct SEM fit to average Mann PSD

A final strategy was to average the PSD of the Mann generated turbulence across an entire wake section (defined by a static y-z plane in the wake reference system) and directly approximate the predicted PSD of the SEM turbulence output to it (Figure

7-11). The resulting approach shows a similar fit as the adjustment to an approximate curve (Figure 7-12) but seems to better approach the Mann turbulence at all locations. Convergence of cumulative time averaged values behaves in a similar manner as the other two methods (Figure 7-13).

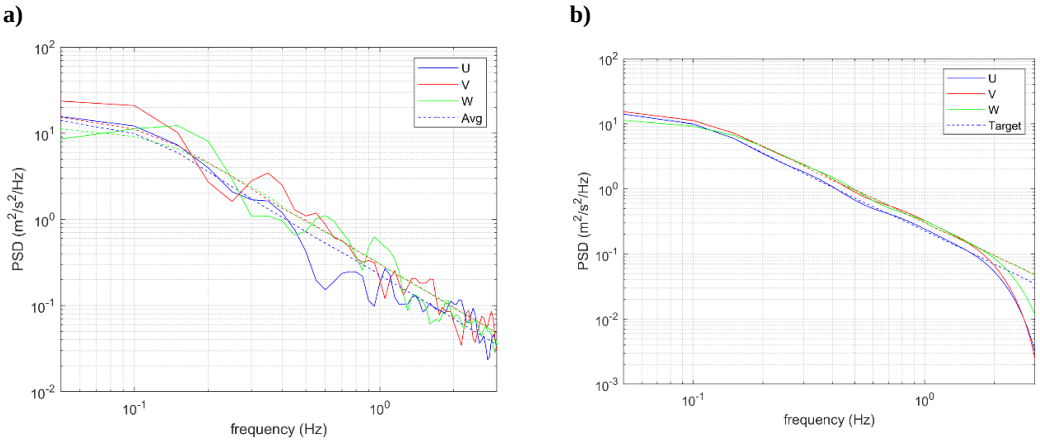

Figure 7-11: a) Mann turbulence PSD at centre point of box, compared with averaged PSD for entire box, b) Fit of SEM parameters to averaged Mann turbulence.

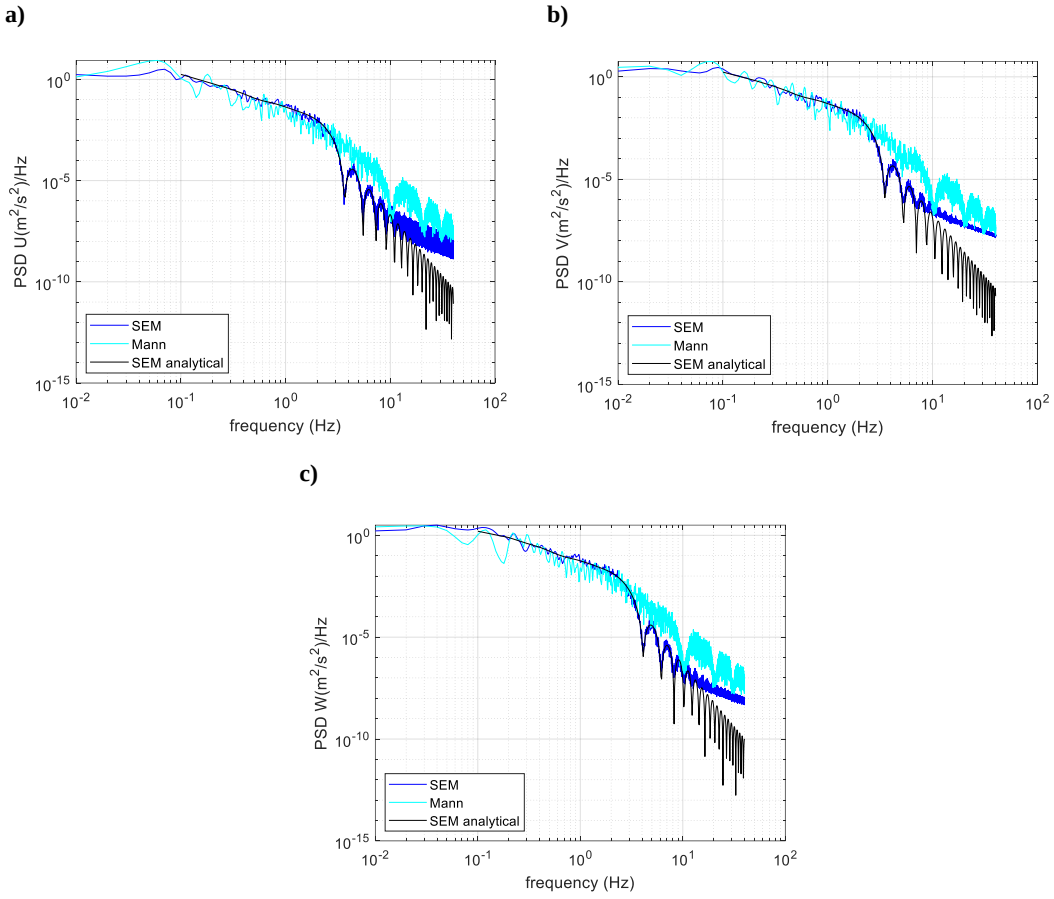

Figure 7-12: Direct PSD fit of SEM turbulence (blue line: result, black line: analytical) to Mann turbulence fit (red dashed line), compared with Mann turbulence output (cyan line) for main flow direction (a) and lateral and vertical direction (c).

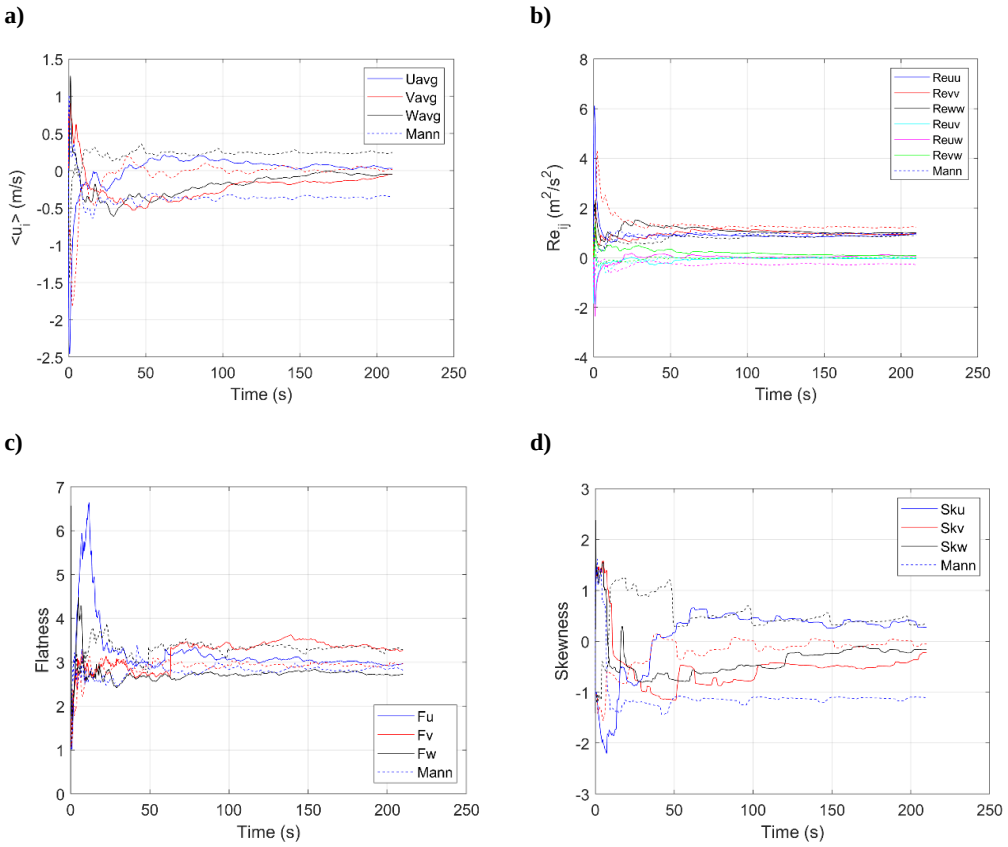

Figure 7-13: Cumulative time averaged values on fuselage ACP of: a) turbulent velocity components, b) Reynolds stresses, c) flatness and d) skewness for σ = 3m.

7.3.4 Comparison of turbulent flow:

A set of offline simulations were produced to compare the turbulence fields generated by the two models and the three fitting strategies. To this effect a series of Mann wakes were generated and integrated into FLIGHLTAB and corresponding SEM parameters were computed using the three fitting strategies. Due to a lack of a boundary model in FLIGHTLAB, the correction for spectral shear was not used and Γ was set as 0 for all wakes. Parameters of generated wakes are summarized in Table 7-3, while the SEM fitting parameters are given in Table 7-4.

All the results presented in this chapter correspond to offline simulations performed under a 20kts wind, 0deg azimuth.

Table 7-3: Input parameters for Mann generated turbulence flow fields

Parameter	Values				
Grid size ($N_x \times \mathrm{N_y} \times N_z$)	$512 \times 128 \times 64$				
Grid resolution (dx ; dy ; dz)	1m ; 1m ; 1m				
$\alpha\epsilon^{\frac{2}{3}}$	1.0				
Γ	0.0				
L (m)	5	15	30	45	60
Number of files generated	1	2	2	2	1

Table 7-4: Input parameters for SEM fit to Mann wakes.

Parameter	Values				
Fit	von Karman (VK)		Curve Fit		Direct Fit
Number of Eddy series	4				
Frequency range ; increments (Hz)	0.05 – 3 ; 0.05				
σ_{min} = Minimum eddy size (m)	2				
L (m)	5	15	30	45	60

PSD plots of generated turbulence for the L = 30m Mann wake and the three different fitting strategies for the SEM method are shown in Figure 7-14. The three strategies provide a relatively good fit for lower frequencies but start diverging for frequencies higher than 0.5Hz, where PSD values of the SEM induced turbulence decay with frequency at a slower rate than for the Mann wakes, especially for turbulence generated in the wind direction, with PSD values of SEM turbulence at 1Hz being two or three times those of Mann induced turbulence. This is especially so for the curve fitting strategy, while the fit to the theoretical von Karman spectra seems to provide the best fit. This situation reverses for above 3Hz, where the PSD of the SEM generated turbulence decays with frequency at a faster rate than for the Mann generated wakes, being an order of magnitude below the PSD from Mann induced turbulence around the 5Hz region.

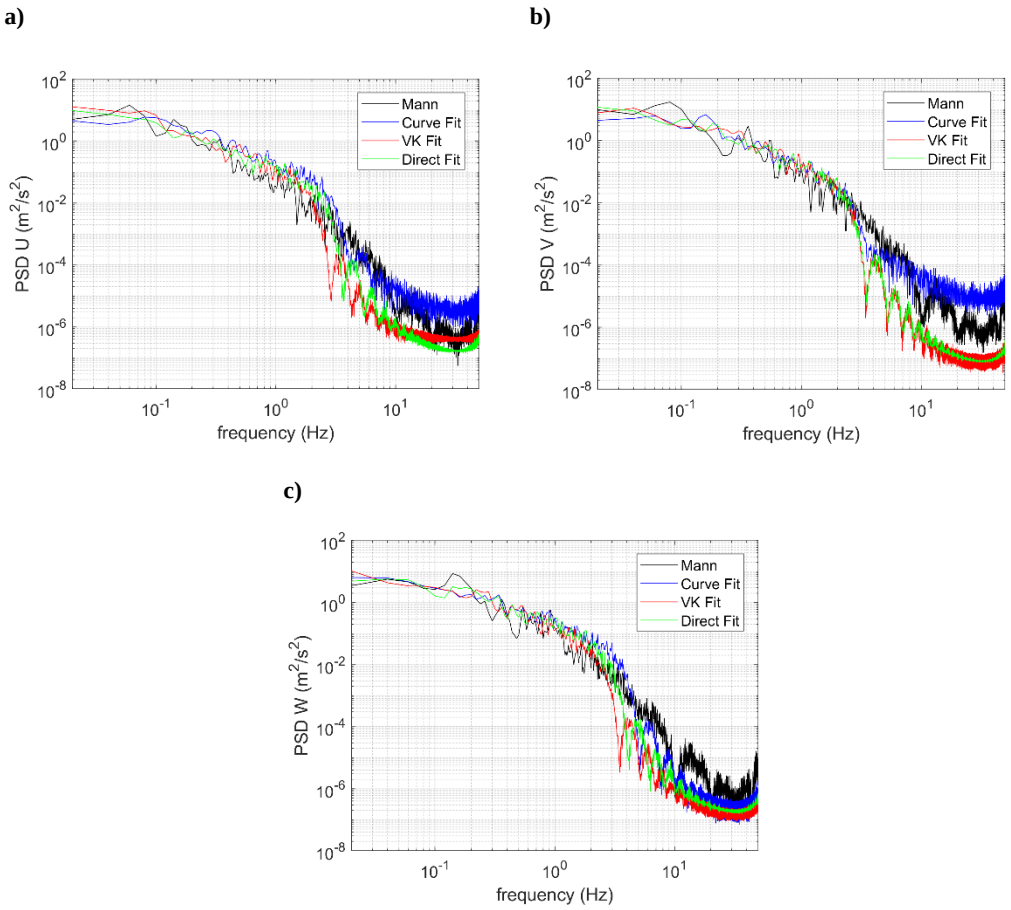

Figure 7-14: Comparison of turbulence PSD generated by the Mann wake and the three fitting strategies for the case of Re = 3 m^2/s^2 and L = 30m.

The variation in average frequency of the induced turbulence is shown in Figure 7-15. Bigger wavelengths result in lower average frequencies, and this holds true for both turbulence models and fitting strategies. Average frequency of SEM induced turbulence is consistently higher as a result of the higher power density of the SEM model within the 1Hz – 2Hz region. This difference is the largest when adjusting SEM parameters using an intermediate curve, while the average frequency when using the adjustment to the von Karman spectra is the closest to the original Mann model.

Figure 7-16 provides a comparison of RMS values, between 0.1Hz and 2Hz, of the turbulent flow velocity in all three axes against turbulence wavelength. This frequency range is considered to be where disturbances have the largest impact on pilot workload.

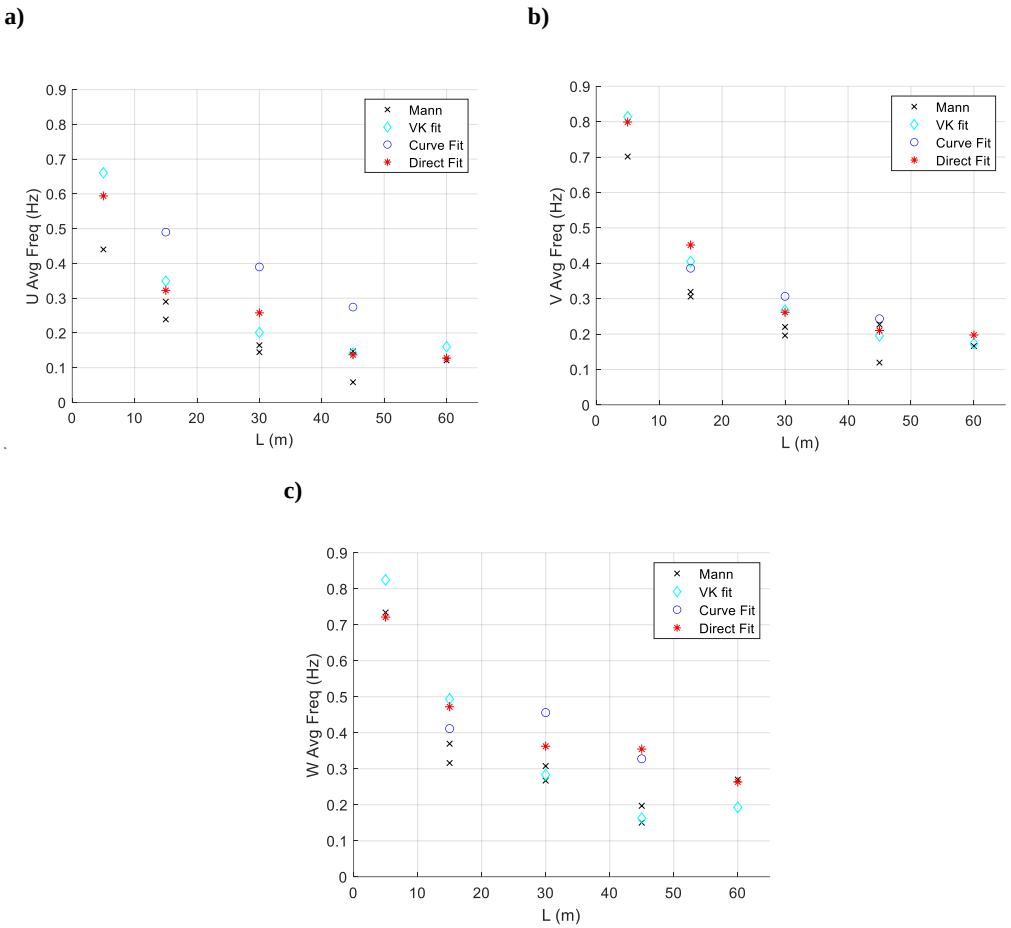

Figure 7-15: Average frequency of turbulence induced flow velocity against wavelength in a) longitudinal flow, b) lateral flow, c) vertical flow.

Generated turbulence presents a trend of lower RMS values for larger wavelengths. Although the Mann generated wakes present a slight decrease in turbulence RMS for wavelengths of $L \leq 30m$. In general, SEM generated turbulence presents higher RMS values than Mann generated wakes for a given wavelength. The fit to an approximate curve seems to present the largest deviation from the Mann wakes, while the approximation to the von Karman curve seems to result in the best fit, although the variability is large for the range of cases studied.

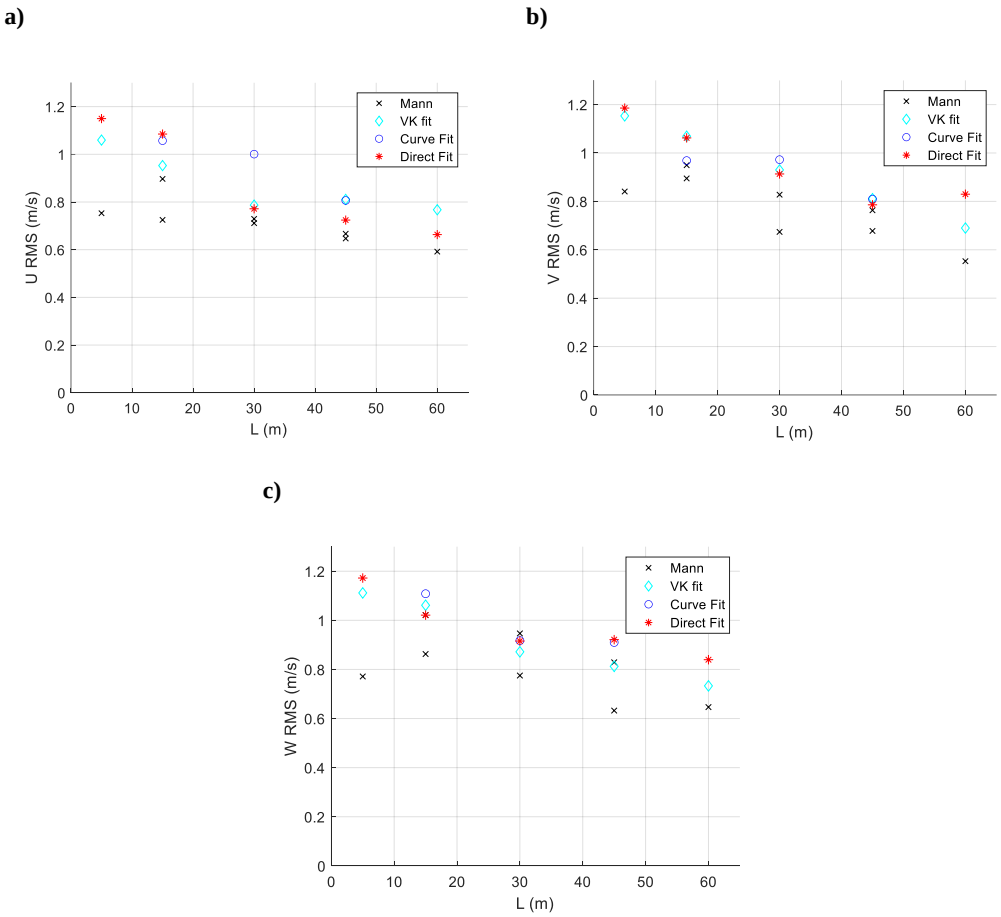

Figure 7-16: RMS of induced turbulent flow against turbulence wavelength for Mann induced turbulence and three fitting strategies for the SEM model for a) X – axis velocity component, b) Y – axis velocity component, c) Z – axis velocity component.

7.4 Offline simulations - Aircraft responses against different turbulence models:

7.4.1.1 Simulations with the aircraft frozen.

An initial set of simulations was performed with the aircraft displacements and rotations completely deactivated and with the SCAS system deactivated in order to get an overview of the forces and moments induced on the bare airframe helicopter by the different turbulence models. The simulations were performed under a 20kts wind with azimuths of 0 degrees (wind from the nose of the aircraft). For a 0 degree azimuth, under the Mann and SEM turbulence conditions tested, the SCAS system of the Bell 412 was able to contain the amplitude of oscillations in roll pitch and, in contrast to the turbulence conditions tested in previous chapters, also in yaw. Hence, the head wind was chosen to allow for better comparison between offline simulations and piloted simulation trials.

While convergence of cumulative time averaged variables slows significantly after the first minute of simulation for all models and fitting strategies (see Figure 7-6, Figure 7-9 and Figure 7-13), loads on the blades achieves full convergence for all cases as shown in Figure 7-17 a. Impact of turbulence on blade flapping is shown in Figure 7-17 b, presenting a very similar response for all the turbulence models, with the main differences being within the 1 – 3Hz range, where the fit to the von Karman spectra and to an intermediate curve seem to respectively under predict and over predict flapping PSD values when compared to the Mann generated wakes. At frequencies beyond 2Hz, most relevant impact comes from the four main rotor blades. Beyond frequencies of four times the rotor speed, the high frequency PSD of the induced disturbances is largely artificial, due to the repeated loop of the Mann turbulence and the cut-off effect from the limited simulation time (see discussion in Sections 5.2.4 and 5.2.5).

a) **b)**

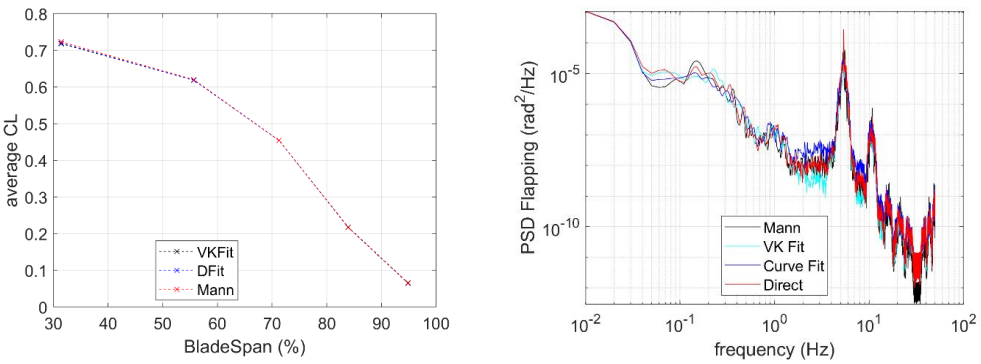

Figure 7-17: Impact of turbulence on main rotor: a) cumulative time averaged lift coefficient along blade, b) PSD of blade flapping angle, for the case of Re = 3 m^2/s^2 and L = 30m.

PSD of turbulence induced moments and vertical forces on the aircraft on the case of L = 30m and $Re_{ii} = 3\frac{\mathrm{m}^2}{\mathrm{s}^2}$ are shown in Figure 7-18. Differences in induced forces and moments between the turbulence models follow a similar pattern as shown for induced turbulent flow velocities (see Figure 7-14). PSD of SEM induced forces is higher near frequencies of around 1 Hz with the curve fitting strategy showing the largest discrepancies.

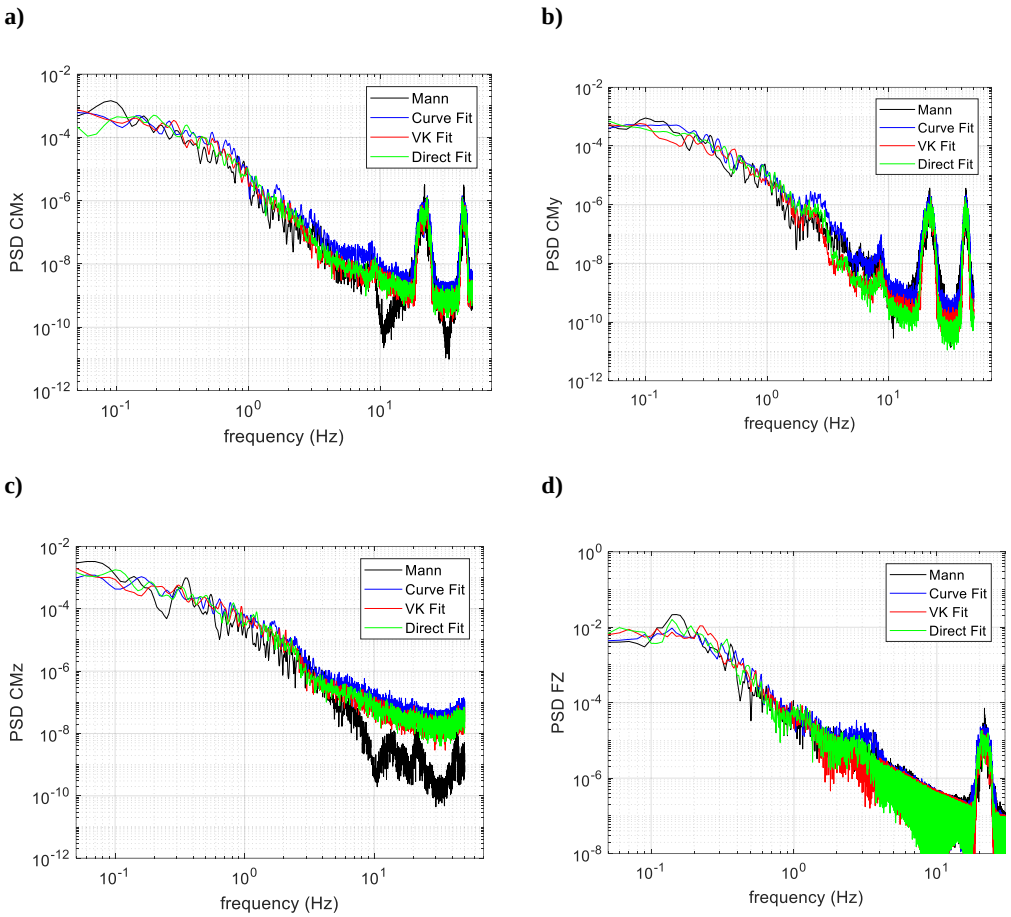

Figure 7-18: PSD of moment and force coefficients acting on the aircraft in a) roll, b) pitch, c) yaw and d) vertical force for the case of Re = 3 m^2/s^2 and L = 30m

RMS of induced moments and forces has been related to increased pilot workload in the past [61], especially for disturbances in the vertical axis. RMS of induced forces and moments during the simulation and RMS of induced turbulence velocities are shown in Figure 7-19. A trend of increases in RMS of turbulent flow velocities leading to increases in RMS of forces and moments acting on the aircraft can be clearly distinguished. With longitudinal turbulence (u) impacting pitch moments (M_Y), turbulence in the lateral direction (v) impacting roll (M_X) and yaw (M_Z) moments as well as turbulence in the vertical axis (w) and induced pitch moments (M_Y) and vertical forces (F_Z). While RMS values of induced turbulence from the SEM model are overall higher than for the Mann model for the same conditions, similar values of flow velocity RMS result in similar values of induced forces and moments across all models. However, the cases corresponding to the SEM turbulence using the direct fitting strategy show a stable value of RMS for F_Z against changes in RMS of turbulence, except for the smaller wavelength of $L = 5m$ which results in the highest values of RMS for w turbulence and lowest RMS of F_Z.

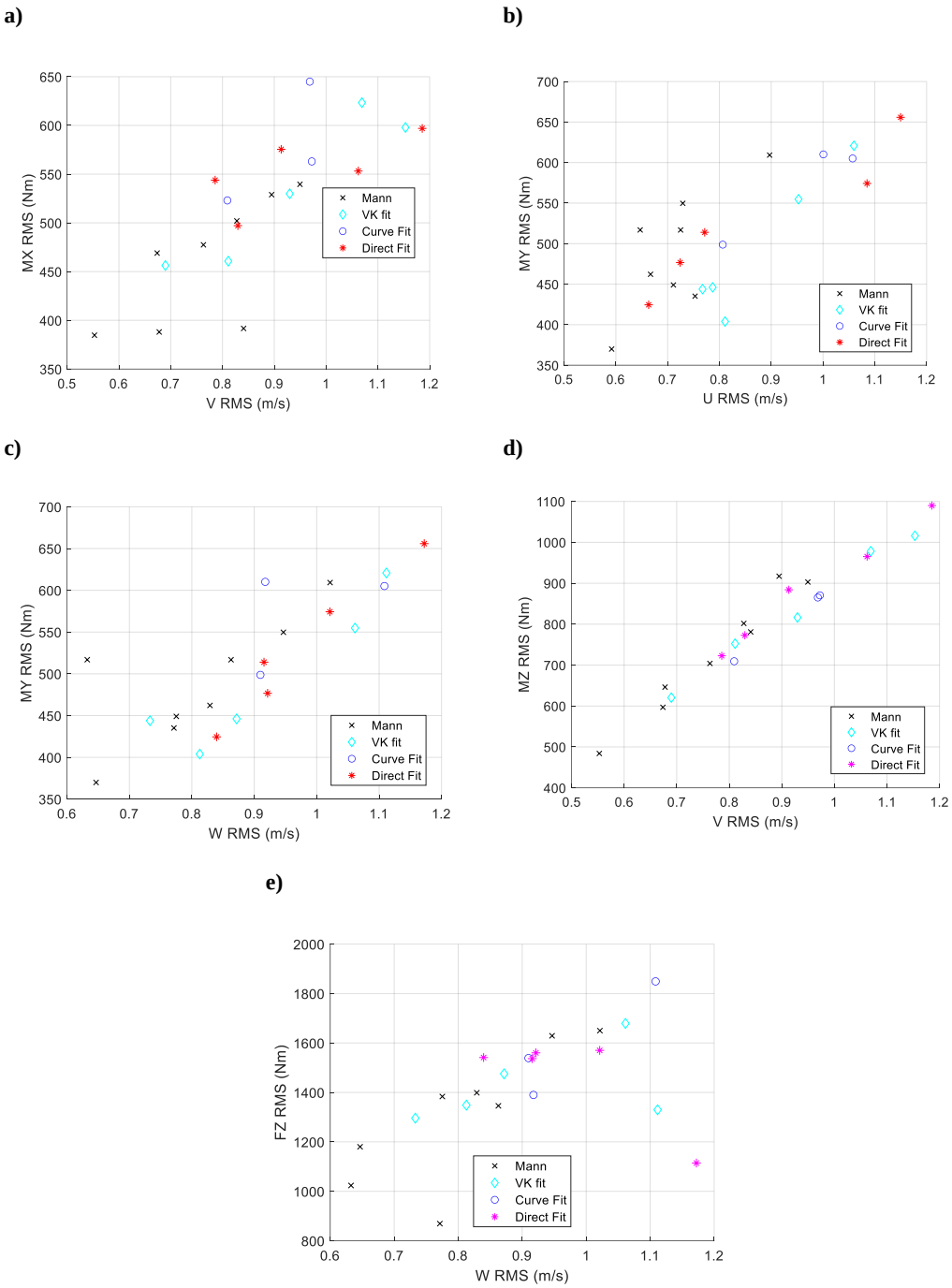

Figure 7-19: RMS of forces and moments acting on aircraft against RMS of turbulent flows: a) roll moments against lateral turbulence, b) pitch moments against longitudinal turbulence, c) pitch moments against vertical turbulence, d) yaw moments against lateral turbulence, e) vertical forces against vertical turbulence.

RMS of turbulence induced moments and forces against turbulence wavelength are shown in Figure 7-20. Trends follow a similar pattern as RMS of induced flow velocities (Figure 7-16), especially when the aircraft was subjected to Mann induced turbulence, this being most apparent for M_X and M_Z against lateral flow. All models show a fall in total RMS for F_Z under turbulence of the lowest wavelength of L = 5m.

Again, the trend is for SEM induced turbulence to lead to higher induced moments and forces. Although all three fitting strategies result in induced forces of similar magnitude and how well they approach the Mann model varies between each case.

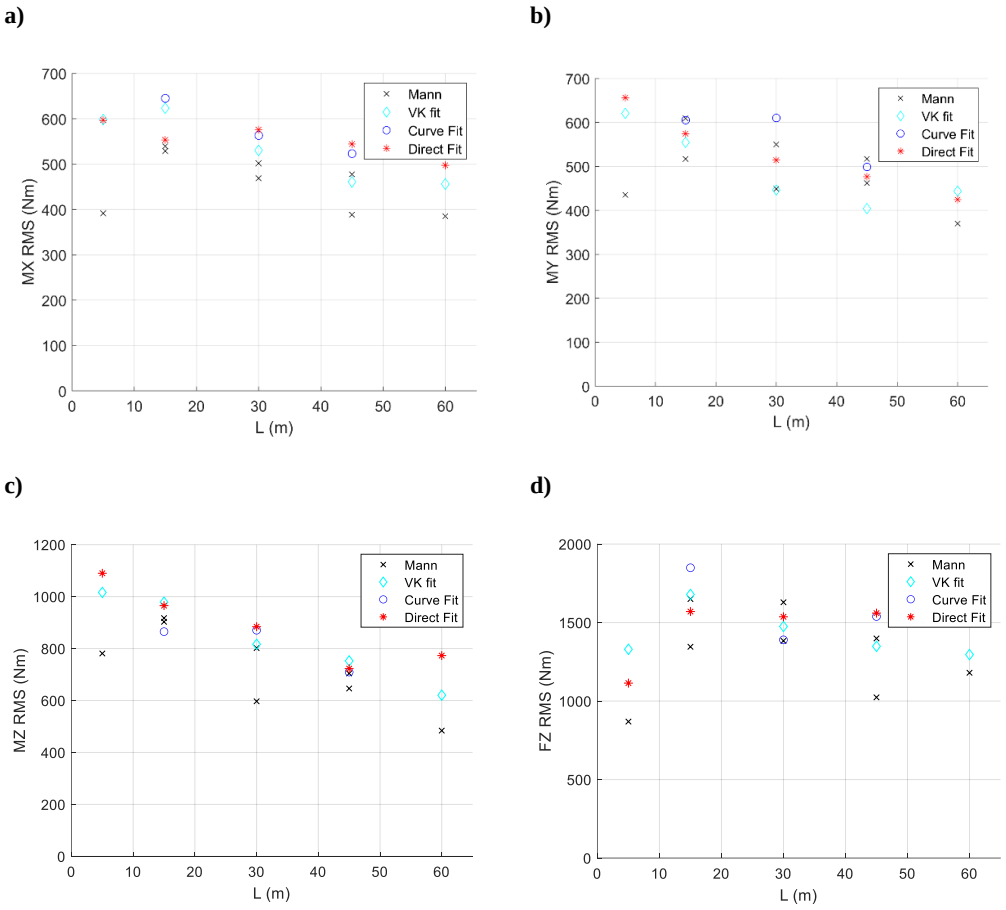

Figure 7-20: RMS of forces and moments acting on the aircraft against turbulence wavelength for the aircraft with displacements and attitudes frozen and SCAS deactivated: a) roll moment, b) pitch moment, c) yaw moment, d) vertical forces.

7.4.1.2 Simulations with attitudes unfrozen

A second series of simulations was performed in which aircraft attitudes were allowed to change and the SCAS system was activated and configured as RCAH. The aircraft was allowed to rotate freely in the roll, pitch and yaw axis, while the position was kept frozen. This allowed testing of the impact of turbulence on aircraft attitude and the capability of the SCAS system to reject disturbances providing an idea of the compensation effort required from the pilot in order to keep the aircraft in position.

PSDs of turbulence induced moments and vertical forces on the aircraft for the case of $L = 30$m and $Re_{ii} = 3\ m^2/s^2$ are shown in Figure 7-21, and the RMS for forces and moments across the range of wavelengths simulated are shown in Figure 7-22. They show a similar pattern of behaviour with L as seen in the frozen bare airframe (Figure 7-20).

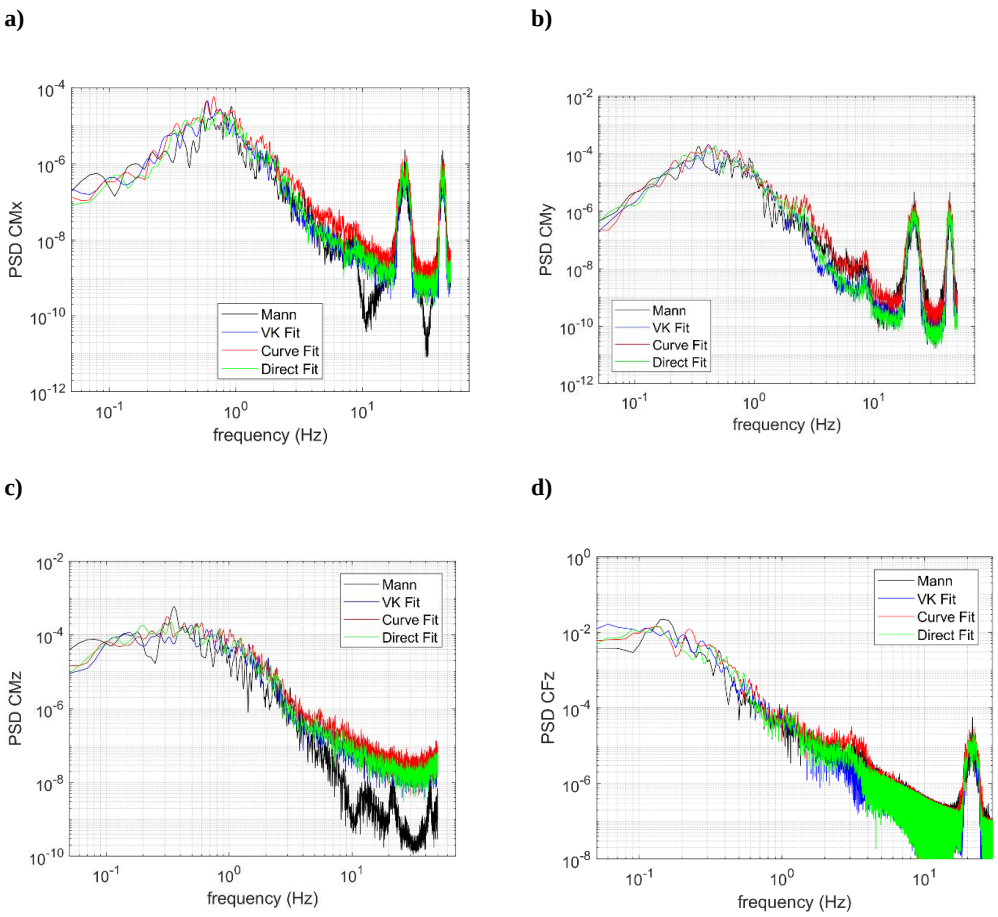

Figure 7-21: PSD of moment and force coefficients acting on the aircraft in a) roll, b) pitch, c) yaw and d) vertical force.

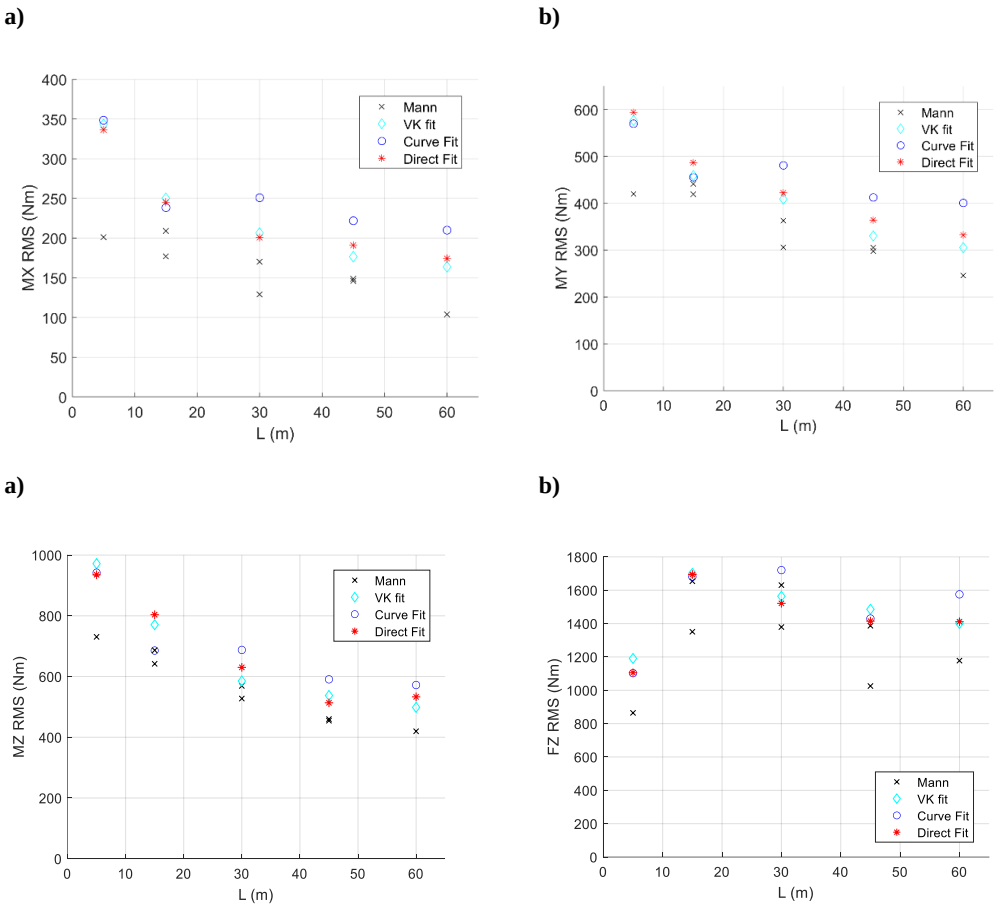

Figure 7-22: RMS of forces and moments acting on the aircraft against turbulence wavelength for the aircraft with free attitude changes and RCAH configured SCAS: a) roll moment, b) pitch moment, c) yaw moment, d) vertical forces.

The differences between the turbulence models in their impact on the aircraft seem to follow those observed for the simulations without SCAS and frozen movements in the previous section of this chapter. SEM turbulence results in somewhat larger disturbances within the 1Hz to 2Hz frequency range than the Mann model. Although there is again a consistent trend of the curve fit offering the worst fit and the approach to the von Karman curve offering the best fit for most of the wavelengths studied.

The impact of the SCAS systems can be appreciated as a significant reduction in the magnitude of induced moments acting on the aircraft. Especially in the region of frequencies below 1Hz. This is explained because the SCAS system mainly operates at and mitigates disturbances in low frequencies as can be seen in Figure 7-23 which depicts PSD of blade pitch angles for main and tail rotor. No significant change is evident in vertical forces, as the aircraft lacks any stability system in the heave axis.

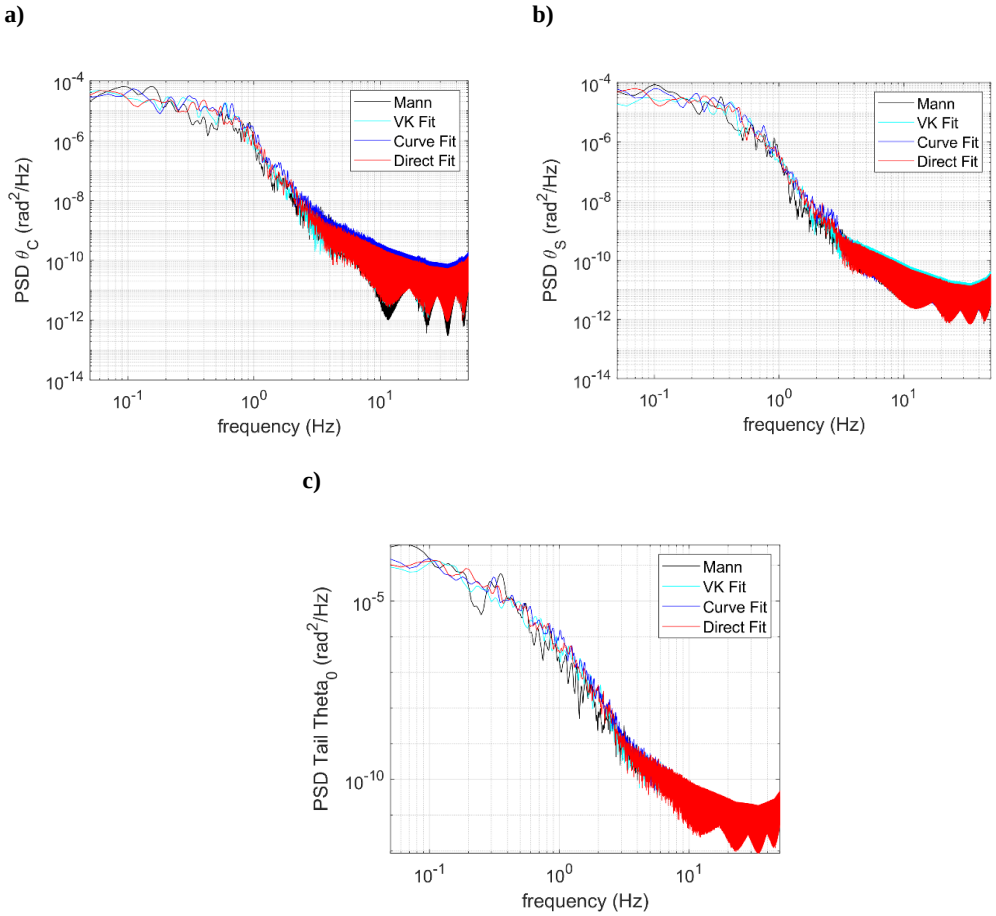

Figure 7-23: PSD of blade pitch angles for a) main rotor lateral pitch, b) main rotor longitudinal pitch, c) Tail rotor blade pitch.

7.5 Chapter Summary

This chapter has focused on the calibration of the multi-scale SEM model for the generation of turbulence with specific characteristics.

A turbulence field generator, using a Mann turbulence model, was used to rapidly produce a series of pre-computed turbulence flow fields, which were coupled with FLIGHTLAB and used as a target for the calibration of the SEM parameters. The values that define the properties of the eddies were obtained by a least squares fit to the PSD curve of the turbulent flow velocities generated by the Mann model. Three calibration strategies, were tested, targeting either the analytical von Karman spectra, a curve approaching the turbulent PSD at the centre of the Mann pre-generated wakes and a direct fit to the PSD of the turbulence averaged across an entire wake region.

Outputs of both models were then evaluated by comparing turbulent flow convergence of time averaged Reynolds stresses, frequency spectra, RMS in the 0.1Hz – 2Hz frequency range and average frequency.

Overall, the turbulence generated by the SEM presents a similar behaviour to the Mann turbulent wakes, across different input values of Reynolds stress tensor and turbulence wavelength. Although SEM generated turbulence seems to have a higher PSD within the 0.1Hz to 1Hz frequency range covered by the main lobe of the eddies shape function as the Mann generated wakes.

Offline simulation was then employed to compare disturbances on the aircraft induced by turbulence from both models, focusing on PSD and RMS of induced forces and moments and main rotor blade pitch oscillations due to commands from the stability system. Aircraft response to turbulence shows a similar behaviour for both models, especially within the 0.1Hz – 2Hz range. Although SEM generated turbulence seems to produce larger disturbances on the aircraft than the Mann generated airwakes.

Targeting the analytical von Karman Spectra seems to present the best results, followed with fitting to the average PSD of the wake. These two methods resulted in the closest similarity between the SEM PSD curves, RMS and average frequency with the Mann wakes. The Curve – Fit strategy seems to result in the largest discrepancies and was not employed in the next chapter. It seems to consistently generate turbulence of greater average frequency and RMS of flow velocities resulting in higher turbulence induced forces and moments on the aircraft than the turbulence of the Mann wakes it is intended to reproduce. However, this strategy might be useful to obtain a PSD curve at a specific point in scenarios where turbulence conditions might change significantly at different locations such as the turbulent airwake behind an obstacle.

The methods tested here can be applied to multiple different datasets of unstructured turbulence. Examples could be measurements of atmospheric turbulence, experimental measurements or CFD simulations. The correct selection of input parameters allows the SEM model to generate a random turbulence field in real time that reproduces the behaviour of the original data.

In the next Chapter 8, the VK- Fit and Direct–Fit strategies were further assessed using piloted flight simulation, performing a precision hover MTE under the two turbulence models. The aim was to test whether aircraft and pilot behaviour responded

in a similar manner to changes in Reynolds stress tensor and turbulence wavelength under all models and fitting strategies.

8 Piloted flight simulation comparison of turbulence models and calibration strategies.

8.1 Introduction

In the previous chapter, three different strategies were discussed and tested with the aim to obtain values for the input parameters of the SEM model that reproduce the turbulence frequency spectrum from a dataset of recorded or simulated turbulence.

These methods were used on a series of turbulence fields generated using a Mann atmospheric turbulence model and implemented as a moving turbulence field in FLIGHTLAB. SEM generated turbulence was compared with these flow fields and offline simulations were conducted to assess disturbances on the rotorcraft. Results show that, by appropriately choosing the values of the input parameters, the SEM model generates turbulence of similar characteristics which produces similar impact on the rotorcraft, although of higher intensity than the Mann generated wakes.

This chapter describes piloted flight simulation trials to evaluate if the SEM generated turbulence produces a similar impact on pilot workload, task performance and aircraft handling as the Mann airwakes across different turbulence conditions.

The parameters of the SEM model were calibrated using a least squares fit to the PSD curve of the Mann generated wakes and to the theoretical von Karman spectra. These two approaches seemed to produce a better fit in the previous chapter than the fit to a curve approximating the turbulence PSD of the dataset at a specific point.

The trials consisted of several runs, during which the pilot performed an ADS – 33 precision hover MTE as described previously in Section 6.5.2.1, flying under different turbulence conditions generated by both models. Pilot ratings and feedback and recorded flight simulation data were used for the evaluation of both models, focussing on comparing pilot ratings, standard deviation of aircraft position and heading from the target during the hover task and RMS and PSD plots of pilot control activity.

The chapter is structured in four parts. Mann and SEM turbulence conditions employed for the trials are described in Section 8.2 and the trials are described in Section 8.3 with the turbulence conditions and pilot ratings for each run presented. Section 8.4 presents the results from the trials which are discussed in Section 8.5.

8.2 Selection of turbulence conditions

The turbulence conditions chosen for simulator tests with the Mann model are shown in Table 8-1. Given that the Mann wakes were generated without shear, $\Gamma = 0$, the resulting turbulence of the Mann generated wakes should approach the von Karman turbulence spectrum.

Table 8-1: Input parameters for Mann generated turbulence flow fields used for piloted flight simulation testing

Parameter	**Values**			
Grid size ($N_x \times N_y \times N_z$)	$512 \times 128 \times 64$			
Grid resolution (dx ; dy ; dz)	1m ; 1m ; 1m			
$\alpha\epsilon^{\frac{2}{3}}$	1.0			
Γ	0.0			
L (m)	5	15	30	45
Number of different wake files generated	1	1	2	1

From results in Section 7.4 the curve-fit approach to adjusting the SEM parameters to reproduce turbulence of the same spectrum as the Mann wakes seems to consistently result in the SEM generating turbulence of higher intensity and resulting in greater forces and moments induced on the aircraft than the Mann generated wakes and the method was therefore discarded for the piloted flight trials. These discrepancies with the Mann wakes were greater than adjusting SEM parameters using the VK-fit or the Direct-fit methods which were the approaches used for the piloted simulation trials presented in this chapter.

To limit the number of wakes needed for each wavelength, turbulence velocities were scaled to adjust the turbulent output to the values of Reynolds stress tensor to be applied on each test run. They would be determined during the trials to obtain a measurable impact on task performance without impeding aircraft handling.

A wavelength value of $L = 30m$ was used as the reference condition from which changes in Reynolds stress tensor or wavelength where evaluated. Therefore two different wake files were generated for this case in order to avoid the risk of the pilot "learning" the airwake after several flights under turbulence of the same wavelength.

Table 8-2 depicts the SEM fit to the Mann model chosen for the piloted flight simulation testing.

Table 8-2: Input parameters for SEM fit to Mann wakes used for piloted flight simulation testing

Parameter	Values			
Fit	von Karman (VK)		Direct Fit	
Number of Eddy series	4			
Frequency range for PSD fit; Step size (Hz)	0.05 – 3 ; 0.05			
σ_{min} = Minimum eddy size (m)	2			
L (m)	5	15	30	45

8.3 Runs performed and pilot ratings

The flight simulation trial performed was the same ADS-33 PH MTE, described in Section 6.5.2.1, using the Bell 412 FLIGHTLAB model discussed in Section 6.3. The trial was flown by an experienced former Royal Navy test pilot who has experience in deck landing operations and has flown the Bell 412 helicopter. After each flight, BWRs and HQRs were awarded.

Tests runs were performed under a 20kts, 0degree azimuth (ahead) wind, which was chosen to allow for comparison with offline simulations. Turbulence generators and/or conditions were varied between each run. An initial run was performed without turbulence under uniform wind. Further runs were performed using the SEM turbulence model with the von Karman fitting strategy under a turbulence wavelength of $L = 30m$ and increasing values of Re_{ii}, until a suitable testing point was found at a value of $Re_{ii_{Target}} = 2\,m^2/s^2$. At these conditions the BWRs and HQRs that the pilot awarded were in the mid to high level 2 range and his feedback suggested a strong, but still controllable impact of turbulence on the aircraft. This gave enough margin for task difficulty to increase or decrease in response to changing turbulence model and/or wavelength values, without eliminating the impact of turbulence or inducing uncontrollable upsets.

Successive runs were then performed under different values of $Re_{ii_{Target}}$ and L under turbulence induced by Mann airwakes and by the SEM model using the two fitting strategies. These are summarised in Table 8-3, together with BWR and HQR ratings:

Table 8-3: List of performed runs, turbulence model and conditions applied and awarded pilot ratings.

Run	Turbulence	Fit/Wake no	L (m)	$Re_{ii\ Target}$ (m^2/s^2)	BWR	HQR
1	NO	--	--	0	3	3
2	SEM	VK	30	1	4	4
3	SEM	VK	30	3	6	7
4	SEM	VK	30	2	5	5
5	Mann	1	30	2	4	5
6	SEM	Dfit	30	2	6	4
7	Mann	2	30	1	4	4
8	Mann	1	30	2	4	5
9	Mann	1	45	2	3	3
10	SEM	Dfit	45	2	4	4
11	SEM	VK	45	2	5	4
12	SEM	VK	15	2	5	5
13	Mann	1	15	2	5	4
14	SEM	Dfit	15	2	5	5
15	SEM	Dfit	30	1	4	4
16	SEM	Dfit	30	2	6	5
17	SEM	Dfit	30	3	6	6
18	Mann	2	30	3	5	4
19	Mann	1	45	3	5	4
20	SEM	Dfit	45	3	5	5
21	SEM	VK	45	3	5	5
22	SEM	VK	5	2	4	4
23	SEM	Dfit	5	2	4	4
24	Mann	2	5	2	3	3

8.4 Analysis of results

8.4.1 Impact of turbulence and increases in Reynolds stresses

Addition of turbulence has an important impact on pilot workload and PH task performance. Flying under turbulence from all three models under increasing values of Re_{ii} led the pilot to award increasingly higher workload and handling quality ratings (see Figure 8-1). For values of $Re_{ii} \geq 2$, flying under SEM-produced turbulence resulted in overall higher workload and lower performance than under turbulence produced by the Mann model.

a)

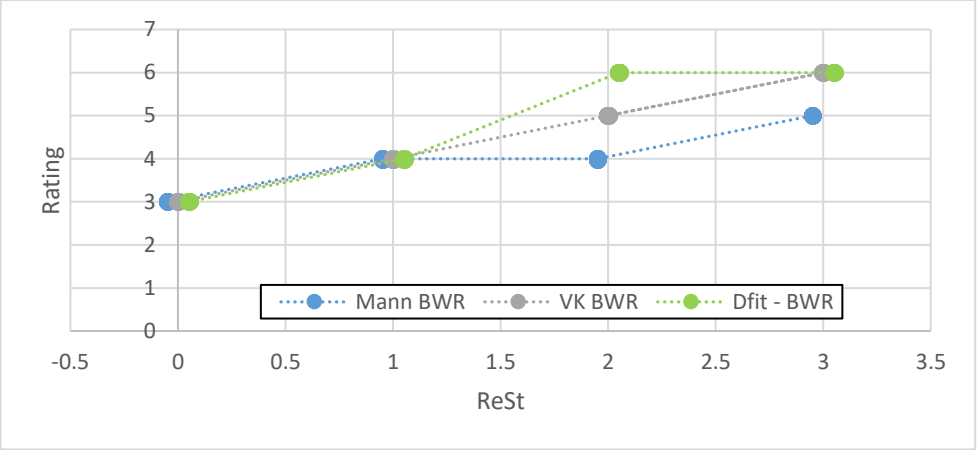

b)

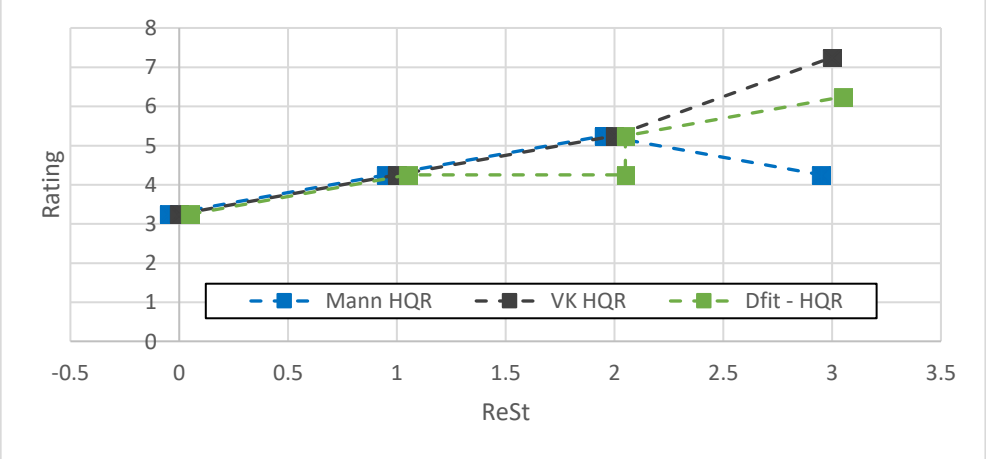

Figure 8-1: Pilot awarded ratings against increasing values of Re_{ii} under all three turbulence models for a wavelength of L = 30m: a) BWRs b) HQRs.

Pilot workload was driven mainly by impact of turbulence during the stabilization and hover phases of the MTE, due to the increased effort by the pilot to keep the aircraft deviations within the defined adequate or desired boundaries. According to the pilot, degradation of handling qualities and increased workload was mainly driven by deviations in altitude and longitudinal position and pilot effort to compensate for them. Lack of stability augmentation in the heave axis and the limited visual cueing to assess the longitudinal position (an issue with the precision hover MTE as defined in ADS – 33) were the root causes of this. Under the highest level of turbulence intensity, $Re_{ii} = 3\frac{m^2}{s^2}$, control limits in heave were an important issue leading to the high BWRs and HQRs, with torque limits warnings being triggered on several occasions.

The pilot was not aware beforehand of which turbulence model and conditions were setup for each run. However, when flying under turbulence resulting from the Mann model, there was an underlying, low intensity, high frequency vibration in all axes that could be felt across the entire cockpit. The Mann model turbulence presents higher PSD values in the high frequency regions than the SEM model, which is limited by the maximum number of eddies simulated (and therefore limits their minimum size).

This vibration did not have any noticeable impact on aircraft upsets, task performance or handling but contributed to enhance the realism of the resulting turbulence.

Pilot comments and ratings on how turbulence impacts his workload and task performance are confirmed when studying recorded test data. Plots for performance during the hover phase under turbulence of $L = 30m$ and $Re_{ii} = 2\frac{m^2}{s^2}$ under all three turbulence models, corresponding to runs number 4, 5 and 6 in Table 8-3, and without turbulence, run 1, are shown in Figure 8-2 for heading and altitude and Figure 8-3 for longitudinal and lateral position, dashed cyan and magenta lines indicate desired and adequate deviation boundaries for the hover task. All three turbulence models produced similar multi-axis disturbances on the aircraft, but the pilot was easily able to contain heading and lateral deviations within desired limits. Vertical and longitudinal position, however, often slide into adequate and occasionally outside of it, with the amplitude and frequency of disturbances being higher under turbulence induced by the synthetic eddy model.

a)

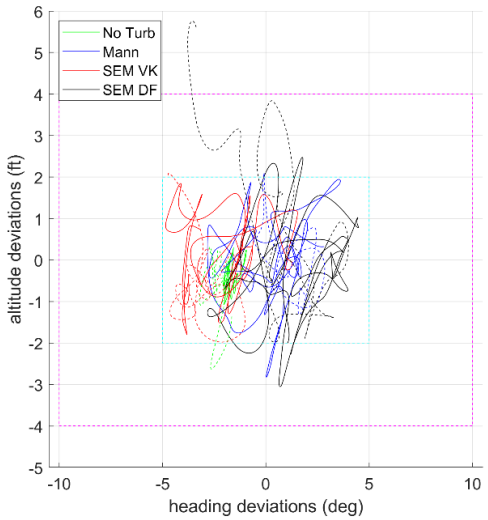

b)

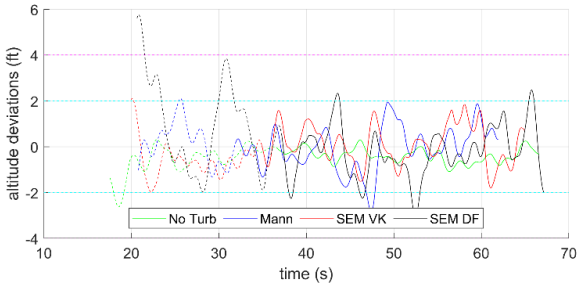

c)

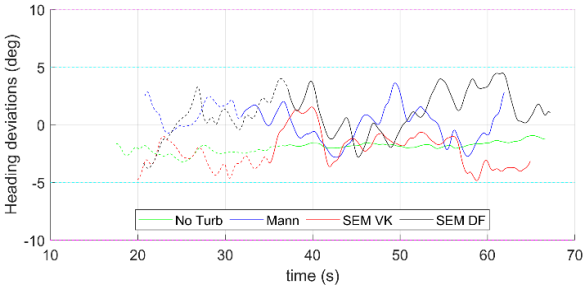

Figure 8-2: Performance during hover phase, Altitude and heading: a) Altitude and heading profile, b) altitude deviations, c) heading deviations. 30s hover phase indicated by continuous track. Under no turbulence (run 1) and turbulence conditions of Re_{ii} = 2m^2/s^2, L = 30m under Mann (run 5), SEM VK fit (run 6) and SEM direct fit (run 16). Dashed cyan and magenta lines indicate desired and adequate deviation boundaries respectively.

a)

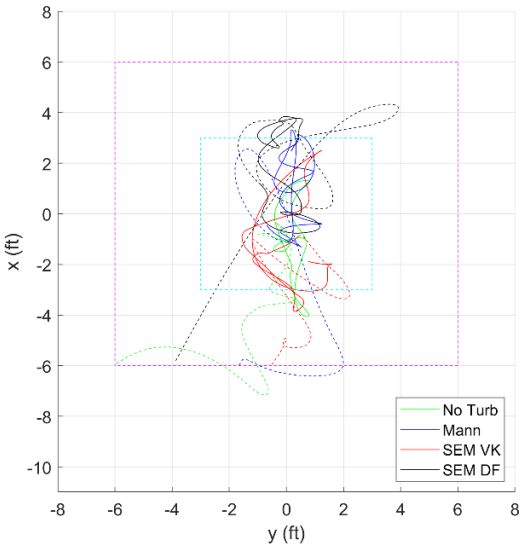

b)

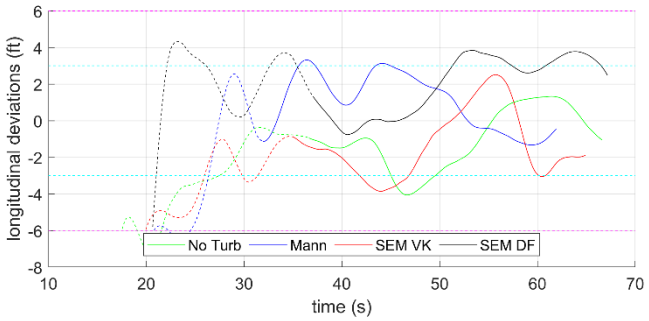

c)

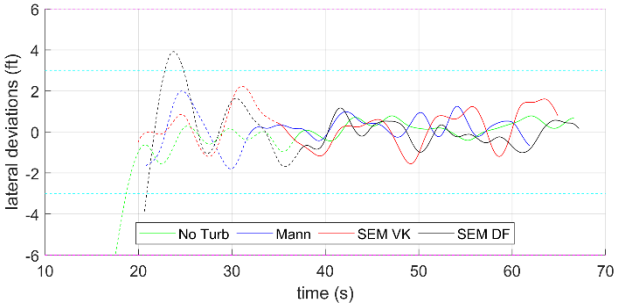

Figure 8-3: Performance during hover phase, Longitudinal and lateral position: a) ground track, b) longitudinal deviations, c) lateral deviations. 30s hover phase indicated by continuous track. Under no turbulence (run 1) and turbulence conditions of Re_{ii} = 2m^2/s^2, L = 30m under Mann (run 5), SEM VK fit (run 6) and SEM direct fit (run 16). Dashed cyan and magenta lines indicate desired and adequate deviation boundaries respectively.

The impact of heave control limits on task performance can be seen on Figure 8-4, which depicts main rotor mast torque as a percentage of nominal torque (Figure 8-4 a) and altitude deviations from hover position (Figure 8-4 b) for the runs under the highest values of turbulence strength, $Re_{ii} = 3\frac{m^2}{s^2}$. Mast torque limits are exceeded shortly after the 40s mark in run 3 (SEM, VK fit) and shortly before the 40s mark in run 17 (SEM Direct fit), as the pilot attempts to counteract a sudden loss of altitude. These limits were cited by the pilot as a relevant factor for the high workload and handling qualities ratings awarded. These limits were not exceeded for the run performed under Mann turbulence, although it also presents large oscillations in altitude and torque.

a)

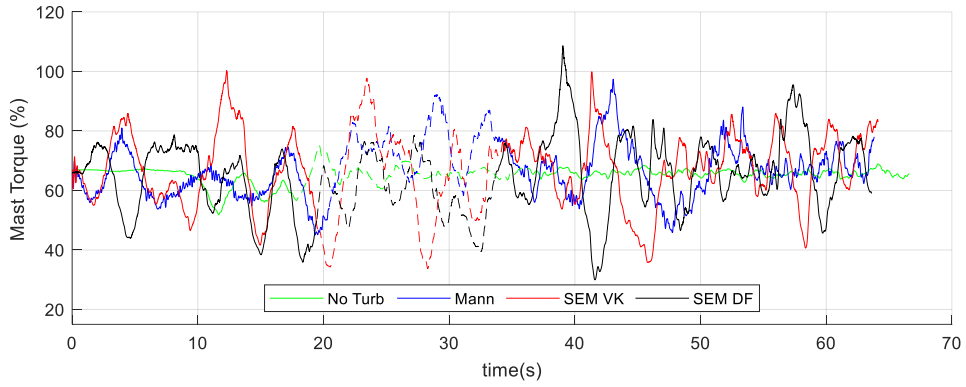

b)

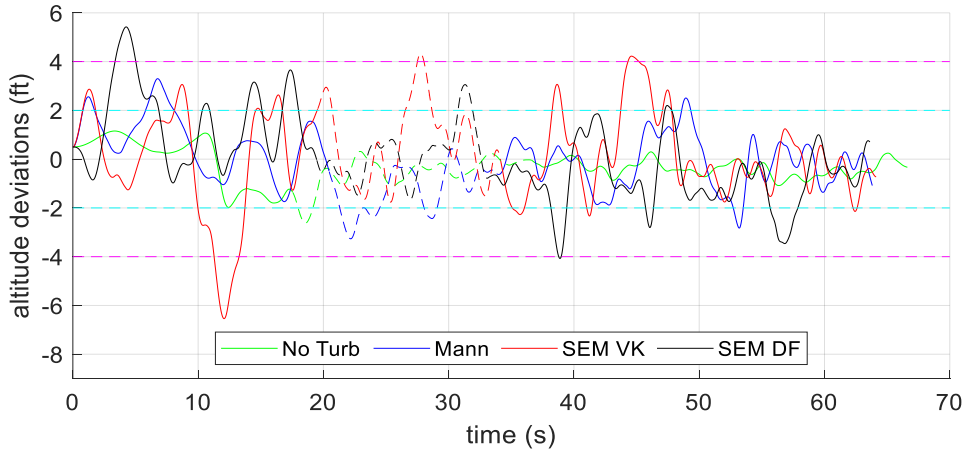

Figure 8-4: heave control under turbulence of $Re_{ii} = 3\frac{m^2}{s^2}$, corresponding to runs 1 (no turbulence), 3 (VK), 17(Direct Fit), 18 (Mann). Graphs of: a) Mast torque as % of nominal, b) altitude deviations. Continuous lines indicate approach and hover phase, dashed lines indicate capture phase.

Figure 8-5 depicts standard deviation of lateral position (Figure 8-5 a), longitudinal position (Figure 8-5 b), vertical position (Figure 8-5 c) and aircraft heading (Figure

8-5 d). Overall trends agree with pilot comments and awarded HQR, showing increased standard deviation of upsets with increased values of turbulence Re_{ii} generated by all three models.

Deviations in longitudinal position and altitude were particularly large when compared to desired and adequate limits (see Table 6-3). In the case of longitudinal position, deviations are already very large when flying under no turbulence, confirming pilot feedback that insufficient visual cueing was one of the main factors influencing longitudinal positioning of the aircraft.

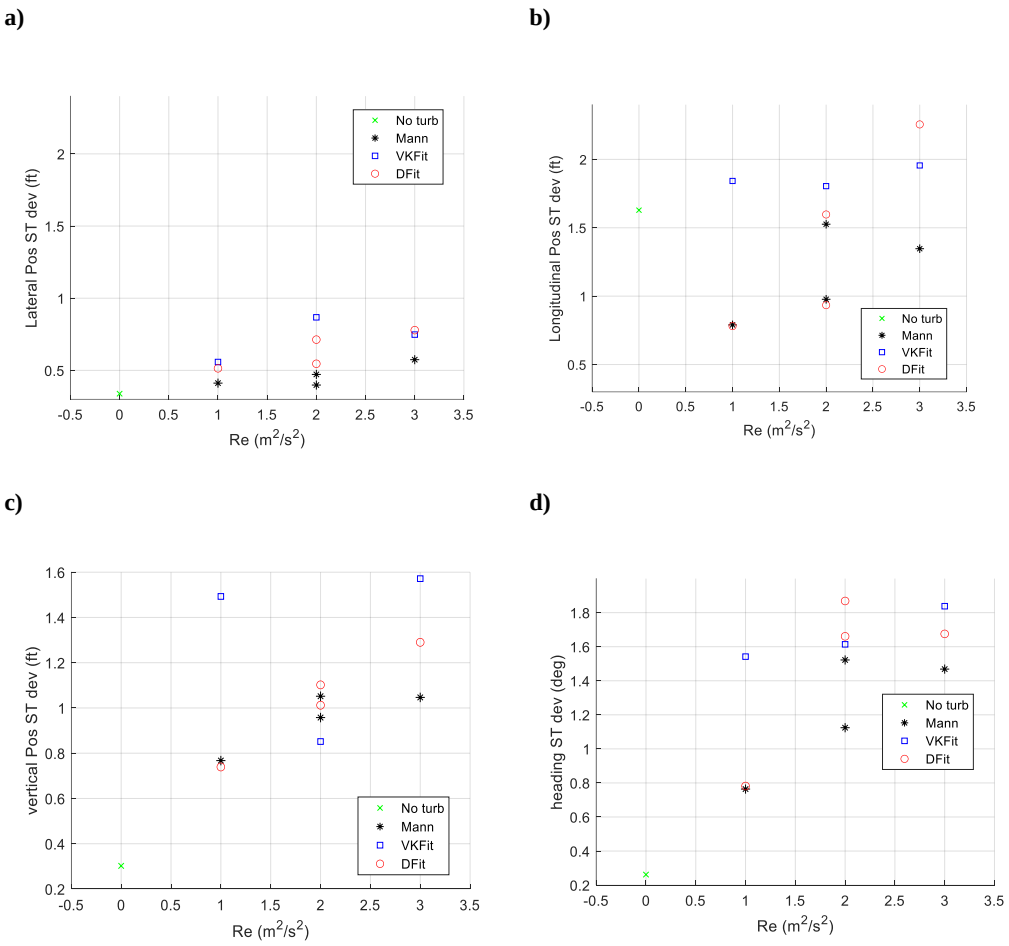

Figure 8-5: Standard deviation from hover point in a) lateral position, b) longitudinal position, c) altitude, d) heading against value of Reynolds stresses.

Flying under SEM generated turbulence usually results in larger deviations than under the Mann generated atmospheric wake. Large deviations from the hover point can be noticed for the case of the von Karman fitting strategy under a value of $Re_{ii} = 1m^2/s^2$ which correspond to the first run under turbulence (Run 2).

Pilot workload was driven by the hover phase, as boundaries on allowed deviations meant that the pilot was forced to continuously react as soon as possible to disturbances in order to keep deviations from building up and exceeding the defined limits.

No such limits on deviations are defined for the translation to the hover point. Demand on the pilot to compensate for turbulence induced disturbances was therefore limited to avoid collision with the ground and to attempt to perform a smooth manoeuvre.

But turbulence still has a noticeable effect on the aircraft. Figure 8-6 shows aircraft ground track (a), approach rate to the hover point (b) and deviations in altitude from hover (c) during the full MTE. Dashed lines correspond to a capture period, which starts as soon the aircraft position over the ground enters the region defined by the adequate boundaries on deviations in longitudinal and lateral position and ends once the 30s hover phase starts. This period contains the pilot inputs and manoeuvres required to stabilize the aircraft over the hover point.

When flying under turbulence, the pilot found it more difficult to maintain a uniform rate of approach to the hover point, as seen in Figure 8-6 b. Spikes in the rate of approach become especially pronounced once the aircraft enters within adequate limits in longitudinal and lateral position. Oscillations in aircraft altitude, shown in Figure 8-6, are prevalent throughout the entire translation under turbulence and only reduce their amplitude once the pilot starts counteracting the disturbances to stabilize the aircraft and maintain the required altitude for the hover phase.

All three turbulence models result in very similar disturbances acting on the aircraft. Although large oscillations in approach rate and aircraft altitude can be distinguished during the capture phase of run 8, corresponding to the case of SEM induced turbulence and adjusted through the direct fitting strategy.

a)

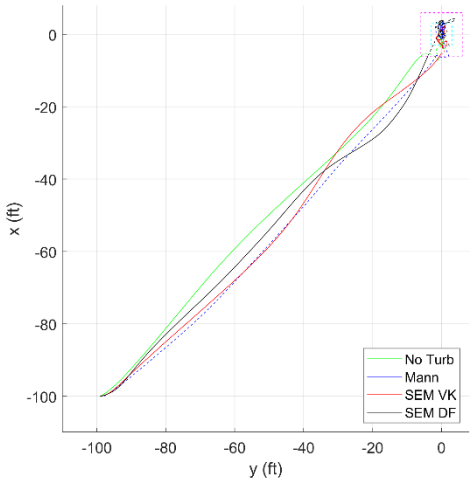

b)

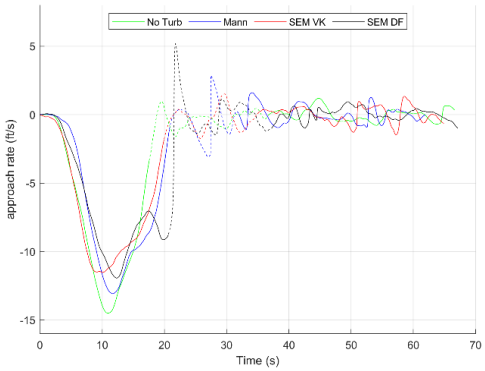

c)

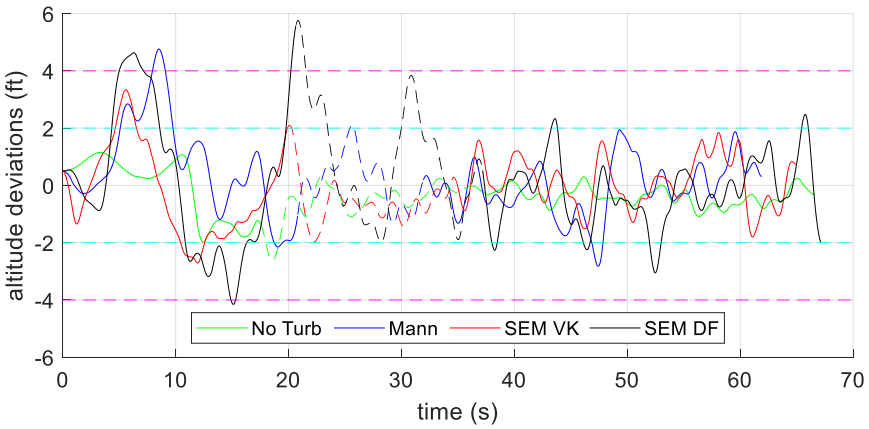

Figure 8-6: Approach to hover point and stabilization: a) Ground track, b) speed of approach to hover point, c) altitude deviations from hover point. Continuous lines indicate approach and hover phase, dashed lines indicate capture phase. Under no turbulence (run 1) and turbulence conditions of Re_{ii} = $2m^2/s^2$, L = 30m under Mann (run 8), SEM VK fit (run 6) and SEM direct fit (run 16).

Pilot control inputs during the full MTE are shown in Figure 8-7 for lateral stick (Figure 8-7 a), longitudinal stick (Figure 8-7 b), collective (Figure 8-7 c), and pedal (Figure 8-7 d). When performing the task without turbulence (run 1), the pilot is able to perform a smooth translation to hover, requiring minimal inputs, mainly in the longitudinal axis in order to control approach velocity. Large amplitude inputs, mainly in lateral and longitudinal are visible when capturing the hover point (dashed lines). Followed during the hover phase by small high frequency inputs in lateral, longitudinal and collective in order to maintain aircraft position and attitude. Pedal inputs remain small and sparse throughout the entire task.

Flying under turbulence, by contrast, requires frequent multi-axis pilot inputs throughout the entire duration of the task. Amplitude of inputs increases at the start of capture manoeuvres and stays so for the entire duration of the hover phase. Suggesting a constant need to stabilize the aircraft during the hover phase in order to limit disturbances.

Analysis PSD of pilot control inputs during the task, see Figure 8-8 for translation to the hover point and Figure 8-9 for the hover phase, further confirms the patterns mentioned above. It also provides insight to differences on the impact on handling from the three turbulence models. Flying under turbulence requires pilot inputs of larger amplitude, especially for station keeping over the hover point. Peak of pilot input PSD is usually at a frequency below 0.5Hz.

Amplitude of pilot inputs during translation seems to be of larger magnitude when flying under SEM induced turbulence rather than Mann. In addition, keeping hover requires the pilot to work across a wider frequency range under SEM induced turbulence than within the Mann generated wake, with PSD of inputs in longitudinal (Figure 8-9 b) and collective (Figure 8-9 c) presenting a second peak above a frequency of 0.5Hz.

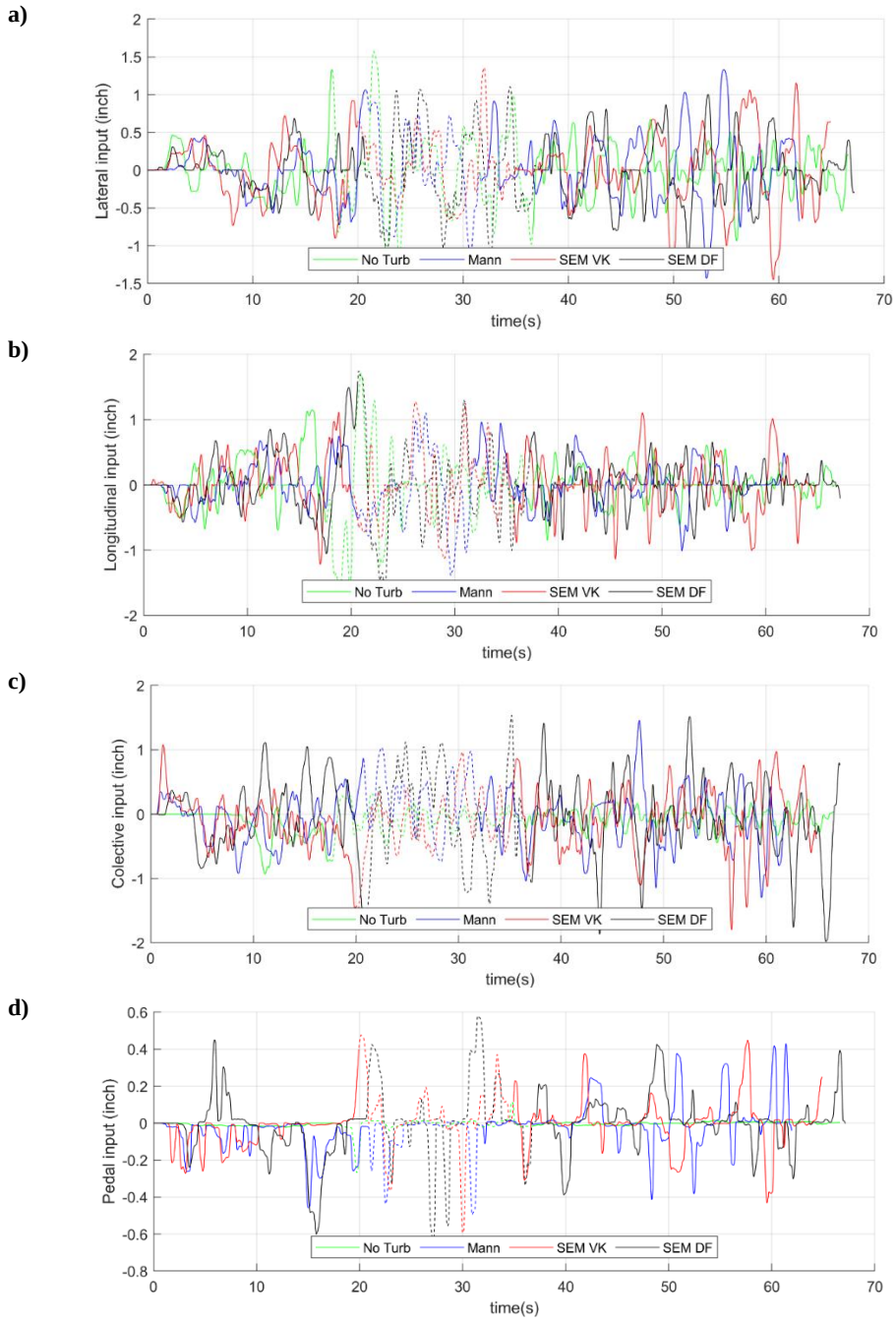

Figure 8-7: Pilot control inputs during the full hover MTE in a) lateral stick, b) longitudinal stick, c) collective, d) pedal. Flying under no turbulence (run 1) and turbulence conditions of $Re_{ii} = 2m^2/s^2$, L = 30m under Mann (run 8), SEM VK fit (run 6) and SEM direct fit (run 16). Continuous lines indicate translation and hover phase, dashed lines indicate capture of hover point.

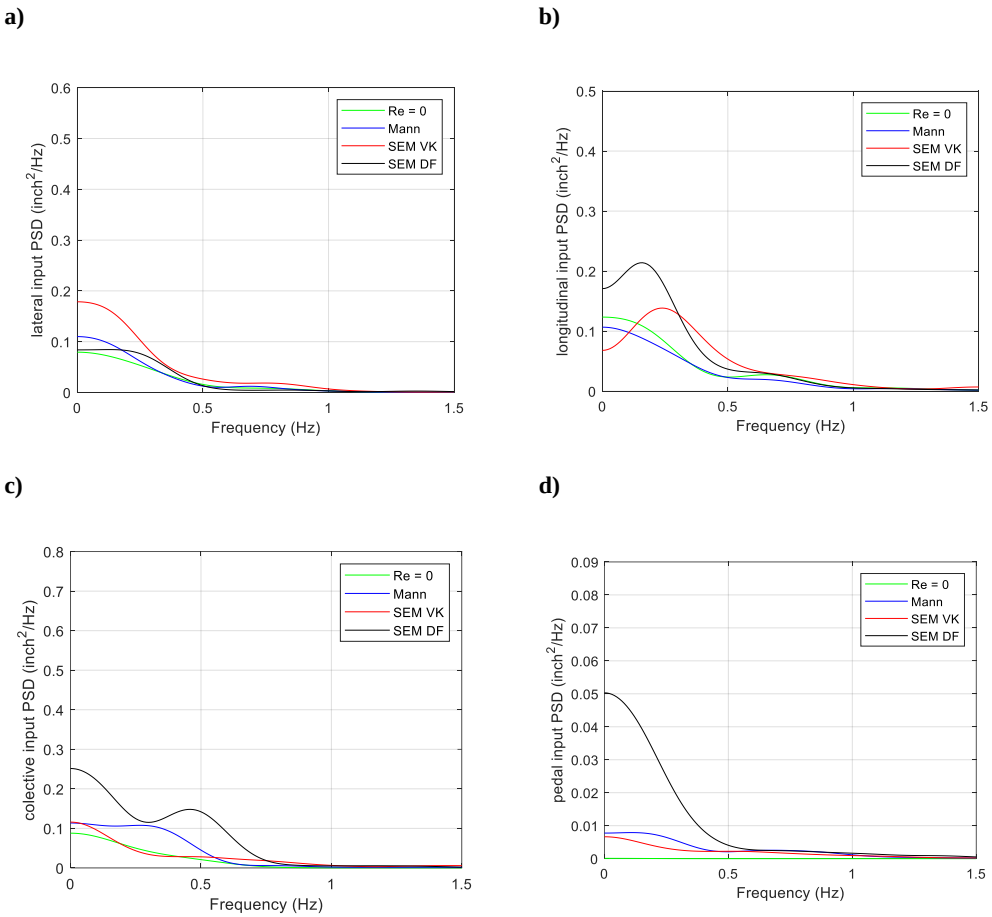

Figure 8-8: PSD of pilot inputs during translation to hover point under turbulence of Re = $2m^2/s^2$ and L = 30m in a) lateral, b) longitudinal, c) collective, d) pedal. Flying under no turbulence (run 1) and turbulence conditions of Re_{ii} = $2m^2/s^2$, L = 30m under Mann (run 8), SEM VK fit (run 6) and SEM direct fit (run 16).

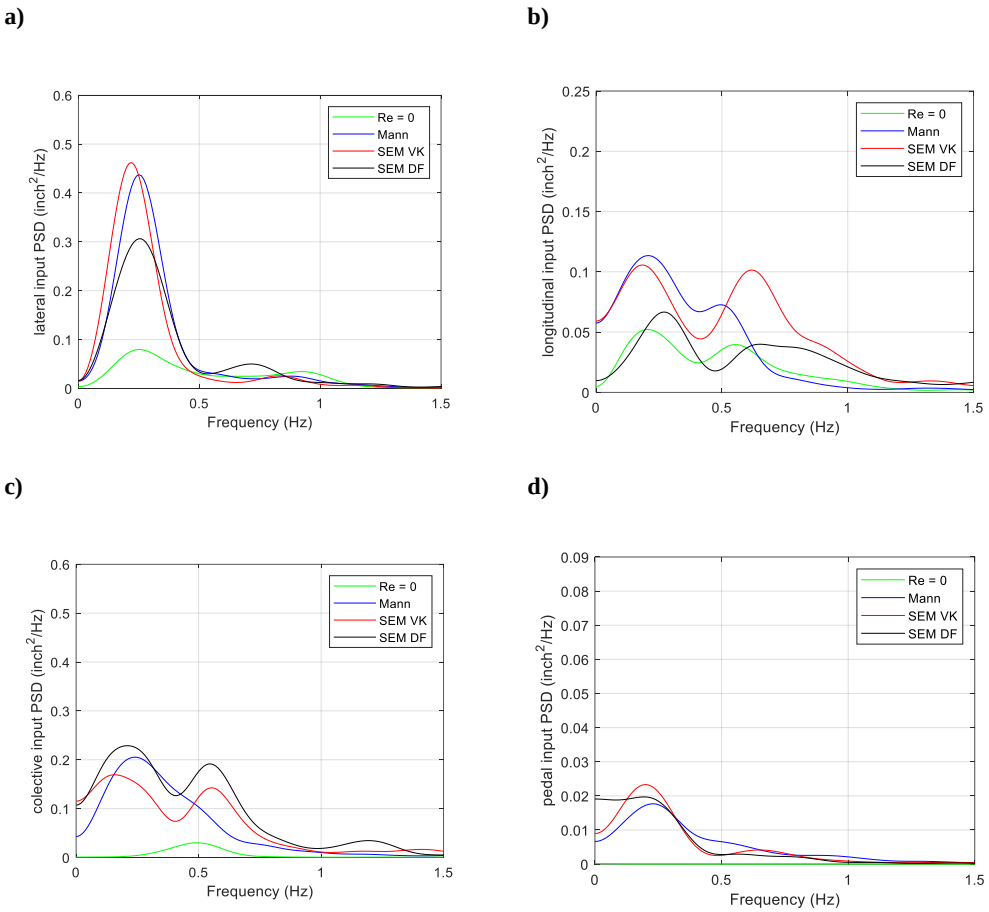

Figure 8-9: PSD of pilot inputs during hover for turbulence of Re = 2m²/s² and L = 30m in a) lateral, b) longitudinal, c) collective, d) pedal. Flying under no turbulence (run 1) and turbulence conditions of Re_{ii} = 2m²/s², L = 30m under Mann (run 8), SEM VK fit (run 6) and SEM direct fit (run 16).

RMS of pilot inputs during the hover phase, for turbulence of wavelength $L = 30m$ and varying values of Re_{ii} are shown in Figure 8-10. Results from flight simulation trials described in Section 5.3 suggests a correlation between RMS of pilot inputs, especially in the collective and pilot workload. Under all three models, a trend of increasing demand for the pilot in longitudinal, collective and pedal is apparent when increasing turbulence Re_{ii}. The impact being in general greater when flying under SEM than under Mann generated turbulence.

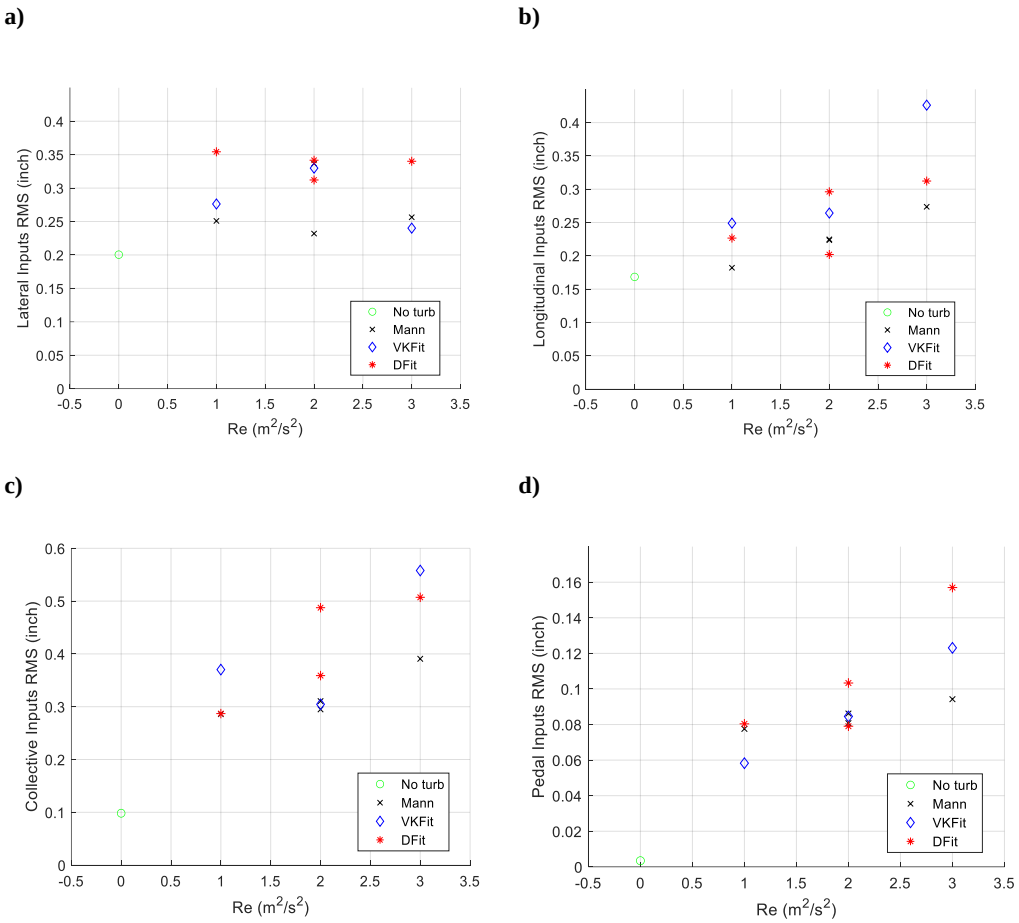

Figure 8-10 RMS of pilot control inputs during hover phase in a) Lateral, b) Longitudinal, c) Collective, d) Pedal.

8.4.2 Impact of turbulence wavelength:

To assess the impact changes in turbulence wavelength have on handling the aircraft, a series of runs were performed under turbulence produced by all three modelling methods with wavelengths of $L = 5m\,; 15m\,; 30m$ and $45m$ while keeping the value of Reynolds stress tensor constant at $Re_{ii} = 2\,\frac{m^2}{s^2}$. Pilot ratings are presented in Figure 8-11 showing that, depending on the turbulence modelling method, workload and handling qualities ratings peaked when flying under wavelengths of 15m and/or 30m and then tend to fall for wavelengths of 45m.

a)

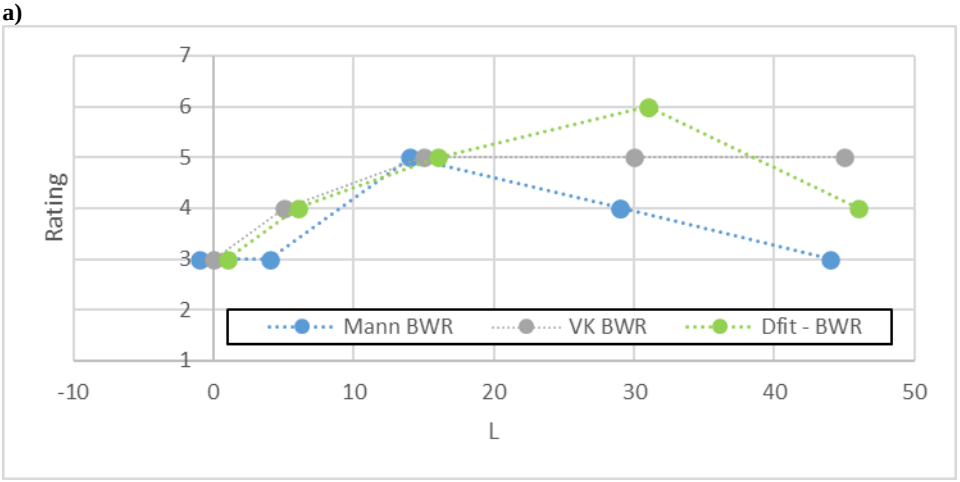

b)

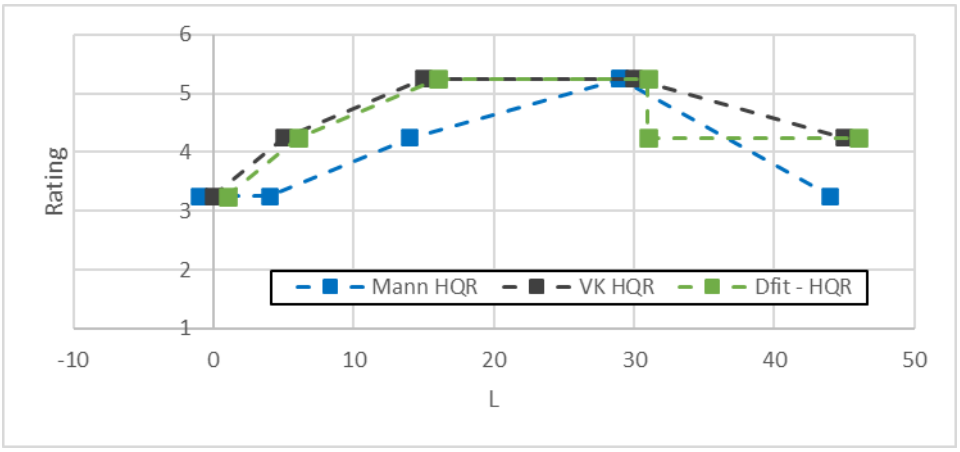

Figure 8-11: Pilot awarded ratings against increasing values of L under all three turbulence models for a Reynolds stress tensor of Re_{ii} =2m²/s²: a) Workload ratings b) Handling qualities ratings. L = 0 is reference to no turbulence conditions.

Across all wavelengths, workload increases and degradation in task performance was driven by turbulence induced upsets in vertical position and required activity in the collective as well as insufficient cueing to counteract upsets in longitudinal position.

This observation is visualized in Figure 8-12 which depicts standard deviation in lateral (Figure 8-12 a), longitudinal (Figure 8-12 b) and vertical (Figure 8-12 c) position as well as aircraft heading (Figure 8-12 d). Deviations in longitudinal position stay high across all wavelengths, even in the case of no turbulence, while deviations in vertical position peak at a wavelength of $L = 15m$ and then decay for $L = 45m$ under all three turbulence methods. Heading deviations seem to follow the same pattern as with vertical position and are probably a result of inter-axis couplings between collective and yaw, while lateral deviations stay low for all cases. Flying under SEM induced turbulence results in larger disturbances than under Mann

generated wakes. But all models exhibit this pattern by which turbulence of $L = 15m$ and of $L = 30m$ result in the largest deviations from the hover point.

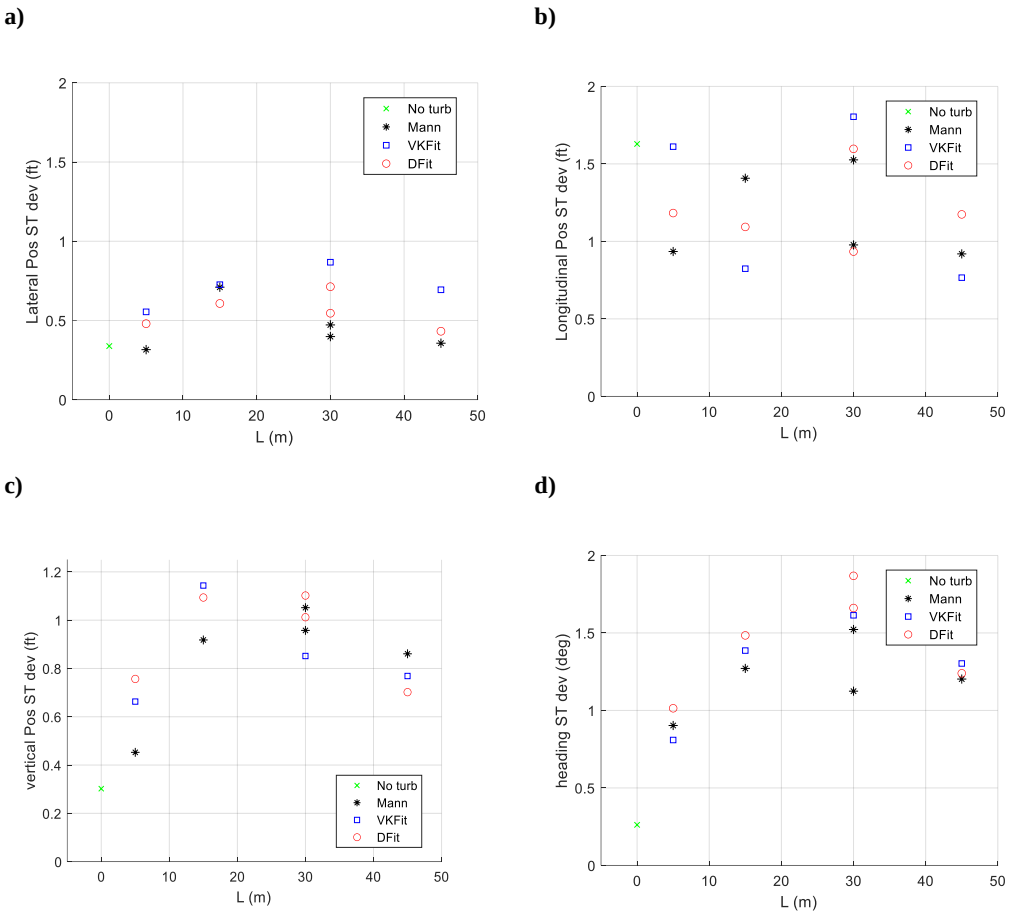

Figure 8-12: Standard deviation from hover point in a) lateral position, b) longitudinal position, c) altitude, d) heading against value of turbulence wavelength.

Figure 8-13 shows plots of pilot input RMS during the hover phase against turbulence wavelength. It further confirms the trends suggested by pilot ratings and standard deviation in position and heading. Input RMS in longitudinal (Figure 8-13 b), collective (Figure 8-13 c) and pedal (Figure 8-13 d) are higher when flying under turbulence of wavelengths $L = 15m$ or $L = 30m$ produced by all three models, although SEM induced turbulence once again results in higher demand of pilot control activity.

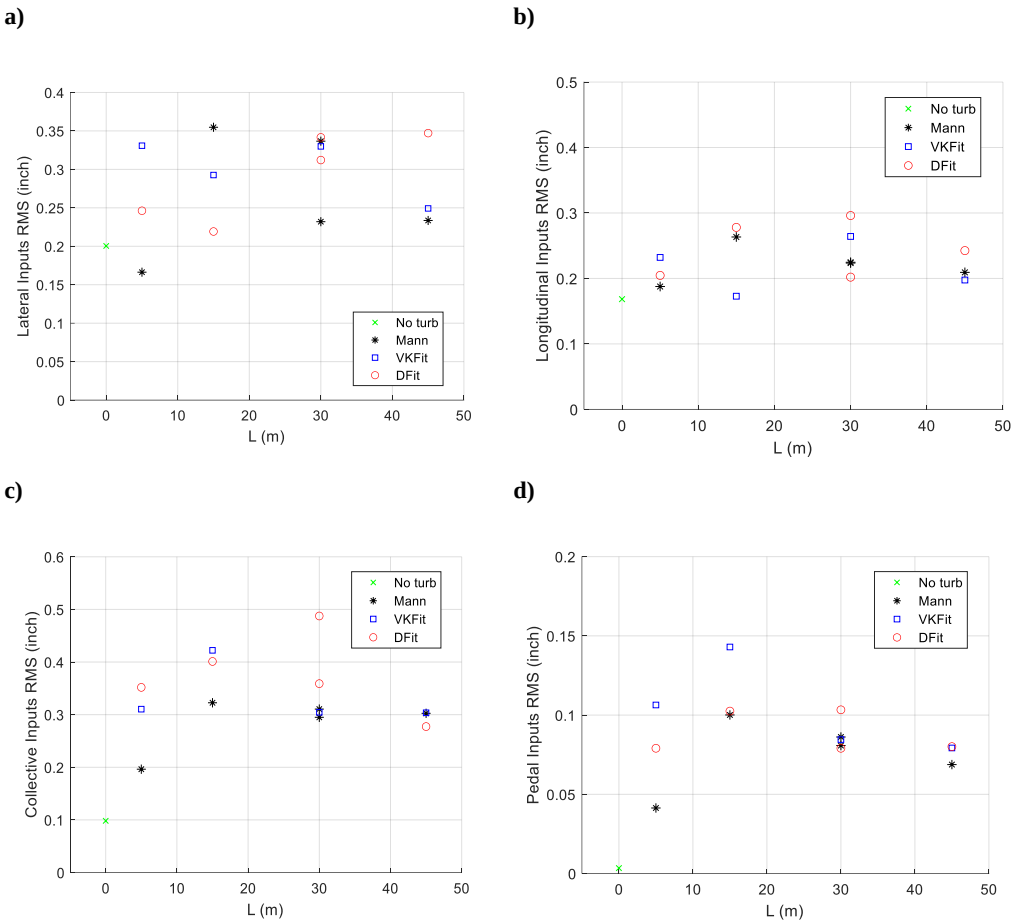

Figure 8-13: RMS of pilot control inputs during hover phase in a) Lateral, b) Longitudinal, c) Collective, d) Pedal.

Runs flown under a turbulence wavelength of L = 45m (runs: 9 – Mann, 10 – Direct-Fit, 11 – VK-Fit) present the largest similarity between models in standard deviation from the hover target position and RMS of pilot inputs. Power spectral density of pilot control inputs during hover (Figure 8-14) also show similar pilot control activity when flying under all three turbulence models, except for activity in lateral stick inputs.

From offline simulations, results shown in previous Sections 7.3.4 and 7.4, do not suggest a better fit of the SEM generated turbulence to the Mann wake output (see average frequency of turbulent flow in Figure 7-15 and RMS of turbulent flow in Figure 7-16 at different wavelengths). Rather as suggested in Figure 7-20 and Figure 7-22, which show forces and moments acting on the aircraft, it is a similar aircraft response to turbulence from all models at this particular condition.

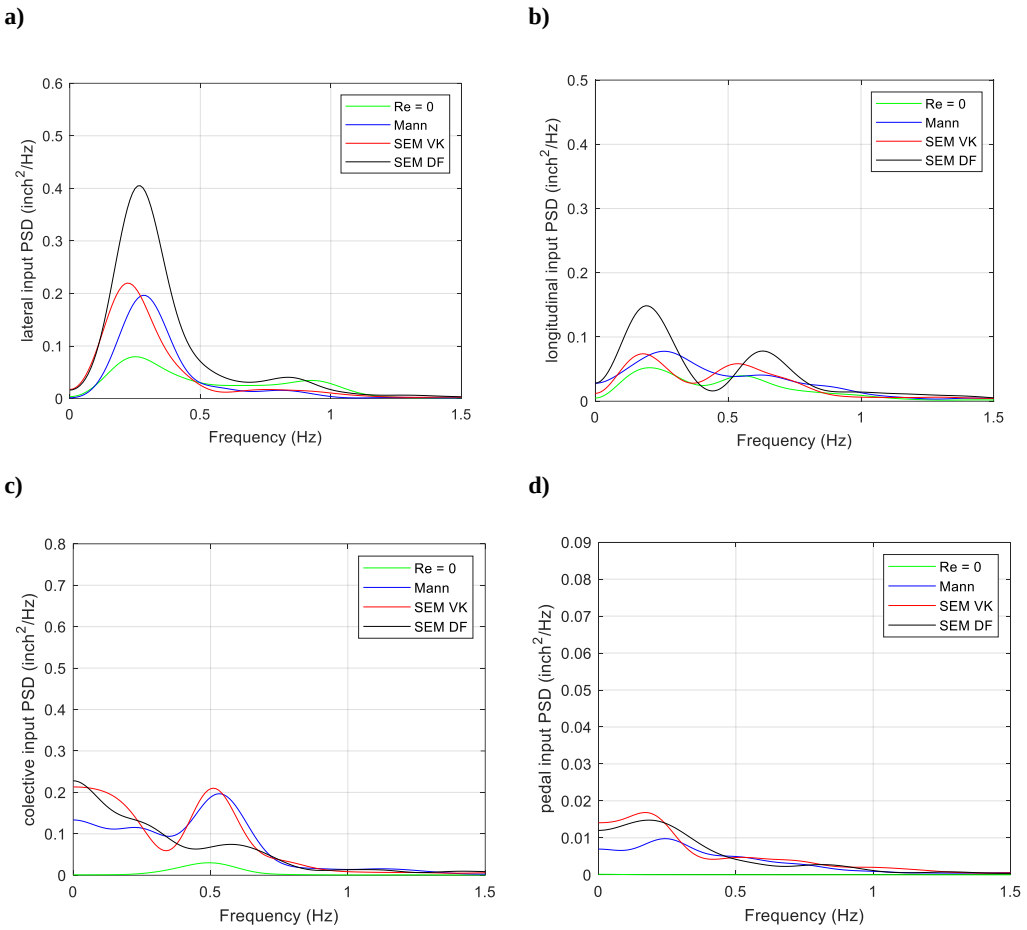

Figure 8-14: PSD of pilot inputs during hover for turbulence of Re = $2m^2/s^2$ and L = 45m in a) lateral, b) longitudinal, c) collective, d) pedal.

8.4.3 Overall impact on handling:

Figure 8-15 shows pilot awarded BWRs and RMS of control inputs in longitudinal (Figure 8-15 a and b), collective (Figure 8-15 c) and pedal (Figure 8-15 c) against RMS of turbulent flows in the relevant direction for all piloted flight simulation runs. Increases in RMS of turbulent flow tends to result in increases in RMS of pilot input, which is related to higher pilot workload ratings, especially for turbulent flows in the vertical direction and collective. RMS in control inputs with turbulence follow a similar pattern to that seen for moments and forces acting on the aircraft in Figure 7-19.

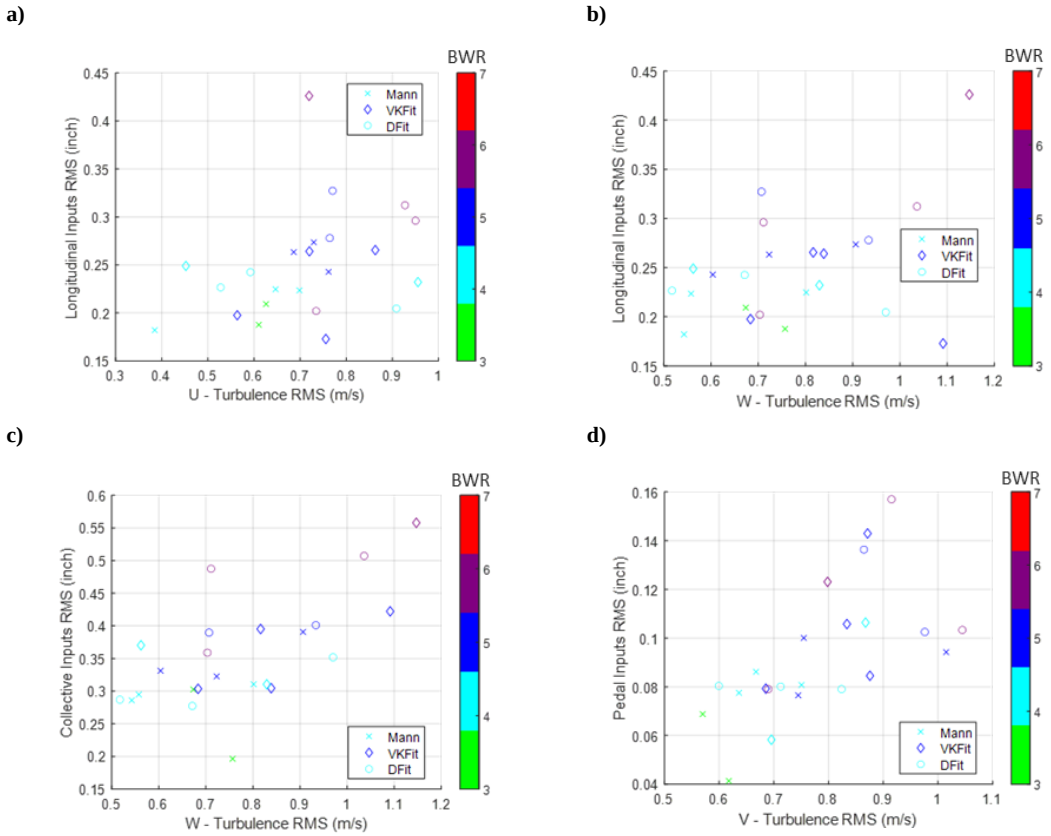

Figure 8-15: Pilot input RMS and awarded BWRs (marker colour) against RMS of turbulent flow at fuselage ACP a) Longitudinal inputs and longitudinal turbulence, b) Longitudinal inputs and vertical turbulence, c) collective input and vertical turbulence, d) pedal input and lateral turbulence.

Pilot workload ratings are compared to average frequency and standard deviation of turbulent flow velocities in Figure 8-16. Low frequency turbulence of large standard deviation tends to result in larger pilot workload ratings, with the trend being more consistent for vertical flow.

These relationships stay for all three turbulence models. Overall SEM generated turbulence results in higher RMS values as well as larger standard deviations of turbulent flow velocities than Mann generated wakes, a result already seen in offline simulations (see Section 7.4). Therefore, runs under SEM generated turbulence resulted in overall higher pilot effort and workload ratings.

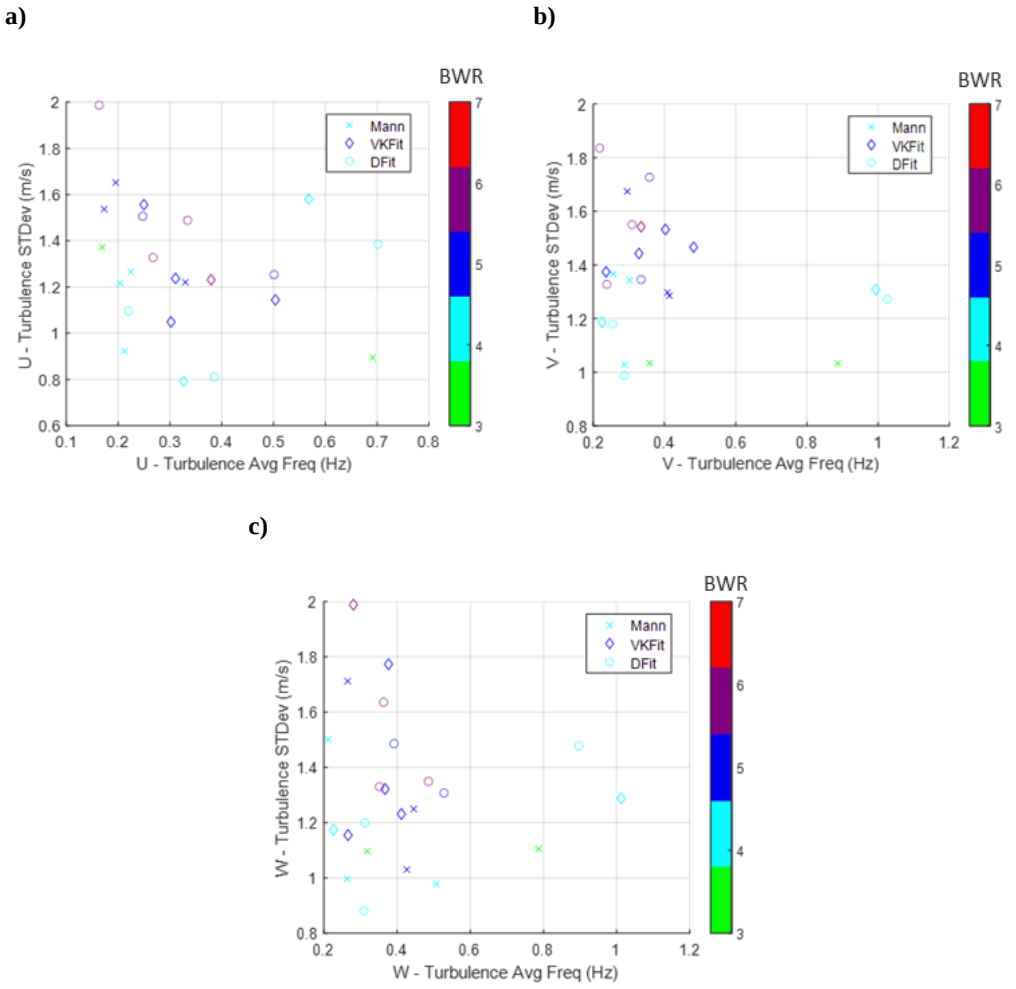

Figure 8-16: Pilot awarded BWRs against average frequency and standard deviation of turbulent flow at aircraft fuselage ACP in a) x – axis flow velocities, b) y – axis flow velocities.

8.5 Chapter Summary:

This chapter details piloted flight simulation trials conducted to test the tuning of the SEM input parameters and to compare if the generated turbulence produces a similar impact on aircraft disturbances and pilot workload as the pre-generated Mann wakes whose PSD was replicated by the SEM.

Two of the calibration strategies described in the previous chapter were tested: a fit of the SEM model to the theoretical von Karman spectrum which is also the intended output of the Mann wake and a direct fit of the SEM model to the average spectrum across the entire wake section.

The trials consisted of a series of ADS-33 PH MTEs under a 20 kts headwind and turbulence produced by the two models at different values of Reynolds stress tensor and turbulence wavelength. Aircraft flight parameters and pilot control inputs were recorded for each run as well as pilot feedback and ratings in workload and flight handling qualities.

Both turbulence models impacted aircraft response and handling, task performance, and pilot compensation in the same manner, without any discernible advantage of any of the two calibration strategies for the SEM. Similar to the results obtained in Chapter 6, the main difficulties were in maintaining aircraft longitudinal and vertical position within the MTE defined boundaries during the hover phase. Higher intensity turbulence led to worse task performance, higher pilot workload ratings and higher RMSs of pilot control activity, especially in the heave and longitudinal axes.

Depending on the turbulence model, the impact on workload and task performance peaked at a wavelength of 15m for the Mann wakes and between 15m and 30m for the SEM turbulence. RMS values of pilot inputs and standard deviation values in aircraft position and heading, presented similar peaks in the same conditions.

As a result of the higher turbulence intensity generated by the SEM model within the 0.1Hz – 2Hz frequency range, the overall impact on task performance and pilot workload was greater when flying using this model compared with the Mann wakes and PSD plots of pilot activity show a greater pilot activity at a broader range of frequencies.

The slower decay of the Mann turbulence spectra at higher frequencies also led to the presence of a general, high frequency broadband vibration that did not impact aircraft response or pilot workload but was deemed highly realistic by the pilot. This vibration could not be replicated by the SEM model due to computational limits on the total number of eddies and therefore maximum frequency that can be simulated in real-time.

Overall, the results point towards the feasibility of calibrating the SEM model to reproduce turbulence properties from the targeted pre-generated Mann wakes. Although further work might be needed in improving the calibration criteria or expanding the frequency range covered by the SEM model by increasing the number of eddies.

The methodology applied in Chapters 7 and 8 should also be applicable to other datasets of simulated or recorded turbulence, allowing values of eddy properties to be selected in order for the SEM model to generate turbulence with a similar frequency spectrum.

Only the values of the input parameters of the SEM need to be stored and loaded beforehand for the SEM model to generate random turbulence in real time. This is an advantage over higher fidelity methods, such as time – accurate CFD solutions, which require the storage of large datasets which have to be loaded before a simulation session and are reproduced in a repeating loop should the simulated flight last longer than the recorded data.

9 Conclusions and Recommendations:

The thesis describes the work performed during a project on the modelling of airwake hazards for helicopter flight simulation. A literature review has shown a lack of significant research on the effects of rotorcraft encounters with airwakes in settings outside of shipboard or offshore operations, and especially when it comes to the field of operations in support for wind energy. There is also no standard methodology to accurately reproduce the impact of airwakes and turbulence on helicopter flight during real-time flight simulations. Most applications use either high fidelity time accurate CFD solutions, which are time consuming and complex to prepare, or random turbulence models adapted from methods used for fixed wing simulations. Whilst the latter have low computational costs and are easy to implement, they are difficult to calibrate and have limitations for rotorcraft applications. The research reported in this thesis has addressed these limitations with the development of new methods for modelling rotorcraft operations in turbulent environments.

This chapter presents the main conclusions from the research and details several recommendations on how the new modelling and simulation tools can be developed in future work.

9.1 Conclusions

New contributions to the state of the art have been described in the previous chapters. The main conclusions from the work have been grouped into three topics relating to hazard assessments, new methods for generating turbulence models for real-time rotorcraft applications and assessment of those methods.

9.1.1 Identification of hazards:

To identify hazards arising from accidental encounters with wind turbine wakes, a series of flight simulation trials of such encounters were performed. A simulation scenario was developed that was representative of a Search and Rescue mission within an offshore wind farm with the rescue aircraft encountering the wake generated by a 5MW wind turbine.

The wake was a steady state solution implemented using the Virtual AirDyn tool at Liverpool, for a straight and level flight condition. The pilot was instructed to

maintain initial flight conditions and recover as soon as safely possible from any upsets.

1. Flight safety was never compromised during the encounters. Airwake encounters mainly produced deviations in aircraft heading and roll angle. These resulted in moderate, not objectionable excursions, requiring pilot corrective action with moderate urgency.
2. The effect of the wake encounter was greater when flying under red side-wind conditions. Whilst trimming under these conditions required a greater proportion of available pedal control range, it was the greater 'sensitivity' of the aircraft's yaw response to a disturbance, and the corrective pedal inputs required to stabilise the aircraft, that caused difficulties for the pilot rather than a lack of available control authority.
3. The tests highlighted possible aircraft characteristics that might impact mission safety. The main driver of increased workload and encounter severity was aircraft response in pitch due to cross couplings from pilot pedal inputs when attempting to recover from wake induced disturbances, especially at high flight speeds and exacerbated by the lack of SAS.
4. Pedal to pitch cross couplings are not addressed in ADS – 33, and therefore a new metric, based on current criteria for pitch – roll cross couplings, was proposed in order to evaluate the observed helicopter response.

However, these results should be taken with caution as the trial was conducted using a steady, time–averaged airwake to simulate the encounter. The inclusion of time dependent phenomena, by using time accurate airwakes or a turbulence model in the simulation, might result in additional upsets not captured in this experiment.

9.1.2 Identify fidelity requirements and new modelling techniques:

The search for an option that could provide greater fidelity than a standard turbulence model e.g., von Karman or Dryden models, but that offered more flexibility and simpler implementation than time accurate airwakes, led to the adaptation of a synthetic eddy method as a turbulence model for use in real-time rotorcraft flight simulations. This method is based on randomly placing turbulence generating eddies within a control volume surrounding the aircraft and displacing them with ambient flow velocities. Preserving the location of the eddies near the aircraft, ensures that the turbulence field induced is coherent in space and time across all of the aircraft's ACPs

even if aircraft flight velocities experience large changes in a small number of time steps. The rotation of the rotor blades relative to the turbulence field is also automatically included. Adjustment of Reynolds stress values of eddies allows for adjustment of turbulence space and time cross-correlation as well as strength, while average frequency of resulting turbulence is inversely proportional to eddy size. The control volume needs to be filled by eddies, so the total number of eddies is inversely proportional to the cube of eddy size or proportional to the cube of average frequency.

5. The new SEM model can be implemented into a real-time piloted environment using the Simulink framework that was developed in this thesis. The computational costs are proportional to the number of eddies in the model, placing a limit to the real time simulation of very high frequency turbulence. Nevertheless, as currently implemented the model was capable of working in real-time to generate disturbances within the 0.1Hz – 2Hz frequency range which has the largest impact on pilot workload and task performance.
6. The eddy shape can be altered and multiple series of eddies with differing properties can be combined to adjust the shape of the turbulent PSD curve to generate different turbulence profiles for use in simulation assessments.
7. During the hover MTE, shaping of the SEM disturbances has shown that it impacts the resulting pilot response. During steady and level flight, the aircraft and pilot response did not show a significant difference between using multiple series of eddies or a single series with the same values of Reynolds stresses and size.
8. It was shown that calibration of the SEM model is possible, by adjusting the size and strength of different series of eddies, to reproduce the turbulence generated using other modelling techniques. The SEM has been calibrated to match the PSD output of an airwake generated using a Mann atmospheric turbulence model. The SEM model resulted in higher amplitude of disturbances within the 0.1Hz – 2Hz frequency range resulting in a higher impact on workload and task performance. It also presented lower amplitude at higher frequencies, an issue related to the limits in the number of small eddies that can be modelled with the available computational resources. This resulted in a lack of background high frequency vibrations, which were present during when using the Mann model and reduced the feeling of realism

for the pilot. However, these high frequency disturbances did not have any impact on handling.

The overall impact of both models was similar in the nature of the disturbances generated and how they affected pilot control response. Demonstrating that the SEM model can be calibrated to provide desired disturbances based on external data. The calibration techniques applied to the turbulence fields pre-generated using the Mann model, can also be applied to datasets from other sources, such as CFD simulations or real-world flow velocity measurements.

9.1.3 Testing the feasibility of new tools to explore criteria and requirements for mitigation of hazards:

Piloted flight simulation tests were conducted using a Bell 412 helicopter model. Two tasks were performed to assess impact of the SEM turbulence model on two flight conditions: a precision hover task as defined by the Aeronautical Design Standards – 33 and a custom designed steady and level flight task, performed at 40kts and 60kts.

9. Testing showed that the model was capable of working in real time and produces multi-axis disturbances that impact pilot workload and task performance and exposes handling qualities deficiencies of the aircraft. Pilot feedback suggested a realistic feeling of turbulence, being particularly representative of high-altitude conditions over offshore environments.
10. Precision hover was the task most affected by turbulence. In the case of the Bell 412 helicopter, which lacks any stability augmentation in heave, the main impact of turbulence was the degradation of height control. This then also translated into disturbances in heading due to cross couplings, and longitudinal positioning due to the longitudinal instability of the Bell 412 and the standard ADS-33 hover track providing poor visual cueing.
11. Simulation results show a trend of a higher turbulence intensity, of lower average frequency, resulting in larger workload increases. This coincides with findings reported from previous work. It is interesting to note that most operational guidance on operating under turbulence only provides limits on turbulence intensity or standard deviation (see CAA limits in Section 2.1.2.3).
12. The SEM model also impacts forward flight, although greater aircraft stability during forward flight and reduced requirements of the task resulted in much lower impact on workload and task performance. In these conditions,

increases in pilot workload are mainly driven by increased activity in the lateral and longitudinal controls in order to maintain lateral positioning and constant flight speed. Workload seems to peak when, including effect of aircraft flight speed, turbulence experienced by the aircraft has an average frequency of around 1Hz to 1.5 Hz, a frequency near bandwidth limits in the lateral and longitudinal controls of the aircraft.

13. When input parameters to the SEM model have been calibrated to match the turbulent spectra of a Mann turbulence field, the impact of turbulence on helicopter flight and pilot activity is similar for both models. During a precision hover MTE the most significant disturbances for both models were in the longitudinal and heave axis and required similar corrective pilot activity to compensate for the effect of the disturbance. For a given turbulence intensity, highest impact on workload and task performance was for wavelengths between 15m and 30m, with both models having a lower impact at larger or smaller wavelengths.

9.2 Recommendations for Future Work

9.2.1 Additional research in wind turbine wake encounters:

Flight simulation trials of wind turbine wake encounters performed during the project have provided insight into future applications in support of offshore missions and highlight possible handling qualities issues that might arise. Further research is needed to ascertain the effects on safety of an accidental encounter between rotorcraft and wind turbine wakes. This can be achieved by expanding the dataset by performing additional tests with different pilots and a wider range of aircraft models. Validation with real world data, such as helicopter Fight Data Monitoring records, should be a priority. Research is required to investigate the relationship between helicopter attitude deviations in yaw and pitch and during higher severity wake encounters that will be produced from the planned increase in wind turbine blade diameter. Assessments of methods to detect wake hazards e.g. in-flight LiDAR, and the possibility of reducing hazards by mitigating these upsets through displays for pilots are also aspects that merit further examination.

9.2.2 Further development and applications of the SEM turbulence model for flight simulation:

The SEM method has been proposed as an intermediate approach between high fidelity turbulent modelling approaches, requiring complex setup or previous data collection, and the flexibility, simplicity and variability of stochastic models. Testing in this project has shown that the SEM method has the potential to be used as a turbulence modelling method for real-time flight simulation and hazard assessments.

The SEM model is applicable for the simulation of unstructured turbulence and airwakes and can be tuned to reproduce turbulence with a desired frequency power spectrum, by modifying the eddy shape function, number of series of eddies, the size of eddies within these series and their value of Reynolds stress tensor. This tuning can be based on data from measurements or simulations, or just by adjustment to a theoretical turbulence spectrum such as the von Karman or Dryden model. This allows the SEM to be employed using different degrees of fidelity depending on the simulation objectives. The SEM generates random turbulence in real time using only a small number of parameters as input, without the need to store the pre-computed wakes and load the entire dataset in advance of each simulation session. There is however a need to compare the model against real word flight data under conditions of turbulence which was not available for this thesis.

A drawback of the SEM approach is that average frequency of the generated turbulence is inversely proportional to the size of eddies, which have to fill the control volume of interest. This makes computational costs of the model directly proportional to the cube of the desired average frequency. While the current implementation has shown to be able to work in real-time and produce disturbances in the frequencies of interest, lack of high frequency background vibrations reduced the feeling of realism during piloted flight simulation.

The current model was built and run using Mathworks Simulink modelling tool, which allowed rapid turnaround and concept testing of models but requires large computational resources. Use of faster programming languages might improve the speed of the model. In addition, turbulent flows induced by each eddy on each ACP is not dependent on the rest of the eddies or ACPs, meaning that the model should be relatively easy to parallelize.

An interesting possibility for future development of the model is to adjust the parameters of the eddies based on their location. This could be developed from tabulated data based on available experimental measurements or higher fidelity fluid dynamics simulations. Such options might present a route to more realistic but still random turbulence models.

Potential applications for such a tool would be in the creation of flight simulation scenarios of turbulent environments. Going back to the initial goal of addressing impact of wind turbine wakes on helicopter operations, the SEM model could be used to generate background atmospheric turbulence, based for example on available wind velocity measurements from the wind farm meteorological station, and combined with a prescribed vortex model for the near wake of the wind turbine.

A tabulated dataset of SEM input parameters based on location can be developed in the future to reproduce the unstructured turbulence near obstacles, for example near the wind turbine nacelle during winching operations or within the far – wake of other turbines to account for accidental encounters (see for example Figure 2-6).

Other flight simulation scenarios in which the SEM could be applied are the modelling of the turbulent airwake over the helideck of ships or offshore platforms or for low level flight within urban environments for eVTOL aircraft.

References

[1] F. D. Harris, “No Accidents That’s the Objective; The 26th Alexander A. Nikolsky Lecture,” *J. Am. Helicopter Soc.*, vol. 52, no. 1, pp. 3–14, Jan. 2007, doi: 10.4050/JAHS.52.3.

[2] M. Masson, M. Van Hijum, M. Bernandersson, and A. Evans, “The European Helicopter Safety Team (EHEST): 2008/2009 achievements,” *35th Eur. Rotorcr. Forum 2009, ERF 2009*, vol. 1, pp. 113–126, 2009.

[3] G. Quaranta, M. Pavel, G. Barakos, M. White, and M. Mulder, “NITROS : An Innovative Training Program to Enhance Rotorcraft Safety,” *AHS Int. 74th Annu. Forum Technol. Disp.*, 2018.

[4] E. Rooseleer, Frederic and E. Treve, Vincent, “Recat-EU, European Wake Turbulence Categorisation and Separation Minima on Approach and Departure,” *Rep. - Eurocontrol*, 2015.

[5] S. Schönhals, M. Steen, and P. Hecker, “Towards wake vortex safety and capacity increase: the integrated fusion approach and its demands on prediction models and detection sensors,” *Proc. Inst. Mech. Eng. Part G J. Aerosp. Eng.*, vol. 227, no. 1, pp. 199–208, Jan. 2011, doi: 10.1177/0954410011422478.

[6] J. Ehlers, D. Fischenberg, and D. Niedermeier, “Wake Impact Alleviation Control Based on Wake Identification,” *J. Aircr.*, vol. 52, no. 6, pp. 2077–2089, Nov. 2015, doi: 10.2514/1.C033157.

[7] UK Civil Aviation Authority, “CAA PAPER 2004/03 Helicopter Turbulence Criteria for Operations to Offshore Platforms,” 2004.

[8] I. Owen, M. D. White, G. D. Padfield, and S. J. Hodge, “A virtual engineering approach to the ship-helicopter dynamic interface – a decade of modelling and simulation research at the University of Liverpool,” *Aeronaut. J.*, vol. 121, no. 1246, pp. 1833–1857, Dec. 2017, doi: 10.1017/aer.2017.102.

[9] B. Lawrence and G. D. Padfield, “Wake vortex encounter severity for rotorcraft in final approach,” *Aerosp. Sci. Technol.*, vol. 12, no. 5, pp. 385–397, Jul. 2008, doi: 10.1016/j.ast.2007.09.006.

[10] WindEurope, “Wind in power 2017,” no. February, pp. 1–12, 2018, [Online]. Available: https://windeurope.org/wp-content/uploads/files/about-wind/statistics/WindEurope-Annual-Statistics-2017.pdf.

[11] Y. Wang, M. White, and G. Barakos, “Wind Turbine Wake Encounter Study,” Mar. 2015. doi: 10.1016/j.tics.2013.12.009.

[12] R. Roorman, “Assessing Viability in Offshore Wind,” *Rotor and Wind*, 2018. .

[13] Safety & Airspace Regulation Group, “CAP 764: CAA Policy and Guidelines on Wind Turbines,” *Civ. Aviat. Auth.*, 2016, [Online]. Available: http://www.caa.co.uk/docs/33/cap764.pdf.

[14] “Offshore wind turbine suction and safe helicopter operations, NLR Report,” 2016. [Online]. Available: https://maritime-spatial-

planning.ec.europa.eu/practices/offshore-wind-turbine-suction-and-safe-helicopter-operations.

[15] I. De Visscher, G. Winckelmans, and V. Treve, “A Simple Wake Vortex Encounter Severity Metric - Rolling Moment Coefficient due to Encounter of an Aircraft with a Wake Vortex,” *Proc. Elev. USA/Europe Air Traffic Manag. Res. Dev. Semin.*, pp. 1–10, 2015.

[16] G. Van Baren, V. Treve, F. Rooseleer, P. Van der Geest, and B. Heesbeen, “Assessing the severity of wake encounters in various aircraft types in piloted flight simulations,” in *AIAA Modeling and Simulation Technologies Conference*, Jan. 2017, no. January, pp. 1–16, doi: 10.2514/6.2017-1084.

[17] EUROCONTROL, “RECAT-EU Separation Scheme.”

[18] R. Luckner, G. Höhne, and M. Fuhrmann, “Hazard criteria for wake vortex encounters during approach,” *Aerosp. Sci. Technol.*, vol. 8, no. 8, pp. 673–687, 2004, doi: 10.1016/j.ast.2004.06.008.

[19] *CS - 27 Certification Specifications and Acceptable Means of Compliance for Small Rotorcraft*. European Aviation Safety Agency, 2016.

[20] *CS - 29 Certification Specifications and Acceptable Means of Compliance for Large Rotorcraft*. European Aviation Safety Agency, 2016.

[21] “Aeronautical Design Standards - Performance Specification Handling Qualities Requirements for Military Rotorcraft,” *United States Army Aviat. Missile Command*, vol. E-PRF, 2000.

[22] R. H. Hoh, D. G. Mitchell, B. L. Aponso, D. L. Key, and C. Blanken L., “Special Report RDMR-AD-16-01: Background Information and User’s Guide for Handling Qualities Requirements for Military Rotorcraft,” *Aviat. Dev. Dir. Ames Res. Cent.*, 1989, [Online]. Available: https://apps.dtic.mil/dtic/tr/fulltext/u2/1000418.pdf.

[23] J. A. Lusardi, W. von Gruenhagen, and S. Seher-Weiss, “Parametric Turbulence Modeling for Rotorcraft Applications, Approach, Flight Tests and Verification,” *Rotorcr. Handl. Qual.*, no. November, pp. 4–6, 2008, [Online]. Available: http://scholar.google.com/scholar?hl=en&btnG=Search&q=intitle:Parametric+Turbulence+Modeling+for+Rotorcraft+Applications+Approach+,+Flight+Tests+and+Verification#0.

[24] T. Berger, C. M. Ivler, M. G. Berrios, M. B. Tischler, and D. G. Miller, “Disturbance Rejection Handling Qualities Criteria for Rotorcraft,” *Am. Helicopter Soc. 72nd Annu. Forum, West Palm Beach, FL*, 2016.

[25] A. J. Garcia and G. N. Barakos, “Helicopter Wake Encounters in the Context of Recat - Eu,” *Eur. Rotorcr. Forum (ERF 2017)*, pp. 12–15, 2017.

[26] F. Köpp, “Wake-vortex characteristics of military-type aircraft measured at airport oberpfaffenhofen using the DLR laser doppler anemometer,” *Aerosp. Sci. Technol.*, vol. 3, no. 4, pp. 191–199, Jun. 1999, doi: 10.1016/S1270-9638(99)80042-X.

[27] P. H. Lehmann, M. Jones, and M. Höfinger, “Impact of turbulence and degraded visual environment on pilot workload,” *CEAS Aeronaut. J.*, vol. 8, no.

3, pp. 413–428, 2017, doi: 10.1007/s13272-017-0246-3.

[28] W. A. Memon, I. Owen, and M. D. White, “SIMSHOL: A Predictive Simulation Approach to Inform Helicopter–Ship Clearance Trials,” *J. Aircr.*, vol. 57, no. 5, pp. 854–875, Sep. 2020, doi: 10.2514/1.C035677.

[29] UK Civil Aviation Authority, “CAP 437 Standards for Offshore Helicopter Landing Areas,” 2013.

[30] “CAA Paper 2009 / 03: Offshore Helideck Environmental Research,” 2009.

[31] C. Aragon and K. Long, “Airflow Hazard Visualization for Helicopter Pilots: Flight Simulation Study Results,” *Am. Helicopter Soc. June 2005, Grapevine, Texas*, [Online]. Available: https://ntrs.nasa.gov/archive/nasa/casi.ntrs.nasa.gov/20050184140.pdf.

[32] C. A. Macdonald and R. Bradley, “Derivation of control activity metrics for the rule-based prediction of helicopter pilot workload,” *Aeronaut. J.*, no. 2862, pp. 245–254, 2004.

[33] Offshore Energy Liaison Officer, HM Coastguard, and MCA, “Offshore Renewable Energy Installations: Requirements, Guidance and Operational Considerations for Search and Rescue and Emergency Response,” no. November, pp. 1–56, 2018, [Online]. Available: https://assets.publishing.service.gov.uk/government/uploads/system/uploads/attachment_data/file/762365/OREI_SAR_Requirements_v2.0.pdf.

[34] R. Krishnamurthy, J. Reuder, B. Svardal, H. J. S. Fernando, and J. B. Jakobsen, “Offshore Wind Turbine Wake characteristics using Scanning Doppler Lidar,” *Energy Procedia*, vol. 137, pp. 428–442, 2017, doi: 10.1016/j.egypro.2017.10.367.

[35] M. Carriõn, R. Steijl, M. Woodgate, G. Barakos, X. Munduate, and S. Gomez-Iradi, “Computational fluid dynamics analysis of the wake behind the MEXICO rotor in axial flow conditions,” *Wind Energy*, vol. 18, no. 6, pp. 1023–1045, Jun. 2015, doi: 10.1002/we.1745.

[36] A. C. Kirby, A. Hassanzadeh, D. J. Mavriplis, and J. Naughton, “Wind Turbine Wake Dynamics Analysis Using a High-Fidelity Simulation Framework with Blade-Resolved Turbine Models,” *Am. Inst. Aeronaut. Astronaut.*, pp. 1–22.

[37] M. Carrión, M. Woodgate, R. Steijl, G. N. Barakos, S. Gomez-Iradi, and X. Munduate, “Understanding Wind-Turbine Wake Breakdown Using Computational Fluid Dynamics,” *AIAA J.*, vol. 53, no. 3, pp. 588–602, 2015, doi: 10.2514/1.J053196.

[38] J. N. Sorensen, R. F. Mikkelsen, D. S. Henningson, S. Ivanell, S. Sarmast, and S. J. Andersen, “Simulation of wind turbine wakes using the actuator line technique,” *Philos. Trans. R. Soc. A Math. Phys. Eng. Sci.*, vol. 373, no. 2035, pp. 20140071–20140071, 2015, doi: 10.1098/rsta.2014.0071.

[39] A. N. Kolmogorov, “The local structure of turbulence in incompressible viscous fluid for very large Reynolds numbers,” *Proc. R. Soc. London. Ser. A Math. Phys. Sci.*, vol. 434, no. 1890, pp. 9–13, Jul. 1991, doi: 10.1098/rspa.1991.0075.

[40] N. M. Komerath, M. J. Smith, and C. Tung, “A Review of Rotor Wake Physics and Modeling,” *J. Am. Helicopter Soc.*, vol. 56, no. 2, pp. 22006–2200619, 2011, doi: 10.4050/JAHS.56.022006.

[41] B. Sanderse, S. P. van der Pijl, and B. Koren, “Review Of CFD For Wind-Turbine Wake Aerodynamics,” *Wake Model.*, pp. 1–28, 2010, doi: 10.1002/we.458.

[42] T. Göçmen, P. Van Der Laan, P. E. Réthoré, A. P. Diaz, G. C. Larsen, and S. Ott, “Wind turbine wake models developed at the technical university of Denmark: A review,” *Renew. Sustain. Energy Rev.*, vol. 60, pp. 752–769, 2016, doi: 10.1016/j.rser.2016.01.113.

[43] W. R. M. Van Hoydonck, H. Haverdings, and M. D. Pavel, “A review of rotorcraft wake modeling methods for flight dynamics applications,” in *35th European Rotorcraft Forum 2009*, 2009, pp. 1–27.

[44] Y. Wang, V. Leble, M. White, and G. N. Barakos, “Wake Characteristics of Large-scale Wind Turbines,” *2015 Eur. Rotorcr. Forum*, pp. 87–98, 2015.

[45] G. C. Larsen *et al.*, “Dynamic wake meandering modeling,” 2007. [Online]. Available: http://orbit.dtu.dk/en/publications/dynamic-wake-meandering-modeling(0941893d-2a96-437e-9a19-8dd7dd7a3141).html.

[46] W. . Jones and B. . Launder, “The prediction of laminarization with a two-equation model of turbulence,” *Int. J. Heat Mass Transf.*, vol. 15, no. 2, pp. 301–314, Feb. 1972, doi: 10.1016/0017-9310(72)90076-2.

[47] J. M. O’Brien, T. M. Young, J. M. Early, and P. C. Griffin, “An assessment of commercial CFD turbulence models for near wake HAWT modelling,” *J. Wind Eng. Ind. Aerodyn.*, vol. 176, no. February, pp. 32–53, 2018, doi: 10.1016/j.jweia.2018.03.001.

[48] N. S. Dhamankar, G. A. Blaisdell, and A. S. Lyrintzis, “An Overview of Turbulent Inflow Boundary Conditions for Large Eddy Simulations (Invited),” Jun. 2015, doi: 10.2514/6.2015-3213.

[49] N. Jarrin, “Syntethic Inflow Boundary Conditions for the Numerical Simulation of Turbulence,” *Univ. Manchester - PhD Thesis*, 2008, [Online]. Available: papers3://publication/uuid/30C73EC3-BF64-4638-9A13-2FDF556EE3C0.

[50] T. S. Lund, X. Wu, and K. D. Squires, “Generation of Turbulent Inflow Data for Spatially-Developing Boundary Layer Simulations,” *J. Comput. Phys.*, vol. 140, no. 2, pp. 233–258, Mar. 1998, doi: 10.1006/jcph.1998.5882.

[51] J. Mann, “Wind field simulation,” *Probabilistic Eng. Mech.*, vol. 13, no. 4, pp. 269–282, Oct. 1998, doi: 10.1016/S0266-8920(97)00036-2.

[52] V. Leble, “Integrated simulation of off-shore wind turbine,” University oif Glasgow, 2016.

[53] M. Klein, A. Sadiki, and J. Janicka, “A digital filter based generation of inflow data for spatially developing direct numerical or large eddy simulations,” *J. Comput. Phys.*, vol. 186, no. 2, pp. 652–665, 2003, doi: 10.1016/S0021-9991(03)00090-1.

[54] N. Jarrin, S. Benhamadouche, D. Laurence, and R. Prosser, “A synthetic-eddy-

method for generating inflow conditions for large-eddy simulations," *Int. J. Heat Fluid Flow*, vol. 27, no. 4, pp. 585–593, Aug. 2006, doi: 10.1016/j.ijheatfluidflow.2006.02.006.

[55] G. H. Gaonkar, "Review of Turbulence Modeling and Related Applications to Some Problems of Helicopter Flight Dynamics," *J. Am. Helicopter Soc.*, vol. 53, no. 1, p. 87, 2008, doi: 10.4050/JAHS.53.87.

[56] J. A. Lusardi, M. B. Tischler, C. L. Blanken, and S. J. Labows, "Empirically Derived Helicopter Response Model and Control System Requirements for Flight in Turbulence," *J. Am. Helicopter Soc.*, vol. 49, no. 3, pp. 340–349, 2009, doi: 10.4050/jahs.49.340.

[57] J. W. Bunnell, "An Integrated Time-Varying Airwake In a UH-60 Black Hawk Shipboard Landing Simulation," 2001.

[58] S. J. Hodge, J. S. Forrest, G. D. Padfield, and I. Owen, "Simulating the environment at the helicopter-ship dynamic interface: research, development and application," *Aeronaut. J.*, vol. 116, no. 1185, pp. 1155–1184, Nov. 2012, doi: 10.1017/S0001924000007545.

[59] S. A. Polsky, "A computational study of unsteady ship airwake," *40th AIAA Aerosp. Sci. Meet. Exhib.*, vol. 069, no. May, pp. 7–11, 2002, doi: 10.2514/6.2002-1022.

[60] P. Scott, I. Owen, and M. White, "The effect of ship size on the flying qualities of maritime helicopters," *Annu. Forum Proc. - AHS Int.*, vol. 2, no. January 2016, pp. 862–872, 2014, [Online]. Available: https://www.researchgate.net/publication/277637802_The_Effect_of_Ship_Size_on_the_Flying_Qualities_of_Maritime_Helicopters.

[61] N. A. Watson, M. F. Kelly, I. Owen, and M. D. White, "The aerodynamic effect of an oblique wind on helicopter recovery to the Queen Elizabeth class aircraft carrier," *Vert. Flight Soc. - Forum 75, Philadelphia, PN*, 2019.

[62] G. R. Whitehouse and R. E. Brown, "Modeling the mutual distortions of interacting helicopter and aircraft wakes," *J. Aircr.*, vol. 40, no. 3, pp. 440–449, 2003, doi: Doi 10.2514/2.3139.

[63] C. Crozon, R. Steijl, and G. N. Barakos, "Coupled flight dynamics and CFD – demonstration for helicopters in shipborne environment," *Aeronaut. J.*, vol. 122, no. 1247, pp. 42–82, Jan. 2018, doi: 10.1017/aer.2017.112.

[64] T. von Karman, "Progress in the Statistical Theory of Turbulence," *Proc. Natl. Acad. Sci.*, vol. 34, no. 11, pp. 530–539, Nov. 1948, doi: 10.1073/pnas.34.11.530.

[65] H. L. Dryden, "A review of the statistical theory of turbulence," *Q. Appl. Math.*, vol. 1, no. 1, pp. 7–42, Apr. 1943, doi: 10.1090/qam/8209.

[66] B. Etkin, "Turbulent Wind and Its Effect on Flight," *J. Aircr.*, vol. 18, no. 5, pp. 327–345, May 1981, doi: 10.2514/3.57498.

[67] R. A. Hess, "Rotorcraft Handling Qualities in Turbulence," *J. Guid. Control. Dyn.*, vol. 18, no. 1, pp. 39–45, 2008, doi: 10.2514/3.56654.

[68] R. I. Harris, “Some further thoughts on the spectrum of gustiness in strong winds,” *J. Wind Eng. Ind. Aerodyn.*, vol. 33, no. 3, pp. 461–477, 1990, doi: 10.1016/0167-6105(90)90001-S.

[69] G. H. Gaonkar, “Nonlinear Stochastic Modeling of Airwake Turbulence for Helicopter Shipboard Operations,” *Am. Helicopter Soc. Phoenix, Arizona; May 2006*, p. 3.

[70] “MIL-STD-1797A: Interface Standard, Flying qualities of piloted aircraft,” *Dep. Def. Handb.*, 1997.

[71] Y. Y. Dang, S. Subramanian, and G. H. Gaonkar, “Modeling Turbulence Seen by Multibladed Rotors for Predicting Rotorcraft Response with Three-Dimensional Wake,” *J. Am. Helicopter Soc.*, vol. 42, no. 4, pp. 337–349, Oct. 1997, doi: 10.4050/JAHS.42.337.

[72] R. E. Mcfarland and K. Duisenberg, “Simulation of rotor blade element turbulence,” *NASA Tec. Memo. 108862*, 1995.

[73] H. Ji, R. Chen, L. Lu, and M. D. White, “Pilot workload investigation for rotorcraft operation in low-altitude atmospheric turbulence,” *Aerosp. Sci. Technol.*, vol. 111, p. 106567, 2021, doi: 10.1016/j.ast.2021.106567.

[74] J. a Lusardi, C. L. Blanken, and M. B. Tischler, “Piloted Evaluation of a UH-60 Mixer Equivalent Turbulence Simulation Model,” *AHS 53th Annu. Forum Am. Helicopter Soc.*, pp. 1–12, 2003, [Online]. Available: papers2://publication/uuid/E451EED5-635E-4EA6-ADAD-AE1EEA8EFC79.

[75] S. Seher-Weiss and W. Von Gruenhagen, “Development of EC 135 turbulence models via system identification,” *Aerosp. Sci. Technol.*, vol. 23, no. 1, pp. 43–52, 2012, doi: 10.1016/j.ast.2011.09.008.

[76] R. A. Hess, “Technical note a simplified and approximate technique for scaling rotorcraft control inputs for turbulence modeling,” *J. Am. Helicopter Soc.*, vol. 49, no. 3, pp. 361–366, Jul. 2004, doi: 10.4050/jahs.49.361.

[77] W. R. Mantay, G. T. Holbrook, R. L. Campbell, and R. L. Tomaine, “Helicopter Response to an Airplane ’ s Trailing Vortex,” vol. 14, no. 4, 1977, doi: 10.2514/3.58784.

[78] S. Saito, A. Azuma, K. Kawachi, and Y. Okuno, “STUDY OF THE DYNAMIC RESPONSE OF HELICOPTERS TO A LARGE AIRPLANE WAKE,” 1986.

[79] S. SAITO, A. AZUMA, Y. OKUNO, and T. HASEGAWA, “NUMERICAL SIMULATIONS OF DYNAMIC RESPONSE OF FIXED AND ROTARY WING AIRCRAFT TO A LARGE AIRPLANE WAKE,” in *13th EUROPEAN ROTORCRAFT FORUM*, 1987, no. 1.

[80] G. P. Turner, G. D. Padfield, and M. Harris, “Encounters with Aircraft Vortex Wakes: The Impact on Helicopter Handling Qualities,” *J. Aircr.*, vol. 39, no. 5, pp. 839–849, Sep. 2002, doi: 10.2514/2.3004.

[81] G. D. Padfield, B. Manimala, and G. P. Turner, “A Severity Analysis for Rotorcraft Encounters with Vortex Wakes,” no. Ref 3, pp. 1–14, 2002.

[82] B. Lawrence, G. D. Padfield, and A. Taghizad, “Rotorcraft Wake Vortex

Encounters : a Flight Mechanics Perspective," in *32nd European Rotorcraft Forum*, 2006, pp. 1–32.

[83] D. Vechtel, A. Stephan, and F. Holzäpfel, "Simulation study of severity and mitigation of wake-vortex encounters in ground proximity," *J. Aircr.*, vol. 54, no. 5, 2017, doi: 10.2514/1.C033995.

[84] Y. Wang, M. White, and G. Barakos, "Helicopter Wake Encounter Study; University of Liverpool Report for CAA," 2015.

[85] J. S. Forrest, I. Owen, G. D. Padfield, and S. J. Hodge, "Ship-Helicopter Operating Limits Prediction Using Piloted Flight Simulation and Time-Accurate Airwakes," *J. Aircr.*, vol. 49, no. 4, pp. 1020–1031, 2012, doi: 10.2514/1.C031525.

[86] M. D. White, P. Perfect, G. D. Padfield, A. W. Gubbels, and A. C. Berryman, "Acceptance testing and commissioning of a flight simulator for rotorcraft simulation fidelity research," *Proc. Inst. Mech. Eng. Part G J. Aerosp. Eng.*, vol. 227, no. 4, pp. 663–686, Apr. 2013, doi: 10.1177/0954410012439816.

[87] Z. C. Z. Thomas E. Mulinazzi, "Wind Farm Turbulence Impacts on General Aviation Airports in Kansas," no. January, 2014.

[88] Z. Yang, P. Sarkar, and H. Hu, "Visualization of the tip vortices in a wind turbine wake," *J. Vis.*, vol. 15, no. 1, pp. 39–44, Feb. 2012, doi: 10.1007/s12650-011-0112-z.

[89] D. Kocurek, "Lifting Surface Performance Analysis for Horizontal Axis Wind Turbines," 1987.

[90] T.S. Beddoes, "A Wake Model for High Resolution Airloads."

[91] D. J. Schmidt, D. E. Daniele, and D. B. Stoevesandt, "Boenbelastung von UL-Flugzeugen durch den Turbulenten Nachlauf von Windenergieanlagen," 2014.

[92] C. Varriale, A. De Marco, E. Daniele, J. Schmidt, and B. Stoevensandt, "Flight Load Assessment for Light Aircraft Landing Trajectories in Windy Atmosphere and Near Wind Farms," *Aerospace*, vol. 5, no. 2, 2018, doi: 10.3390/aerospace5020042.

[93] R. Bakker *et al.*, "Wind turbine wakes and helicopter operations, an overview of the GARTEUR HC-AG23 activities," *44th Eur. Rotorcr. Forum*, 2018.

[94] B. G. Van Der Wall and P. H. Lehmann, "About the Impact of Wind Turbine Wake Vortices on Helicopter Trim and Rotor Blade Motion," *Eur. Rotorcr. Forum; Sept. 2017; Milan, Italy*.

[95] B. G. Van Der Wall, "Orthogonal Vortex-Rotor Interaction: Impact on Rotor Controls, Blade Flapping, Thrust and Power," *Eur. Rotorcr. Forum; Sept. 2018; Delft, Netherlands*, 2018.

[96] B. Benoit, A.-M. A. Dequin, K. Kampa, W. Grünhagen, P.-M. Basset, and B. Gimonet, "HOST, a General Helicopter Simulation Tool for Germany and France," 2000, no. May.

[97] A. Visingardi and Marilena D. Pavel, "Numerical Investigations of the Aerodynamics and Handling Qualities of a Helicopter Flying across a Wind

Turbine Wake," 2018.

[98] J. Jonkman, S. Butterfield, W. Musial, and G. Scott, "NREL/TP-500-38060: Definition of a 5-MW Reference Wind Turbine for Offshore System Development," *Natl. Renew. Energy Lab.*, 2009, doi: 10.2172/947422.

[99] T. E. Andronikos, G. Papadakis, and V. Riziotis, "Aerodynamic Analysis of Helicopter in Interaction With Wind Turbine's Wake," 2018.

[100] A. Burtsev, "Helicopter Encounters with Wind Turbine Wakes, University of Liverpool, Internal Report," 2018.

[101] R. W. Du Val and C. He, "Validation of the FLIGHTLAB virtual engineering toolset," *Aeronaut. J.*, vol. 122, no. 1250, pp. 519–555, Apr. 2018, doi: 10.1017/aer.2018.12.

[102] V. Leble and G. Barakos, "10-MW Wind Turbine Performance Under Pitching and Yawing Motion," *J. Sol. Energy Eng.*, vol. 139, no. 4, p. 041003, Aug. 2017, doi: 10.1115/1.4036497.

[103] C. H. Kääriä, J. S. Forrest, and I. Owen, "The virtual AirDyn: A simulation technique for evaluating the aerodynamic impact of ship superstructures on helicopter operations," *Aeronaut. J.*, vol. 117, no. 1198, pp. 1233–1248, 2013, doi: 10.1017/S0001924000008836.

[104] V. L. OKULOV and J. N. SØRENSEN, "Maximum efficiency of wind turbine rotors using Joukowsky and Betz approaches," *J. Fluid Mech.*, vol. 649, p. 497, Apr. 2010, doi: 10.1017/S0022112010000509.

[105] C. J. Ockier, "Forschungsbericht 98-07: Evaluation of the ADS-33 Handling Qualities Criteria Using the Bo 105 Helicopter," *DLR*, 1998.

[106] G. D. Padfield, *Helicopter Flight Dynamics*, 2nd ed. Blackwell Publishing, 1996.

[107] A. H. Roscoe and A. H. Ellis, "Technical Report TR 90019: A subjective rating scale for assessing pilot workload in flight: A decade of practical use," *R. Aerosp. Establ.*, 1990.

[108] M. D. Pavel, M. White, G. D. Padfield, G. Roth, M. Hamers, and A. Taghizad, "Validation of mathematical models for helicopter flight simulators past, present and future challenges," *Aeronaut. J.*, vol. 117, no. 1190, pp. 343–388, Apr. 2013, doi: 10.1017/S0001924000008058.

[109] G. Padfield and M. White, "Measuring simulation fidelity through an adaptive pilot model," *Aerosp. Sci. Technol.*, vol. 9, no. 5, pp. 400–408, Jul. 2005, doi: 10.1016/j.ast.2005.03.004.

[110] P. Perfect, M. D. White, G. D. Padfield, and A. W. Gubbels, "Rotorcraft simulation fidelity: new methods for quantification and assessment," *Aeronaut. J.*, vol. 117, no. 1189, pp. 235–282, Mar. 2013, doi: 10.1017/S0001924000007983.

[111] A. W. Gubbels and S. J. R. P. Carignan, "Handling qualities assessment of the effects of tail boom strakes on the Bell 412 helicopter," *Aerosp. Sci. Technol.*, vol. 9, no. 5, pp. 436–444, Jul. 2005, doi: 10.1016/j.ast.2004.12.008.

[112] F. F. Dizaji, J. S. Marshall, and J. R. Grant, "A stochastic vortex structure

method for interacting particles in turbulent shear flows," *Phys. Fluids*, vol. 30, no. 1, 2018, doi: 10.1063/1.5007743.

[113] D. T. McRuer, "Interdisciplinary interactions and dynamic systems integration," *Int. J. Control*, vol. 59, no. 1, pp. 3–12, Jan. 1994, doi: 10.1080/00207179408923067.

[114] Y. Luo, H. Liu, Q. Huang, H. Xue, and K. Lin, "A multi-scale synthetic eddy method for generating inflow data for LES," *Comput. Fluids*, vol. 156, no. March 2019, pp. 103–112, 2017, doi: 10.1016/j.compfluid.2017.06.017.

[115] A. W. Gubbels, S. J. R. P. Carignan, and D. K. Ellis, "The NRC Bell 412 Advanced Systems Research Aircraft - Facility description and results of initial in-flight evaluation," *Am. Helicopter Soc. 58th Annu. Forum, Montr.*, 2002.

[116] W. A. Memon, I. Owen, and M. D. White, "Motion fidelity requirements for helicopter-ship operations in maritime rotorcraft flight simulators," *J. Aircr.*, vol. 56, no. 6, pp. 2189–2209, 2019, doi: 10.2514/1.C035521.

[117] G. E. Cooper and R. P. Harper, "NASA Tecnical Note: TN-D-5153: The use of pilot rating in the evaluation of aircraft handling qualities," Moffett Field, CA, 1969. [Online]. Available: https://ntrs.nasa.gov/archive/nasa/casi.ntrs.nasa.gov/19690013177.pdf.

[118] G. D. Padfield, J. P. Jones, M. T. Charlton, S. E. Howell, and R. Bradley, "Where Does The Workload Go When Pilots Attack Manoeuvres? An Analysis Of Results From Flying Qualities Theory And Experiment," *Twent. Eur. Rotorcr. Forum*, no. September 1994, 1994.

[119] S. Henriquez Huecas, M. White, and G. Barakos, "A turbulence model for flight simulation and handling qualities analysis based on a synthetic eddy method," *76th Vert. Flight Soc. Forum, Virginia Beach, VA*, 2020.

[120] Y. A, "Mann 64bit turbulence generator." Technical University of Denmark, 2018, [Online]. Available: https://www.hawc2.dk/download/pre-processing-tools.

[121] J. Mann, "The spatial structure of neutral atmospheric surface-layer turbulence," *J. Fluid Mech.*, vol. 273, no. February 1994, pp. 141–168, Aug. 1994, doi: 10.1017/S0022112094001886.

[122] N. Jarrin, R. Prosser, J. C. Uribe, S. Benhamadouche, and D. Laurence, "Reconstruction of turbulent fluctuations for hybrid RANS/LES simulations using a Synthetic-Eddy Method," *Int. J. Heat Fluid Flow*, vol. 30, no. 3, pp. 435–442, 2009, doi: 10.1016/j.ijheatfluidflow.2009.02.016.

[123] Y. Luo, H. Liu, Q. Huang, H. Xue, and K. Lin, "A multi-scale synthetic eddy method for generating inflow data for LES," *Comput. Fluids*, vol. 156, pp. 103–112, 2017, doi: 10.1016/j.compfluid.2017.06.017.

[124] R. G. Lee and S. J. Zan, "Wind Tunnel Testing of a Helicopter Fuselage and Rotor in a Ship Airwake," *J. Am. Helicopter Soc.*, vol. 50, no. 4, pp. 326–337, Oct. 2005, doi: 10.4050/1.3092869.

Appendix

A. Bedford workload rating scale [107]:

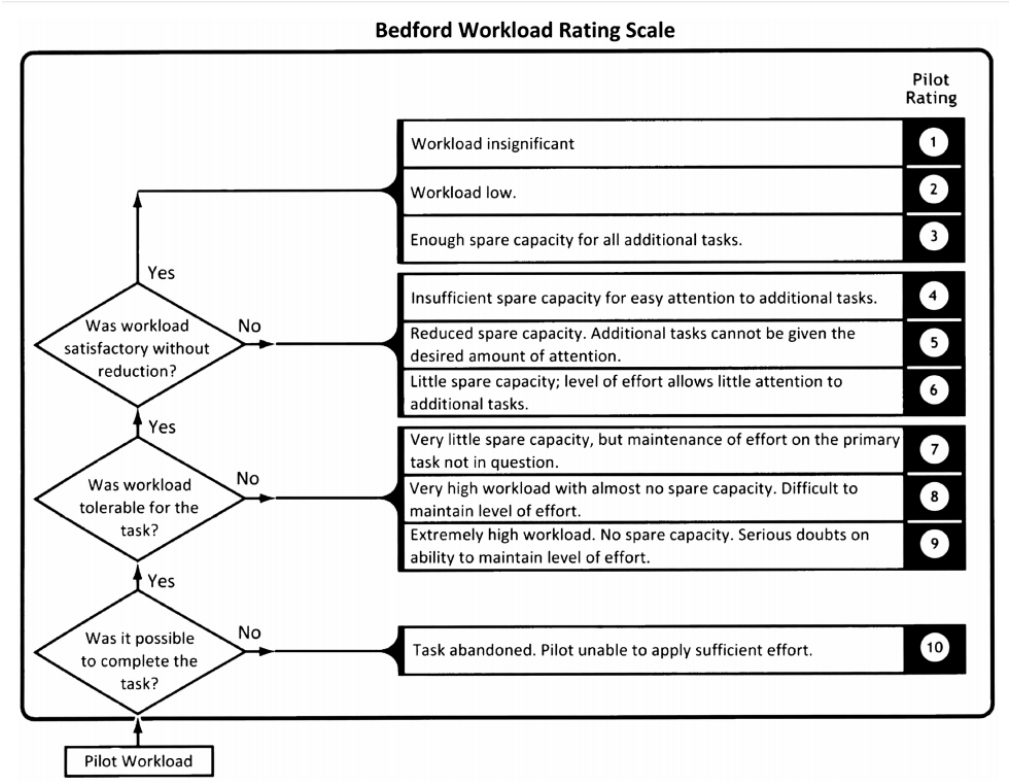

B. Cooper – Harper handling qualities rating scale [111]:

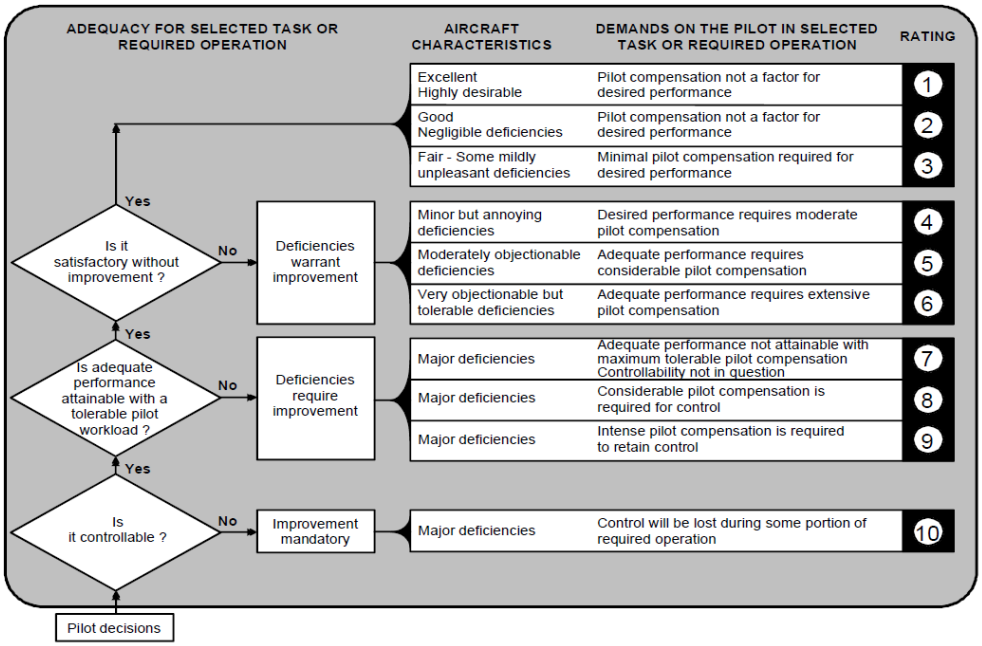

C. Questionnaire: Relevance of parameters to rating:

Mission (primarily intended for approach and hover scenarios):

Was mission abandoned due to safety concerns? (Go around)

Pilot's focus:

0 → Parameter was not important. Has not been monitored and/or required no pilot effort to control.

1 → Parameter was not important. Has been monitored and/or required limited pilot effort to control.

2 → Parameter was important. Required frequent monitoring and/or important pilot effort to control.

3 → parameter was very relevant. Dominated pilot's attention and effort during the encounter.

Parameter	0	1	2	3
Aircraft Attitude				
Roll				
Pitch				
Yaw				
Roll rate				
Pitch rate				
Yaw rate				
Proximity to the ground				
Height				
Vertical speed				
Environment				
Turbulence				
Mission:				
Trajectory relative to ground				
Horizontal speed				

Others:

Aircraft response to control inputs

Difficulty in stabilizing aircraft in the following axis was a relevant factor for the rating:

None	
Roll	
Pitch	
Yaw	
Vertical axis	

(If more than one, indicate order according to relevance.)

Aircraft control limits in the following axis were a relevant factor for the rating:

None	
Roll	
Pitch	
Yaw	
Vertical axis	

(If more than one, indicate order according to relevance.)

Delays in aircraft response to control inputs were a relevant factor for the rating:

None	
Roll	
Pitch	
Yaw	
Vertical axis	

(If more than one, indicate order according to relevance.)

Cross couplings between the following axes were a relevant factor for the rating:

None	
Pitch – Roll	
Roll – Pitch	
Yaw – Collective	
Collective – Yaw	

Others:

(If more than one, indicate order according to relevance.)

Unconventional or unexpected aircraft response in the following axes was a relevant factor for the rating:

None	
Roll	
Pitch	
Yaw	
Vertical axis	

(If more than one, indicate order according to relevance.)

If possible, please explain the nature of the response:

Pilot Induced Oscillations:

Have PIOs been experienced?

If yes, on which axis?

Roll	
Pitch	
Yaw	
Heave	
Other (specify): _____	

Additional comments

D. SEM Model MATLAB code

SEM MODULE MATLAB CODE – INITIALIZATION FUNCTION:

Executes once at the beginning of each simulation and is used to set SEM parameters for the simulation, establish initial conditions and create initial distribution of Eddies:

```
%Init_SEM: Set initialization variables and set initial distribution of
eddies

%for Synthetic Eddie Method:

%% Function outputs:

 % SEM Parameters:

    % InitSeed: Random seed for this simulation (integer)

    % dt: Simulation time step (s)

    % NACP: number of aircraft aerodynamic computation points (integer)

    % EdSeries: Number of different eddy series (integer)

    % NEddiesSeries: Number of Eddies for this series, N^m in equation [6-2]
(integer, 1 x EdSeries)

    % NEddies: Total number of Eddies (integer)

    % EddieSeries: Index indicating which series this eddy belongs to
(integer, 1 x NEddies)

    % BoxEdges: Location of box edges in box reference frame (ft, 3 x 2 x
EdSeries)

    % BoxVol: Total volume of box (ft^3)

    % Sigma: Reference size of Eddies (ft, 1 x 3)

    % A: Reference Cholesky decomposition of Reynolds stresses (ft/s, 3 x 3)

    % SigmaSc: Size scaler for each eddy series: q_m in equation [6-1],
(non-dimensional, 1 x EdSeries)

    % ReSc: ReSt scaler for each eddy series: p_m in equation [6-1], (non-
dimensional, 1 x EdSeries)

    % Shapefunction: Select Shape function (integer)

    % kParam: Decay Power for Gaussian shape function, k in equation [5-20]
(scalar)

    % GaussScale: Value of C for Gaussian shape function, C in equation
[5-20] (scalar)

  % Initial conditions:
```

```
    % Wind: Initial wind velocity in wind frame (ft/s, 1 x 3)

    % Vel0: Initial Aircraft speed in inertial frame (ft/s, 1 x 3)

    % PosEddie: Initial position of Eddies in inertial frame, x^k in equation
[6-4] (ft, NEddies x 3)

    % epsilon:  Initial eddy influence sign, ε in equation [6-4] (1 or -1,
NEddies x 3)

%%%%%%%%%%%%%%%%%%%%%%%%%%%%%%%%

%% User inputs

%Define if initial seed for random placement of Eddies is set randomly for
this run:

SetRandomSeed = true;

%Unit conversion Constants:

FtToMeter = 0.3048;

KnotToMeterS = 1.852/3.6;

DegToRad = pi/180;



%%FLIGHTLAB model parameters

%Number of aerodynamic computation points of aircraft model:

NACP = 25;

%Set simulation time step (s):

dt = (2*pi/33.9292)/12;

%For this case, FLIGHTLAB Bell 412 model:

% Rotor nominal speed = 33.9292 rad/s

% Steps per rotor revolution: 12



%%Initial conditions:

%Environment:

% Horizontal wind velocity (in ft/s)

WindMagh = 10*KnotToMeterS/FtToMeter;

% Horizontal Wind azimuth (in deg, 0deg: wind from north, 90deg: wind from
the east):

WindAzi = 90*DegToRad;

% Vertical wind velocity (ft/s)
```

```
WindMagv = 0;

%Flight conditions:

%Aircraft Starting position in FLIGHTLAB reference frame

%(right handed coordinate system, x points north, z points down, in ft):

PosHel0 = [0,0,-1000];


%Aircraft initial ground speed (magnitude in kts):

GroundSpeed = 0;

%Aircraft initial Ground track (in deg, 0 points north, positive turn
towards east):

GroundTrack = 0;

%Aircraft initial vertical speed (ft/s)

VClimb = 0;


%%SEM parameters:

%Number of Eddie Series:

EdSeries = 3;

%Size of reference Eddie (ft):

Sigma = [3, 3, 3]./FtToMeter;

%Reynolds stress tensor for reference Eddies ((ft/s)^2):

ReSt = [3, 0, 0; 0, 3, 0; 0, 0, 3]./(FtToMeter^2);

% Shape function used: 1 = Tent; 2 = Gauss

Shapefunction = 2;

% k parameter for Gauss Function:

kParam = 9/2;

%Size scaler for each eddy series: q_m;

SigmaSc = [1, 2, 3];

%ReSt scaler for each eddy series: p_m

ReScale = [1, 2, 3];

%ControlVolumeBox:

%Lenght of half a side for deffault box (ft):
```

```
BoxSideDef = 10.5/FtToMeter;
%Define min Num of Eddies in a box:
MinEddies = 10;

%%%%%%%%%%%%%%%%%%%%%%%%%%%%%%%%
%Start initialization function:
if SetRandomSeed == true
    %Set rng for Matlab initialization
    rng('shuffle')
    %Seed for random number generator:
    InitSeed = randi(1000000);
elseif SetRandomSeed == false
    InitSeed = 0;
end
% Set initial wind velocity vector:
WindX = WindMagh*cos(WindAzi);
WindY = WindMagh*sin(WindAzi);
WindZ = WindMagv;
Wind = [WindX, WindY, WindZ];
% Set initial aircraft speed vector:
VelX = GroundSpeed*cos(GroundTrack)*KnotToMeterS/FtToMeter;
VelY = GroundSpeed*sin(GroundTrack)*KnotToMeterS/FtToMeter;
VelZ = - VClimb;
Vel0 = [VelX, VelY, VelZ];
%Incoming aerodynamic velocity:
Vinc = -Vel0 + Wind;
%Obtain Orientation of incoming aerodynamic velocity, see [5-13]:
AlphaB = asin(-Vinc(3)/(norm(Vinc)));
BetaB = acos(Vinc(1)/(sqrt(Vinc(1)^2 + Vinc(2)^2)))*sign(Vinc(2));
%Cholesky decomposition of Reynolds stresses, equation [5-2]:
A = zeros(3,3);
```

```
A(1,1) = sqrt(ReSt(1,1));

A(2,1) = ReSt(2,1)/A(1,1);

A(2,2) = sqrt(ReSt(2,2)-A(2,1)^2);

A(3,1) = ReSt(3,1)/A(1,1);

A(3,2) = (ReSt(3,2)-A(2,1)*A(3,1))/A(2,2);

A(3,3) = sqrt(ReSt(3,3)-A(3,1)^2-A(3,2)^2);

%If eddy shape is Gaussian: Compute Gauss constant with equation [5-21]:

if Shapefunction == 2

    %Gauss scaling for normalization:

    GaussScale                                                                    =
(((2*kParam)^(1/2))/((pi^(1/2))*erf((2*kParam)^(1/2))))^(1/2);

else

    GaussScale = 0;

end

%Define Location of control volume edges in Box coordinates, the box is
always centered at the aircraft location and should contain all points used
for aerodynamic flow sampling, see Figure 5-2:

BoxEdgesDef = [ -BoxSideDef, BoxSideDef;

-BoxSideDef, BoxSideDef;

BoxSideDef, -BoxSideDef];

%Define total box volume

BoxVolDef = prod(abs(BoxEdgesDef(:,2)-BoxEdgesDef(:,1)));

%%Set number of Eddies and control volume box for each series:

nCount = 0;

%Iterate through each eddy series

for nS = 1:EdSeries

    %Define box size for this series as default box size:

    BoxSide(nS) = BoxSideDef;

    BoxEdges(:,:,nS) = [ -BoxSide(nS), BoxSide(nS);

    -BoxSide(nS), BoxSide(nS);

    BoxSide(nS), -BoxSide(nS)];

    BoxVol(nS) = prod(abs(BoxEdges(:,2,nS)-BoxEdges(:,1,nS)));

    %Volume of Eddie:
```

```
    SigmaVol(nS) = prod(Sigma*SigmaSc(nS));

    %Number of Eddies for this series in the box, should completely fill the
box, see equation [6-2]:

    NEddiesSeries(nS) = floor(BoxVol(nS)/SigmaVol(nS));

    %However, if this series has too few Eddies, create a larger box for
this specific series, see equation [6-3].

    %Big enough for the minimum number of Eddies

    if NEddiesSeries(nS) < MinEddies

        BoxVol(nS) = MinEddies*SigmaVol(nS);

        BoxSide(nS) = (BoxVol(nS)^(1/3))/2;

        BoxEdges(:,:,nS) = [ -BoxSide(nS), BoxSide(nS);

         -BoxSide(nS), BoxSide(nS);

         BoxSide(nS), -BoxSide(nS)];

        %Recompute the number of Eddies for this Series

        NEddiesSeries(nS) = floor(BoxVol(nS)/SigmaVol(nS));

    end

end

%Total Number of Eddies: sum of all eddies across all series.

NEddies = sum(NEddiesSeries);

%Fill the box with Eddies, Each Eddie is placed in the box following a
uniform random distribution :

PosEddie0 = zeros(NEddies, 3);

EddieSeries = int16(zeros(NEddies,1));

%Iterate through all Eddie series:

for nS = 1:EdSeries

    %Iterate through all Eddies of this series:

    for n = 1:NEddiesSeries(nS)

        %Iterate through each dimension

        for d = 1:3

            %Randomly place eddy in Box

            PosEddie0(n    +    nCount,d)    =    rand*(BoxEdges(d,2,nS)    -
BoxEdges(d,1,nS)) + BoxEdges(d,1,nS);

            %Randomly generate sign for each direction
```

```
            epsilon0(n + nCount,d) = randsample([-1,1],1);

            %Identify to which Series this eddy belongs to:

            EddieSeries(n + nCount) = nS;

        end

        %Asign Corresponding scaler for the eddy:

        EddieScale(n + nCount) = SigmaSc(nS);


        %Transform eddy coordinates: from box reference system to global

        %reference system:

        %Rotation:

        [PosEddie0(n + nCount,:)] = BoxToGlobal(PosEddie0(n + nCount,:)',
AlphaB, BetaB);

        %Translation to helicopter location:

        PosEddie0(n + nCount,:) = PosEddie0(n + nCount,:) + PosHel0;

    end

    nCount = nCount + NEddiesSeries(nS);

end
```

SEM MODULE MATLAB CODE – MOVEMENT OF EDDIES:

Executes once every time step. Moves Eddies with wind velocity and regenerates Eddies that fall outside control volume box:

```
function [ PosEddie, epsilon, StatusSeed, Vel, SEMUpdateStepPrev,
StatusSeed, VelPrev, PosHelPrev] = SEMUpdateEddies(SEMUpdateStepPrev,
FLStep, PosHel, PosEddie, epsilon, PosHelPrev, dt, NEddies, Wind,
BoxEdges,VelPrev, StatusSeed, InitSeed, EddieSeries)

%Inputs from Initialization function:

    % InitSeed: Random seed for this simulation (integer)

    % dt: Simulation time step (s)

    % NEddies: Total number of Eddies (integer)

    % BoxEdges: Location of box edges in box reference frame (ft, 3 x 2)

    % BoxVol: Total volume of control volume box (ft^3)

    % EddieSeries: Index indicating which series this eddy belongs to
(integer, 1 x NEddies)

%Inputs from previous time step and outputs to next time step:
```

```
    % SEMUpdateStepPrev: Previous FLIGHTLAB time step (integer)

    % StatusSeed: Was random seed set at start of simulation? (boolean)

    % VelPrev: Aircraft speed in inertial frame at previous timestep (ft/s,
1 x 3)

    % PosHelPrev: Aircraft location in inertial frame at previous timestep
(ft, 1 x 3)

    % PosEddie: Eddie location in inertial frame at previous timestep (ft,
NEddies x 3)

    % epsilon: Eddie influence sign at previous time step (1 or -1, NEddies
x 3)

%Inputs from FLIGHTLAB:

    % FLStep: Current FLIGHTLAB timestep (integer)

    % PosHel: Current Aircraft location in inertial frame (ft, 1 x 3)

    % Wind: Current Wind velocity in wind frame (ft/s, 1 x 3)

% Outputs:

    % PosEddie: Updated position of Eddies in inertial frame, x^k in equation
[6-4] (ft, NEddies x 3)

    % epsilon: Updated eddy influence sign, ε in equation [6-4](1 or -1,
NEddies x 3)

    % StatusSeed: Random seed was set at simulation start (boolean)

%%%%%%%%%%%%%%%%%%%%%%%%%%%%%%%

%Declare variables

Vel = single(zeros(1,3));

% Set Random seed selected at initialization:

if StatusSeed == false

    rng(InitSeed);

    StatusSeed = true;

end

% Define number of FLIGHTLAB steps elapsed since last simulink

% step (ideally should be 1, but this is set as a failsafe)

StepsElapsed = FLStep - SEMUpdateStepPrev;

% Determine how much simulation time has passed since last

% simulink step:

TimeElapsed = StepsElapsed*dt;
```

```
% Compute current aircraft velocity:
if TimeElapsed > 0
    Vel = (PosHel - PosHelPrev)./TimeElapsed;
else
    Vel = VelPrev;
end
%Transform wind velocity to simulation reference frame:
Vinf = WindToGlobal(Wind')';
%Total aerodynamic inflow Velocity:
Vinc = -Vel + Vinf;
%Obtain direction angles of inflow (to orient box accordingly:
AlphaB = asin(-Vinc(3)/(norm(Vinc)));
BetaB = acos(Vinc(1)/(sqrt(Vinc(1)^2 + Vinc(2)^2)))*sign(Vinc(2));
%Iterate through all Eddies
for n = 1:NEddies
    % Identify to which series this eddy belongs to:
    nS = EddieSeries(n);
    %Move The Eddie with wind:
    PosEddie(n,:) = PosEddie(n,:) + Vinf*TimeElapsed;
    %Transform position of Eddies to box coordinates:
    [PosEddie(n,:)] = GlobalToBox((PosEddie(n,:) - PosHel)', AlphaB, BetaB);
    %Determine if Eddies are within box:
    EddieInBox = true;
    for d = 1:3
        if PosEddie(n,d) < min(BoxEdges(d,:,nS)) || PosEddie(n,d) >
max(BoxEdges(d,:,nS))
            EddieInBox = false;
        end
    end
    %If Eddie is outside box.
    if EddieInBox == false
```

```
        %Randomly locate Eddie on Box entry:

      %Local x - axis is oriented along Vinc: regenerate eddy at a random
point between inflow and a distance equal to Vinc*TimeElapsed (ideally,
TimeElapsed should be equal to dt, but this is set as a failsafe):

       PosEddie(n,1)  =  rand*min(norm(Vinc)*TimeElapsed,BoxEdges(1,2,nS)  -
      BoxEdges(1,1,nS))    + BoxEdges(1,1,nS);

      %Local y - axis and z -axis form a right handed system with x.
Regenerate Eddies at a random location within the box:

       PosEddie(n,2)          =          rand*(BoxEdges(2,2,nS)          -
BoxEdges(2,1,nS))+BoxEdges(2,1,nS);

       PosEddie(n,3)          =          rand*(BoxEdges(3,2,nS)          -
BoxEdges(3,1))+BoxEdges(3,1,nS);

       for d = 1:3

           %Randomly generate sign for each direction

           epsilon(n,d) = randsample([-1,1],1);

       end

   end

   %Transform position of Eddies back to global coordinates

   [PosEddie(n,:)] = BoxToGlobal(PosEddie(n,:)', AlphaB, BetaB);

   PosEddie(n,:) = PosEddie(n,:) + PosHel;

end

%Output Data for next time step:

PosHelPrev = PosHel;

SEMUpdateStepPrev = FLStep;

VelPrev = Vel;



end
```

SEM MODULE MATLAB CODE – COMPUTE TURBULENCE:

Executes once every time step. Computes induced turbulence induced by each eddy on each aerodynamic computation point by applying equation [6-4]:

```
function [TurbVel]     = SEMTimeStepvTest(XAero, PosEddie, epsilon, NEddies,
A, SigmaVol, Sigma, BoxVol, SigmaSc, ReScale, NEddiesSeries, EddieSeries,
Shapefunction, GaussScale, kParam)

%Inputs from Initialization function:
```

```
    % A: Reference Cholesky decomposition of Reynolds stresses (ft/s, 3 x 3)

    % ReSc: ReSt scaler for each eddy series: p_m in equation [6-1], (non
dimensional, 1 x EdSeries)

    % Sigma: Reference size of Eddies (ft, 1 x 3)

    % SigmaVol: Volume of this series Eddies (ft^3, 1 x EdSeries)

    % SigmaSc: Size scaler for each eddy series: q_m in equation [6-1], (non
dimensional, 1 x EdSeries)

    % NEddies: Total number of Eddies

    % BoxVol: Total volume of box (ft^3)

    % EddieSeries: Index indicating which series this eddy belongs to
(integer, 1 x NEddies)

    % NEddiesSeries: Number of Eddies for this series (integer, 1 x
EdSeries)

    % Shapefunction: Selector for eddy shape function (integer)

    % kParam: Decay Power for Gaussian shape function, k in equation [5-20]
(scalar)

    % GaussScale: Value of C for Gaussian shape function, see equation
[5-20] (scalar)

%Inputs from update turbulence field:

    % PosEddie: Eddie location in inertial frame at previous timestep, x^k in
equation [6-4] (ft, NEddies x 3)

    % epsilon: Eddie influence sign at previous time step, ε in equation
[6-4](1 or -1,NEddies x 3)

%Inputs from FLIGHTLAB:

    % XAero: Position of aircraft aerodynamic computation points (ACP) in
inertial reference frame,  x^ACP in equation [6-4] (ft, NACP x 3)

% Outputs to FLIGHTLAB:

    % TurbVel: Turbulent velocity at each ACP in inertial frame, u'_i^ACP in
equation [6-4] (ft/s, NACP x 3)

%%%%%%%%%%%%%%%%%%%%%%%%%%%%%%%

%Declare variables

TurbVelACP = single(zeros(1,3));

TurbVel = single(zeros(size(XAero,1),3));

%Iterate through all Eddies

for n =1:NEddies

    %nS = series this eddy belongs to
```

```
    nS = EddieSeries(n);

    %Iterate through all ACPs:

    for p = 1:size(XAero,1)

        %Compute shape function:

        fSigma = (BoxVol(nS)/(SigmaVol(nS)))^(1/2);

        for d = 1:3

            r = abs((XAero(p,d) - PosEddie(n,d))/(Sigma(d)*SigmaSc(nS)));

            if r < 1

                if Shapefunction == 3

                % Select cosine eddy Shape

                fSigma = fSigma * (1/sqrt(3))*(1+cos(pi*r));

                elseif Shapefunction == 2

                % Select Gaussian eddy Shape

                fSigma = fSigma * GaussScale*exp(-(kParam)*r^2);

                elseif Shapefunction == 1

                % Select Tent eddy Shape

                fSigma = fSigma * sqrt(3/2)*(1-r);

                end

            else

                fSigma = fSigma * 0;

            end

        end

        % Turbulent velocity induced by this eddy on this ACP:

        VelEdACP                                                                =
((1/(single(NEddiesSeries(nS))^(1/2)))*(A*epsilon(n,:)')'*fSigma).*(ReScale(
nS)^(1/2));

        % Total turbulent velocity on this ACP is sum of turbulence induced
by all Eddies:

        TurbVel(p,:) = single(TurbVel(p,:) + VelEdACP);

    end

end
```

SEM MODULE MATLAB CODE – AXIS SYSTEM MATRIXES:

Transformation between control volume box coordinates (Box) and simulation inertial coordinates (Global):

```
%GlobalToBox

function [VectorBox] = GlobalToBox(VectorGlobal, AlphaB, BetaB);


T1 = [cos(BetaB), -sin(BetaB), 0;

      sin(BetaB), cos(BetaB),  0;

                0,          0,  1];

T2 = [cos(AlphaB), 0, sin(AlphaB);

                0, 1,           0;

     -sin(AlphaB), 0, cos(AlphaB)];

T = T1*T2;

VectorBox = T'*VectorGlobal;

End


%BoxToGlobal

function [VectorGlobal] = BoxToGlobal(VectorBox, AlphaB, BetaB);

T1 = [cos(BetaB), -sin(BetaB), 0;

      sin(BetaB), cos(BetaB),  0;

                0,          0,  1];

T2 = [cos(AlphaB), 0, sin(AlphaB);

                0, 1,           0;

     -sin(AlphaB), 0, cos(AlphaB)];

T = T1*T2;

VectorGlobal = T*VectorBox;

end
```

Transformation between FLIGHTLAB wind inertial coordinates (Wind, not a right handed system) and simulation inertial coordinates (Global):

```
%WindToGlobal

function [VectorBody] = WindToGlobal(VectorGlobal);

T = [-1, 0, 0;
```

```
      0, -1, 0;
      0, 0,-1];
VectorBody = T*VectorGlobal;
End
```